Université du Québec
Institut national de la recherche scientifique
Materials, Energy, and Telecommunications Center

The *in-situ* doping of sputtered titanium dioxide thin-films for their efficient visible light sensitization and use for the electro-photocatalytic degradation of pollutants in water

By

Nazar Delegan

Thesis presented for the degree of
Philosophiae Doctor, Ph.D.
in Materials and Energy

Evaluation committee

External examinator	Prof. Luc Stafford Université de Montréal
External examinator	Prof. Dilip Sarkar UQAC
Internal examinator	Prof. Andreas Ruediger INRS-EMT
Research supervisor	Prof. My Ali El Khakani INRS-EMT
Research co-supervisor	Prof. Patrick Drogui INRS-ETE

Acknowledgments

This whole experience has been simultaneously fun, enriching, demoralizing, challenging, exciting, enraging, and exhausting. Nevertheless, somehow, with the support of my family, friends, colleagues, and advisors, I got through it.

While this project has tested my patience, it was nothing compared to my mom's weekly interrogations: "When are you done?", "Do you know you could have been a doctor by now?!", "Do you know how much money doctors make?!", "Why haven't you mowed the lawn yet?", etc. But I can't complain. As I write this on her kitchen table, and empty out most of her fridge, I realize that: while my own table and fridge would do just fine, being around family that cares and supports you is all you need to work through that last hurdle. Whether that's the last version of a paper, a rebuttal to unreasonable referees, or in this case, the acknowledgments section of your thesis. Honorable mentions go out to the rest of my family, who have done a stellar job in pretending to be interested and stay awake during my explanations of "more concretely, what it is that I do". Дякую вам всім.

To my friends and girlfriend, I'm sorry to say, but if it wasn't for you guys, this whole thesis business would have probably taken a lot less time. However, to say that I would have kept my sanity in the process is an uncertainty. You kept me grounded, entertained, and inebriated during the good times and the bad. Nothing prepares you for an elevator pitch of your thesis topic like a friend at a bar with a two minute attention span. In their defense, even my supervising post-doc would tell me to shut up when I was talking shop too much; thanks Rajesh!

On the same note, I would like to thank my colleagues, who have mastered turning five minute coffee breaks into two hour debate sessions on everything from modern scientific theory, to politics, and to eccentric animal mating habits (with everything in between). All jokes aside, thank you to so many of you, whether you are in the university administration, technical staff, or part of the student body. You all helped me accomplish so much, whether its because you cut through some of the bureaucracy, showed me how to refurbish a PLD heater, how to find a faulty relay by tapping on it with an oddly specific brand of screwdriver, or allowed me to lead the student body. In that vein, I would like to single out my colleagues at the INRS-ETE with my research co-supervisor: Prof. Patrick Drogui; with whom we were able to build a lasting and fruitful collaboration.

To Prof. Takashi Teranishi, ありがとうございました. You took me into your lab in Okayama. This resulted in some great science, but also an extremely enriching personal experience. Thank you for sharing your knowledge of dielectrics, Li-ion batteries, good ramen places, izakayas, and biiru!

Finally, to say that none of this would be possible without the help and guidance of my research advisor, Prof. My Ali El Khakani, would be an understatement. You provided me with the

opportunity to develop scientifically and professionally. You pushed when I needed pushing and focused me when I was getting lost. You taught me good science and even some magic. Who would have thought that a quick fifteen minute meeting actually lasts four hours?! Not that I minded. I learned more about current affairs and university politics from those meetings than any newsreel could provide. Merci pour tout!

Abstract

The purpose of this work is to develop photoactive TiO_2 films for the electro-photocatalytic degradation of water pollutants under sunlight. Radio frequency magnetron sputtering (RF-MS) was used to synthesize *in-situ* N-doped TiO_2:N films in order to shift their photoactivity from the UV to visible light domain. Careful tuning of the nitrogen-to-argon mass flow rates during sputter-deposition allowed the growth of TiO_2:N films with a wide range of N-dopant contents ranging from 0 at.% to 13 at.%. These studies indicated that most of the N-doping atoms were in the desired substitutional states (*i.e.* $N_O^{\bullet}$). UV-Vis absorption and spectroscopic ellipsometry measurements were used to quantify the bandgap (E_g) variation of the TiO_2:N thin films as a function of their N content. This was used to point out the existence of an optimal nitrogen loading level that reduces the bandgap from 3.2 eV for TiO_2 to 2.2 eV for ∼3.5 at.% nitrogen doped TiO_2:N. This gain in visible-light photosensitivity was assessed for the 1.5AM light driven electro-photocatalytic (EPC) degradation of an emerging pollutant, chlortetracycline (CTC). Thus, TiO_2:N photoanodes have been shown to achieve CTC degradation efficiencies of up to 98 % (within 2 h treatments under simulated solar light). Moreover, the EPC performance of the TiO_2:N was shown to be directly correlated to their optoelectronic properties, sharing a common optimal point between E_g shrinkage and EPC degradation efficiency. However, a more exhaustive analysis revealed that the increase in EPC performance was disproportional with the photosensitization, with many photogenerated charges seemingly lost. Further studies revealed that nitrogen doping was synonymous with the formation of oxygen vacancy (V_O) defects that can reduce the per-photon efficiency of the material by acting as charge recombination centers. In order to circumvent this limitation, tungsten doped TiO_2:W thin films were developed, as they were theoretically proposed to increase V_O defect formation energy. To this end, RF-MS deposition was used to fabricate undoped TiO_2, oxygen deficient (TiO_{2-x}), and tungsten doped (TiO_2:W) films with varying dopant levels. The compositional analysis of the W-dopant bonding states revealed the presence of substitutional W^{VI} (W''_{Ti}) and W^{IV} ($W^{\times}_{Ti}$) type dopants with the total concentration in from 0 at.% to 10 at.%. Additionally, XPS studies revealed a significant recovery of oxygen stoichiometry upon small W incorporations. On the other hand, high frequency spectroscopy measurements (HF-DS) confirmed an optimal tungsten doping of ∼2.5 at.% associated with the lowest ϵ' contribution from the $2\,Ti^{III}{-}V''_O$ defect pair (two orders of magnitude reduction of the V_O dielectric contribution as compared to TiO_{2-x}). Consequently, this reduction in V_O was exploited by integrating the optimally doped TiO_2:W films as photoanodes in visible-light-driven electro-photocatalytic degradation of atrazine (ATZ), another emerging pollutant. The pseudo-first order degradation kinetic constants were shown to increase from $0.027\,min^{-1}$ for TiO_2 and V_O-doped TiO_{2-x} to $0.053\,min^{-1}$ for the optimally doped TiO_2:W photoanodes as a direct result of the reduction in V_O. Interestingly, it was revealed that optimally doped TiO_2:W photoanodes performed on par with the visible-light photosensitized TiO_2:N ones. This confirmed that while TiO_2:N had higher EPC performance due to an increased amount of usable photons, TiO_2:W had better photocharge transport properties, resulting in higher relative per-photon efficiency. In light

of these results, and guided by theoretical models, RF-MS was used to synthesize acceptor-donor passivated, *in-situ* WN-codoped TiO_2:WN thin films. Thus, by varying the reactive RF-MS deposition parameters, we were able to tune the *in-situ* incorporation of both N and W dopants in the TiO_2:WN films over a wide concentration range. The objective of the co-doping was twofold: (i) narrow the bandgap of the TiO_2:WN films through N-doping to extend their photosensitivity as far as possible in the visible, and (ii) passivate the N-doping induced V_O defect centers through appropriate WN-codoping. Systematic analysis by means of XPS and XRD techniques revealed that both W and N dopants were mostly of substitutional nature. Nitrogen doping was found to be the key component in narrowing the optical-band-gap down to 2.3 eV for both TiO_2:N & TiO_2:WN. Most importantly, XPS analysis hinted that the codoping approach greatly reduced the density of V_O in the TiO_2:WN films as compared to TiO_2:N ones. This reduction in defects translated into improved crystalline structure, and increased dopant solubility. The suppression of V_O via the acceptor-donor passivating approach was directly confirmed by HF-DS measurements showing a marked reduction in the density of $2\,Ti^{III}{-}V''_O$ defect pairs with the codoping of tungsten and nitrogen as compared to N-monodoped samples. This defect reduction was shown to increase photocharge characteristic lifetimes using visible light flash photolysis time-resolved microwave conductivity measurements (FP-TRMC). Photocharge lifetime analysis indicated the presence of three distinct decay processes: charge trapping, recombination, and surface reactions. These characteristic lifetimes of the codoped TiO2:WN films (*i.e.* 0.08 µs, 0.75 µs, and 11.5 µs, respectively) were found to be about 2.5 times longer than those of their nitrogen monodoped TiO_2:N counterparts (*i.e.* 0.03 µs, 0.35 µs, and 6.8 µs). This quantitatively confirms the effective passivation of the WN-codoping approach developed here. Finally, the developed TiO_2:WN's practicality was confirmed by integrating them as photoanodes for the visible-light driven EPC decontamination of ATZ. A significant increase in the degradation kinetics, resulting in up to a four-fold increase in the pseudo-first order degradation constant k for the optimally codoped TiO_2:WN photoanodes ($k = 0.106\,min^{-1}$), in comparison with the undoped TiO_{2-x} & TiO_2 ones (both having a $k = 0.026\,min^{-1}$). Most importantly, the optimal TiO_2:WN photoanodes showed a twofold increase in degradation kinetics as compared to TiO_2:W ($k = 0.057\,min^{-1}$) & TiO_2:N ($k = 0.047\,min^{-1}$) as a direct consequence of both increased photocharge lifetimes and visible light photosensitivity.

Keywords: RF-magnetron sputtering, *in-situ* doping, nitrogen and tungsten codoping, TiO_2:WN, photoanodes, bandgap narrowing, electronic acceptor-donor passivation, sunlight driven electrophotocatalysis, pollutant degradation.

Table of Contents

List of Figures

List of Tables

Nomenclature & Abreviations

χ	Electron affinity
Φ	Work function
E_F	Fermi energy level
I_p	Ionization potential
APCVD	Atmospheric pressure chemical vapour deposition
ATZ	Atrazine
CBM	Conduction band minimum
CL	Cody-Lorentz
CTC	Chlortetracycline
CVD	Chemical vapor deposition
DOS	Density of states
DOS-FLAPW	Density of states - full potential linearized augmented plane wave method
DSSC	Dye-sensitized solar cells
E_g	Forbidden energy gap of a semi-conductor. In this work, this term will sometimes be loosely used to also describe the absorption edge of the material (*i.e.* approximate the effective band-gap of the material via its absorption spectra red-shift due to isolated dopant E_g energy levels).
EPC	Electro-photocatalytic
EPR	Electron paramagnetic resonance
ERD-TOF	Elastic recoil detection time-of-flight
ESCA	Electron spectroscopy for chemical analysis
FP-TRMC	Flash-photolysis time resolved microwave conductivity
FTIR	Fourier transform infrared spectroscopy
FWHM	Full width at half the maximum
HF-DS	High-frequency dielectric spectroscopy

KE	Kinetic energy
Kröger–Vink	Set of conventions that are used to describe electric charge and lattice position for point defect species in crystals *e.g.* Substitutional W atom in a Ti location with two negative net charge: W''_{Ti} & Substitutional N atom in an O location with one net positive charge: $N^{\bullet}_{O}$
LDA	Local density approximation
MOCVD	Metal-organic chemical vapour deposition
NHE	Normal hydrogen electrode
PAW	Projector-augmented wave method
PCE	Power conversion efficiency
PCE	Power conversione efficiency
PECVD	Plasma-enhanced chemical vapor deposition
PVD	Physical vapor deposition
QDSSC	Quantum-dot sensitized solar cells
RF-MS	Radio-frequency magnetron sputtering
RSF	Relative sensitivity factor
SE	Spectroscopic ellipsometry
SEM	Scanning electron microscopy
TEM	Transmission electron microscopy
TL	Tauc-Lorentz
UPS	Ultraviolet photoelectron spectroscopy
UV	Ultraviolet portion of the light spectrum, *i.e.* >3.0 eV
UV-Vis	Ultraviolet-visible reflectance and transmittance spectroscopy
VBM	Valence band maximum
W-H	Williamson-Hall
XPS	X-ray photoemission spectroscopy
XRD	X-ray diffraction
YAG	Yttrium aluminum garnet

Part I

Main Text

Chapter 1

Introduction, motives, and methodology

"Begin at the beginning," the King said, very gravely, "and go on till you come to the end: then stop."

Lewis Carroll, Alice in Wonderland

1.1 Introduction

Environmental pollution, in conjunction with the lack of sustainable energy sources remain some of the most serious challenges that humanity currently faces. Water resources are particularly important to safeguard, as they are fundamental for all life. Complicating this is the fact that waterways currently serve as trash bins of choice for both solid and liquid waste. While the former is visually disruptive, the latter presents much broader ecological and economical risks. These realities dictate the need for novel decontamination schemes that are both clean and sustainable. In this context, we propose that titania driven photocatalysis is ideal for the degradation of emerging pollutants in water, fulfilling both criteria perfectly. The titanium dioxide photocatalyst is widely abundant, can be powered by the inexhaustible 1.989×10^{30} kg nuclear reactor in the sky and critically, is ecologically benign.

Using TiO_2 for solar energy conversion is not, in itself, a novel idea. In 1932, Renz confirmed a mechanism proposed by Baur et al. eight years earlier explaining the observed oxidation and reduction of various substances on the TiO_2 surface under UV illumination[19, 20]. Interestingly, Baur's research was based on an even earlier observation highlighting the partial reduction of titania with the presence of organic compounds published in 1921[21]. This photocatalytic process was, over the years studied and developed upon, culminating in a landmark 1972 paper by Fujishima and Honda, demonstrating simultaneous photo-generation of H_2 and O_2 using a TiO_2 photoanode with a Pt dark cathode[4].

While this work was successful in attracting much attention to the field as a whole, it was soon remarked upon that electro-photocatalytic (EPC) processes were greatly limited in that they could only be driven by high energy UV photons. This limitation, intrinsically linked to the bandgap of TiO_2 (*i.e.* in the UV) greatly reduced the materials' applicability to large scale applications in both solar energy harvesting (photolysis of H_2 & O_2 from H_2O) and organic compound oxidation (decontamination via EPC)[22, 23, 24, 25, 26, 27, 28, 29]. In this context, enabling TiO_2-photoanodes to operate with a higher proportion of solar energy is a highly interesting perspective for the EPC field as a whole.

1.2 Motives

The photocatalytic process is activated by the absorption of a photon with energy equivalent or higher than the forbidden gap (E_g) of a photoactive material. The absorbed light then "bumps" an electron into the conduction band, while leaving a hole in the valence band, creating an exciton (electron-hole pair). These photogenerated electrons and holes can then participate in reduction and oxidation processes, respectively. Their probabilities to do so, are guided by their active "range", as determined by lifetimes, trap sites, recombination mechanics, etc. While this summary does not pretend to be exhaustive, it points to some key features required for effective and efficient EPC reactions:

(i) E_g amplitude dictates the number of solar photons available for photocatalytic processes.

(ii) E_g band edges define the potential energies of the electrons and holes in the reduction and oxidation processes, respectively (*i.e.* conduction band minimum (CBM) must be above the aimed reduction reaction energy, and valence band maximum (VBM) must be below a targeted oxidation reaction energy).

(iii) Generated photo-charges must have sufficient lifetimes as to allow for the desired reactions to occur (*i.e.* sufficient mean free path to come into contact with the reactant molecules).

Upon comparison of various semi-conductors with their E_g, conduction band minimum, and valence band maximum, as depicted in figure 1.1, one can note a few possible candidates for either EPC water splitting (*i.e.* H_2/H_2O & O_2/H_2O redox pair) or organic pollutant decontamination (*i.e.* O_2/O_2' & $OH^\bullet/H_2O$ redox pair).

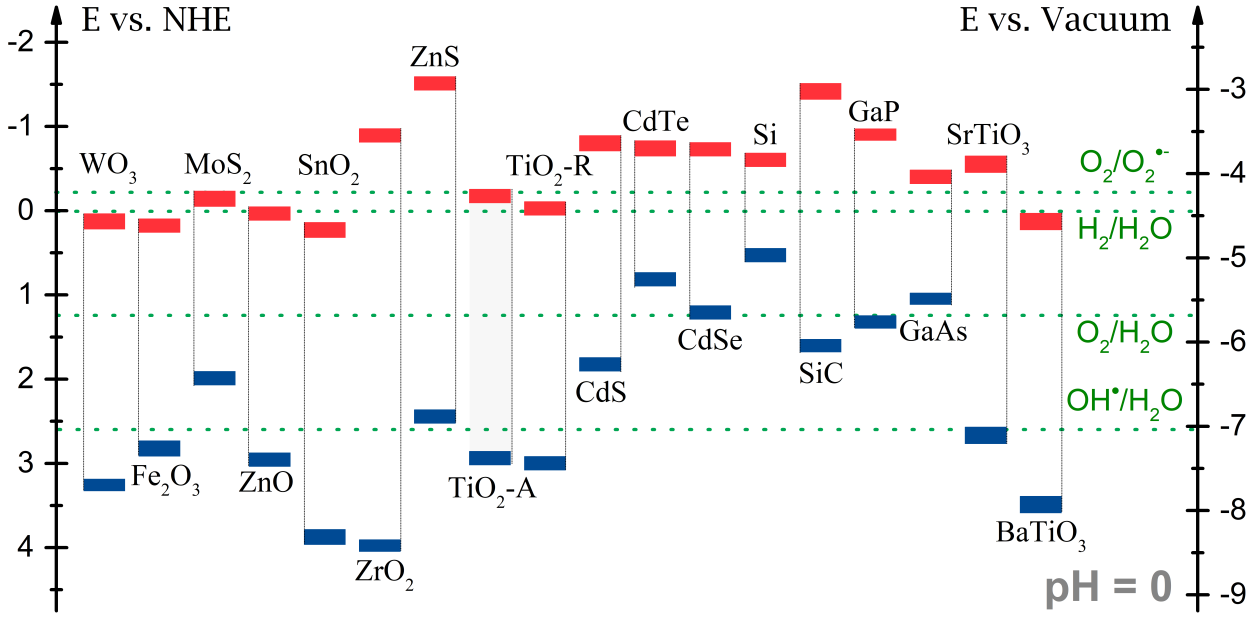

Figure 1.1 – Comparison of the conduction band minimum (CBM) in red and valence band maximum (VBM) in blue for various semiconducting oxides on a potential scale *vs* the normal hydrogen electrode (NHE) on the left and vacuum energy on the right. Data taken from: [1, 2, 3], normalized for 0 pH.

By considering different factors such as cost, environmental compatibility, availability, and stability, TiO_2 arises as the most promising candidate[30, 31]; specifically, the anatase polymorph (denoted TiO_2-A in figure 1.1). While its band alignment is better suited for most applications,

the indirect nature of its E_g is an additional advantage over the direct bandgap of rutile (this difference will be elaborated upon in section 2.3)[32].

Fundamentally, TiO_2 is a large bandgap, n-type semiconductor (*i.e.* 3.2 eV and 3.0 eV for the anatase and rutile polymorphs, respectively). Unfortunately, this limits the materials photoactivity to the UV portion of the solar spectrum, which represents only ≈4 % of the total irradiance of the sun (see figure 1.2 hereafter).

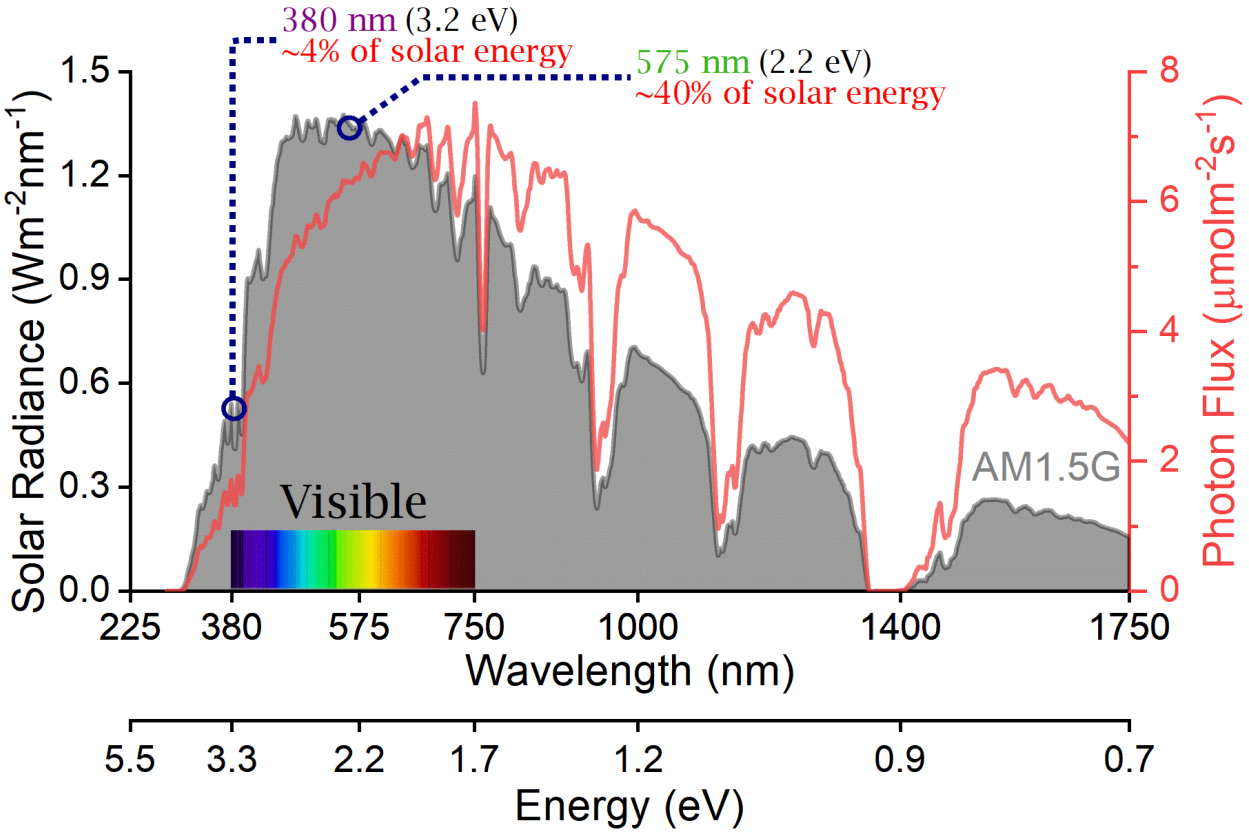

Figure 1.2 – AM 1.5G solar spectrum taken from the NREL database (black line, left Y-axis) and total photon flux at AM 1.5G (red line, right Y-axis). The 3.2 eV cutoff (representing ~4 % of total solar energy) and The 2.2 eV level (~40 % of total solar energy) are shown as visual guides.

This limitation is a major bottleneck for effective TiO_2 based electro-photocatalysis with sunlight. Ideally, for efficient EPC the E_g edges should straddle the potential energies required to create the targeted REDOX pair. This, in essence states that the materials forbidden gap should be closer to the solar spectrum maximum (around 575 nm or 2.2 eV, as shown in figure 1.2) while maintaining proper band positioning and other advantageous characteristics of TiO_2 (*e.g.* photostability).

Asahi et al. have proposed that doping TiO_2 could be a viable approach for shifting its bandgap towards the visible[33]. Nevertheless, much debate remains as to the underlying charge carrier mechanisms altered and brought up by doping[34, 35]. Often contradicting results are found due to lack of control over exact dopant type (*e.g.* interstitial *vs* substitutional), synthesis impurities, etc. In other words, if TiO_2 doping is to be properly studied, a contaminant-free, highly controllable, reproducible, and flexible synthesis method should be used. All these conditions can be fulfilled by the radio-frequency magnetron sputtering (RF-MS) technique we used in the context of this PhD project to deposit TiO_2 films under different experimental conditions, with a very large process latitude. As it will be discussed in this work, the RF-MS method was used to deposit TiO_2 films not only at different deposition temperatures, pressures, etc. But most importantly, with different *in-situ* doping schemes.

1.3 Objectives

The ultimate objective of this thesis is to develop visible light sensitive TiO_2 films, as to better utilize sunlight for the EPC degradation of pollutants. This photosensitization is achieved via *in-situ* doping of the material during its RF-MS growth process. While the bandgap narrowing of the doped TiO_2 films was a key priority, particular care was given to maintaining appropriate potential energy levels for both the CBM and VBM suitable for pollutant degradation. With the RF-MS process optimized, and the doping of TiO_2 films fine-tunned (in terms of their optoelectronic properties), these films were integrated as photoanodes in EPC cells aimed at the degradation of emerging pollutants. In other words, this thesis has the following objectives:

(i) Develop a radio-frequency magnetron sputtering deposition process for preparing *in-situ* doped, visible-light active TiO_2 films.

(ii) Characterize and optimize the optoelectronic properties of the deposited TiO_2 thin films as a function of their preparation parameters (*i.e.* sputtering-target RF power, substrate temperature, doping level, etc.). Of particular interest is the material's bandgap shrinkage and the photocharge lifetime increase.

(iii) Consolidate the results of objectives (i) & (ii) by integrating the TiO_2 based thin films as photoanodes to be used in an EPC reactor intended for the degradation of water contaminants. This part will be done in collaboration with colleagues at the INRS-ETE center (under the supervision of Prof. Patrick Drogui).

(iv) Combine both physical and chemical results (objectives (ii) and (iii)) in order to better understand possible relationships between the physical characteristics of the photoanodes and their EPC performance towards the degradation of two selected pollutants, namely chlortetracycline (CTC) and atrazine (ATZ).

It is important to note that some key parameters will be fixed in this thesis as to allow a clearer picture form a material science point of view. It is commonly established that nanostructuring (increase in the active surface, decrease in charge transport obstacles, etc.) and nanoparticle decoration (SPR & heterojunction effects) are known methods for improving the EPC performance of titania (see section 2.3)[34, 31, 5, 6]. In the context of this thesis, focus is put on the specific structural and bonding changes resulting from the varied doping schemes of the RF-MS sputter-deposited TiO_2 films.

1.4 Methodology

1.4.1 TiO_2 deposition

Radio frequency magnetron sputtering is a physical vapor deposition (PVD) method based on the sputtering of a given metallic or oxide target with inert gas ions (typically Ar^+), which are produced in the RF generated plasma and accelerated by a magnetron produced electromagnetic field[14, 36]. This process is typically performed under a residual background pressure in the mTorr range. Prior to sputter-deposition, the chamber is pumped down to about 1×10^{-8} Torr. The plasma can be created with either a DC (metallic targets) or an RF (insulating targets, as it prevents charge buildup) discharge from the cathode. This sputtering plasma ejects the target's atoms, creating an atomic flux, which can condense on the substrate. It is also possible to perform reactive sputtering, by injecting a small amount of chemically active gas along with the inert sputtering gas. This added

gaseous component can be partially ionized and incorporated in the growing film on the substrate (and to a certain extend into the sputter-target itself, *i.e.* poisoning). A somewhat similar atomic mixing can be also achieved via concomitant sputtering of two or more targets, running under either DC and/or RF regimes. Any changes to sputtering deposition parameters such as the relative target sputtering power density, substrate temperature, pressure, reactive gas partial pressure, will affect the atomic species within the plasma, and therefore the composition and properties of the deposited thin films. The sputtering method is well known for the high purity of its deposited fims and a tight control of their composition. A more detailed description of RF-MS is presented in appendix A.1.

1.4.2 Physical, chemical, and optoelectronic characterizations

Scanning electron microscope (SEM) observations allow the direct observation of the thin films' thickness and morphology; key parameters for controlling the deposition process and for secondary analysis such as Tauc plot extrapolation, spectroscopic ellipsometry modeling (SE), high-frequency dielectric spectroscopy (HF-DS), etc. The crystalline properties of the films were systematically studied via X-ray diffraction (XRD). More specifically, grazing angle XRD was used since our TiO_2 films were of sub-µm thickness. The chemical bonding nature of the obtained thin films were also characterized by using Fourier transform infrared spectroscopy (FTIR). The chemical composition and detailed chemical bonding of the films were studied by means of X-ray photoemission spectroscopy (XPS). The XPS derived compositions were complemented by time-of-flight elastic recoil detection (ERD-TOF) measurements. UV-Vis (Ultraviolet and visible) reflectance and transmittance measurements were used to study the optical properties of the sputter-deposited films. The obtained UV-Vis transmittance/reflectance spectra were analyzed by using the Tauc plot extrapolation in order to quantify the optical bandgap of the films. Given the importance of an accurate determination of E_g, we have also independently characterized the TiO_2 films using spectroscopic ellipsometry (SE) measurements and fitted the obtained spectra with appropriate models (various material electronic models, the film's thicknesses, surface roughness, dopant uniformity, etc.). The dielectric properties of the sputter-deposited films were studied by means of high frequency dielectric spectroscopy (HF-DS) measurements. The photocharge characteristics were studied via flash photolysis time resolved microwave conductivity measurements (FP-TRMC). The technical details of the methods and analysis used throughout this PhD project can be found in appendix A.2.

1.4.3 EPC testing

In order to properly study the electro-photocatalytic performance of the developed TiO_2 films, a homemade EPC reactor was designed and built in collaboration with Prof. Patrick Drogui's group (INRS-ETE). For these EPC tests, the TiO_2 thin films were deposited on deployed Ti grids and used as photoanodes in the EPC reactor. A quartz window in this reactor allows for transmission of the solar radiation. A cathode is used to complete the electrochemical circuit (typically, glassy carbon, BDD, or graphite was used). The system is sufficiently flexible as to allow the study of various parameters such as: flow rate, solar power, applied potential/intensity, gas bubbling, inter-electrode distance, etc. These studies were all performed at Prof. Drogui's lab at the INRS-ETE center. A detailed schematic and further technical information about the EPC reactor is provided in appendix A.3.

1.5 Thesis plan

This thesis document is presented in the format of a thesis by articles (*i.e. thèse par articles*), and will be organized as follows: following this introduction, chapter 2 presents the scientific context and fundamentals of TiO_2 based photocatalysis. It starts with a short historical overview of the EPC field in section 2.1. Followed by an overview of the basic principles guiding EPC processes on the TiO_2 surface in section 2.2. Understanding the EPC process will allow us to establish the various material parameters of interest. The crystallographic and optoelectronic properties of pristine and doped TiO_2 are presented in section 2.3. Certain topics will be left open-ended as to allow the results chapters to develop upon. Additionally, throughout this document, Kröger–Vink notation will be used (*e.g.* Substitutional W atom in a Ti location with two negative net charge: W''_{Ti} & Substitutional N atom in an O location with one net positive charge: $N^{\bullet}_{O}$). Finally, a brief overview of commonly used synthesis methods for TiO_2 based materials is presented in section 2.4.

The results obtained during the course of this doctoral thesis are summarized in Chapter 3. The results will be separated into three main sections, namely (i) section 3.1 discusses visible-light sensitive TiO_2:N thin films fabricated using a reactive RF-MS process. Various structural and chemical properties originating from nitrogen doping will be discussed. Most notably, the visible light sensitivity of the TiO_2:N films will be emphasized. The added benefits of N incorporation for EPC

applications were assessed via degradation studies of chlortetracycline (CTC) under visible light illumination. Some inherent drawbacks of nitrogen doping will be highlighted. Thereafter, (ii) section 3.2 discusses the beneficial properties TiO_2:W thin films, with emphasis placed on defect center passivation via W''_{Ti} incorporation. Finally, (iii) section 3.3 proposes a solution to circumvent the various drawbacks of TiO_2:N, which consists of acceptor-donor passivated TiO_2:WN codoping of the films. The associated photocharge lifetimes were measured and will be discussed with concomitant visible light photosensitivity of the TiO_2:WN. This results section will be supported by refering to the papers we have already published in the context doctoral project (see part IV). It is to noted that this results chapter will serve to compliment and place into perspective the already published scientific articles and will therefore avoid repeating things unnecessarily. In other words, the results chapter does not present all the scientific data exhaustively (as this is left for the articles), but focuses on the main achievements and messages, while serving to place the varied standalone works into the broader context of this thesis as a whole.

Finally, a summary and conclusion of this project is presented in chapter 4. Key contributions will be highlighted and some interesting research perspectives presented.

1.5.1 Scientific publications

At the end of this document, the six (6) scientific papers arising from this PhD project are presented. For these works, the first author was responsible for the material synthesis, characterization, and writing of the associated papers. The exception for this is article 2, in which the two first authors contributed equally.

In addition, four (4) papers were co-authored with our collaborators from INRS-ETE are also included. These papers used the TiO_2 photoanodes developed in the context of this doctoral project. They focus on the electrochemical processes used for the EPC degradation of water pollutants. Contribution to these works was limited to the synthesis of EPC materials (photoanodes), their characterizations, and composition of selected sections of the text.

Main topic publications

- Article 1: Bandgap tailoring of *in-situ* nitrogen-doped TiO_2 sputtered films intended for electrophotocatalytic applications under solar light
- Article 2: Probing the Electronic Surface Properties and Bandgap Narrowing of in situ N, W, and (W,N) Doped Magnetron-Sputtered TiO_2 Films Intended for Electro-Photocatalytic Applications
- Article 3: Direct evidence of defect pair reduction in magnetron sputtered TiO_2:W films leading to improved electro-photocatalytic performance – a dielectric spectroscopic study
- Article 4: Lifetime Enhancement of Visible Light Induced Photocharges in Tungsten and Nitrogen in situ Codoped TiO_2:WN Thin Films
- Article 5: *In-situ* co-doping of TiO_2:WN films deposited by means of a magnetron reactive co-sputtering process for the development of photoanodes intended for visible-light electro-photocatalytic degradation of emerging pollutants
- Article 6: Sputter deposited WN-codoped TiO_2 thin-films for visible light applications – a dielectric and structural study of defect-pair passivation

Collaborative EPC work with the INRS-ETE center

- Daghrir, R.; Drogui, P.; Delegan, N.; El Khakani, M. A. *Electrochemical Degradation of Chlortetracycline Using N-Doped Ti/TiO2 Photoanode under Sunlight Irradiations.* Water Res. 2013, 47 (17), 6801–6810.
- Daghrir, R.; Drogui, P.; Delegan, N.; El Khakani, M. A. *Removal of Chlortetracycline from Spiked Municipal Wastewater Using a Photoelectrocatalytic Process Operated under Sunlight Irradiations.* Sci. Total Environ. 2014, 466–467, 300–305.
- Komtchou, S.; Dirany, A.; Drogui, P.; Delegan, N.; El Khakani, M. A.; Robert, D.; Lafrance, P. *Degradation of Atrazine in Aqueous Solution with Electrophotocatalytic Process Using TiO2-x Photoanode.* Chemosphere 2016, 157, 79–88.

- Komtchou, S.; Delegan, N.; Dirany, A.; Drogui, P.; Robert, D.; El Khakani, M. A. *Removal of atrazine by photoelectrocatalytic process under sunlight using WN-codoped TiO_2 photoanode* Journal of Applied Electrochemistry. 2018, 1-9.

Chapter 2

Scientific context and fundamentals

In hip hop no one cares, no one stands up for it, and it's a mess. We need order so we can all follow the tradition of where we came from. We need to keep referring to the pioneers.

Nas

Before proceeding to the results and findings of this doctoral project, the scientific context which supported and guided this work is herein presented. Firstly, the scientific history of photocatalysis (and EPC) is discussed (section 2.1). Secondly, basic principles of photocatalysis on the TiO_2 surface are presented (section 2.2). In this context, key properties of TiO_2 will be highlighted in section 2.3. Specifically, the crystalographic properties of TiO_2 will be explored (section 2.3.1), followed by some intrinsic properties of TiO_2 (section 2.3.2), concluding with some methods for enhancing visible light sensitivity of titanium dioxide (sections 2.3.3,2.3.4, and 2.3.5). This will be followed by a brief overview of some popular synthesis methods while highlighting their advantages/drawbacks (section 2.4). Finally, the chapter will be completed with a short overview of common applications for EPC TiO_2 materials and a highlight of some best-of-class performance figures (section 2.5).

2.1 History of TiO_2 based photocatalysis

The earliest work describing TiO_2 based photocatalysis dates back to 1921, when Renz from the University of Lugano in Switzerland reported the partial reduction of titania under illumination with the presence of an organic compound[21]. It was noted that under solar illumination, while in the presence of glycerol, the TiO_2 darkened in appearance from an initially white color (this effect was also noted for compounds such as CeO_2, Nb_2O_5, and Ta_2O_5), sometimes even becoming fully black (much later understood to arise from a reduction of the material). The first applied experiments of photocatalysis however, can be attributed to Baur et al. from the Swiss Federal Institute of Technology (in 1924)[20]. They deposited metallic-silver from a silver salt via photocatalysis on the surface of ZnO. More importantly, they proposed that both oxidation and reduction were simultaneously involved. This idea was reiterated in a subsequent publication where they demonstrated the production of hydrogen peroxide on the surface of ZnO via photocatalysis[37].

This newly proposed Baur redox mechanism was reiterated by Renz in 1932 who reported on the photocatalytic reduction of silver nitrate and gold chloride to their respective metallic forms via illumination on various oxides, including TiO_2[19]. This was further developed upon by Goodeve and Kitchener from University College London in 1938[38, 39]. They concluded that titania powder was a catalyst and determined its quantum yields for the photocatalytic decomposition of a dye with considerations for the absorption spectra of the material. Parallel to this, the origin of anodic and cathodic currents from similar, purely electrochemical systems was investigated by Wagner and Traud (Technical University of Darmstadt)[40]. They concluded that the anodic component arose from the dissolution of ZnO and oxidation of redox species, whereas the cathodic component arose from the reduction of O_2 into H_2O_2.

In 1949, Jacobsen (National Lead Company USA, 1949) attempted to explain the commonly observed paint chalking effect in the presence of titania[41]. He noted a correlation between the tendency of TiO_2 powders to undergo photo-induced reduction while exposed to organic compounds and their chalking. He elaborated upon this and determined that the photo-induced reduction could be measured as a loss of reflectivity due to the various oxygen-deficient forms of TiO_2 (explaining the blacking first observed in 1921), all the way down to Ti_2O_3. This process was noted to be cyclic, with the reduced titanium dioxide being able to recover oxygen from the air via subsequent

oxidation, but the oxidized organic components were irreversibly degraded into water-soluble acids and CO_2.

Subsequent studies in the 1950s confirmed and clarified the overall reaction mechanisms, making it apparent that an organic compound was oxidized while atmospheric oxygen was reduced whereas the involvement of hydroxyl radicals ($OH^{\bullet}$) and other radical species was noted[42, 43, 44, 45, 46, 44]. These works and many others by Markham et al. (Catholic University of America and St.Joseph's College, USA) developed the overall reaction mechanism first proposed by Baur into the following form:

$$RHOH + H_2O + O_2 \longrightarrow H_2O_2 + R(OH)_2 \tag{2.1}$$

Markham and Laidler had attempted to use TiO_2 for their photocatalytic tests, but subsequently abandoned it for ZnO (like many other authors) as they were unable to obtain any significant quantity of H_2O_2 from it[42]. This work lead Markham and Upreti to construct illuminated ZnO-based (as photoanodes) photo-assisted fuel cells with several alcohols as the organic substrates[47]. However, even after trying many redox mediators at the dark platinum cathode, the inevitability of ZnO photo-corrosion prevented this system from reaching practical application.

In 1958, Kennedy et al. (University of Edinburgh) studied photo-adsorption of O_2 on TiO_2 as to achieve a better understanding of the photocatalytic processes involved[48]. It was determined that electrons are transferred to O_2 as a result of this photo-excitation. The newly reduced O_2^- species are then adsorbed on the TiO_2 surface. Additionally, an important observation was made by these authors: the ability of titania to decompose chlorazol sky blue (a dye used in the experiment) was directly correlated to its photo-adsorption of O_2.

Two studies in 1959 from the university of St.Petersburg compared the photocatalytic performance of ZnO and TiO_2 regarding the oxidation of isopropanol[49, 50]. They noted that the reaction on ZnO only partially reduced O_2 into H_2O_2, whereas TiO_2 was fully able to reduce the adsorbed

O_2 into H_2O. This allowed them to formulate a much more detailed version of the Baur cycle (see eq. 2.1) that involved an interaction with a surface lattice oxygen atom:

$$\begin{aligned} TiO_2^{\times} + (CH_3)_2CHOH &\longrightarrow (CH_3)_2CO + TiO + H_2O \\ TiO + \frac{1}{2}\,O_2 &\longrightarrow TiO_2 \end{aligned} \tag{2.2}$$

In 1964, Kato et al. (Kyoto Institute of Technology) found that various types of titania powders had different photocatalytic activities; highlighting for the first time that anatase seemed more active than rutile[51]. Shortly after, it was shown by McLintock and Ritchie (University of Edinburgh) that photocatalytic oxidation of ethylene and propylene at the TiO_2 surface could lead to complete oxidization of the organic compounds (mineralization) into CO_2 and H_2O via the production of super-oxide oxygen, supporting previous observations[52, 44]:

$$\begin{aligned} C_2H_4 + 3\,O_2 &\longrightarrow 2\,CO_2 + 2\,H_2O \\ O_2 + e^- &\longrightarrow O_2^{\bullet -} \end{aligned} \tag{2.3}$$

In 1966, Lohmann (Cyanamid European Research Institute) published a study investigating the photocatalytic and electrochemical behavior of a full, self-contained photo-electrochemical (EPC) process on ZnO[53]. Their investigations showed that both the anodic and cathodic components were contributing to the overall ZnO photo-current, building on the purely electrochemical findings of Wagner and Traud[40]. The redox couple contribution to such reactions was further developed upon by Morrison and Freund (Stanford Research Institute)[54]. They explored the effects of adding, balancing, or removing redox couples on the ZnO EPC processes, currents, and byproducts. It was concluded that these varied greatly based on the presence of cathodically generated super-oxides, which in turn were strongly dependent on the initial redox couples used.

The authors Fujishima and Honda (University of Tokyo), frequently associated with the meteoric rise of photocatalysis as a field, began their work on photochemistry in the late 1960s with two key publications highlighting that O_2 evolution on titania happens at potentials very much in disagreement with thermodynamic expectations[55, 56]. These studies demonstrated that photo-excitation is very efficient at converting photons into chemical energy, allowing for generated holes to have tremendous reactivity with either water or any compound in their active vicinity. These

discoveries culminated in the publication of their seminal work: Electrochemical Photolysis of Water at a Semiconductor Electrode (Nature, 1972)[4]. This report demonstrated the simultaneous photo-generation of H_2 and O_2 using a relatively simple set-up with a TiO_2 photoanode and Pt dark cathode. The implications of this work on solar energy conversion gathered much attention to the EPC field as a whole. This can be illustrated, if be it not very formally, simply by comparing the amount of citations the Fujishima and Honda 1972 paper received as compared to all articles that hold key words associated with TiO_2 and photocatalysis in their title as shown in figure 2.1. While these results do not include all articles in the field of photocatalysis and exclude many publications in other languages/title phrasing choices/related fields, they are nevertheless sufficient to illustrate why the Fujishima and Honda Nature 1972 publication is often considered the birth of modern interest in photocatalysis.

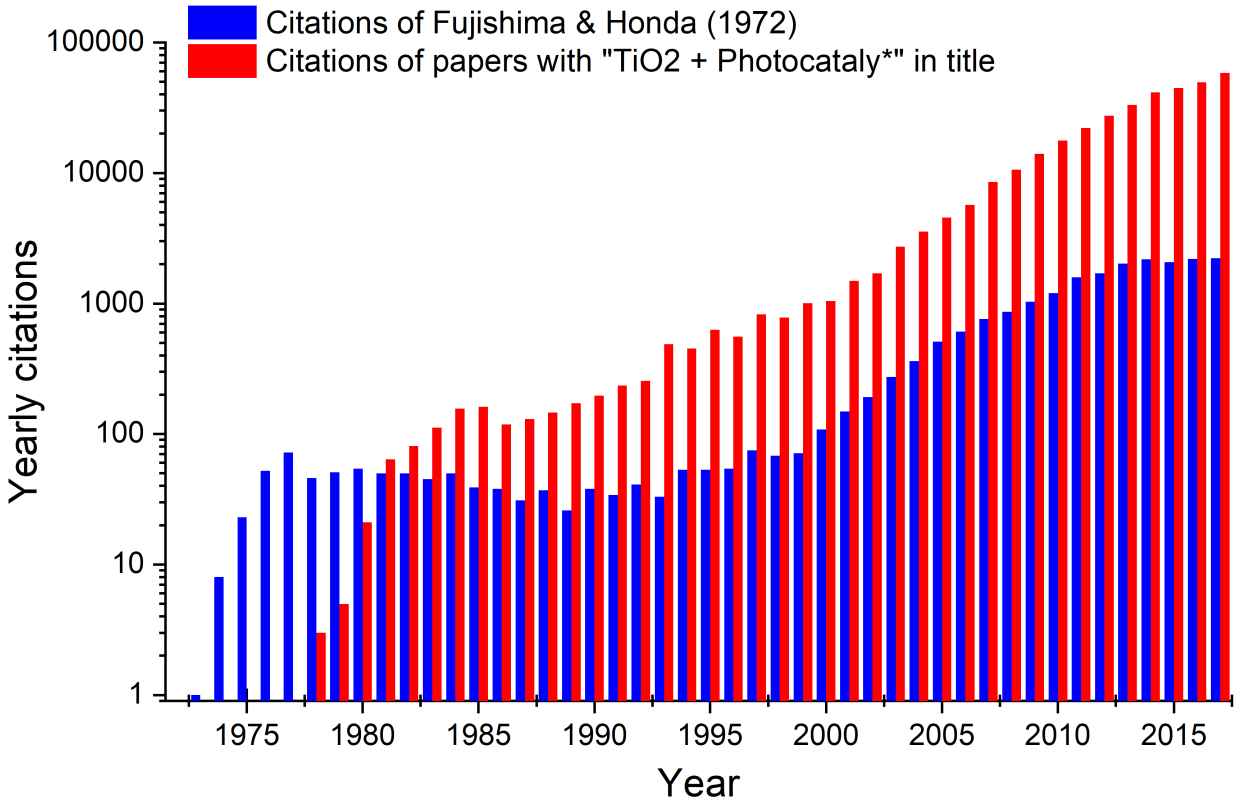

Figure 2.1 – Semi-log plot of the number of citations for the Fujishima and Honda 1972 Nature paper [4] *vis-à-vis* the citations of articles having the "TiO2" & "photocataly*" terms in their title as compiled from Web of Science search results (basic search, with proceedings, non-English, and non-material science papers excluded; surveyed in April of 2018).

Understandably, from this point in time, it becomes difficult to keep track of all advances in the fields of photocatalysis and photochemistry given the sheer amount of publications, findings, and in some cases apparently contradicting results. There are however some key papers/groups that need to be mentioned.

Bard and co-workers at the University of Texas published four studies from 1977 to 1978 that highlighted the possibility of using TiO_2 and other oxides for light driven purification of water[57, 58, 59, 60]. Essentially, they aimed at applying the photocatalytic process to the decomposition of various pollutants such as cyanide and sulfite, degrading them into cyanate and sulfate, respectively. They speculated that, not only could such photocatalytic processes be used for environmental remediation, but also for the photo-synthesis of key economically interesting products. It is important to mention that they determined such photocatalytic oxidations possible on other semiconductors, including CdS, WO_3, Fe_2O_3, and ZnO (which they determined to be the candidate of choice due to its superior photo-activity). Finally, the Bard group suggested that given proper energy band alignments, each photocatalytic particle could be approximated as a mini EPC cell, showing both photo-assisted oxidation and reduction.

Various publications and reviews expanded upon these results, especially in the fields of water detoxification via non-selective oxidation of organic compounds and air purification[22, 23, 24, 25, 26, 27, 28, 29]. Most of these works concluded that such application are indeed possible if powerful UV light sources are incorporated into the EPC cell design. Thus, for titania based large scale photocatalytic applications to be viable, TiO_2 light harvesting capabilities would need to improve beyond the UV. This constitutes one of the main objectives of the present thesis work, and became one of the dominant research axis in the field.

Nevertheless, attention was also given to applications for which only a small number of UV photons was required. The most famous of these is the decomposition of very thin organic (or bacterial) films[61, 62], leading to the so-called "self-cleaning/sterilizing solid surfaces". These technologies pushed the development of various TiO_2 deposition methodologies on varied surfaces. Many of these coating technologies have been transfered into commercial products such as self-cleaning highway lamps, low maintenance high-rise windows, etc.

This limitation of titania as a UV photocatalyst would normally stall interest in the topic. However, the number of publications on TiO_2 EPC has continued to increase exponentially as

shown in figure 2.1. This was, in part due to the uncovered possibility of photosensitizing titania for the visible spectrum. Indeed, first studies on the cationic doping of TiO_2 paved the way for what is now commonly referred to as second-generation TiO_2 photocatalysts[63, 64, 65, 66, 67, 68]. The mainstream scientific attention was drawn to visible light sensitive TiO_2 by a landmark study from Asahi and al. demonstrating that TiO_2 can be photosensitized via nitrogen doping[33]. Such notions of titania band gap engineering and nanostructuring will be further developed upon in the next section (2.3).

2.2 Principles of TiO_2 photocatalysis

When a semiconductor absorbs a photon of energy equivalent or superior to the material's bandgap (E_g), an electron is promoted (bumped) from its valence band into the material's conduction band, leaving a positively charged hole behind in the valence band. In the case of anatase TiO_2, this process can be described as follows:

$$TiO_2 + h\nu \xrightarrow{h\nu \geq 3.2\,eV} e^- + h^+ \tag{2.4}$$

From this, it is clear that the usable solar photon count is low. If one intends to use the sunlight for EPC, only photons with energies above 3.0 eV (410 nm) and 3.2 eV (384 nm) can participate in the photoexcitation of the rutile and anatase polymorphs, respectively.

The photocatalytic efficiency of a material can be measured by the formation rate of products (from e^- reduction & h^+ oxidation) divided by the incident photon flux (photons with $h\nu \geq E_g$), typically refereed to as the photonic efficiency ζ:

$$\zeta(\%) \approx \frac{e^- + A \longrightarrow A^- \parallel h^+ + B \longrightarrow B^+}{h\nu \geq E_g} \tag{2.5}$$

From equation 2.5, we can see that while consideration for photoexcitation is the triggering event for the photocatalytic reaction, identifying the factors that govern the kinetics of photogenerated charges is of equal importance for the development of efficient EPC materials and systems. If for

any reason, the photocharges are unable to reach the reactants, efficiency will be severely affected. Typically, three competing pathways are possible:

(i) The photogenerated e^- (equation 2.4) can make its way to a molecule with compatible reduction potential (CBM of sufficiently negative potential) and/or the h^+ to a species that it can oxidize (VBM of sufficiently positive potential). If this reaction is non-symmetric, considerations must be made for charge regeneration.

(ii) Photogenerated electrons or holes can get trapped by a defect sites (such as: dopants, vacancies, grain boundaries, surface defects, etc.), preventing them from reaching their redox targets.

(iii) Recombination of the $e^- - h^+$ pair, dissipating the absorbed photon energy as phonons and/or radiation.

The probabilities (timescales) of each process depend strongly on the structural/optoelectronic properties of the host material and/or transient energy levels available for the photocharges (heterojunctions, co-catalysts, etc.). Figure 2.2 presents some typical photocharge reaction timescales for the TiO_2 photocatalyst. This highlights that careful consideration of different factors such as crystal arrangement, band structure, stoichiometry, and surface states is key for the optimization of an efficient photoactive material. These factors will be of particular interest in the secondary theme of this doctoral work. In other words, the shrinkage of the TiO_2 bandgap will be thoroughly discussed in the following sections, while always making considerations for the overall efficiency of the photogenerated charge dynamics intended for EPC applications.

2.3 Properties of TiO_2

In order to understand the photocatalytic process, one must investigate the physico-chemical properties of the photocatalyst itself, in our case: TiO_2. The following subsections will elaborate on TiO_2 crystalline structure (subsection 2.3.1), its intrinsic properties (subsections 2.3.2), and possible improvements to its light absorption capabilities (sections 2.3.3, 2.3.4, and 2.3.5). Thereafter

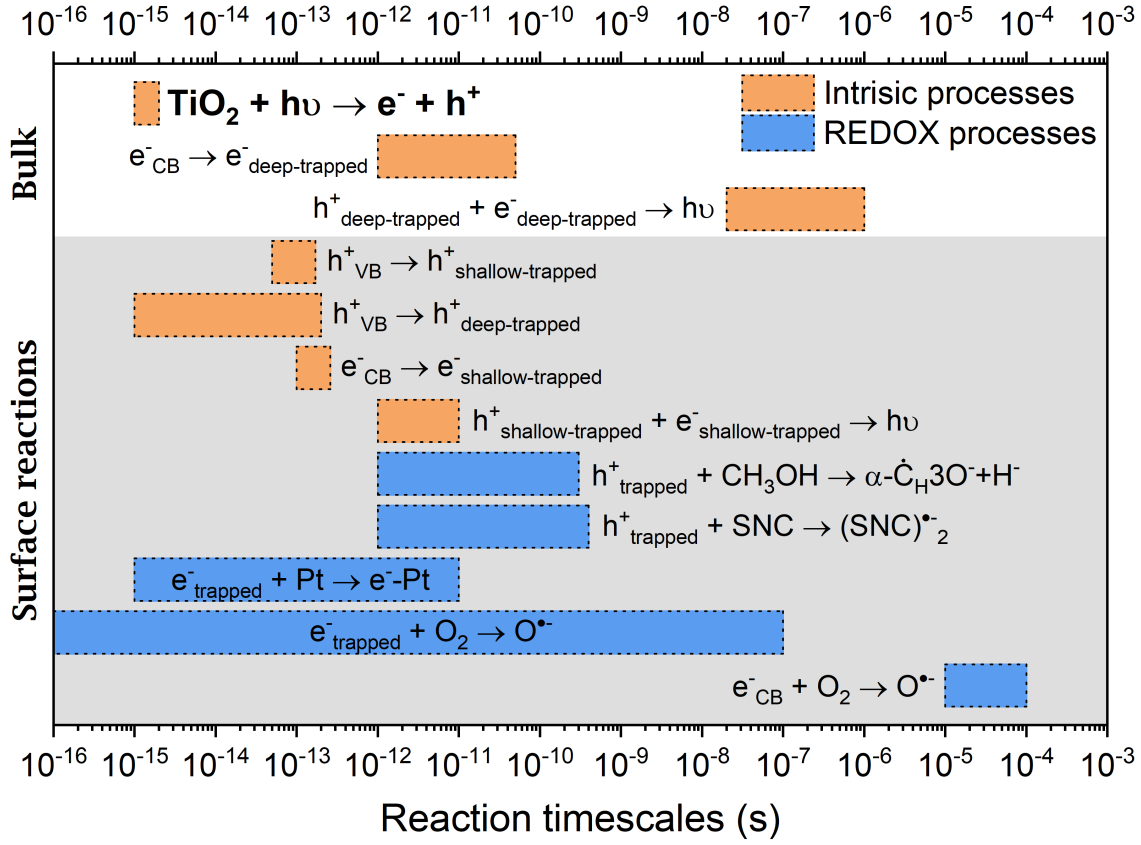

Figure 2.2 – Photoreaction timescales at the bulk and surface level for both intrinsic TiO_2 and with some common redox target species. Raw data taken from: [5, 6]

a relatively short summary of the various synthesis methods commonly used in literature will be presented (section 2.4).

2.3.1 Crystal structure

It is commonly accepted that TiO_2 is tri-morphous with all three phases *i.e.* rutile, anatase, and brookite having an orthogonal crystal family ($\alpha = \beta = \gamma = 90°$)[7, 8]. The unit cells (at room temperature) of each (using JMOL-3D imaging) are presented in figure 2.3. Brookite is commonly considered the most exotic of the three polymorphs, as it is difficult to synthesize (without other phases being present), therefore most studies report findings with anatase and/or rutile.

From a crystallographic perspective, the two main polymorphs differ only by a slight distortion of each $Ti-6O$ octahedron and the way these structures assemble. Anatase is distorted to a point where its symmetry is lower then that of a typical orthorhombic structure, leading to longer $Ti-Ti$ bonds (5.35 Å [10]) and shorter $Ti-O$ bonds. This leads to the anatase structure having each octahedron in contact with four neighbors via edge sharing and four others via corner sharing (essentially a zig-zag along <211>). The rutile structure is significantly less distorted, (closer to a typical orthorhombic structure) leading to 10 immediate neighbors and shorter $Ti-Ti$ bonds (2.96 Å [10]); two sharing edge oxygen pairs and eight sharing corner oxygen atoms. These small structural differences lead to slightly different electronic band structures and effective masses that dictate the various distinct optoelectronic properties of each polymorph. Stability as a function of crystallite size for both anatase and rutile has been observed, but it varies strongly with synthesis methods used[10]. Thermodynamically speaking, anatase and brookite tend to exist only in nanoscale polycrystalline forms with rutile being the stable phase present in larger crystals and at higher synthesis temperatures. Typically, this leads to anatase being stable for TiO_2 nano-particles smaller than ∼50 nm and showing a clear transition to rutile at temperatures ∼850 K[69, 70]. The anatase-rutile transformation starts at the nanoparticle interfaces leading to said particle growth[71]. Highlighting not only the nanoparticle size effect but also the important role that inter-facial defects play in either accelerating or delaying the transition.

Interestingly, it was noted that the brookite-to-rutile transition does not occur directly, it must first pass through the anatase phase (below ∼1050 K) [72]; the inverse process was however observed at 973 K[73].

Two of the three rutile faces are quite low in energy, the (110) and the (100) (therefore useful for stable polycrystalline materials)[74]. The third and highest energy face (001), is thermally less stable to a point that it actually tends to restructure at temperatures above 475 °C making it more challenging to study. Typically, in order to ensure stable rutile structures, amorphous or anatase TiO_2 is annealed at temperatures above 600 °C. Since the (110) face is the most thermodynamically stable, it is typically the most widely studied. It is mainly composed of bridging O atoms each linked to two 6-coordinate Ti atoms with rows of 5-coordinate Ti atoms running parallel to these rows of oxygen atoms. It is important to distinguish these 5-coordinate titanium atoms from the 6-coordinate Ti sites as the 5-coordinate titanium atoms are actually low in electron density (synonymous to Lewis acid sites) and are often invoked to help understand certain research results.

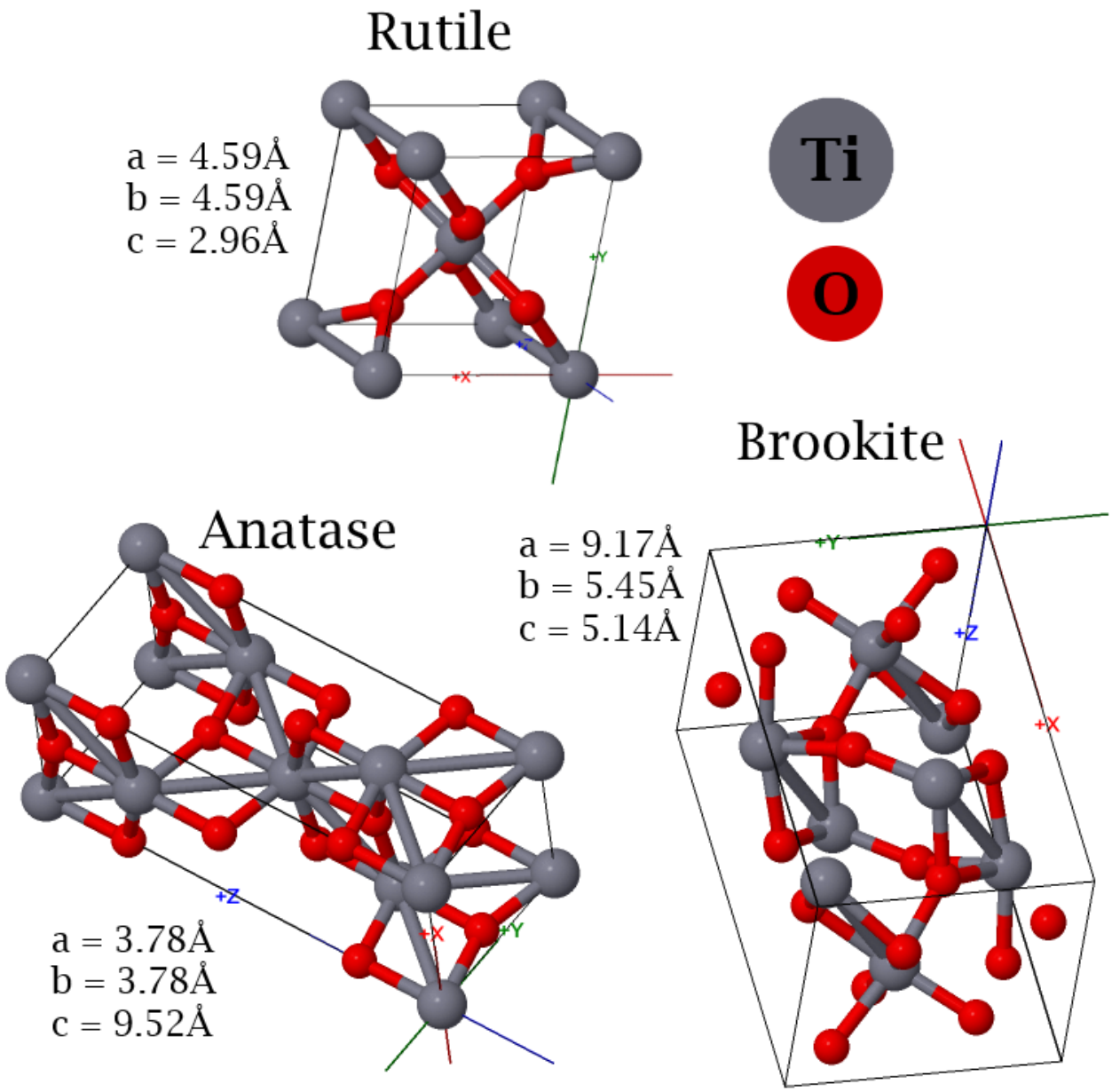

Figure 2.3 – JMOL-3D rendered unit cells for Rutile (top center, with the P42/mnm space group), Anatase (bottom left, with the I41/amd space group), and Brookite (bottom right, with the Pbca space group) polymorphs of TiO_2 with their respective parameters [7, 8]. Orthorhombic structure dictates that: $\alpha = \beta = \gamma = 90°$.

Interestingly, the (100) face also has these alternation Ti and O sites, however, given the (100) titanium sites are in a geometrically different arrangement, they are less often discussed. Finally, the (001) face is composed of a double row of bridging O atoms with single rows of equatorial type Ti atoms[5, 74].

While the anatase unit cell is significantly more complex, it follows a similar pattern of face properties, with two low energy (101)/(001) faces and a higher energy (100) face. The (101) face is the most prevalent for polycrystalline thin films, it tends to be corrugated with alternating rows of 5-coordinate Ti atoms with bridging O atoms[75]. The (001) face is relatively featureless, flat, and has a tendency to quadruple in the b direction during face reconstruction *i.e.* (1×4) in Wood's notation[76]. Typically, the (100) face is rarely reported. Nevertheless it has been shown to exist on rod-like anatase prepared hydrothermally under very basic conditions. Additionally, it can undergo (1×2) reconstruction with alternating double-rows of 5-coordinate Ti with O in between[77, 5].

The brookite phase is relatively rare, there have been however recent reports highlighting its suitability for photocatalytic applications, leading to a surge of development in synthesis methods. Many of these recent successes in this matter have been reported by Di Paola et al.[78]. In general, the hydrothermal method is used with relatively exotic precursors such as the titanium-glycolate complex (it molecularly mimics the brookite structure) all while under very basic conditions. The thermodynamic stability of the brookite faces is generally ranked in the following order: $(010) < (110) < (100)$, as determined from DFT calculations[79].

It is to be noted that the above-discussed these three polymorphs are not the only possible phases of TiO_2. In the early 1990s, Feist et al. were able to demonstrate the existence of a fourth, monoclinic ($C_{2/m}$) polymorph of titania referred to as TiO_2−(B). This form derived mainly from proton exchange and subsequent dehydration of layered titanates composed of corrugated sheets consisting of both edges and corners shared $Ti - 6O$ octahedra[80]. However, not much has been reported about this polymorph in terms of photocatalytic performance. Similarly, in 2001, Dubrovinsky et al. synthesized a highly exotic form of TiO_2 with titanium being nine-coordinated to oxygen (cotunnite structure). This was accomplished by heating TiO_2 with a laser to temperatures in excess of 1600 K, compressing the material to about 60 GPa, and then quenching it in liquid nitrogen[81]. While not surpassing elements such as diamond or cubic boron nitride, the cotunnite-like TiO_2 was shown to be the hardest known oxide[81]. Mattesini et al., in 2004, predicted that fluorite and pyrite type TiO_2 would have interesting visible-light optical transitions, making them ideal for photocatalytic applications such as hydrolysis[82]. While not completely successful, they used a homologous high pressure approach to synthesis structures similar to those predicted.

Finally, a key concept related to the crystallography of TiO_2 that requires attention is the existence of so-called Magneli phases (quite commonly referred to as sub-stoichiometric TiO_2 or TiO_{2-x} in this thesis)[83]. These are, in essence, Ti_nO_{2n-1} titania with $\sim [4 < n < 12]$. Typically they have a modified crystal ordering due to the oxygen vacancies (written V_O in the Kröger–Vink notation) creating prominent slip planes which lead to face-share $Ti - 6O$ octahedra instead of corner-shared ones, and/or other such deformations of the periodicity. This leads to Ti atoms being closely localized, increasing their electronic interactivity[84, 85]. The presence of V_O and these closely interacting Ti atoms are important to consider as they play a key role in the electrical properties of the material[86]. This aspect which will be discussed in the following section.

2.3.2 Pristine & oxygen deficient TiO_2

In the case of pristine titania, the density of states (DOS) are mainly composed of: Ti e_g , Ti t_{2g} (*i.e.* d_{xy}, d_{yz}, d_{zx}), O p_σ, and O p_π[9, 10, 11]. The valence band is composed of three regions: the σ bonding lower energy region, the π bonding middle energy region, and the O p_π states at the highest energy region. This is, with the σ bonding being the prevalently dominant contribution. Above the E_g, the conduction bands can be decomposed into Ti e_g and Ti t_{2g} bands above >5 eV and below <5 eV respectively. The molecular-orbital bonding scheme of pristine titania is shown in figure 2.4. It is important to note the non-bonding O p_π and Ti t_{2g} d_{xy} states populate the VBM and CBM, respectively. This feature tends to be much more prevalent in the anatase polymorph. This is a direct consequence of the titania octahedra assembly variance between the two crystal structures described in section 2.3.1. Given that anatase is less dense than rutile and has larger metal-metal distances (around twice that of rutile), its Ti t_{2g} d_{xy} orbitals composing the CBM are quite isolated in comparison.

It is now accepted that the structural differences between rutile and anatase also result in different E_g types (as demonstrated via DOS calculations and observed experimentally) for the TiO_2 polymorphs: anatase has an indirect forbidden gap whereas rutile and brookite posses direct band gaps[87, 32, 88]. The magnitude of this gap between the O p_π and Ti t_{2g} d_{xy} states is also polymorph dependent, with experimentally determined values of 3.2 eV and 3.0 eV for anatase and rutile, respectively (table 2.1)[9, 10, 11, 35, 6]. Albeit rutile is slightly more complicated in that it has a degenerated direct gap of around 3.0 eV with an indirect gap just ∼0.05 eV above[16].

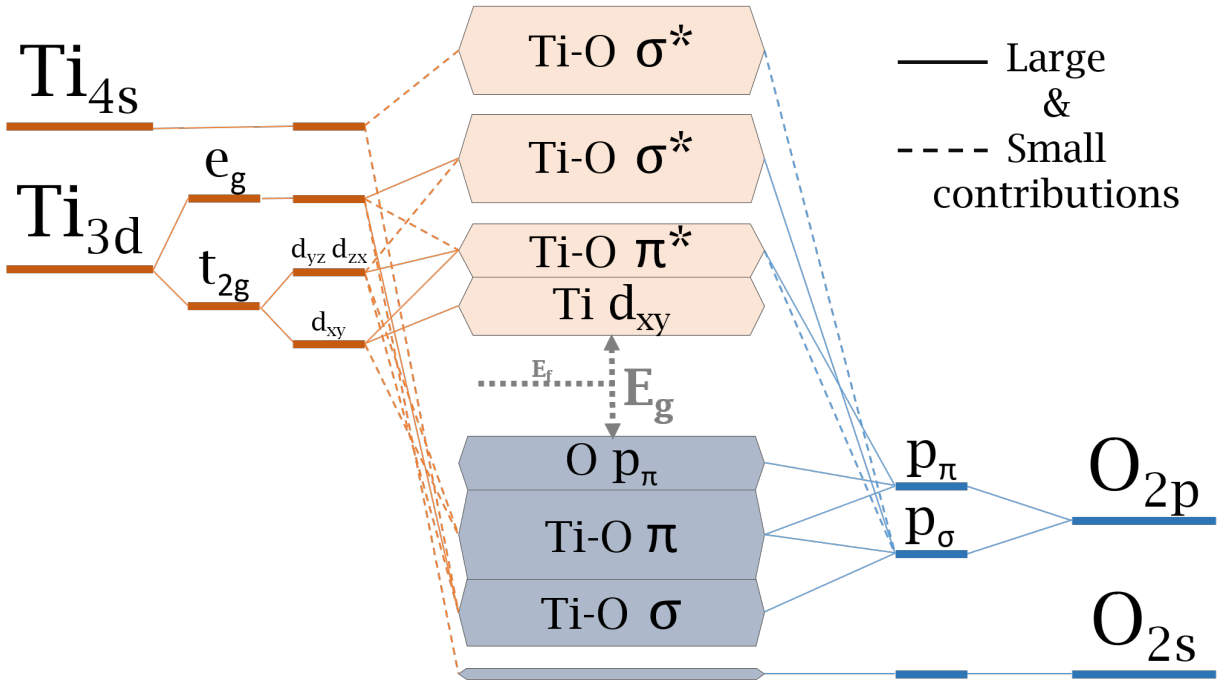

Figure 2.4 – Anatase molecular-orbital bonding structure (not to scale) with dashed and full lines representing small and large contributions respectively[9, 10, 11].

While theoretical models of pristine, non-deficient titania are interesting, it has been understood since the early 1940s that both rutile and anatase are, in most real situations, intrinsic n-type semiconductors unless annealed above 600 °C in high O_2 partial pressures[89]. With time, it was recognized that O_2 annealing fills the V_O in the titania lattice. This reduction of V_O, in turn, leads to smaller Ti^{III} populations, now known to be responsible for the electrical conductivity in titania. The observed temperature and O_2 partial pressure dependence could be explained by equation 2.6.

$$O_O \rightleftharpoons \frac{1}{2} O_2 + V_O^{\bullet\bullet} + 2\,e' \tag{2.6}$$

Interestingly, even with this behavior being present in both polymorphs, the resulting electronic properties in rutile and anatase were shown to be manifest differently[5, 16]. For instance, Tang et al. noted that after reduction in vacuum at 400 °C to 450 °C, the rutile films maintained measurable activation energies of 0.076 eV to 0.060 eV accordingly, whereas the anatase films became essentially metallic showing no change in resistivity with temperature[16]. The observed difference in conductivity is now understood to arise from greatly different donor state radii (as shown in table 2.1). In rutile, the donor state radii are very close to the Ti^{IV} states, leading to almost no

	Anatase	**Rutile**
Band gap E_g (eV)	3.2	3.0
Band gap type	Indirect	Direct
Static dielectric constant	30	100
Effective electron mass (m_e)	1	20
Donor state radius (Å)	15	2.6

Table 2.1 – Comparison of optoelectronic properties for the anatase and rutile polymorphs[16].

overlap of donor waves; whereas anatase allows for a better overlap of donor states due to a much higher donor radius. This, combined with the significantly lower effective electron mass, leads to the metallic like conductivity of anatase in highly reduced states. The activation energies for single crystal anatase was determined by Foroo et al. to be of ∼0.004 eV[90].

Cronemeyer et al. reported, in the early 50s that the main rutile absorption band was at 3.05 eV[91, 92]. However, it was also noted that reduced rutile crystals had a broad absorption peak at ∼0.7 eV (1.8 µm) associated with a bluish tint of the crystals. Interestingly, upon heating and application of an electrical potential it was noted that the coloring migrated to the negative electrode, indicating that the responsible atomic species migrated. The authors proposed that this could be associated to V_O, however could not disprove that this could be due to $H_i^{\bullet}$. Additionally, upon examining various samples reduced at 300 °C to 1150 °C it was noted that the conductivity increased with reduction time and confirmed that room temperature activation energies were ∼0.07 eV. This was settled when the role of V_O in titania's conductivity was elegantly demonstrated by measuring the O_2 weight loss that ensued after heating of a ceramic disk at 800 °C in H_2 atmosphere (∼0.1 % weight lost) and directly matching this result to conductivity values obtained via Hall effect measurements[92].

The V_O contribution to conductivity in rutile crystals was further elaborated upon by Breckenridge and Hosler in 1953[93]. They demonstrated that the effective electron mass was $30\,m_e$ to $100\,m_e$ and showed that Ti^{III} states (formed as a consequence of V_O) were responsible for the conductivity in rutile. These oxygen vacancies could have distinct energies based on their reduction state with: unreduced $V_O^{\bullet\bullet}$, singly reduced $V_O^{\bullet}$, and fully reduced $V_O^{\times}$ being present. Cronemeyer et al. noted that these could be responsible for localized energy states 0.75 eV to 1.18 eV below the

CBM[13]. In other words, V_O were responsible for extended energy bands below the CBM as shown in figure 2.6 (b). The presence of Ti^{III} in bulk titania (therefore V_O) was directly demonstrated by the electron paramagnetic resonance (EPR) and was confirmed to be directly responsible for visible light absorption of TiO_{2-x} films[94].

Kitano et al. and Dholam et al. used the natural tendency of RF-MS to preferentially sputter O atoms to fabricate highly deficient TiO_{2-x} films[95, 96]. These photoanodes were able to produce H_2 and O_2 under visible light illumination with the presence of sacrificial agents; the visible light sensitivity was directly attributed to the presence of V_O defect bands in the bandgap of the TiO_2 films.

2.3.3 Surface modified TiO_2

A popular group of strategies for achieving visible-light photoactive TiO_2 revolves around the combination of the material with various surface photo-sensitizers *e.g.* narrow E_g semiconductor coupling, organic dye decoration, metal nanoparticle sensitizing, etc. In essence, TiO_2 is a wide gap semiconductor, and can therefore be easily coupled with materials that absorb longer wavelength light. These can in turn, transfer the photogenerated charges into the titania band structure (if there is appropriate band alignment). The exact direction of charge transfer depends on the relative CBM and VBM positions (or analogous notions such as HOMO/LUMO) of the two materials. Unless a potential barrier is present, e^- will tend to move towards positive energies, and h^+ in the opposite direction (see figure 2.5 (a)). While this approach has the obvious benefits of not requiring complex and delicate intrinsic modifications of TiO_2, it requires efficient charge generation and transfer from the excited sensitizers, which comes with its own challenges.

Interestingly, TiO_2 has been shown to form such heterojunctions with itself. It has been noted that specific rutile and anatase mixtures (such as the industry standard, the Degussa, now Evonik-Degussa P25 with about 75 % anatase and 25 % rutile) exhibit better EPC performance than similar materials of mono-polymorph nature[31]. In 2013, Scanlon et al. demonstrated that due to the differing coordination environments and energy band levels, rutile and anatase could form this heterojunction, increasing e^- & h^+ separation efficiency across the phase junction while using the benefits of each polymorph[97].

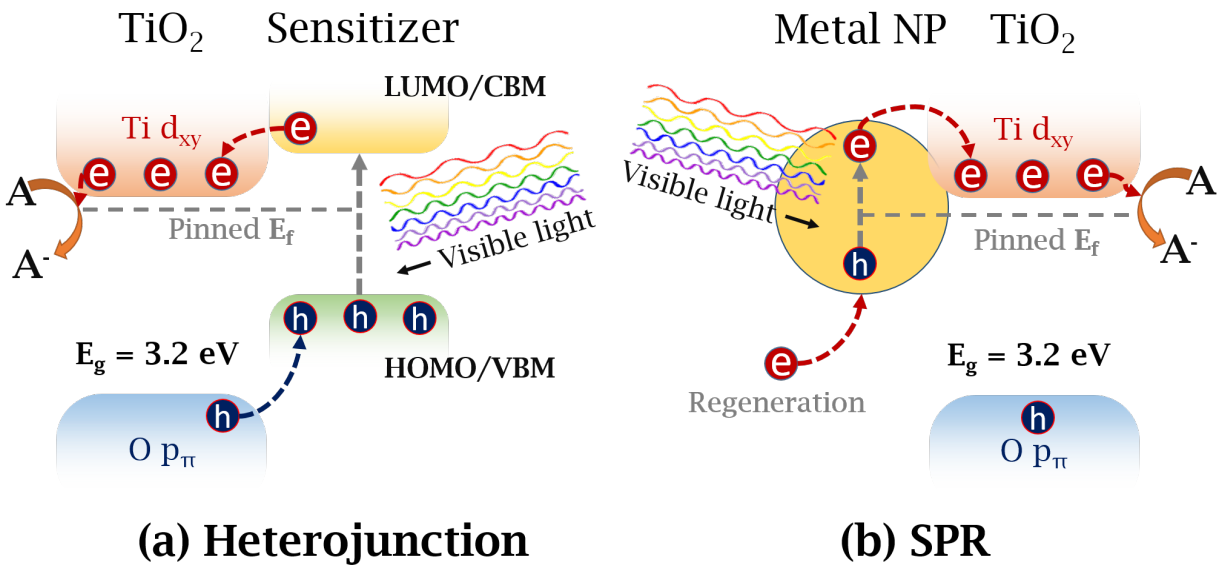

Figure 2.5 – Schematic representation of TiO_2surface sensitization: (a) formation of a heterojunction with either a smaller E_g semiconductor or organic dye with matching HOMO/LUMO levels (analogous to VBM/CBM levels in a semi-conductor), and (b) surface plasmon resonance effect due to a metal nanoparticle [12]. It is to be noted that scenario (a) can be inversed, if the energy levels of the sensitizer are lower then those of the TiO_2, in this case, the e^- and h^+ direction are inverted.

Hoyer et al. synthesized PbS nanoparticles (∼2.5 nm, ∼0.4 eV E_g) and coupled them with a porous titania matrix[98]. They remarked that photogenerated electrons could be directly injected into the TiO_2, resulting in a visible light driven photocurrent. Around the same time, Fitzmaurice et al. demonstrated that AgI (2.8 eV E_g) on TiO_2 nanoparticles could produce excitons with lifetimes of >100 µs[99]. This charge separation phenomenon was developed upon by Vogel et al. who demonstrated that the relative positions of the energetic levels at the sensitizer-nanoparticle interface could be optimized using the size quantization effect[100]. It was also noted that the receiving TiO_2 nanoparticles needed to be sufficiently large in size as to efficiently accept said photocharges[101]. After attempting sensitization of nanoporous TiO_2 with a slew of materials (*e.g.* PbS, Ag_2S, CdS, Sb_2S_3, and Bi_2S_3), they noted that the electrode photostability was significantly enhanced while decorating with CdS nanoparticles[100]. While not directly dealing with visible light sensitivity of TiO_2, Xiang et al. fabricated TiO_2 & MoS_2 decorated graphene sheets[102, 103]. These constructs seemed to greatly improve charge separation efficiencies (if only the TiO_2 nanoparticles were visible-light sensitive). They proposed that the graphene acted as an electron acceptor to its lower potential reduction energy as compared to the TiO_2-CBM; this would in turn increase charge separation. By

adding MoS_2 as a hybrid co-catalyst on the TiO_2, they were able to achieve H_2 production quantum efficiencies of 9.7 % at 365 nm (165.3 µmol h^{-1} of H_2).

Similarly, organic dye sensitizers have been used to varying degrees of success in surface modified, optically improved TiO_2 compounds. These have been mostly used for the fabrication of DSSCs (dye-sensitized solar cells)[104, 1, 105]. Typically these are transition metal complexes (*e.g.* Ru^{II}, Zn^{II}, Mg^{II}, Fe^{II}, and Al^{III}) with low lying excited states having ligands formed by nitrogen heterocyclics with delocalized π or aromatic ring systems. Synthesis of these TiO_2-sensitizer compounds is possible by creating a variety of bonds (*e.g.* covalent bonds via linking agents, electrostatic interactions, hydrogen bonding, or even Van der Waals forces). The basic mechanism of their functionality revolves around the dye absorbing light and then transferring generated photocharges to the attached TiO_2 nanoparticles. Naturally, this outlines some characteristic requirements to be fulfilled by the dye: (i) it should have good absorption efficiency for a wide range of wavelengths, (ii) its excited states should have long lifetimes, and (iii) it needs to have compatible electronic energy levels with those of TiO_2[106]. If these criteria are met, the electron transfer from the dye to its underlying TiO_2 matrix happens in under 200 fs[107]. Nevertheless, charge recombination and stability of Ru-dye systems are typically problematic[35]. Additionally, metal based sensitizers tend to carry a high environmental and economical cost, making them unsuited for industrial scale application[35, 6]. While organic dies, do not have such problems, they tend to be unstable in EPC environments. Additionally, charge injection from the dye molecules to the TiO_2 remains inefficient. While some methods have shown promise in remediation of these issues, further research and development are still required[35, 6].

Ohko et al. determined that TiO_2 films could be sensitized with Ag nanoparticles, seemingly showing behavior distinct from dye sensitizers or coupling semi-conductors[108]. Interestingly, the perceived coloration of the films was reversible, turning brownish-gray under UV light due to the reduction of Ag^+ and matching the color of visible illuminating light due to oxidation of Ag by O_2. The film color was determined by the Ag nanoparticle size, changing the plasmon-based metal particle absorption within confinement of the titania matrix. Tian and Tatsuma found that nanostructured TiO_2 films loaded with noble particles such as Au or Ag exhibited negative potential changes and anodic currents under visible light[109]. The $Au-TiO_2$ system responded coherently with Au nanoparticle photoexcitation due to plasmon resonance; this was typically accompanied with charge separation and transfer of photoexcited electrons into the TiO_2 conduction band[110].

This being said, it was also found that following UV illumination, TiO_2 nanorods could hold more conduction band electrons once they were decorated with Au or Ag nanoparticles; this indicated that there was a trapping and storage effect in play[111]. Because the work function of noble metals is usually larger than most semiconductors, e^- transfer from the CB of TiO_2 to the metal is not uncommon, and it is actually the basic working principle of a very popular Pt (work function $\sim$5.12 eV to 5.93 eV) co-catalyst approach[35, 31]. Noble metal co-catalysis is often regarded as a necessary implementation if no sacrificial agents are used for the production of H_2 via water splitting. It is important to distinguish this from the plasmonic effect commonly exploited with $Au-TiO_2/Ag-TiO_2$ pairs (see figure 2.5), as they are quite different[112].

In sum, while these surface sensitized assemblies show great visible-light response, they suffer from high rates of photo-corrosion and typically rely on expensive, toxic, and complex metal based dyes[113].

2.3.4 Doped TiO_2

As previously mentioned, the band structure of TiO_2 can be roughly estimated to be delimited by Ti_{3d} orbitals (non-bonding Ti t_{2g} d_{xy}) at the conduction band edge and O_{2p} orbitals (non-bonding O p_π) at the valence band edge. Logically, inserting dopants (with energy levels above the VBM or below the CBM) into the titania lattice would create intermediate energy levels that can act as either electron acceptors or donors depending on the dopant type and lattice configuration. Schematically, this is presented in figure 2.6(c).

Studies of bandgap engineering via doping date back to the early 1980s. Borgarello et al. reported visible light driven photocatalytic H_2O water splitting on Cr doped TiO_2 nanoparticles (albeit this is questionable as both Pt and RuO_2 were loaded as co-catalysts)[63]. The visible light absorption was attributed to photoexcited transitions of excited e^- from the newly created Cr^{III}_{3d} levels into the CBM (Ti_{3d}). Anpo et al. developed on this via implantation of various metal ions such as V, Cr, Fe, Co, and Ni with differing levels of effectiveness[64, 66, 65]. Regardless of EPC performance, almost all of these metal dopants were able to effectively reduce the E_g of titania (as verified via light absorption red-shift).

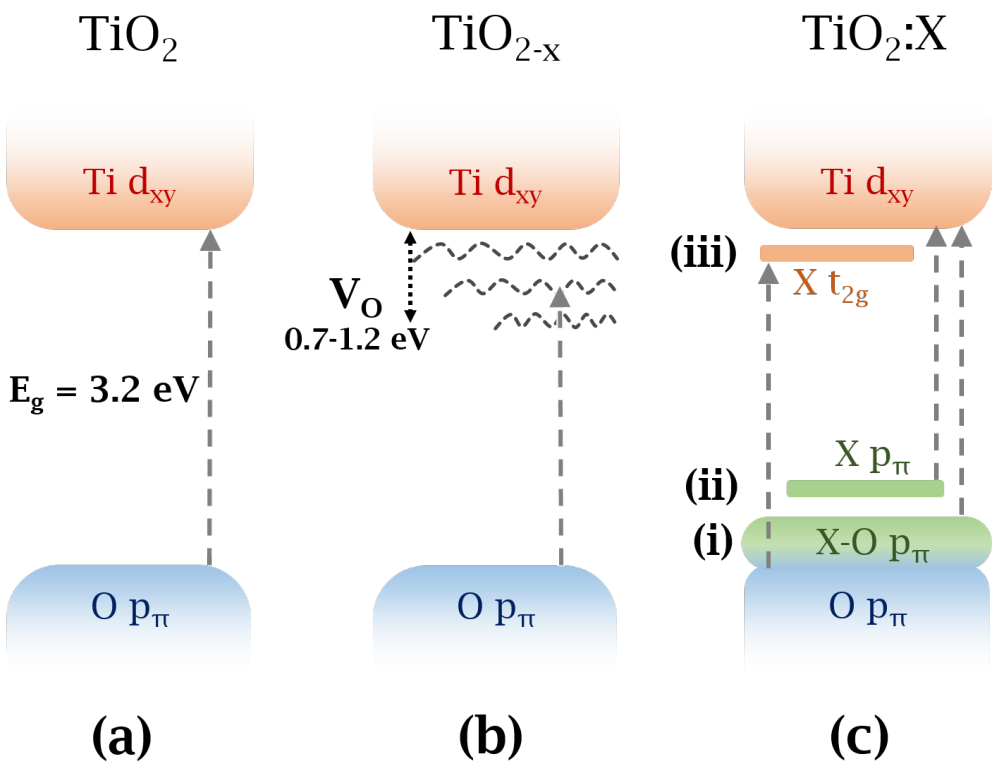

Figure 2.6 – Schematics of gap structure for (a) pristine anatase TiO_2, (b) sub-stoichiometric TiO_{2-x} with localized V_O states between 0.75 eV and 1.18 eV below the CBM [13], and (c) for X doped TiO_2 with three highlighted possible outcomes: (i) hybridization of the O p_π and X p_π states (ii) insertion of dopant states above the VBM (usually non-metallic X p_π levels) (iii) insertion of dopant states below the CBM (typically metallic X t_{2g} levels)[10, 5]. Typically, most real systems are a mix of (b) and (c) type energy levels. It is to be noted that other scenarios, such as deep mid gap states are also possible and entirely depend on the dopant induced formation of energy states.

Umebayashi et al. later demonstrated (using DOS-FLAPW simulations) that the dopants each created specific states within the TiO_2 E_g mainly via insertion of their t_{2g} levels into the gap structure (see figure 2.6(c)). The exact placement of these new states varied, ranging from straddling the CBM (V; anodic current only), to mid gap states (Cr, Mn, and Fe), to almost overlapping the VBM (Co), and in extreme cases contributing to the VBM (Ni doping)[114]. They indicated that e^- leaving the CB would lead to cathodic current and h^+ leaving the VB to anodic current. From a bonding perspective, 3d metal doping leads to stronger metal-O bonds as compared to pristine titania (most dopants would form strong t_{2g} to O p_π bonds) and produces a plethora of levels deep in the CB and VB that could shift based on the atomic loading.

From the variety of metal doping candidates, Iron showed the most promise for TiO_2 doping. Indeed, Khan et al.[68] and Dholam et al.[67, 115] demonstrated that Fe ions could efficiently delay the charge recombination of photo excited species by trapping both electrons and holes ($15.6\,\mu mol\,h^{-1}$ of H_2), while Cr could only trap one type of charge carrier ($5.3\,\mu mol\,h^{-1}$ of H_2). This was then generalized to include Cu and Mn ions as good candidates for such charge-symmetrical trapping[67, 68, 115]. This was an important realization, as it highlighted the necessity for a deeper understanding of charge mechanics within the photocatalyst, beyond the simplified ideal of visible-light sensitivity. Simply put, certain cationic dopants were known to increase EPC activity while not contributing to visible light absorption of the doped TiO_2, factors such as an increase in active surface area, photocorrosion resistance, particle dispersion, lower over-potential, charge lifetimes all required careful consideration[35, 6].

Niishiro et al.[116] and Sun et al.[117] proposed that codoping with two cations having different incorporated net valence can result in a charge balancing effect, increasing the photocatalyst's stability while reducing defect formation. This was demonstrated by codoping TiO_2 with Ni & Nb or Fe & Ni ($361.64\,\mu mol\,h^{-1}\,g^{-1}$ of H_2 under visible light)[116, 117]. This codoping approach will be revisited by other authors in the case of anionic and cationic doping, and will also be investigated in this doctoral work.

While cationic doping was shown to be successful in certain situations, many of these approaches suffered from thermal instability, were expensive (required sophisticated ion implantation facilities), would hinder photocharge mechanics, lead to the creation of intermediate E_g states (that would reduce the electron reduction energy), and most importantly lead to quite localized d states deep in the E_g of TiO_2 (acting as the recombination centers)[66, 33, 35]. To circumvent these drawbacks, Asahi et al. (2001)[33] highlighted the criteria for determining valid doping candidates leading to viable increases in visible-light photoreactivity of TiO_2:

(i) Doping should produce states in the E_g of TiO_2 that maximize visible light absorption.

(ii) The newly formed levels should be as high/low as the H_2/H_2O redox levels (or those of other targeted redox couples).

(iii) These dopant E_g levels should overlap sufficiently with the native states as to transfer photoexcited carriers to reactive sites at the catalyst surface within their lifetimes.

It was concluded that in order for conditions (ii) and (iii) to be met, anionic doping species would be required. In order to determine the best candidate for anatase doping, FLAPW (full-potential linearized augmented plane wave) in the LDA (local density approximation) framework was used to calculate the DOS for anionic type dopants such as: C, N, F, P, and S. In the case of nitrogen, it was shown that the observed gap narrowing was due to the newly created dominant optical transition between N p_π states just above the VBM (predominantly O p_π) and the Ti t_{2g} d_{xy} levels at the CBM[33]. This approach highlighted substitutional nitrogen ($N_O^\bullet$) as a prime candidate whereas interstitial nitrogen (N_i) doping was shown be detrimental due to formation of very deep gap states that could not effectively satisfy condition (iii). The other candidates all had major issues: sulfur having too big of an ionic radius (also would sometimes take the S_{Ti} state [118]), and carbon/phosphorous creating overly deep gap states (not meeting condition (iii)).

These conclusions were somewhat corroborated by Nakano et al.[119] who determined the formation of three distinct deep levels in the TiO_2 E_g as a consequence of C doping; two of these levels at 2.34 eV and 1.30 eV below the CBM were due to C $_{2p}$ levels with another 0.86 eV level being intrinsic to the TiO_2 (while authors did not attribute them to this, they were likely V_O states as shown in figure 2.6(b))[119]. Nevertheless, interesting EPC results have been reported using C doped TiO_2. Khan et al.[120] demonstrated C doped TiO_2 synthesised via controlled combustion of a Ti sheet that showed visible light sensitivity to $\sim$535 nm; once used as a photoanode, an 11 % hydrolysis efficiency at 0.3 V was achieved. Krengvirat et al.[121] prepared C doped nanotubular TiO_2 photoanodes via rapid anodic oxidation; these photoanodes showed H_2 evolution rates of $\sim$508.3 mL min^{-1} cm^{-2} with a conversion efficiency $\eta \sim 2.3$ % under a 0.3 V bias.

Di Valentin et al.[122] noted that anatase was a better candidate for N doping as DOS indicated a contraction of the O p_π valence band for doped rutile. However, this distinction has not been

clearly observed experimentally yet. Heating TiO_2 in a mixture of urea, Yuan et al.[123] were able to synthesize TiO_2:N. This material was shown to be active in H_2 production in a Na_2SO_3 solution under visible light irradiation. Most notably, the absorption spectum of this material was shifted up to ∼600 nm, in part due to the $N_O^{\bullet}$ and partly due to the molecularly chemisorbed N_2 (however, the exact nature of the states can be debated as they were loosely identified)[123, 33].

Nakano et al.[124] found deep levels located ∼1.18 eV and ∼2.48 eV below the CBM in TiO_2:N associated with V_O and N dopants, respectively. It was remarked that the oxygen vacancy states were efficient generation-recombination centers, greatly hindering the photocharge kinetics of the doped titania. Furthermore, Okato et al.[125] noted that high N incorporation was inefficient at O substitution, leading to the formation of undesirable deep-level defects instead. Indicating that ideally, low nitrogen dopant loadings were preferred. In other words, while nitrogen doping seemed suitable and fairly efficient at red-shifting the bandgap of TiO_2 well into the visible energy range, it also caused a plethora of defect states that required careful consideration. In order to tackle some of these issues, authors have attempted anionic codoping of B into N doped TiO_2 to increase e^- & h^+ lifetimes as to improve the overall EPC performance of the photoanodes[126, 127].

While technically the idea of a band-gap red-shift is a gross abuse of language and is a bit at odds with the formal and theoretical definition of the term: band-gap, i.e. E_g. For the purposes of this work, the term E_g will be used to describe both the formal meaning and what can best be described as the effective band-gap of a material (*i.e.* absorption edge).

2.3.5 Codoped TiO_2

In both the anionic and cationic doping cases, codoping for charge compensation seems to be a reoccurring theme. Recently, theoretical calculations indicated that codoping with matching anion-cation pairs can reap the benefits from both species while reducing defect formation arising from lattice charge disparities[128, 129, 130, 131].

Using the frozen-core projector-augmented-wave (PAW) method within the LDA framework, Gai et al.[128] highlighted several cation-anion dopant pairs (V−N, Mo−C, Cr−C, and Nb−N) that once co-introduced into the titania lattice would mutually passivate the local charge defects, all while effectively shrinking the E_g. They found that Mo−C doping could raise the VBM while leaving

the CBM unchanged, ideal for water splitting under visible light. Interestingly, DFT calculations performed by Yin et al.[131] identified that codoping pairs could vary based on desired dopant concentration ranges. They highlighted that Nb−N and Ta−N pairs are best in highly doped TiO_2, whereas Mo−2 N and W−2 N would be best in the "low doping" regime. The codoping scheme to be studied in this doctoral project was selected by taking into account the suggestions of Okato et al.[125] for low N-dopant loading, along with the theoretically proposed W−2 N passivation pair of Yin et al.[131].

At this point, in order to avoid any further ambiguities, some otherwise loose terms need to be defined. For the purposes of this work, the term "low doping" will mean anything in the 0.1 at.% to 7 at.% range. While this can seem like blasphemy to anyone coming from a microelectronics and MOSFET background (which typically deal with dopants in the ppm (1×10^{-4} at.%) range). We define it as such to differentiate from and find a middle ground with typical doping ranges observed in wet-chemistry synthesis of photocatalysts (ranging from 1 at.% to 20 at.%).

Experimentally, Sasikala et al.[132], using a polyol synthesis method obtained In−N codoped films that had a significant red-shift of the absorption edge and showed increased H_2 production as compared to pristine or monodoped TiO_2. Sun et al.[133] used sol-gel to prepare Ce−N codoped TiO_2 which showed absorption all the way to ∼600 nm and H_2 evolution rates of 120 µmol h^{-1}, about 20 times higher than their reference TiO_2. While they attributed this increase of performance to the E_g narrowing due to N−Ti and N−Ti−O type bonds, their XPS spectra showed the presence of other N species, with the exact role and contribution of each being difficult to distinguish. Results presented by Sasikala et al. and other authors suffer form similar shortcomings [134, 132, 135]. This is a recurring theme in most chemically synthesized codoped TiO_2, making it difficult to discern between optoelectronic and EPC contribution of each impurity state. This fact is commonly invoked to explain contradictory or nonsensical studies[35]. Additionally, often, little attention is attributed to factors such as surface area, charge lifetimes, and other important factors that are known to affect the overall EPC performance. In other words, controlled synthesis and in-depth investigation of a wide range of properties for the codoped titania system is still lacking.

2.4 Synthesis methods

Titanium dioxide can be prepared under various forms, including as nano/micro-powders, thin films, or even crystals. It is difficult to outline all the possible synthesis routes available. Nevertheless, this section aims to present the most commonly used methods while briefly summarizing some key features. In fact, TiO_2 and doped-TiO_2 synthesis methods can be separated into three categories: (i) wet chemistry, (ii) electrochemical synthesis, and (iii) vapor deposition. A more detailed description (compared to what is presented herein) of the various preparation methods can be found in some excellent review articles and books[10, 5, 35, 6, 31, 30, 113, 136, 137].

By far, the most popular approach seems to be the sol-gel synthesis route, which can be categorized into the non-alkoxide (use of inorganic salts) and the alkoxide (metal alkoxides as starting material) approaches. During the process, complete loss of solvent leads to the transition from the liquid sol into a solid gel phase (hence the name). This gel can then be applied and sintered as needed. Sol-gel is relatively easy to implement and it allows for coating of large surfaces while having access to a wide range of titanium sources[30]. However, in order to ensure good quality of TiO_2 films, the hydrolysis and condensation steps need to be separated and tempered[138]. Typically, these steps are followed by thermal treatment at 450 °C to 600 °C for the removal of contaminants (never ideal) and to obtain the anatase and rutile polymorphs respectively. Similarly, starting with raw $TiCl_4$/$TiCl_3$, the precipitation of hydroxides by the addition of basic solutions followed by annealing has been shown to produce good quality TiO_2 powders[30, 139]. These precipitation methods typically result in the anatase structure, but have been shown to give rutile under specific conditions, even at room temperature[30, 139]. While they are relatively simple, the precipitation methods are difficult to control, resulting in a wide range of particulate sizes. To avoid this, combustion synthesis has been shown to give highly crystalline, and size controlled particles. This method involves rapid heating (1 min to 3 min) of mixed redox groups at ∼650 °C[140]. In general, these approaches are limited to the synthesis of nano/micro-particles or to the coating of relatively simple surfaces.

Electrochemical synthesis routes may be used for the preparation of much more specialized TiO_2 such as epitaxial thin films, superlattices, quantum dots, and nanoporous surfaces[30, 31]. One approach is incorporating the substrate surface as the cathode in a reducing environment. Thus, the surface to be coated is immersed into a solution containing inorganic salts as Ti sources (e.g $TiCl_3$,

$(NH_4)_2TiO(C_2O_4)_2$, $TiCl_4$, etc.). Trough an electrochemical reduction process, TiO_2 can be formed. Electrochemical synthesis can be easily controlled due to a well developed understanding of the effects of the various preparation parameters (*e.g.* the potential, temperature, current density, pH, etc.). Unfortunately, these reactions require complex solutions and oxygen-free environments as to minimize the natural tendency of salts have to hydrolyze the TiO_2[141]. Similarly, by incorporating raw Ti into an electrochemical circuit as the anode with oxidizing solutions (*e.g.* NH_4F, H_2O_2, etc.), it is possible to form crystalline TiO_2 through a dissolution/precipitation mechanism[31, 5]. This method has gained popularity due to the production of TiO_2-nanotubes with very interesting photocatalytic properties due to their form factors and high surface areas.

Vapor deposition methods refer, in essence, to any method which condenses a given vapor phase into a solid-phase material. By extension, these tend to be methods of choice for the fabrication of thin films, but they can also be used for powder synthesis. Chemical vapor deposition (CVD) refers to any method that requires a chemical transition from a precursor to product while in the gas phase. CVD deposition, while presenting some complexity in regard to chemical precursor selection, presents a key advantage in that it can prepare highly pure TiO_2 films onto large surface areas, regardless of the substrate shape[142, 143, 31]. A number of CVD processes are widely used and differ mainly by which type of precursors are used (*e.g.* Metal-organic chemical vapor deposition (MOCVD), the deposition pressure (*e.g.* Atmospheric pressure chemical vapor deposition (APCVD)), reaction conditions (*e.g.* Plasma-enhanced chemical vapor deposition (PECVD)), supports used in the process chamber, etc[143]. Typically, CVD processes expose the sample support to single or multiple precursors at a controlled temperature, pressure, and phase. These volatilized precursors can then decompose onto the substrate surface, depositing the thin film of choice.

Physical vapor deposition (PVD) in contrast, refers to all methods using a physical process to produce the vapor of the material to be deposited. It generally used solid and stable substances that are transformed into the gas phase[31]. Typically, these processes take place under vacuum conditions as to minimize gas collisions, and insure high purity of films. The magnetron sputtering (RF-MS) method used in this thesis is a PVD approach (see annex A.1 for more details). While PVD methods tend to be technically more elaborate than most other approaches, they allow an unparalleled control of the obtained thin film properties, especially when purity, uniformity, and crystallinity are at stake. Unfortunately, advanced PVD approaches such as sputtering, molecular beam epitaxy, pulsed laser deposition, and electron beam methods tend to be expensive (in compar-

ison to wet chemistry) and frequently associated with very slow deposition rates[31, 30]. Regardless, they continue to attract much attention due to their unparalleled flexibility and control over the characteristics of deposited thin films.

Many authors have used these varied deposition methods in order to ensure incorporation of desired dopants into the TiO_2 lattice. These will be separated based on dopant type in the following subsections.

Metal doped TiO_2 (cationic doping)

Choi et al.[66] produced an impressive study of sol-gel synthesized TiO_2 doped with 21 different metal-ions. As expected, the metal dopants were shown to greatly influence the photoreactivity of TiO_2. However, these changes were of mixed EPC outcomes, in a large part due to their negative effects on the photocharge transport (lifetimes, inter-facial charge transfer, etc.). Using a solution combustion method, Nagaveni et al.[140] incorporated a variety of metal-dopants (W, V, Ce, Zr, Fe, and Cu) into anatase. They noticed that a solid solution of the respective oxides happened above a small range of concentrations, limiting the amount of actual chemical dopant incorporation allowed by the structure. This was developed upon by Anpo et al.[64, 65] who used an ion implantation technique to incorporate V, Cr, Fe, Co, and Ni into the titania lattice, corroborating Choi et al.[66] observations of the metal-dopant's effects on photocharge lifetimes and dynamics. Additionally they noted that regardless of performance, most dopants were able to reduce the E_g of TiO_2 via new dopant or V_O states. In fact, comparative studies confirmed that regardless of the synthesis route (sol-gel or impregnation), the doping results depended mainly on concentration and nature of the dopants (in their case, alkaline dopants such as Li, Na, and K)[144]. This result would later be completed upon by demonstrating that lattice location plays also an important role in the doping mechanism[113]. On the other hand, it has been shown, that for CVD synthesized TiO_2 doped with various metals (Cr, V, Fe, Co, and Sn) distinct oxide phase segregations would form upon annealing above certain cation dopant concentrations[145, 146]. Interestingly, it was noted that the nature of dopants determines the concentration of surface defects, as well as the final crystalline phase of TiO_2 (anatase or rutile)[145, 146].

Non-metal doped TiO_2 (anionic doping)

Simple approaches used for C doping are direct combustion of Ti-sheets in a natural gas fueled flame or annealing titania in a CO atmosphere at high temperatures (∼800 °C)[147, 148, 120]. Both approaches resulted in significant changes of optical properties of TiO_2:C in accordance with the creation of dopant and defect associated gap states. It was noted however that for a given atomic metal doping species, different doping methods produced diverging results. TiO_2:S synthesized via mixing of TTIP (titanium (IV) isopropoxide) with thiourea produced $S^{IV/VI}$ dopant states (cationic doping), while heating with TiS_2 or sputtering with S produced the desired S^{2-} oxidative states[118, 149, 150]. This is key, as simply incorporating a desired dopant is simplistic and insufficient. The exact state of the dopant within the lattice needs to be fine-tuned for achieving the desired EPC outcome. Neglecting this fact is the likely cause of many contradicting results in the literature. Similarly, fluorine (F) incorporation could be achieved by mixing TTIP with a mixture containing NH_4F, or exposing TiO_2 to HF at high temperatures, or even ion-implanting F directly into the TiO_2 matrix[151]. A similar preparation methodology also applies to synthesis of nitrogen doped TiO_2:N[152, 153, 154, 155, 156, 157]. In fact, facile nitrogen incorporation can be assured via hydrolysis of TTIP in a H_2O/amine mixture or from Ti-bipyridine, or via ball milling of TiO_2 in NH_3. High temperature synthesis is also possible by heating TiO_2 under NH_3 gas flux (∼550 °C), or by calcination of $Ti(SO_4)_2/NH_3$ byproducts[158, 159]. On the other hand, plasma assisted approaches have also been quite successful with either gas-phase decomposition of $TiCl_4$ using a microwave plasma torch or simply via sputtering under the presence of nitrogen containing background gas[33, 158, 160]. However, as highlighted by Asahi et al.[33], and reiterated for S doping, a particulate care must be given to ensure that nitrogen is incorporated in the desired lattice location with the appropriate chemical state to ensure the predicted beneficial properties. It is commonly accepted that substitutional nitrogen ($N_O^{\bullet}$) is the most effective dopant for visible light active TiO_2[33, 113, 34].

2.5 Applications and some performance figures

As detailed in the previous section, TiO_2 can be fabricated in many shapes and forms using a variety of different, effective methods. Owing to this flexibility of manufacturing and its unique physico-

chemical properties, TiO_2 has attracted much attention for applications such as: EPC degradation of pollutants, CO_2 reduction, light-driven water splitting, solar cells, etc. This section aims to provide a quick overview of these applicative avenues for TiO_2, while providing some quantitative benchmarks that have been achieved in each field. It is important to note that this work focuses on applications that rely on light excitation of the material, therefore some subjects such as super-capacitors, Li-ion batteries, and others will be intentionally left out.

2.5.1 Solar cells

Titania is a promising candidate for solar cell architectures. These come in two main flavors: dye-sensitized and quantum-dot sensitized solar cells[137, 6]. Dye-sensitized solar cells (DSSCs) are schematically, a sandwich-like assembly of a transparent nanocrystalline TiO_2 conducting substrate and a catalytic counter-electrode (typically carbon based, or from noble metals), separated by an electrolyte. Typically, in order to allow visible-light absorption, a dye-sensitizer is adsorbed on the TiO_2 scaffolding[104, 1, 105]. These dyes can be of varying nature as has been discussed earlier in this chapter. Upon illumination, the dye is photo-excited and injects photogenerated e^- into the TiO_2-electrode (then extracted to an external circuit). The oxidized dye is then regenerated (reduced) by the electrolyte, which is itself, in turn, regenerated by the counter-electrode, completing the electrochemical circuit. DSSCs have low production costs and relatively high solar-to-electric energy conversion efficiency[104, 1, 105, 137, 6]. In 2008 Gao et al.[161] reported TiO_2/Ru-dye based DSSCs with a power conversion efficiency (PCE) of 10.53 %. This was then surpassed by Mathew et al.[162] in 2014, reporting a 13 % efficiency for DSSCs with a zinc porphyrin dye and $Co^{II/III}$ tris(bipyridine) based redox electrolyte. Parallel to this, a perovskite (*i.e.* $CH_3NH_3PbX_3$ where X can be Cl, Br, or I) sensitized DSSCs with a power conversion efficiency of 15 % by Burshka et al.[163] in 2013. Quantum-dot sensitized solar cells (QDSSC) are a variation of DSSC, employing quantum-dots to ensure visible-light absorption of the cell. This has a few key advantages such as higher light absorption, and longer cycling stability as compared to traditional DSSCs[137]. As with DSSCs, QDSSCs are composed of a quantum-dot covered TiO_2 photoanode, a counter electrode, and a redox electrolyte. In 2014, Rao et al.[164] reported a PCE of 4.20 % for a CdS/CdSe co-sensitized TiO_2 based QDSSC. In 2017, Lee et al.[165] reported a 3.35 % PCE for TiO_2/CdS QDSSCs with a Cu–ZnS passivation layer. Recently (2018), Sehn et al.[166] reported Zn–Cu–In–Se solar paint sensitized QDSSCs with a PCE of 4.13 %. While DSSCs/QDSSCs have shown promising results,

they can theoretically be greatly simplified with the use of a visible-light absorbing photoanode that would remove the need for complex dye/quantum-dot sensitized electrodes.

2.5.2 EPC water splitting (H_2 production)

Some of the earliest breakthroughs in the use of TiO_2 for the photocatalytic conversion of solar light were intended for efficient H_2 & O_2 generation[56]. Photocatalytic H_2 production happens as the photogenerated electrons at the CBM reduce H^+ ions to generate hydrogen and holes at the VBM react with water to generate hydroxyl radicals. Both of these processes are happening simultaneously, within the same TiO_2 particle. Electro-photocatalytic H_2 production relies on photoexcited electrons moving from the TiO_2 CBM to a counter electrode (this process is often supported by applying an external bias), where they reduce H^+ into H_2. Parallel to this, the associated h^+ oxidize H_2O at the TiO_2 surface. A proton exchange membrane separates the two electrodes, completing the electrochemical circuit. In recent years a variety of architectures have been employed to try and increase EPC H_2 production from the original quantum efficiency benchmark of 10 % set by Fujishima and Honda in 1972[56]. In 2016, Zhu et al. [167] reported a 5713.6 $\mu mol\, h^{-1}\, g^{-1}$ H_2 production under visible light using a Pt decorated C/TiO_2 hollow spheres. Using whispering gallery mode resonances, in 2016, Zhang et al.[168] reported a 647 000 $\mu mol\, h^{-1}\, g^{-1}$ H_2 production under Vis-NIR light (*i.e.* >420 nm) on Au−TiO_2 nanohybrids. Using a TiO_2:N photoanode, Wang et al. (2013)[169] were able to achieve a 601 $\mu mol\, h^{-1}\, g^{-1}$ H_2 generation (around 50 times higher than what was reported for Degussa P25). Using a purely photocatalytic, solar light driven process on graphitic-C_3H_4 nanosheets decorated with TiO_2:N nanofibers, Han et al. (2015)[170] reported 5713.6 $\mu mol\, h^{-1}\, g^{-1}$ H_2 generation rates.

2.5.3 Photocatalytic reduction of CO_2

From an environmental and economical viewpoint, photocatalytic CO_2 reduction into hydrocarbon energy fuels is both promising and meaningful. The first demonstration of the reduction of CO_2 on a TiO_2 photoanode was done by Inoue et al. (from the Fujishima and Honda group) in 1979[171]. It was showed that the photogenerated h^+ could react with H_2O to generate hydrogen ions, while the electrons at the CBM could reduce CO_2 into various carbon based forms such as: CH_4 (−0.24 V *vs* NHE at 7 pH), CO (−0.53 V *vs* NHE at 7 pH), CH_3OH (−0.38 V *vs* NHE at 7 pH), etc[136]. That

being said, ideally, the EPC process is tuned as tu maximize the generation of CH_4. Typical CH_4 generation efficiencies for sol-gel synthesized TiO_2 are $\approx 1\,\mu mol\,h^{-1}\,g^{-1}$ under UV illumination[137]. In 2014, Wang et al.[172] demonstrated an optimized $Pt-TiO_2$ photocatalyst that was able to simultaneously generate $22\,mmol\,h^{-1}\,g^{-1}$ of H_2, $0.7\,mmol\,h^{-1}\,g^{-1}$ of C_2H_6, and $15\,mmol\,h^{-1}\,g^{-1}$ of CH_4 under visible light illumination. In 2015, Zhang et al.[173] reported on a nanorod-like TiO_2:N photocatalyst that was able to achieve $\approx 80\,\mu mol\,h^{-1}\,g^{-1}$ of CH_4 under simulated solar light.

2.5.4 EPC degradation of pollutants

As discussed previously in this chapter, EPC (and plain photocatalytic) degradation of pollutants is a major topic of interest for TiO_2 systems. Both volatile organic compounds and water dissolved pollutants can be degraded with TiO_2 based systems, albeit with designs adapted to each use-case. In any case, the working principles remain the same, oxidation and/or reduction at the TiO_2 surface via the photogenerated h^+ and e^-, respectively. Unfortunately, given the sheer abundance of degradation targets and TiO_2 configurations reported, it is difficult to propose quantitative benchmark figures that are representative of the field as a whole. Nevertheless, Teh et al.[174] and Shayegan et al.[175] do a great job in summarizing some recent advances in the field of pollutant degradation for water dissolved and volatile gas phase pollutants, respectively.

2.6 Summary

In summary, while many approaches have been highlighted allowing for visible-light photosensitizing TiO_2, few are of intrinsic nature to the material. While surface sensitization approaches have been successful in achieving visible-light photoactive TiO_2-compounds, they suffer from high rates of photo-corrosion whereas the dyes used are generally unstable, expensive, and their handling is rather complex[113].

Cationic type doping, while successful in red-shifting the absorption edge of TiO_2 have been shown to suffer from thermal stability, and integration complexity. However, TiO_2 doping with anionic elements (*i.e.* F, C, N, etc.) has shown best results. Most notably, nitrogen doping presents itself as a candidate of choice due to both size compatibility with the anatase titania lattice (possibility of N substitution of O atoms, *i.e.* $N_O^{\bullet}$) and band energy alignment (N_{2p} states

just above the VBM O_{2p} states). Additionally, it was highlighted that N-doping is ideal in low dopant loading configurations. This TiO_2:N definitely needs more attention as to better understand the mechanisms governing the dopant incorporation into the titania matrix. Its association, in the low doping scheme with other cationic dopants (such as W) is of a particular interest as to achieve not only TiO_2 bandgap narrowing (*i.e.* visible-light photosensitization), but most importantly, improved photocharge transport through effective codopant passivation. These concluding remarks constitute the main objectives of the present doctoral project. The following chapter summarizes the results we have obtained in the context of this PhD work.

Chapter 3

Results

Tell me the facts and I'll learn. Tell me the truth and I'll believe. But tell me a story and it will live in my heart forever.

Native American Proverb

The following chapter will present the results of this doctoral project. It starts with TiO_2:N thin films being highlighted as candidates of choice for achieving visible light photoactive TiO_2 intended for EPC applications. The choice of RF-MS deposition method is shown to be a necessity for the desired control of N incorporation in the TiO_2 films. The chapter will then present and discuss results obtained on the sputter deposited *in-situ* doped TiO_2:N films (section 3.1). This will be concluded with some drawbacks of the nitrogen mono-doping approach, and propose a pathway to mitigate such undesired consequences using an acceptor-donor passivating scheme. The subsequent section will explore a candidate of choice (tungsten) as the cationic co-dopant for nitrogen in the passivated TiO_2 system (section 3.2). Finally, section 3.3 will explore tungsten-nitrogen, acceptor-donor passivated, codoped TiO_2:WN thin films with both visible light photosensitivity and reduced charge recombination defect states.

Most of the results discussed herein are taken directly from or will serve to compliment the scientific publications found in part IV of this text. However, this section will use the advantage of hindsight and completeness to place all the results into perspective and context.

3.1 Nitrogen doped TiO_2:N thin-films

Chapter 2 highlighted that TiO_2 widespread use was sparked by the pioneering work of Fujishima and Honda (1972)[56] on titanium dioxide based water splitting. However, it has continued to attract much attention due to a unique combination of features such as: its band-gap potential energy levels (see figure 1.1), high photochemical stability, and availability[56, 104, 120, 34, 176, 33, 31, 113]. Fundamentally, TiO_2 is an n-type semiconductor (see section 2.3.2) with a wide intrinsic band-gap. The exact values depend on the polymorph, with rutile and anatase having an E_g of 3.0 eV and 3.2 eV, respectively. This large bandgap limits the use of pure TiO_2, in many light driven photocatalytic applications, to the UV portion of the lightr spectrum, which represents only $\approx 4\%$ of the total sun irradiance as shown in figure 1.2. In the perspective of sunlight driven photocatalytic applications, visible light activated TiO_2 is of great interest[113].

Many of the strategies discussed to accomplish visible-light photo-sensitization involved complementing TiO_2 with dyes, co-catalysts, or combining it in heterojunctions (see section 2). While these approaches are interesting and yet challenging, they do little to modify the intrinsic properties of the material, catapulting doping as the approach of choice to ensure visible light sensitive TiO_2. Specifically, anionic type dopants (*e.g.* C, F, S, N, etc.) were outlined as prime candidates[33, 9]. On the other hand, most transition metals, and V_O doped (*i.e.* TiO_{2-x}) titania were eliminated as they have been showed to suffer from thermal instability, increase of carrier-recombination centers, lower photocharge mobility, and the formation of energy levels below the CBM (e.g. $\approx$0.75 eV to 1.18 eV below the CBM for TiO_{2-x}) leading to a reduction in the electron redox potential (see figure 1.1)[66, 33]. Among anionic dopant species, substitutional nitrogen (*i.e.* $N_O^{\bullet}$) arises as the most effective dopant for the two main following reasons[34, 9, 33]:

(i) Nitrogen's ionic radii allows for $N_O^{\bullet}$ type doping within the TiO_2 lattice. Sulfur, while satisfying all other criteria, is too big, which often leads to the formation of S_{Ti} type doping; and

(ii) $N_O^{\bullet}$ doping is expected to contribute to the band-gap narrowing by creating N_{2p} states above the VBM and by mixing with O_{2p} states, with the dominant electronic transitions at the absorption edge being from N_{2p} to Ti_{dxy}[113].

It is to be noted that most of the papers on N-doped TiO_2 (TiO_2:N) have used chemical synthesis routes (*i.e.* sol-gel, hydrothermal, and others, see section 2.4), which resulted mainly in interstitial type N-doping (*i.e.* N_i, typically forming $NO^{\bullet}$ type interstitial species), and suffered from reproducibility issues (due, in part to uncontrolled contaminant residues)[30, 34, 35, 6, 31, 113]. For these reasons, physical vapor deposition methods offer a better alternative to achieve fundamental studies on the doping of highly pure TiO_2 films while singling out the effect of each varied experimental parameter. While PVD methods have been also used for the doping of TiO_2 films [30, 34, 35, 6, 31, 113], systematic studies on the effect of various key parameters (such as the doping level, substitutional-to-interstitial N-doping ratios, chemical/structural nature of the films, their correlated EPC performance, etc.) are still to come. This doctoral thesis aims at filling that gap, all the while targeting visible-light driven degradation of pollutants in water as an applicative testbed. Radio frequency magnetron sputtering (RF-MS) was used in this work for the study and optimization of the *in-situ* doping of TiO_2 films intended for visible light EPC applications.

3.1.1 Reactive radio-frequency magnetron sputtering of TiO_2:N

The TiO_2:N and reference TiO_2 thin films were deposited from a 7.62 cm diameter TiO_2 RF-magnetron sputtering target (99.99% purity) with a constant power density of $7.7\,W\,cm^{-2}$ applied to the target at 13.56 MHz. The sputtering chamber was maintained at an inter-deposition base pressure of 2×10^{-8} Torr. High purity Ar sputtering gas (99.999% purity) was introduced into the chamber prior to deposition. Both the sputtering target and substrates were systematically sputter-cleaned using Ar ions for 15 min with the shutters closed. This *in-situ* cleaning process had two purposes: (i) clean the substrate of any surface contaminants such as carbonaceous species, and (ii) remove any sputtering target surface contaminants originating from previous deposition cycles. The TiO_2:N films were simultaneously deposited onto different substrates as to allow for the various characterization methods and purposes. The substrates were: (i) undoped and double side-polished Si(100), (ii) quartz, and (iii) deployed (10 cm by 11 cm) Ti grids. They were mounted on a holder located off-axis at a distance of 20 cm from the target, and heated by a quartz lamp heater of which temperature was kept constant at 650 °C during deposition; this nominal temperature on the heater corresponds to an on-substrate temperature of 470 °C, just below the anatase-rutile transition point. This on-substrate temperature was achieved with a heating ramp of $10\,°C\,min^{-1}$. After Ar sputter-cleaning, the gas flow rates were monitored to keep a constant pressure of 1.44 mTorr in

the chamber. This pressure domain ensures film morphologies of with columnar-like grain growth characteristic of the T zone in the Thornton model[15] (figure A.3, further details in section A.1). In addition to the Ar carries gas, another reactive gas was co-introduced via a gas-ring with radially inward pointing inlets at 5 cm substrate distance, along the target's atomic flux path as shown in figure A.4.

Under typical magnetron-sputtering conditions, sub-stoichiometric growth of sputter deposited titania thin films occurs. This is due to two main reasons:

(i) The target surface can sub-stoichiometric due to preferential sputtering effects. Typically, in a TiO_2 target, under the same Ar^+ ion sputtering conditions, the O atoms are easier to sputter as compared to the Ti ones due to atomic mass (m_A) and radii (r_A) differences (*i.e.* sputtering yield $\propto \frac{r_A}{m_A}$)[14, 36].

(ii) Lighter sputter ejected atoms tend to diffuse more than heavier ones as they travel through a constant Ar gas environment, leading to less O atoms reaching the substrate. This effect is minimized by depositing at a relatively low sputtering pressure (of 1.44 mTorr)[14, 36].

In order to counteract these effects and ensure stoichiometric growth of reference TiO_2 thin-films, O_2 gas was co-introduced with a relative mass flow ratio R_{O2} of 15% during the sputter deposition process; *i.e.* $R_{O2} = 100\% \times [O_2] \div ([O_2] + [Ar])$ where $[O_2]$ and [Ar] denote the flow of O_2 and Ar gases (in sccm), respectively. In similar fashion, TiO_2:N thin films were grown with a relative nitrogen mass flow rate ratio R_{N2} varied between 0 and 25%, *i.e.* $R_{N2} = 100\% \times [N_2] \div ([N_2] + [Ar]) = 0 \rightarrow 25\%$. No sputter deposition was carried out with both O_2 and N_2 gases within the chamber as to not promote the formation of NO_x type species. No post acceleration voltage was applied to the substrates during the deposition process (they were nonetheless subjected to a built-in plasma sheath bias of -13 V during their growth).

Further theoretical and experimental description of the RF-MS deposition method can be found in annex A.1. Finally, the TiO_2:N film thicknesses were *in-situ* monitored by means of a calibrated quartz-crystal micro-balance. These thin film thicknesses were also *ex-situ* measured through cross-sectional SEM observations as detailed in the following section. By having access to accurate film

thickness measurements, we were able to determine the deposition rates of our RF-MS deposition process under the various growth conditions investigated in the present doctoral project.

3.1.2 Properties of RF-MS deposited TiO_2:N

TiO_2:N chemical and structural properties

The chemical composition of the sputter deposited TiO_2:N thin-films as a function of R_{N2} was systematically studied via XPS analysis. High resolution binding energy (BE) of O_{1s}, Ti_{2p}, and N_{1s} core level spectra were collected by using an ESCALAB 220i-XL spectrophotometer (Thermo VG Scientific Ltd., UK). This spectrophotometer was equipped with a monochromatized $Al_{K\alpha}$ (1486.6 eV) twin-anode source. Scans were taken after a systematic *in-situ* surface cleaning by means of 5 keV Ar^+ ion sputtering gun with an average 0.15 mA current (see section A.2.1 for a detailed description of the experimental method).

The XPS analysis revealed that the addition of reactive N_2 gas in the sputter-deposition process was successful in incorporating nitrogen within the titania lattice as shown in figure 1(a) of article 1. Additionally, elastic recoil detection with time of flight (ERD-TOF) measurements revealed that dopant concentrations were homogeneous throughout the film thickness (figure 1(b) of article 1). Critically, upon N_{1s} BE spectra deconvolution, the characteristic Ti−N BE was observed at 396.9 eV. This signature is associated with $N_O^{\bullet}$ type doping within the TiO_2 lattice (*i.e.* nitrogen replacing a lattice O)[177, 33, 113]. Figure 5 of article 1 shows the fitted XPS spectra for the sputter deposited TiO_2:N thin films with an R_{N2} of 0.0 % (*i.e.* R_{O2} = 15.0 %), 7.5 %, 10.0 %, and 15.0 %. Interestingly, we can observe the main nitrogen component systematically accompanied by a second component, maintaining an approximate 1 : 2 ratio at ≈1.3 eV higher BE. The exact nature of this component is still debated in the literature. However, based on recent DFT models, interstitial type nitrogen dopant signatures should manifest at slightly higher BE as compared to $N_O^{\bullet}$. Specifically, N_i, NO_O, and NO_i signatures are expected at ∼1.9 eV, ∼2.4 eV, and ∼3.9 eV higher BE, respectively[113]. However, all the lattice incorporated species should be present below ≈402.0 eV, as this is assigned to chemisorbed N≡N molecules, which have the highest expected bonding strength[34, 31, 178, 177, 179]. From the figure, we also note a systematic increase in relative intensity of the nitrogen signal with increasing R_{N2}. This relationship is seen to follow a saturation-like behavior as shown by Figure 1 of article 1. While at lower nitrogen gas flow

rates, it follows a quasi-linear increase as more nitrogen is available in the deposition plasma to be integrated in the films. At higher R_{N2}, the dopant incorporation efficiency plateaus, likely due to process reaching the maximum energy available for the dissociation of N_2 gas.

This effect is simultaneously observed in the film sputter deposition rates. The increase of R_{N2} (*i.e.* $0\,\% < R_{N2} < 25\,\%$) is seen to increase the deposition rates. However, the sputter-deposition effectiveness is seen to plummet at high nitrogen flow rates and under oxygen flow rates (*i.e.* $R_{N2} = 25\%$ & $R_{O2} = 15\%$, respectively). It can be proposed that both gases, at relatively high mass flow rates sap much of the sputtering effectiveness. Oxygen is seen to achieve this at lower relative pressures due to its higher reactivity. Four processes can be invoked to explain this: (i) increasing reactive gas relative pressure increases the sputtering energy required to break up these molecules, reducing effective magnetron target sputtering energy, (ii) these dissociated atomic species end up poisoning the target surface (hindering target sputtering), (iii) higher reactive gas partial pressure results in an increase of in-flight atomic reactions, leading to the formation of gaseous species that are then evacuated by the pump, and (iv) the collisional cross sections of both O_2 and N_2 are higher than those of Ar, reducing the amount of species that effectively reach the substrate.

However, this variation of sputtering effectiveness with R_{N2} did not influence the TiO_2:N film morphology. Figure 3.1 shows the SEM cross-sectional images of samples deposited at $R_{N2} = 0\%, 10\%,$ and 20%. We note that the entire range of samples shows smooth, dense, and columnar-like grain growth consistent with zone *T* of the Thornton model (see figure A.3). This is expected, as the sputtering pressure and temperature remained constant throughout the varying R_{N2} deposition run, allowing for a dense, columnar-like growth of the TiO_2 crystal domains.

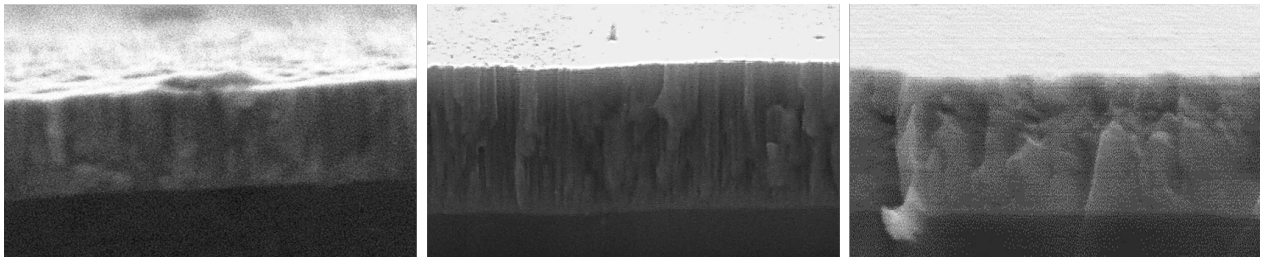

Figure 3.1 – Cross-sectional scanning electron microscopy images of sputter deposited TiO_2:N thin films, from left to right, we see: 0.0 at.% sample of 132 nm thickness, 3.4 at.% sample of 796 nm thickness, and 5.9 at.% sample of 619 nm thickness. These correspond to samples deposited with $R_{N2} = 0\%$, 10%, and 20%.

As discussed in section 2.3, the anatase phase of TiO_2 is more appropriate for EPC applications as compared to rutile because of its indirect band-gap (forbidden direct k recombination vector) which is associated with longer lifetimes of the photocharges[32, 113]. XRD and FTIR were used to reveal the crystallographic nature of the polycrystalline-domains (see figures 3 & 4 of article 1) as a function of their nitrogen doping level (XRD experimental details are given in section A.2.4). We noted that at low N content (low R_{N2}), there were insufficient anions to fill the oxygen deficiencies, and the rutile phase was favored during film growth. This is likely driven by the fact that rutile is the denser polymorph as compared to anatase. Whereas at higher doping levels, the anatase phase was observed due to $N_O^{\bullet}$ filling of sufficient V_O, reversing this trend. Interestingly, at highest R_{N2}, the presence of a secondary oxynitride phase was observed in the XRD spectra and somewhat in the FTIR spectra. This phase is known to originate from substitutional type nitrogen doping (*i.e.* $N_O^{\bullet}$) in highly sub-stoichiometric Ti_3O_5-like phases of titania, in direct agreement with the XPS observations[180].

Optoelectronic properties and EPC performance of TiO_2:N

It is important to recall that the main purpose of the nitrogen doping is to photosensitize TiO_2:N films into the visible light spectrum. Thus, the effect of nitrogen doping on the UV and visible optical absorption properties of the TiO_2:N films was systematically investigated (see section A.2.2 for experimental details). It was clearly observed that nitrogen doping was successful in significantly red-shifting the optical absorption spectra of TiO_2:N thin films. As shown in figure 6(a) of article 1, TiO_2:N films with an optimal N content of 3.4 at.% had the greatest red-shift in their transmittance spectra edge, reaching 450 nm. This can be visually noticed by comparing quartz coated with undoped ($R_{O2} = 15\%$) TiO_2 and optimally doped ($N_{O2} = 10\%$) TiO_2:N films (see top left and top right images of figure 6 in article 1, respectively). Dopant loading above 3.4 at.% did not translate into further red-shift of the transmittance edge. Indicative of the fact that until this point, dopant related induced states within the TiO_2 gap structure continue to form and be filled[113]. Whereas past this point, additional N loading likely serves only to promote the growth of the oxynitride phase with its own distinct properties[180].

These qualitative observations were reinforced with quantitative analysis the UV-Vis spectra. Both Tauc plot model based extrapolation and spectral ellipsometry (SE) measurements (see section

A.2.3 for experimental details) were used to quantify the bandgap of TiO_2:N thin films as a function of nitrogen loading. In full agreement with above-mentioned observations, the narrowest bandgap was observed at 3.4 at.% of N, as shown in figure 7 of article 1. Indeed, the optimally doped TiO_2:N thin films were shown to have a significantly smaller E_g of 2.2 eV. This represents almost a 1 eV reduction as compared to the reference TiO_2 anatase E_g of 3.2 eV. These results confirm that the RF-MS based *in-situ* nitrogen doping is an effective method of photo-sensitizing TiO_2 well into the visible light region.

The effectiveness of E_g narrowing in increasing the visible-light driven EPC performance of the TiO_2:N films was assessed by integrating these as photoanodes in a home-built electro-photocatalytic reactor (see figure A.19). For this purpose, the thin films were deposited on both sides of deployed 10 cm by 11 cm Ti-grids using RF-MS. These were then integrated as photoanodes into a 1 L capacity Plexiglas reactor (with a front facing quartz window as to allow illumination of the TiO_2:N covered Ti-grids). The photoanodes were submerged into a continuously circulating mixture of water and pollutant. The EPC performance of our TiO_2:N photoanodes was directly assessed towards the degradation of a real emerging contaminant, chlortetracycline (CTC). CTC is a widely used antibiotic in the agricultural industry, which is poorly removed by water treatment plants and therefore persists as a residual bioactive pollutant[181, 182]. It is thus highly relevant to develop a reliable approach to degrade CTC with the aid of visible light. To this end, synthetic solutions containing CTC concentrations of $100\,\mu g\,L^{-1}$ were prepared and treated in our EPC reactor under 1.5AM solar simulator light while continuously circulating them for 2 h. Further experimental details on this experiment can be found in section A.3.

While all TiO_2:N photoanodes tested were able to degrade CTC under visible light irradiation to a certain extent, we noted a clear dependence between the EPC degradation efficiency and the photoanode N content (which, in turn, affects its bandgap). This is best highlighted by figure 8 of article 1, which shows that the residual amount of CTC, following the 2 h treatment cycle under 1.5AM illumination, reaches its minimum for the 3.4 at.% optimal doping level of the TiO_2:N photoanodes. This demonstrates that the optimally N-doped TiO_2:N photoanodes degraded 98.5 % of CTC molecules within the treatment time limit, reaching safe environmental recommendation of $2\,\mu g\,L^{-1}$[183]. In sum, the optimization of N-doping level has led not only to the narrowest E_g (*i.e.* $E_g = 2.2$ eV), but also showed the best degradation performance, confirming thereby a direct

correlation between the increased visible light harvesting capabilities of the TiO_2:N photoanodes and their performance in the EPC degradation of CTC.

3.1.3 Summary of TiO_2:N results and drawbacks

In summary, we successfully used RF-MS for the fabrication of nitrogen doped TiO_2:N thin films (and photoanodes) with a relatively wide dopant concentration range (*i.e.* 0 at.% to 6.5 at.%). These films were found to have a dense, smooth, and columnar-like morphology, in accordance with the Thornton model's prediction. All of the N-doped TiO_2 films (with N > 1.4 at.%) were found to crystallize in the anatase phase (preferred for EPC applications). Detailed chemical bond analysis via XPS revealed that most N atoms are incorporated into substitutional locations (*i.e.* $N_O^{\bullet}$) with a non-negligible amount of what is most likely accompanying interstitial species (*i.e.* N_i and $NO_i^{\bullet}$ within the lattice). Spectroscopic ellipsometry and UV-Vis analysis clearly demonstrated the effective E_g narrowing by the incorporation of nitrogen atoms in the TiO_2:N thin films. Most importantly, we were able to pinpoint the existence of an optimal N loading level of 3.4 at.%, corresponding not only to the smallest E_g of 2.2 eV, but also to the best EPC degradation efficiency. This increase in EPC photoactivity (as tested via the degradation of a real emerging pollutant CTC) was demonstrated to result directly from added visible light photoactivity of TiO_2:N.

Unfortunately, while nitrogen doping was effective at narrowing the E_g and improving overall EPC performance of the TiO_2:N photoanodes, this increase was disproportional to the visible light photosensitivity gained. An effective narrowing of the E_g from 3.2 eV to 2.3 eV should, theoretically translate to a ∼fivefold increase in usable photons from the solar spectrum (see figure 1.2). This is far from what is observed (see figure 8 article 1), and can only be explained by the fact that many of the photogenerated charges are simply not contributing to the overall photoreactivity of the material. This is highly likely due to nitrogen doping induced photocharge recombination defect states, which reduces the per-photon efficiency of TiO_2:N as compared to TiO_2[184]. This idea was further developed upon, concluding that these defect states were most likely V_O centers which form as a result of local uncompensated charge disparities brought on via nitrogen incorporation (*i.e.* $N_O^{\bullet}$ and $NO^{\bullet}$)[185, 113]. This calls for a way to counteract the formation of V_O in TiO_2:N, while preserving the visible light photosensitivity of the doped TiO_2 films.

3.2 Tungsten doped TiO_2:W thin-films

It became clear that any anionic doping resulting in local charge disparities suffered from a marked increase in defect states. These, in turn, reduced the material's per-photon photocatalytic efficiency. While this was specifically observed for TiO_2:N, the underlying mechanisms responsible for the V_O formation are universal to any uncompensated acceptor doping system. On the other hand, cationic type doping, most notably TiO_2:W has shown drastically increased photocatalytic performance all the while having minimal visible light photosensitivity (*i.e.* maximum E_g red shift of about 0.2 eV)[186, 187, 188]. The exact phenomenon driving this are debated, with a mixed bag of explanations such as: tungsten doping could increase the surface roughness, grain size, photocharge mobility, and assist charge carrier separation[186, 187, 188]. For our purposes, the latter two phenomena are of interest, as they would contribute to reduce charge recombination defect states. These reports[186, 187, 188], combined with theoretical models[129, 18, 134] showing that W''_{Ti} doping would drastically increase the V_O formation energy (*i.e.* decrease V_O formation during film growth) in TiO_2:W thin films, motivated us to consider codoping of our TiO_2:N thin films with tungsten. Moreover theoretical investigations[129, 18, 134, 131] have suggested that in a low doping regime, W−N codoped TiO_2:WN films could allow for both visible light photosensitivity and reduced defect states (more on this in the following section 3.3). However, before investigating the WN-codoping studies, it was necessary to investigate the properties of tungsten monodoping of TiO_2:W thin films.

3.2.1 Reactive RF-magnetron sputtering of TiO_2:W thin-films

TiO_2:W thin films were deposited from a 7.62 cm-diameter TiO_2 RF-magnetron sputtering target (99.99% purity) with a constant RF power density of 5.5 W cm^{-2}. During sputter-deposition, high purity Ar gas (99.999%) was introduced in the chamber with monitored gas flow rates as to maintain a 1.44×10^{-8} Torr working pressure. Stoichiometric TiO_2 thin films were deposited with R_{O2} = 15% (*i.e.* $100\% \times [O_2] \div ([O_2] + [Ar])$) as to offset the naturally occurring preferential oxygen sputtering. Tungsten incorporation was accomplished via concomitant sputtering of a 7.62 cm-diameter WO_3 target (99.95% purity). The incorporation rate was controlled by varying the applied RF WO_3 power density (*i.e.* W_{power}) from 0.10 W cm^{-2} to 0.70 W cm^{-2}. In order to discern the effects of W incorporation and those of added O atoms in the deposition plasma (from the WO_3

target), secondary depositions with 8.8 W cm^{-2} of TiO_2 target power and concomitant W_{power} from 0.05 W cm^{-2} to 0.25 W cm^{-2} applied to a metallic W target (99.95% purity) were performed (with all other parameters constant). All other deposition parameters were identical to those used for the preparation of TiO_2:N films (see section 3.1.1). A complete description of the RF-MS process can be found in section A.1.

3.2.2 Properties of RF-MS deposited TiO_2:W

Chemical, structural effects, and associated dielectric properties

All of the sputter-deposited TiO_2:W thin films were found to be smooth, dense, with an apparent a columnar-like morphology. A typical cross-sectional SEM image of the TiO_2:W films can be seen in figure 1(b) of article 3. There are no apparent features that would differentiate the morphology of W-doped films from the N-doped ones (shown in figure 3.1). This is interesting as it enables a direct comparison of the EPC performance of TiO_2:N and TiO_2:W based on their optoelectronic properties (as their surface roughness is quite comparable). Additionally, this will allow us to discard the often invoked explanation for the improved EPC performance of TiO_2:W to be caused by an increase of active surface area[186].

The effectiveness of our tungsten atom incorporation as a function of W_{power} was investigated by means of XPS analysis. High-resolution BE core level XPS spectra of the O_{1s}, Ti_{2p}, W_{4d} (overlap with the Ar_{2p} energy window), and W_{4f} (overlap with the Ti_{3p} energy window) were collected and deconvoluted (technical details can be found in section A.2.1). The seemingly redundant tungsten orbital quantifications were performed as to ensure proper deconvolution (and quantification) of the W_{4f} spectra given its inherent overlap with the Ti_{3p} energy levels. Representative deconvoluted XPS spectra for TiO_2:W, TiO_{2-x}, and TiO_2 thin films are shown in figure 3.2 from top-to-bottom, respectively.

All the sputter-deposited thin films had the Ti^{IV} and Ti^{III} oxidation states present within the Ti_{2p} BE window. Specifically, these main $Ti_{2p\ 3/2}$ components could be observed at 458.6 eV and 456.9 eV, respectively. These were systematically accompanied by their corresponding $Ti_{2p\ 1/2}$ doublets at 5.6 eV higher BE. The Ti_{2p} states were synonymous with those recorded from the Ti_{3p} BE window, and mirror derived from associated lattice O atomic signatures, *i.e.* main O_{1s} peak O^A at 529.9 eV

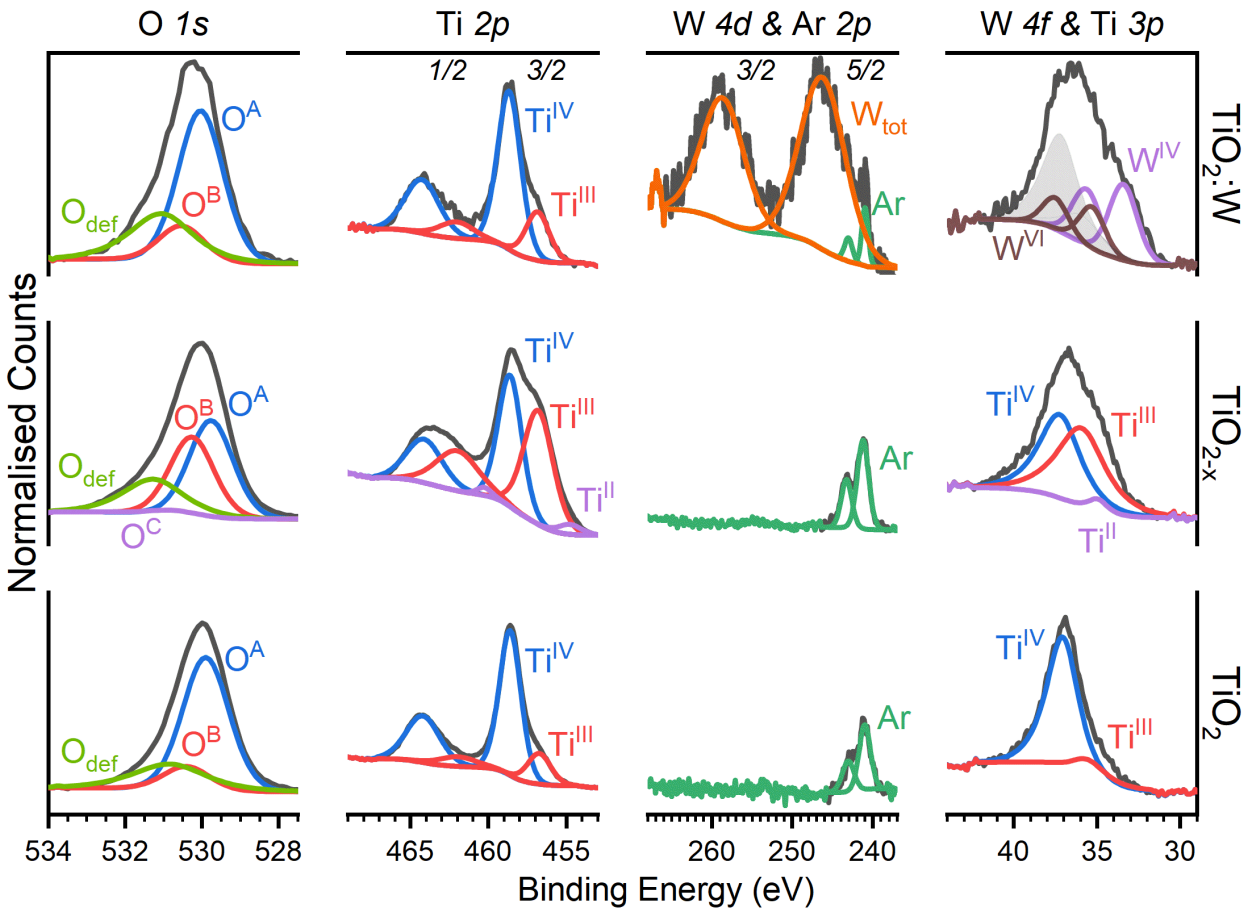

Figure 3.2 – X-ray photoelectron spectroscopy signals with deconvoluted chemical bonding environment for the: $W_{power} = 0.22\,W\,cm^{-2}$ deposited TiO_2:W, $W_{power} = 0\,W\,cm^{-2}$ deposited TiO_{2-x}, and $W_{power} = 0\,W\,cm^{-2}$ deposited TiO_2 with $R_{O2} = 15\%$ thin films from top-to-bottom, respectively. From left to right we see the BE energy windows of the O_{1s}, Ti_{2p}, W_{4d} (overlaps with the Ar_{2p}), and W_{4f} (overlaps with the Ti_{3p}) BE energy windows. The Ti_{3p} signatures within the W_{4f} BE window are greyed out to visually lighten the figure.

assigned to Ti^{IV} linked oxygen and at successively 0.5 eV higher BE for the Ti^{III} bonded O^B, and Ti^{II} bonded O^C. As expected, while all samples had clearly detectable Ti^{III} signatures, synonymous with V_O defect states, this feature was seen to be dominant for the undoped samples deposited without any R_{O2}. In fact, due to preferential sputtering, a high portion Ti was in a reduced oxidative state, forming $2\,Ti^{III}{-}V_O''$ (and to a lesser extent $Ti^{II}{-}V_O''$) defect association pairs as to compensate for local charge disparities that arise in sub-stoichiometric TiO_{2-x}. These defects are known charge recombination sites and were also present in TiO_2:N thin films. While the presence of such defects is expected to contribute to some visible light absorption through the formation of defect bands below the CBM, they greatly hinder the charge transport efficacy of TiO_2:W films[184, 185, 113].

For samples prepared with concomitant WO_3 & TiO_2 targets sputtering, we noted the presence of W_{4f} and W_{4d} features in their corresponding BE windows as shown in the upper row of figure 3.2. It needs to be mentioned that while the W_{4d} spectra allows for general W quantification, it does not provide sufficient resolution to discern oxidative states; this is in part why both the 4 f and 4 d BE windows were investigated. Two W_{4f} doublets were observed, those of W^{VI} and W^{IV} in their oxide forms at 34.5 eV and 33.3 eV respectively; these $W_{4f\ 7/2}$ components were accompanied by their $W_{4f\ 5/2}$ features at 2.2 eV higher BE. These observations, combined with lattice size constraints indicate that W is present in two substitutional forms within the TiO_2:W lattice: $W_{Ti}^{\times}$ (*i.e.* W^{IV} of 0.66 Å atomic radius replacing Ti^{IV} of 0.61 Å atomic radius) and W_{Ti}'' (*i.e.* W^{VI} of 0.61 Å substituting for Ti^{IV})[186, 189, 190]. It was noted that total tungsten incorporation W_{tot} increased almost linearly with increased RF power on the WO_3 target. However, this pseudo-linear trend is not the same for both tungsten oxidation states. Figure 2 of article 3 shows that while W^{IV} increases continuously with target power, the W^{VI} incorporation saturates at $\sim$2 at.% for $\approx W_{power} > 0.3\,W\,cm^{-2}$. This seems to go against the size imposed constraints since W_{Ti}'' doping is expected to be better accomodated within the TiO_2 lattice and therefore, from a purely crystallographic viewpoint, should have a higher solubility limit. This is however clearly seen to be not the case, suggesting that local charge balance (*i.e.* W^{IV} in $W_{Ti}^{\times}$ locations are energetically favored over W^{VI} in W_{Ti}'' sites) dictates the solubility mechanism beyond a certain doping level. However, the ever-increasing incorporation of size mismatched $W_{Ti}^{\times}$ dopants is accompanied by an increase in lattice strain as will be discussed further in the text (XRD section).

Most importantly, figure 3.2 reveals that tungsten incorporation lead to a drastic reduction in the Ti^{III} signal as compared to the Ar-only deposited samples (TiO_{2-x}). In fact, we can note that for the TiO_2:W thin film, the Ti^{III} peak signature is seen to be on par with the R_{O2} deposited TiO_2. Table 1 of article 3 presents the quantified stoichiometries of the TiO_2:W films with their respective deposition parameters. We can note that, while both depositions were performed with a 100% Ar sputtering atmosphere, a significant change in stoichiometry can be observed: from $TiO_{1.74}$ for the $W_{power} = 0\,W\,cm^{-2}$ samples (middle row in figure 3.2) to $TiO_{2.05}$:$W_{0.03}$ for the $W_{power} = 0.11\,W\,cm^{-2}$ deposited one. While some of this can be attributed to the co-sputtering target acting as a source of atomic O, one can propose that most of the effect is a direct consequence of the predicted increase in V_O formation energy due to W^{VI} incorporation[129, 18]. In order to confirm this proposal, the WO_3 sputtering target was replaced by a metallic W target for a parallel

TiO_2:W thin film deposition series (all other parameters remained unchanged). Analysis of samples deposited from a pure metallic W target, with incorporation rates similar to the WO_3 deposited ones showed that the stoichiometry recovered from $TiO_{1.74}$ to $TiO_{1.96}$:$W_{0.02}$ ($0.09\,W\,cm^{-2}$ applied to the W target). This systematic increase in oxygen stoichiometry with both a metallic W and oxide WO_3 sputtering targets can therefore be conclusively assigned to the increase of V_O formation energy as a result of tungsten incorporation in the sputter-deposited TiO_2:W thin films. However, as hinted by the saturation limit of W^{VI} and directly observed in table 1 of article 3, the recovery of TiO_2:W film stoichiometry due to tungsten incorporation is most prevalent at relatively low tungsten doping.

To further develop on the issue of decreased V_O density, high frequency dielectric spectroscopy measurements (HF-DS) were performed on the TiO_2:W samples. HF-DS was used as it allows differentiation of various dielectric contributions (summarized in figure A.14) based on the frequency range in which the material is probed. The total dielectric constant of the material being a combination of interfacial effects, intrinsic dipoles, ionic contributions, and electronic oscillations as shown in figure as shown in figure A.13(b), *i.e.* $\epsilon_{total} \approx \epsilon_{interface} + \epsilon_{dipole} + \epsilon_{ionic} + \epsilon_{electronic}$. Typically, $\epsilon_{interface}$ contributions manifest themselves as dielectric relaxations in ϵ' (real component of the permittivity) at the MHz range and lower, whereas ϵ_{dipole} such as defect association pairs (*e.g.* $2\,Ti^{III}{-}V_O''$) are expected to contribute in the GHz range[191]. Permittivity in the THz and beyond is from resonant ionic polarization oscillations and soft-phonon modes, respectively *i.e.* $\epsilon_\infty \approx \epsilon_{ionic} + \epsilon_{electronic}$. Therefore, we can state that in the MHz to GHz range, we can approximate the dipole contributions as $\epsilon_{dipole} \approx \epsilon - \epsilon_\infty$ with the latter being essentially constant[192, 193].

Figures 5 (a) and (b) of article 3 present a typical fitted ϵ' & ϵ'' (complex component of the permittivity) spectra for the undoped, oxygen deficient, and tungsten doped samples. To better understand this, figures 6 (a) and (b) of article 3 present the ϵ' and $\tan\delta$ (*i.e.* $\frac{\epsilon''}{\epsilon'}$) as a function of W-doping taken at 1 MHz and 1 GHz, respectively. From these spectra, we can note two key features. Firstly, there is a dominant interfacial contribution leading up to and then tapering off in the MHz range that is seen to be unchanged for all but the undoped $TiO_{1.90}$. Indeed, given that all of the TiO_2:W films have crystal grain sizes in the ≈15 nm to 40 nm range as compared to ≈140 nm for $TiO_{1.90}$ (determined by Williamson-Hall analysis), their interfacial ϵ' contribution remains relatively constant. Indicating that, as expected, this dielectric feature arises from interfacial contributions. Secondly, we note a strong dipole contribution in the high MHz to low GHz. As seen in figure 5 (b) of

article 3, this feature is non-existent in the stoichiometric TiO_2 samples ($\epsilon'_{dipole} \approx 60$) and shown to increase by three orders of magnitude ($\epsilon'_{dipole} \approx 35000$) for the V_O doped thin films, *i.e.* the $TiO_{1.7}$ sub-stoichiometric samples. Indeed, this clearly reflects the $2\,Ti^{III}{-}V''_O$ dipole contribution to the permittivity. This defect-dipole dielectric contribution was isolated, *i.e.* $\epsilon_{dipole} \approx \epsilon' - \epsilon'_\infty$ as shown in figure 7 (a) and plotted as a function of W content in figure 7 (b) of article 3. Interestingly, it is seen that the tungsten loading significantly passivates the V_O dipole contributions to the dielectric signature while changing little in the ionic and electronic contributions as shown by the almost constant ϵ'_∞. This suggests that from a structural/defect viewpoint, tungsten is reducing the V_O density without changing the overall structure of the material. While these results are corroborated by the previously mentioned XPS observations, they provide significantly more insight. Most important of these insights is the clear presence of an optimal point at around 2.5 at.% of W (*i.e.* the $TiO_{2.10}W_{0.09}$ sample) which shows the lowest V_O dipole contribution ($\epsilon'_{dipole} \approx 1900$) and by extension, is expected to have significantly improved per-photon efficiency as compared to the samples with high V_O density (*e.g.* TiO_{2-x}). Past this optimal point (tungsten doping level $>\approx 2.5$ at.%), the increased V_O formation energy brought on by substitutional W^{VI} incorporation seems to be offset by the heavy cationic load. At higher doping levels (>8 at.% of W), we note that the $2\,Ti^{III}{-}V''_O$ permittivity contribution ($\epsilon'_{dipole} \approx 30000$) is on par with that of $TiO_{1.7}$ samples.

Optoelectronic properties and EPC performance

Based on the observations of this V_O-passivated optimal point hinted at via XPS observations and directly demonstrated by HF-DS measurements, we predict that optimally doped TiO_2:W (≈2.5 at.% of W) should show significant increases in EPC degradation performance as compared to sub-stoichiometric titania. To assess the validity of such a prediction, the $TiO_{1.9}$, $TiO_{1.74}$, and optimally doped $TiO_{2.10}W_{0.09}$ thin films here were deposited onto 15.24 cm-diameter Ti grids and used as photoanodes in the 1 L EPC reactor. The exact quantification of the bandgap associated with these samples was determined in article 2. Critically, we know that the $TiO_{1.9}$, $TiO_{1.74}$, and $TiO_{2.10}W_{0.09}$ thin films have an E_g value of 3.2 eV, 3.0 eV, and 3.0 eV, respectively. This would allow the sub-stoichiometric and tungsten doped photoanodes to have essentially identical visible light photosensitivity; with both, having this slight decrease in E_g amplitude resulting form the formation of states below the CBM (see article 2). In other words, since both photoanodes have essentially the

same E_g, any improvements in EPC performance is directly attributed to the passivation of charge recombination sites (*i.e.* reduction in V_O).

As in the case of TiO_2:N photoanodes (see section 3.1), the performance of our photoanodes was directly evaluated towards the degradation of an agricultural pollutant, atrazine (ATZ). ATZ is a potent endocrine disruptor widely used in North America as a pesticide. For the purpose of the present study, synthetic solutions containing typical ATZ concentrations of heavily polluted areas (*i.e.* $60\,\mu g\,L^{-1}$) were prepared and treated under AM 1.5G light. Treatment times of about 2.5 h were performed under continuously circulating pollutant solutions as shown in figure 3.3. While all samples reached the environmentally acceptable ATZ limit of around $2\,\mu g\,L^{-1}$ after 2 h of treatment, the TiO_2:W photoanodes showed the best EPC performance as compared to TiO_2 and TiO_{2-x} photoanodes. Indeed, by extracting the pseudo-first-order degradation kinetic constant, we note that the $TiO_{2.10}W_{0.09}$ photoanodes were about twice as efficient ($k = 0.053\,min^{-1}$) as compared to both the $TiO_{1.9}$ ($k = 0.027\,min^{-1}$) and $TiO_{1.74}$ ($k = 0.024\,min^{-1}$) photoanodes. This can be directly assigned to two features: (i) tungsten doped photoanodes have an advantage over undoped TiO_2 in that their E_g is slightly reduced, and (ii) most importantly, they have significantly lower charge recombination centers as compared to equally photosensitized TiO_{2-x} photoanodes. This confirms that for photoanodes with identical bandgaps, we obtain a marked increase in the EPC performance by reducing V_O defects (*i.e.* $2\,Ti^{III}{-}V''_O$) through incorporation of substitutional W. Interestingly, optimally doped TiO_2:W photoanodes ($E_g \approx 3.0\,eV$) were showing EPC degradation kinetics on par with optimally doped and visible light photosensitized TiO_2:N photoanodes ($E_g \approx 2.3\,eV$), highlighting the value of controlling defect centers in the material. This key feature will be discussed further in section 3.3.

3.2.3 Summary of TiO_2:W results

In summary, we used RF-MS for the fabrication of tungsten doped TiO_2:W thin films with a relatively wide concentration range, *i.e.* 0 at.% to 8.5 at.%. Detailed XPS analysis revealed that the dopants were in two substitutional, oxide forms: W''_{Ti} & $W^{\times}_{Ti}$ (*i.e.* substitutional W^{VI} & W^{IV}, respectively). As compared to $TiO_{1.90}$ and $TiO_{1.74}$ films, the W doped thin films showed significant improvement in the reduction of their V_O density mainly because of an increase in the formation energy of such vacancy defects. XRD analysis which revealed that the improved stoichiometry (*i.e.*

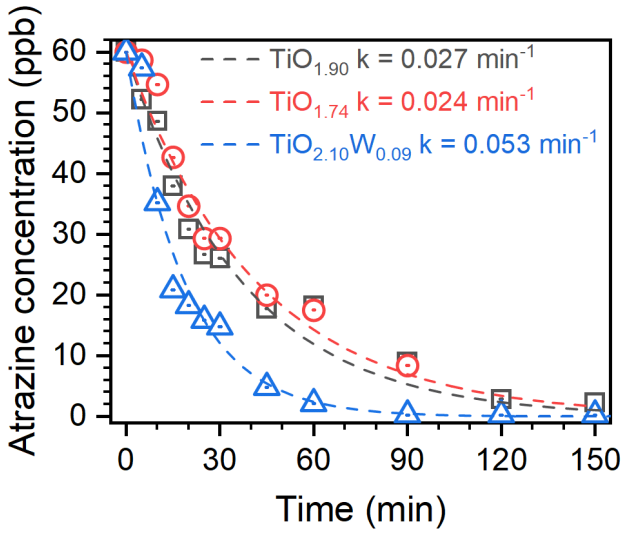

Figure 3.3 – Electro-photocatalytic performance of the $TiO_{1.90}$, $TiO_{1.74}$, and $TiO_{2.10}W_{0.09}$ photoanodes under AM1.5G light with a 60 µg L^{-1} initial concentration of atrazine with the extracted pseudo-first order degradation constants presented.

reduced V_O, hence increased relative O content) resulted in a marked improvement of the rutile phase as compared to the heavily V_O loaded samples. Additionally, the uneven lattice geometry and total incorporation of the W^{VI} & W^{IV} species culminated in the appearance of an anatase-rutile bi-phase polycrystalline structure. Critically, no tungsten oxide cluster formation was observed via XRD.

Most importantly, by combining XPS results and HF-DS measurements we were able to point out an optimal doping level of ~2.5 at.% tungsten, which showed the largest reduction of the $2\,Ti^{III}–V''_O$ defect pair ϵ' contribution (*i.e.* direct evidence of a reduction in V_O defects). The practicality of this was exploited by integrating these optimally doped $TiO_{2.10}W_{0.09}$ films (alongside $TiO_{1.9}$ & $TiO_{1.74}$) as photoanodes for AM1.5G light driven EPC degradation of the ATZ pollutant. The pseudo-first order degradation kinetic constants confirmed that highest EPC performance of the optimally doped $TiO_{2.1}W_{0.09}$ photoanodes as compared with the highly oxygen deficient $TiO_{1.74}$ ones (even though the latter has greater visible light photosensitivity). This is believed to be a direct consequence of the reduced V_O defect states, improving the per-photon efficiency of the material. In other words, optimal tungsten loading was shown to be effective at passivating local charge disparities, and in turn, reducing V_O defects (shown to be a major drawback of nitrogen doped TiO_2:N thin films in section 3.1).

3.3 Tungsten and nitrogen codoped TiO_2:WN thin films

The two previous sections presented the various benefits and limitations associated with monodoping of TiO_2 films with N and W atoms. While it was shown that substitutional nitrogen doping reduced the E_g of TiO_2:N to values as low as 2.2 eV, this photosensitization is found to come at the cost of increased defect states (*i.e.* V_O) that reduce the per-photon photocatalytic efficiency, undermining most of the gains from increased visible light absorption. On the other hand, we have also shown that the formation of V_O can be significantly reduced by incorporating controlled amounts of W dopants, leading thereby to a sizable improvement in the EPC efficiency of TiO_2:W. Intuitively, the combination of advantages from both N and W monodoping schemes should lead to the best trade-off as to achieve visible light photosensitizing of TiO_2 while improving its per-photon efficiency in EPC processes.

As stated before, the experimental approach was guided by theoretical models[131, 194, 17, 129, 18, 130, 128] proposing interesting co-dopant pairs that would maintain proper band alignment, while reducing charge disparity induced defects. Tungsten and nitrogen were pointed out as a valid acceptor-donor codopant pair for three main reasons:

(i) WN-codoped TiO_2:WN should allow for a significant reduction in the E_g, while helping hybridize O_{2p} and N_{2p} states at the VBM, reducing the presence of isolated mid gap states[194, 17, 129, 18].

(ii) While theoretical predictions showed other potential candidates such as V−N, W−C, and W−S, as highly promising for EPC applications, their practical synthesis remains challenging. V−N doping suffered from vanadium's predisposition for forming multiple oxide phases and clusters with different oxidative states[128]. W−C codoping requires an energy that is almost double that of W−N codoping (not to mention the significantly higher number of possible carbonaceous impurity formations)[18, 129]. W−S synthesis was roadblocked by size constraints (*i.e.* sulfur atoms are much bigger than the O locations they are supposed to substitute for). In fact, sulfur has a predisposition to form interstitial SO_x species, making the achievement of substitutional S doping much more difficult[33, 9, 194, 113].

(iii) Practically, we had already demonstrated the beneficial effects of both W-monodoped and N-monodoped TiO_2 (see articles 1 & 3 and sections 3.1 & 3.2). These studies highlighted that both dopants should be incorporated in relatively low concentrations, in agreement with the optimal conditions outlined for W−N-codoping in [113, 131].

Specifically, it was modeled that in an ideal scenario, *i.e.* all of the tungsten in W''_{Ti} (W^{VI}) and all of the nitrogen being in $N^{\bullet}_{O}$ form, a 2 : 1 ratio of N : W would provide for the optimal stoichiometric growth of TiO_2:WN as shown by table 3.1[17, 18]. On a practical basis however, this $W - 2\,N$ ratio will be used purely as an empirical parameter. Because of the variability of dopant configurations and other factors (such as intrinsic V_O formation), the actual compensation N-to-W atomic ratio may differ slightly from this ideal theoretical ratio of 2 : 1.

Dopant(s)	Ti-rich form. E [eV]	O-rich form. E [eV]	a [Å]	b [Å]	c [Å]
TiO_2	-	-	3.8	3.8	9.79
TiO_2:N	-0.12 (0.90)	4.79 (5.90)	3.83	3.78	9.8
TiO_2:W	3.83 (3.40)	-6.00 (-6.60)	3.83	3.84	9.72
TiO_2:WN	1.16 (1.61)	-3.76 (-3.39)	3.86	3.8	9.75
TiO_2:W2 N	-1.29	-1.29	3.89	3.78	9.76

Table 3.1 – Changes in formation energy for TiO_2 lattice species (*i.e.* formation of Ti-rich & O-rich lattice environments) upon dopant incorporation, *e.g.* higher formation E translates to less of said element. From [17], with additional data from [18] in parenthesis.

At the start of this work, some experimental evidence of beneficial W−N-codoping was starting to build. Cui et al.[195] and Thind et al.[196] had independently showed that codoping could lead to a favorable E_g reduction, whereas Kubacka et al.[197] showed similar results while observing an improvement of optoelectronic properties via facilitated $OH^{\bullet}$ radical production. However, in all cases, understanding the exact optoelectronic properties and photocharge transport in WN-codoped TiO_2 was left incomplete. While this was somewhat addressed by Folli et al.[198] and Bloh et al.[199] who reported on a more developed understanding of W−N codoping on the materials band gap structure, their studies focused on wet chemistry synthesized, interstitially doped TiO_2:WN. In fact, understanding of the beneficial acceptor-donor passivated substitutional codoping of TiO_2:WN films and its practical implementation are still to come.

3.3.1 Reactive RF-magnetron sputtering of TiO_2:WN thin films

The sputter deposition procedure used for the preparation of TiO_2:WN films was a combination of those used to prepare TiO_2:N and TiO_2:W. The TiO_2:WN films were sputter-deposited from a 7.62 cm diameter TiO_2 target (99.99% purity) with a constant power density of 5.5 W cm^{-2}. Nitrogen and tungsten incorporations were accomplished by injecting N_2 gas (99.995%) into the chamber and by sputtering of a 7.62 cm diameter WO_3 target (99.95% purity), respectively. N incorporation in the TiO_2:WN films was controlled by adjusting the relative nitrogen mass flow rate ratio R_{N2} (*i.e.* $R_{N2} = 100\% \times [N_2] \div ([N_2] + [Ar])$ from 0 % to 20 %. The W incorporation was controlled by varying the WO_3 target power density (W_{power}) from 0.1 W cm^{-2} to 0.7 W cm^{-2}. Additionally, TiO_2:WN samples with similar dopant loadings were prepared using concomitant sputtering of a metallic W-target as an O free tungsten source. This was done to distinguish between the beneficial effects of additional O atoms sputtered from the WO_3 target, and the intrinsic dopant induced effects. Such depositions were performed with 8.8 W cm^{-2} applied to the TiO_2 target, and by varying the W target power density (W_{power}) from 0.06 W cm^{-2} to 0.25 W cm^{-2}. All other deposition parameters remained identical to procedures used in previous sections. To distinguish between these two types of W-doping, we refer to them as WO_3- and W-deposited TiO_2:WN, respectively. A detailed theoretical and experimental description of the sputter deposition process is presented in section A.1.

3.3.2 Chemical and structural properties of RF-MS deposited TiO_2:WN

All of the RF-MS deposited TiO_2:WN thin films were dense, smooth, had low surface roughness, and apparent columnar-like growth characteristics, as shown in figure 3.4. These morphological features were consistent throughout the varied doping regimes and methodologies (*e.g.* films deposited with a WO_3 versus W target).

The chemical composition of the sputter deposited TiO_2:WN thin films, as a function of both deposition parameters W_{power} & R_{N2} was systematically investigated via XPS analysis. The O_{1s}, Ti_{2p}, N_{1s}, W_{4f}, and W_{4d} core level spectra were studied, deconvoluted, and typical examples are presented in figure 3.5 (a), (b), (c), (d), and (e) for the TiO_2, TiO_{2-x}, TiO_2:W, TiO_2:N, and TiO_2:WN type thin films, respectively. All sputter-deposited films presented at least two components in the $Ti_{2p\ 3/2}$ spectra. These were representative of the Ti^{IV} and Ti^{III} oxidation states at 458.6 eV and

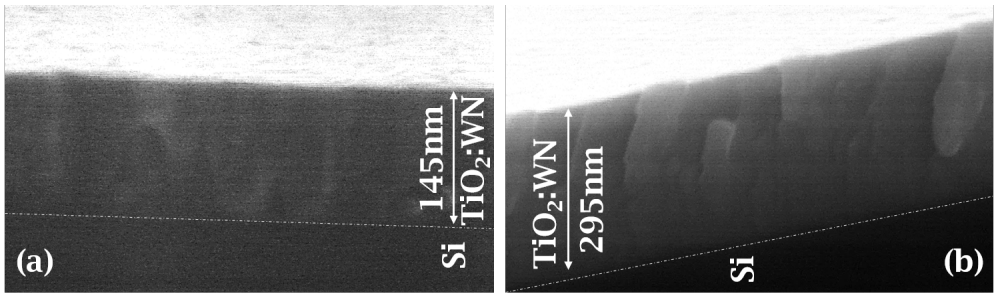

Figure 3.4 – Cross-sectional scanning electron microscopy images of sputter deposited TiO_2:WN thin films; on the left we see a WO_3 target deposited 145 nm film with 3.1 at.% & 4.4 at.% of W & N at thickness, and on the right we see a W target deposited 295 nm film with 1.1 at.% & 6.4 at.% of W & N.

456.9 eV, respectively (corresponding $Ti_{2p\ 1/2}$ doublets at 5.6 eV higher BE)[200]. In highly oxygen deficient samples such as TiO_{2-x}, TiO_2:N, and other sub-stoichiometric thin films we can note the presence of a third titanium peak, associated with the Ti^{II} oxidative state with its $Ti_{2p\ 3/2}$ signature at 455.3 eV ($2\,p_{1/2}$ doublet at 5.6 eV higher BE). The presence of reduced states such as Ti^{III} and in extreme cases Ti^{II} is coherent with sub stoichiometric phases (Magneli phases). These reduced states form in defect association pairs such as $2\,Ti^{III}{-}V''_O$ to preserve charge neutrality. For our purposes it is worth reiterating that these occur for a variety of reasons: (i) uncompensated preferential sputtering as seen in figure 3.5 (b), (ii) lattice level charge imbalance resulting from incorporation of $N^{\bullet}_O$ like species (and other possible N_i species) as seen in figure 3.5 (c)[201]. These defect centers are highly undesirable for photocatalytic applications since they act as potent charge recombination centers.

All of the Ti_{2p} states can be observed in the Ti_{3p} spectra, and their corresponding bonding pairs are typically reflected in the O_{1s} spectra. The main, stoichiometric lattice bonded oxygen O^A peak can be observed at 529.9 eV with species in subsequently decreasing stoichiometric environments denoted by O^B & O^C both at 0.5 eV higher iterations. However, given oxygen's high intrinsic electro-negativity, the resolution of these signatures is difficult without proposing some starting hypotheses. We see an example of this in our resolution of the O^C peak that arises form oxygen bonded to Ti^{II} species in highly deficient environments. While this signature could easily be ignored as it is insufficiently resolved in amplitude or position, its presence is nevertheless highlighted based on our starting assumptions. A final oxygen signature can be seen with the denotation O_{def}, it is typically associated with defective surface oxygen and hydroxide species[202].

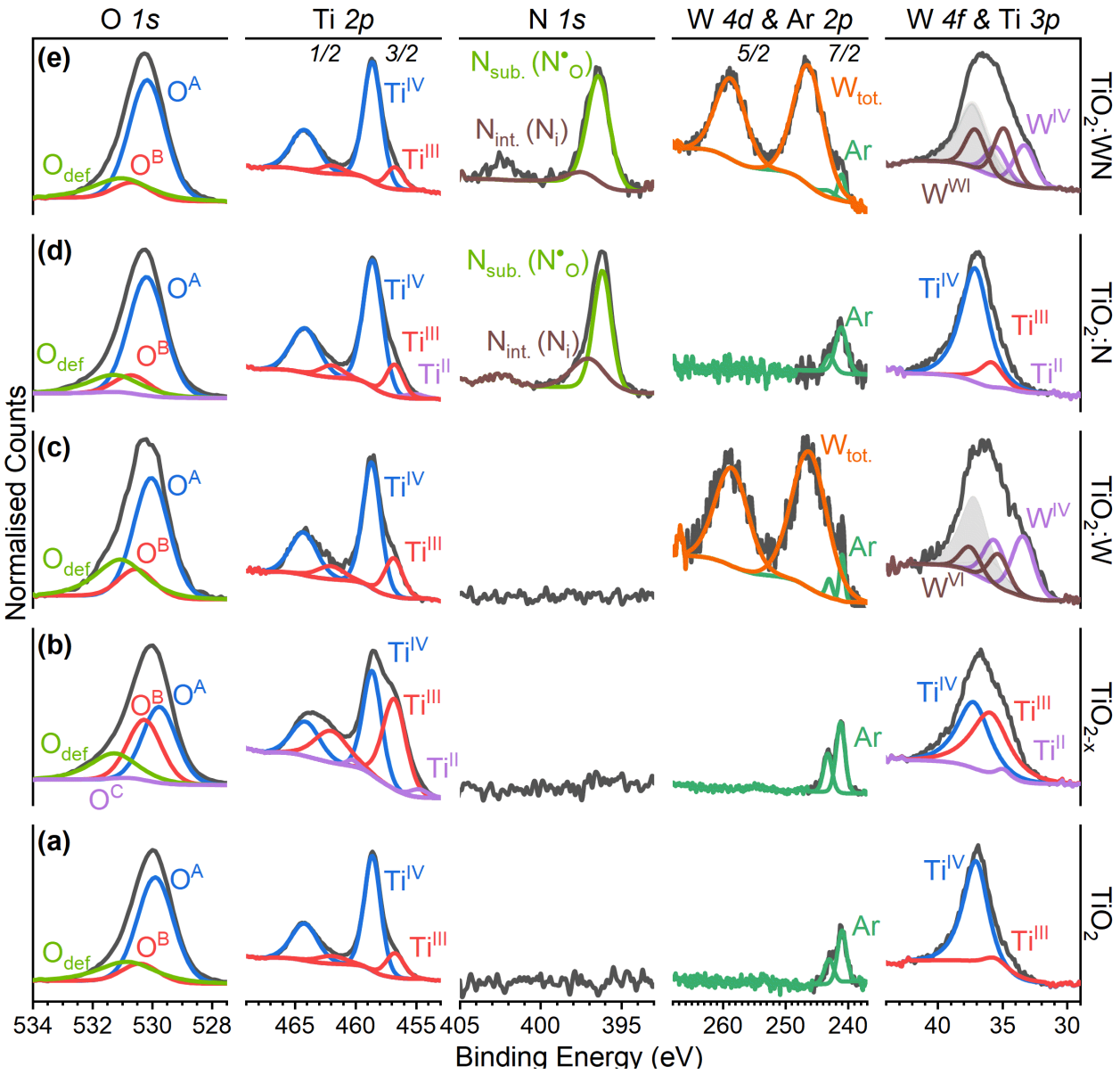

Figure 3.5 – O_{1s}, Ti_{2p}, N_{1s}, W_{4d}, and W_{4f} core level spectra from left-to-right for TiO_2 ($R_{O2} = 15\,\%$), TiO_{2-x} (Ar only), TiO_2:W (WO_3 target $W_{power} = 0.22\,W\,cm^{-2}$), TiO_2:N ($R_{N2} = 10\,\%$), and TiO_2:WN ($R_{N2} = 13\,\%$ & WO_3 target $W_{power} = 0.26\,W\,cm^{-2}$) type films shown from bottom-to-top in (a), (b), (c), (d), and (e), respectively. The Ti_{3p} species are grayed out when there is overlap with W_{4f} signatures as to ease visibility.

Tungsten monodoped samples (TiO_2:W) were systematically synonymous with two main W_{4f} features in their BE window. There are representative of the W^{VI} and W^{IV} states of tungsten it its oxide form with the main $4\,f_{7/2}$ components at 34.5 eV and 32.3 eV, respectively (corresponding $4\,f_{5/2}$ doublets at 2.2 eV higher BE)[186, 189]. The W^{IV} : W^{VI} ratio hovered around the 3 : 2 mark for all W-doped thin films upto the W^{VI} saturation mark as discussed in section 3.2. Typically, the

Ti_{2p} and O_{1s} spectra remained unchanged for TiO_2:W thin films. Except for highly deficient cases (such as samples prepared with metallic W sputtering at high concomitant powers) where one could note a significant increase in the Ti^{III} signature (and in some extreme cases Ti^{II} as well). It is to be noted that given the overlapped nature of the W_{4f} and Ti_{3p} signatures, as discussed in the TiO_2:W section previously, two tungsten BE windows were scanned as to assure proper quantification of the total tungsten loading. Given the orbital nature, the 4 d states provide insufficient resolution as to allow distinction between oxidative species. We can note that all samples show a small Ar_{2p} doublet in the W_{4d} window. This is a direct consequence of the systematic sputter cleaning performed on all samples before XPS spectra collection. This feature in complemented by the W_{4d} features in the case of TiO_2:W & TiO_2:WN samples with the $4\,d_{7/2}$ and $4\,d_{5/2}$ signatures present. Nitrogen doping resulted in the presence of two N_{1s} components at 396.2 eV and 397.2 eV, with the former associated with substitutional $N_O^{\bullet}$ ($-$Ti$-$N$-$Ti$-$ type bonds, also denoted N_{sub}) and the latter with interstitial N_i species (N_{int} denotation)[34, 33, 122, 203, 113]. Most importantly, we note that nitrogen is mostly present in the $N_O^{\bullet}$ form for all N-doped/codoped samples.

When both W and N are introduced into the films (W_{power} & R_{N2}), XPS features of both TiO_2:N and TiO_2:W could be observed simultaneously, indicating that both dopants are in desired substitutional locations within the titania lattice. However, some key differences are present. Firstly, we observed a reduction in sub-stoichiometric Ti species (*i.e.* $([Ti^{II}]+[Ti^{III}]) \div [Ti^{IV}]$) within specific codopant N : W ratios. Specifically, using codoping models as blueprints, this reduction in V_O seems to be correlated with the $W''_{Ti} : N_O^{\bullet}$ ratio. Secondly, both dopants were noted to have significantly higher solubility limits. From an XPS perspective, this can be observed via increased $N_{sub} : N_{int}$ ratios, *i.e.* $N_O^{\bullet} : N_i$ (higher portion of nitrogen in the substitutional doping location as compared to TiO_2:N) & $W^{VI} : W^{IV}$ (increased W^{VI} solubility as compared to TiO_2:W thin films). This can be directly attributed to a synergistic acceptor-donor passivating effect, reducing the formation energy of the W''_{Ti} and $N_O^{\bullet}$ dopant species in accordance with theoretical predictions[17, 18].

This increase in solubility due to a reduction of desired codopant formation energy was clearly observed in the structural characteristics of the TiO_2:WN thin films. Figure 4 of article 6 best illustrates this. The subfigures (a) and (b) show ever increasing dopant loading for the TiO_2:W and TiO_2:N type films, respectively. We can note features identical to those discussed in corresponding sections 3.2 & 3.1. In both cases, there is formation of secondary phases at various doping loading points, *i.e.* W^{IV} incorporation eases rutile formation due to similarities with WO_2-type structures,

whereas nitrogen doping past a critical point results in the formation of a distinct oxynitride phase. Table 3.2 presents the anatase lattice constants and Williamson-Hall calculated strain values for a sample series with a fixed W_{power}; both the theoretical and experimental reference TiO_2 values shown for comparison. Interestingly, when both dopants are co-introduced, regardless of explored dopant levels a well defined poly-crystalline anatase phase can be consistently observed. This holds true for dopant loadings way beyond what was possible in the monodoping regime as shown in figure 4(c) of article 6. Interestingly, this increase in dopant solubility is concomitant with a reduction of internal strain. Williamson-Hall analysis of XRD spectra (for experimental details see section A.2.4) from both the metallic W (see table 1 in article 5) and oxide WO_3 deposited TiO_2:WN thin films revealed that typically, near optimal doping loading levels, the internal strain of the codoped films was much lower than any monodoped system. Additionally, many of the predicted structural lattice features shown in table 3.1 were shown to be in alignment with experimentally observed results (see table 3.2), *i.e.* compression in the c direction, and uniform expansion via the a/b axis while maintaining lattice volumes on par with pristine TiO_2. In fact, this is a direct consequence of properly passivated acceptor-donor codoping. The $N_O^{\bullet}$ atoms and adjacent W_{Ti}'' atoms form coordinate bonds from shared electrons, creating an overlap of their W_{5d} and N_{2p} orbitals which is energetically favorable as compared to the N & Ti overlap (*i.e.* higher covalency of the W−N bond as compared to the Ti−O one). This results in the total charge density of the pure TiO_2 lattice and the properly compensated TiO_2:WN lattice to be almost identical[131, 194, 17, 129, 18, 130, 128]. The ideal ratio of these species is therefore one W_{Ti}'' for every two $N_O^{\bullet}$ as to ensure local charge neutrality. This strong interaction between the W_{Ti}'' and $N_O^{\bullet}$ atoms make the W−O bond longer than the Ti−O one, while having lower binding energy. This is predicted to results in the O_{2p} energy states populating the VBM to be pushed to higher energies, resulting in a homogeneous hybridization of the O_{2p} and N_{2p} states, leading to an improved E_g with a lower density of isolated nitrogen mid-gap states. It needs to be mentioned that the stoichiometries presented in table 3.2 might seem to not align with this. However, this is but an artifact of notation. The TiO_2:WN stoichiometries presented throughout this project represent the total W & N atomic doping, whereas codoping models consider only the W_{Ti}'' & $N_O^{\bullet}$ species. In this context, if we take the last two lines of table 3.2 as an example, the film stoichiometries considering only the W_{Ti}'' & $N_O^{\bullet}$ species are: $TiO_{2.13}$:$W_{0.09}^{VI}N_{0.15}^{sub}$ (written as $TiO_{2.13}$:$W_{0.21}N_{0.20}$) and $TiO_{2.09}$:$W_{0.08}^{VI}N_{0.16}^{sub}$ (written as $TiO_{2.09}$:$W_{0.19}N_{0.25}$), revealing the sought after $\approx 2:1$ ratio of $[N_O^{\bullet}] : [W_{Ti}'']$.

Deposition Parameters	Stoichiometry	$a \pm \delta$ (nm)	$c \pm \delta$ (nm)	Strain $\pm\delta$ (%)
Reference	TiO_2	0.378 ± 0.00	0.950 ± 0.00	-
$R_{O2} = 15\,\%$	$TiO_{1.90}$	0.378 ± 0.05	0.950 ± 0.10	0.32 ± 0.09
$R_{N2} = 0\,\%$	$TiO_{2.10}$:$W_{0.12}$	0.380 ± 0.05	0.949 ± 0.19	0.29 ± 0.05
$R_{N2} = 6\,\%$	$TiO_{2.34}$:$W_{0.22}N_{0.12}$	0.381 ± 0.05	0.943 ± 0.18	0.07 ± 0.06
$R_{N2} = 12\,\%$	$TiO_{2.13}$:$W_{0.21}N_{0.20}$	0.382 ± 0.05	0.943 ± 0.19	0.24 ± 0.11
$R_{N2} = 18\,\%$	$TiO_{2.09}$:$W_{0.19}N_{0.25}$	0.386 ± 0.05	0.917 ± 0.18	0.64 ± 0.54

Table 3.2 – XRD derived anatase lattice constants and Williamson-Hall calculated strain values for a sample series with a fixed $W_{power} = 1.25\,W\,cm^{-2}$ (except for reference $TiO_{1.90}$; reference TiO_2 values shown for comparison.

None of the structural or chemical characterizations revealed signs of secondary oxide/nitride inclusions in the TiO_2:WN films. However, given the sensitivity of our methods (*e.g.* XPS characterization are limited to 0.1 at.%), it cannot be ruled out that micro-inclusions of substances such as WN_2, TiN, or even W_2N are present. That being said, these micro-inclusions should not change any of the conclusions drawn in this work as their influence would be limited compared to the "macro" scale (in comparison) doping levels presented herein. An in-depth TEM analysis could provide further insight into this topic, and will be considered if further studies are performed on these materials.

3.3.3 Optoelectronic properties, defects, and EPC performance of TiO_2:WN

The optical band-gap of the sputter-deposited thin films was calculated by Tauc's relation. Specifically, this was done by extrapolating the linear region of the Tauc plot traced using the absorption coefficient α obtained from the thin-films' transmittance and reflectance spectra in the UV-Vis regime (see section A.2.2). Typical UV-Vis transmittance spectra and their associated Tauc plots, for different doping schemes are shown in figures 4 (a) and (b) of article 5, respectively. In the case of W-doping, a fairly minimal reduction of (of 0.2 eV) in the E_g is observed. This is explained by the formation of new impurity W_{5d} states below the CBM (also, whenever applicable, V_O levels could also have a similar effect). On the other hand, both the TiO_2:N & TiO_2:WN thin films showed a significant red-shift of the E_g, reaching values as low as $E_g = 2.3$ eV. This shrinkage in optical band-gap as a function of dopant concentrations is shown in figure 5 of article 5. Firstly, it was

observed that an optimal dopant loading zone exists. Outside of this zone, dopant concentration increse did not result in further red-shifting of the E_g, but would rather increase defects in the material. Secondly, it was noted that nitrogen was the key factor in photosensitizing the material (as reinforced by figure 5 (b) of article 6), showing that E_g shrinkage is directly correlated with nitrogen incorporation. Thirdly, a large upshift of the VBM towards the Fermi level by 0.7 eV & 0.8 eV was noted for the N-doped & WN-codoped thin films and attributed to the formation of new N_{2p} states above the VBM. These results were obtained via low BE-energy studies (0 eV to 12 eV) of the thin film valence band electronic structure (see figure 4 of article 2). The VBM level is determined as the zero-intensity (no density of states) energy of the lower binding region of the spectrum. The VBM value relative to the E_F is determined by extrapolating the linear portion of the lower energy side of the VB to the spectral baseline. Upon deconvolution of the low energy XPS valence band spectra, as presented in figure 4 (b) in article 2, the VB of TiO_2 is seen to be mainly comprised of O_{2p} non-bonding states. The t_{2g} states are bonded in π orbitals and lie higher in energy than the σ states, whereas the e_g states are σ bonded in the deeper BE region. It needs to be added that a weak Ti_{3d} defect state signature located at 1.2 eV and 1.1 eV below the E_F was found for both the W and WN doped films. It is thought that this arises from defective surface oxygen species, resulting in partially filled Ti_{3d} non-bonding states[204]. The valence band onset for undoped TiO_2 was seen at ∼3.1 eV. For the doped films, significant changes in the peak shape and position of the VBM edge within the band-gap were observed. Indeed, the corresponding VBM value relative to the Fermi energy (E_F) was determined to be 2.8 eV, 2.4 eV, and 2.3 eV for TiO_2:W, TiO_2:N, and TiO_2:WN thin films, respectively. New states above the VBM for nitrogen containing films were responsible behind the observed band gap narrowing.

Energy level positions were obtained using the material's work function Φ. The Φ values were characterized via UV photoelectron spectroscopy (UPS) and extracted using the E_F edge and half height of secondary electron cutoff region E_{cutoff} while substracting the He_I energy of 21.2 eV. Further experimental details can be found in section A.2.1. Significant changes in the Φ of the sputter-deposited TiO_2 thin films were observed as shown in figure 5 of article 2. It was observed that the work function of TiO_2:N thin films decreased to 3.7 eV from 4.6 eV for undoped TiO_2. This was attributed to nitrogen dopant induced V_O formation creating donor energy states below the CBM, raising the E_F, and thereby lowering the Φ. Whereas tungsten doping was shown to not alter the work function Φ as compared to reference TiO_2. This was in alignment with previously

discussed observations indicating that TiO_2:W thin films had higher V_O formation energy. Upon WN-codoping, Φ was seen to increase by about 0.2 eV ($\Phi = 4.8$ eV) as compared to TiO_2 thin films (4.6 eV). As mentioned in the XRD observations, this is likely caused by the newly formed overlap of the W_{5d} and N_{2p} orbitals, lowering the Fermi level towards the VBM.

By combining these XPS, UPS, and UV-Vis observations, the ionization potential (I_p) and electron affinity (χ) can be extracted; completing the list of key features required as to fully plot the energy band diagrams of the doped TiO_2 films (section A.2.2 for full experimental details). Figure 6 of article 2 shows the energy band diagrams of the TiO_2, TiO_2:N, TiO_2:W, and TiO_2:WN thin films. By comparing redox energy levels presented in figure 1.1 to the results obtained, we can conclude that both TiO_2:N and TiO_2:WN thin films are well suited for use as photoanodes in visible-light driven EPC applications as their E_g is small enough, while their VBM is, for the most part below the oxidation levels of interest. However, given the general negative shift of energy levels observed for the TiO_2:N thin films, their oxidative power is considered thermodynamically less favorable for the $OH^{\bullet}/H_2O$ couple as compared to TiO_2:WN[1, 2, 3]. This advantageous VBM placement, combined with the reduction in Ti^{III} defect states as observed in the UPS spectra close to the Fermi edge around a binding energy of 0.9 eV, (see figure 5 of article 2) places TiO_2:WN thin films as the photoanode of choice for visible-light driven EPC applications. It is to be noted that the reduction in Ti^{III} defects is synonymous with a decrease of V_O, which in turn lowest the density of photocharge recombination centers in the case of WN-codoped TiO_2 films.

To further explore the nature of the various defects present in the TiO_2:WN films, we performed systematic HF-DS studies (of which experimental details and the various dielectric contributions are given in section A.2.6 and figure A.14, respectively). We recall here that the total dielectric constant is the sum of the following contributions: $\epsilon_{total} \approx \epsilon_{interface} + \epsilon_{dipole} + \epsilon_{ionic} + \epsilon_{electronic}$. Most importantly, it was noted is section 3.2.2 that $2\,Ti^{III}{-}V_O''$ defect association pairs contributed to the dielectric signal in the MHz-GHz range. Their exact dielectric contribution (*i.e.* ϵ_{dipole}) was approximated by subtracting $\epsilon_\infty \approx \epsilon_{ionic} + \epsilon_{electronic}$ from the total dielectric signal in the MHz-GHz spectral region. It was concluded that tungsten incorporation had an optimal doping point, showing the lowest ϵ_{dipole} contribution from V_O defect centers. Beyond this doping concentration, the increase in V_O formation energy was offset by the heavy cationic loading.

Figures 6 (a) and (b) of article 6 show typical ϵ' and ϵ'' HF-DS spectra for the undoped ($TiO_{1.90}$), oxygen deficient ($TiO_{1.7}$), N-doped ($TiO_{1.5}N_{0.3}$), and WN-codoped ($TiO_{2.4}W_{0.3}N_{0.3}$) type films. All of the samples showed a strong interfacial contribution tapering off in the MHz range. As previously remarked upon (section 3.2.2), the $2\,Ti^{III}{-}V_O''$ dipole contribution is the dominant feature in the GHz range for the substoichiometric films. Interestingly, this feature is seen to be partially reduced for the nitrogen doped samples (shown in figure 7 (a) of article 6). Further insight into this behavior could be obtained by extracting the ϵ' values at 1 GHz as a function of doping (shown in figure 7 (b) of article 6). Indeed, we note that the films dielectric defect dipole contribution is strongly dependent on the nitrogen content of the films and their oxygen deficiency. Interestingly, nitrogen doping effects the ϵ'_{dipole} signal differently weather the TiO_2 is stoichiometric or not (*i.e.* without or with V_O). For the latter (top guiding line in figure 7 (b)), nitrogen doping leads to a reduction of the V_O signature due to filling of the vacancies, whereas for the former (bottom guiding line in figure 7 (b)), $N_O^\bullet$ doping replaces lattice oxygen, creating local charge disparities. Both of these competing effects seem to saturate at high nitrogen doping levels of about >8 at.%. Critically, figure 6 of article 6 shows that optimally WN-codoped samples have a significantly reduced V_O ϵ'_{dipole} signature as compared to both TiO_{2-x} and TiO_2:N films. This is in direct alignment with our previous results, showing that the $W_{Ti}''{-}2\,N_O^\bullet$ codopant-passivation pair reduces the local charge disparities brought on via monodoping. Indeed, figure 3.6 shows the HF-DS spectra of TiO_2:N and TiO_2:WN films with similar N-doping of ≈7.5 at.%, however the latter sample is also doped with ≈7.7 at.% of W. Specifically, the TiO_2:WN film holds a $1:1.7$ $W_{Ti}'' : N_O^\bullet$ dopant ratio, very close to the theoretical ideal. Because of this, the ϵ_{dipole} signal is seen to be almost fully quenched. While some contribution from the $2\,Ti^{III}{-}V_O''$ dipole is still clearly seen, the WN-codoping reduces this signal significantly. Additionally, the higher frequency component found in the TiO_2:N spectra disappears completely, allowing the TiO_2:WN films to show a ϵ_∞ on par with that of undoped TiO_2, *i.e.* $\epsilon_\infty <\approx 90$. This is direct evidence that tungsten introduction serves to passivate local charge defects brought on via nitrogen doping, leading to a drastic reduction in V_O formation. Finally, in order to confirm the interplay of the $W_{Ti}'' : N_O^\bullet$ codopant passivation pair, the ϵ'_{dipole} signature was studied at 1 GHz with each dopant fixed, while the other varied. Figure 8 of article 6 presents these values as a function of nitrogen content at a fixed tungsten content (*i.e.* W ≈ 3.8 at.%) and as a function of tungsten content at fixed nitrogen content (*i.e.* N ≈ 7.5 at.%). Indeed we can note that any increase in nitrogen leads to a higher V_O signature due to the added h^+ ($N_O^\bullet$), whereas any additional W_{Ti}'' passivates these charge disparities, decreasing the formation of V_O.

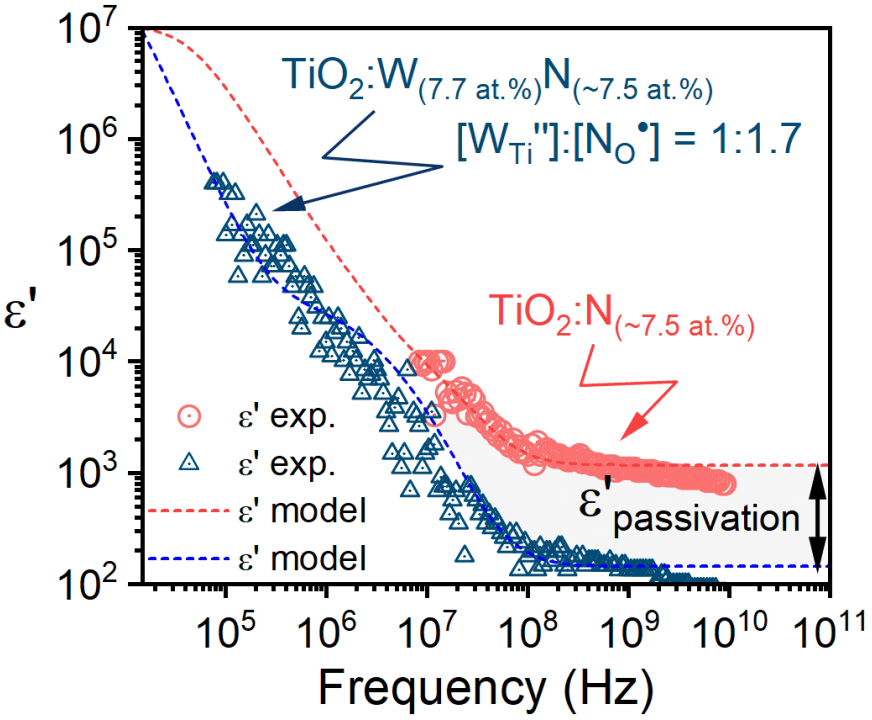

Figure 3.6 – HF-DS spectra of a TiO_2:N deposited with $R_{N2} = 9\,\%$, having a nitrogen content of 7.6 at.% and TiO_2:WN deposited with WO_3 $W_{power} = 1.67\,W\,cm^{-2}$ & $R_{N2} = 12\,\%$, having a tungsten and nitrogen contents of 7.7 at.% and 7.4 at.%, respectively.

To better highlight the positive effects of such a reduction in defects associated with WN-codoping, photocharge lifetimes as a function of doping scheme and loading were measured. To this end, FP-TRMC measurements were carried out to probe the time resolved change in conductivity of the films $\sigma(t)$ following their photoactivation by a short laser excitation pulse (see section A.2.5 for details of the FP-TRMC measurements). After the laser illumination pulse, the change in microwave power transmission ($\Delta P(t)$) from the sample cavity as a function of time is recorded. This change in μ-wave transmission is related to the photo-conductance of the material by a hardware dictated sensitivity factor C, *i.e.* $\Delta P(t)/P(t) = C \cdot \Delta\sigma(t)$. Given that the material's photoconductivity is related to the charge mobility μ and charge population N *i.e.* $\Delta\sigma(t) \approx \mu \cdot \Delta N$, the time evolution of $\Delta P(t)/P(t)$ gives information about the recombination or trapping of charge carriers. In the case of TiO_2, it can be easily approximated that electrons are the majority carrier[113]. Typical TRMC decay signals after the 5 ns laser pulse illumination (at a wavelength of 420 nm) of the sputter-deposited TiO_2 thin films with various doping configurations can be seen in figure 4 of article 4. It needs to be noted that pristine TiO_2 could not be studied due to the excitation wavelength of the laser. While these spectra provide a wide slew of information on the photocharge

species (see section A.2.5), we focused on the extraction of lifetime data from these decay curves as they depend purely on the time variation of the decay and not the overall signal intensity. To accomplish this, the $C \cdot \Delta\sigma(t)$ curves were fitted using exponential functions representative of various charge carrier decay processes, each with its characteristic time constant τ. Thus, $C \cdot \Delta\sigma(t) = \sum_{n=1:m} A_n \cdot exp\left(\frac{t}{\tau_n}\right)$ where A_n and τ_n are the respective proportionality and time constants of each decay process m. For our sputter-deposited films, all the lifetime curves could be separated into three decay regimes (*i.e.* $m = 1:3$) associated with three characteristic lifetimes, namely τ_{trap}, τ_{rec}, and τ_{surf} (with their respective time constants τ on the order of 0.05 µs, 1 µs, and 10 µs respectively)[5]. These are associated with photocharge decay via charge trapping ($e^-|h^+ \rightarrow e^-_{tr}|h^+_{tr}$), charge annihilation ($e^- + h^+ | e^-_{tr} + h^+ | e^- + h^+_{tr} \rightarrow h\nu$), and surface reactions ($e^- + O_2 \rightarrow O_2^-$), respectively. The characteristic lifetimes of each of the three processes were extracted, and reported as a function of the doping scheme of the TiO_2 films in figure 5 of article 4. One can clearly see that while W-doped samples show the overall lifetimes, WN-codoped thin films show a significant increase in photocharge lifetimes as compared to N-doped ones. However, the sole comparison of photocharge lifetimes remains insufficient to derive a relationship between the codoping scheme passivation and photocharge transport.

To better understand the meaning of photocharge lifetimes in the context of the codoping models used to guide this work, we propose an empirical effective passivation parameter P_{WN} such that $P_{WN} = 2[W^{VI}] - [N_{sub}]$; *i.e.* every W''_{Ti} passivates two $N^{\bullet}_{O}$, so that the theoretically ideal empirical passivation parameter is at $P_{WN} = 0$). While both dopants exist in other forms, these are not considered for the purposes of our empirical model. For example, W^{IV} (*i.e.* $W^{\times}_{Ti}$) is assumed to have little to no local electronic effect, and N_i is typically associated with the formation of $-O-N$ type ions. In other words, P_{WN} is expected to be directly associated with the reduction in V_O defect states brought on via local passivation of charge disparities. This, in turn, should manifest itself as an increase of photocharge lifetimes through the reduction of defect centers that would otherwise form in uncompensated environments. Consequently, the variation of photocharge lifetimes as a function of P_{WN} was plotted and is presented in figure 6 of article 4. It clearly appears that the introduction of W''_{Ti} states considerably increases the photocharge lifetimes regardless if a codopant is present or not (*i.e.* both the TiO_2:W and TiO_2:WN type thin films). This is most apparent when compared to TiO_2:N thin films which show very low lifetimes due to local charge defects. Tungsten is seen to passivate these through acceptor-donor interplay, pushing the lifetimes to triple in some

cases for optimally doped TiO_2:WN films. Interestingly, as hinted at in section 3.2, we see that W incorporation increases photocharge lifetimes even in W-monodoped environments, consistent with HF-DS and XPS observations of decreased V_O in such samples. These results cement the idea that codoping with a suitable acceptor-donor pair, (such as W−N), significantly increases the photocharge lifetimes via suppression of the $2\,Ti^{III}{-}V_O''$ defect association states. From an application viewpoint, this enables the material to maintain high photosensitivity (matching that of optimally doped TiO_2:N with $E_g = 2.3\,eV$), while significantly increasing its associated photocharge lifetimes.

In order to explore the added benefits of increased lifetimes on the EPC performance of the TiO_2:WN thin films, the same sputter deposited films studied herein were deposited onto both faces of Ti grids (as large as 15.24 cm in diameter, see figure A.21) which were used as photoanodes in a 1 L home built EPC reactor (see figures A.19 and A.20), details of which are presented in section A.3. The EPC performance of our photoanodes was directly evaluated toward the degradation of ATZ. To this end, synthetic solutions containing ATZ concentrations of $60\,\mu g\,L^{-1}$ (as these are typical concentrations of heavily polluted areas) were prepared and treated in our EPC reactor under AM 1.5G solar simulator while continuously circulating them with treatment times reaching up to 6 h. Typical time-dependent degradation curves of atrazine as function of photoanode type can be seen in figure 7 of article 4 (photoanodes with optimal doping concentrations based on E_g and XRD observations). We can note that while all the photoanodes successfully degraded ATZ to the environmentally acceptable limit of $1.5\,\mu g\,L^{-1}$ after 3 h, the kinetics of the degradation reactions is seen to be dependent on the doping configuration. Indeed, while it took 3 h for the EPC degradation of ATZ to reach the $1.5\,\mu g\,L^{-1}$ threshold using a TiO_{2-x} photoanode (which we saw in section 3.2 performs identically to TiO_2 type photoanodes), this degradation time is reduced for all doped thin films. This time reaches its lowest value of 45 min for the best performing TiO_2:WN photoanode. The pseudo-first-order degradation kinetic constants for the various optimally-doped photoanodes alongside with their E_g values are presented in table 3.3.

It can be seen that compared to TiO_{2-x} photoanodes, TiO_2:N doubles the rate of ATZ degradation, reiterating the benefits of visible light photosensitization, allowing for a higher portion of photons form the solar spectrum to be used. Interestingly, TiO_2:W thin films are seen to slightly outperform nitrogen doped photoanodes, even with minimal visible light photosensitization (only $\approx$0.2 eV reduction in their E_g as compared to TiO_2). This highlights the clear benefit of increased

Photoanode type	E_g (eV)	Degradation constant k (min^{-1})
TiO_{2-x}	3.2	0.026 ± 0.0017
TiO_2:N	2.3	0.047 ± 0.0017
TiO_2:W	3.0	0.057 ± 0.0053
TiO_2:WN	2.3	0.106 ± 0.0090

Table 3.3 – Extracted pseudo-first-order degradation constants for best-tested photoanodes per doping type evaluated by the EPC degradation of ATZ under AM1.5G illumination with their corresponding E_g values.

photocharge lifetimes on the EPC performance of a material, which in a way compensates for their lack of visible light photon sensitivity. In other words, whereas TiO_2:N films profit from their increased photosensitivity to the visible spectrum, the TiO_2:W samples offer longer lifetimes and therefore increased reaction probability of produced photocharges. Upon optimized synergistic codoping of TiO_2:WN photoanodes, we can observe a fourfold increase in the pseudo-first-order degradation kinetics from $0.026 \pm 0.0017\,min^{-1}$ (for TiO_2 & TiO_{2-x}) to $0.106 \pm 0.0090\,min^{-1}$. This has been shown by XPS, XRD, HF-DS, and TRMC measurements to be a direct consequence of W''_{Ti} codopant induced reduction in the $2\,Ti^{III}{-}V''_O$ defect pair density, increasing the photocharge lifetimes, while maintaining visible light photosensitivity from $N^{\bullet}_O$.

3.3.4 Summary of TiO_2:WN results

In summary, we have successfully synthesized *in-situ* codoped TiO_2:WN thin films via a reliable, reproducible, and flexible RF-MS process. Our micro-structural analysis revealed the presence of both tungsten and nitrogen dopants in mostly W''_{Ti} and $N^{\bullet}_O$ states with a significant reduction in the V_O density as compared to the TiO_2:N thin films. Moreover, we have shown that WN-codoping increases the solubility limits for each dopant while drastically improving the crystalline structure of the films, ensuring the anatase polymorph formation for a wide range of doping concentrations.

By combining XPS, UV-Vis, and UPS analyses, we were able to point out that: (i) both the TiO_2:N and TiO_2:WN thin films have a significantly red-shifted E_g, reaching values as low as 2.3 eV, (ii) this apparent reduction in E_g was caused by an upshift of the VBM towards the CBM caused by the integration of N atoms, and that (iii) TiO_2:WN constitute the ideal photoanodes for visible light EPC applications. The defect passivating nature of the codoping regime was highlighted by HF-DS studies which revealed a marked reduction in the $2\,Ti^{III}{-}V''_O$ defect pair upon introduction of tungsten and nitrogen in appropriate ratios. This theoretical ratio was further highlighted using FP-

TRMC analysis. By establishing an apparent passivation parameter (*i.e.* $P_{WN} = 2[W^{VI}] - [N_{sub}]$), we were able to correlate directly the increase in photocharge lifetimes with the reduction in defect density. Thus, the optimally codoped TiO_2:WN photoanodes were shown to be four times more effective that their undoped TiO_2 counterparts for the EPC degradation of ATZ under 1.5AM simulated solar light.

Chapter 4

Conclusion and prospects for future research

I just really hope someone finds it useful.

Nazar Delegan

Titanium dioxide is well-known to be amongst the most practical and prevalent photocatalytic materials due to its unique combination of physico-chemical properties. Moreover, TiO_2 stands out by its chemical stability, bio-compatibility (non-toxicity), abundance, and cost-effectiveness. Most importantly, TiO_2 has almost ideal band-gap VBM and CBM levels, allowing photo-generation of holes with strong oxidizing power and electrons with adequate reducing power. All these uniques features have promoted TiO_2 to be a material of choice for some interesting industrial applications such as self-cleaning surfaces owing to its UV induced super-hydrophilicity. Extending the photoactivity of TiO_2 to the visible (*i.e.* direct use of sunlight) will pave the way for other large scale and cost-effective applications in various domains such as air/water decontamination, H_2-fuel production, and other visible-light fueled photocatalytic applications. This perspective has motivated an even increasing R&D effort to photosensitize TiO_2 in the visible light domain.

This doctoral projects aims at being a contribution to this ongoing international effort. The ultimate objective of this thesis was to enable TiO_2 thin films to drive photocatalytic reactions using a significantly higher portion of readily available sunlight photons. While many pathways were presented, anionic type doping of TiO_2 showed most promise and was selected as methodology

of choice in the present work. Specifically, substitutional-type nitrogen was shown to be effective in red-shifting the TiO_2 bandgap into the visible portion of the solar light spectrum. Experimentally, effective N-doping of TiO_2 needed a control over the dopant content, th impurity incorporation location (substitutional rather than interstitial), and control of film crystallinity. All these stringent requirements were fulfilled by the RF-MS method that we have used to reproducibly grow TiO_2:N films with various doping contents. Chemical analysis revealed that most nitrogen was in the desired oxygen substituting locations, with a small portion in interstitial lattice locations. This nitrogen doping was shown to have an optimal point of about $\approx$4 at.%, where the TiO_2:N films possess the lowest E_g of 2.2 eV while maintaining the anatase polymorph. These visible-light photosensitized TiO_2:N films were successfully integrated into photoanodes for the EPC degradation of an emerging pollutant, chlortetracycline. Degradation rates were shown, for the first time, to be directly correlated to the bandgap of TiO_2:N, with the narrowest bandgap photoanodes showing the highest EPC performance. While these results were promising, it was noted that much of the gains in photosensitivity were not capitalized on in terms of the per-photon efficiency of the TiO_2:N photoanodes. It was noted that this was caused by nitrogen doping induced local charge disparities resulting in the formation of V_O defect centers.

On the other hand, tungsten doped TiO_2:W films were reported to have increased photocatalytic performance. Many varying and sometimes conflicting explanations were proposed for this in the literature. Some suggested that tungsten was responsible for improving photocharge transport properties in the TiO_2:W photocatalyst. Parallel to this, theoretical models identified tungsten as an ideal codoping partner for nitrogen, as it would suppress formation of V_O defect centers. To understand the isolated effects of tungsten doping, and validate its candidacy for the next WN-codoping step, we first synthesized TiO_2:W films by means of RF-MS and studied their physicochemical properties as a function of W-dopant loading. These studies showed that W atoms were in Ti-substituting locations within the TiO_2 lattice, without the formation of tungsten oxide clusters. More importantly, we have been able to use, for the first time, dielectric measurements to show clearly that tungsten incorporation increased the V_O formation energy. We were thus able to identify an optimal W loading point of about $\approx$2.5 at.% that corresponds to the lowest density of V_O defect pairs. Intriguingly, when the optimized TiO_2:W & TiO_2:N photoanodes were compared for their visible-light driven EPC degradation of atrazine, they were found to have almost identical degradation rates. However, these seemingly similar performances were driven by two very different

phenomenon. While TiO_2:N had higher EPC performance (as compared to TiO_2:) due to its increased ability to harvest visible photons, TiO_2:W had better photocharge transport properties (lower recombination rates, therefore longer photocharge lifetimes), resulting in higher relative per-photon efficiency.

In an effort to combine the advantages of both N & W doping, we have completed this doctoral work by focusing on the *in-situ* WN-codoping of TiO_2 by developing and optimizing a reliable RF-MS deposition process. The objective was to maintain N induced visible-light photosensitivity, while preserving improved photocharge transport properties associated with W-doping. The codoped films showed many of the positive characteristic of the monodoped films such as both dopants in desired substitutional locations and improved visible light harvesting properties. However, the codoped TiO_2:WN also showed many improved characteristics as compared to the monodoped films. Firstly, TiO_2:WN had improved crystallinity and dopant solubility; showing a well formed anatase phase for a wide range of codopants. Secondly, at low doping regimes, the TiO_2:WN films had significantly reduced defects as compared to their monodoped counterparts. Thirdly, the WN-codoped films were better suited for EPC applications as they had an E_g width on par with TiO_2:N, but a thermodynamically favored VBM placement, in comparison. Finally, the acceptor-donor codoped passivation scheme resulted in significantly reduced V_O defect density, whih in turn, translated into characteristic photocharge lifetimes up to three times longer than those of N-doped films. In combination, these elements resulted in TiO_2:WN photoanodes being vastly superior to both TiO_2:N and TiO_2:W monodoped photoanodes (two times higher degradation rates) in EPC degradation of atrazine under simulated solar light.

Based on the results obtained in the course of this PhD project, we can confirm that the initially targeted objectives were achieved. These can be summarized in the three following points:

(i) We have successfully developed a radio-frequency magnetron sputtering deposition method for preparing *in-situ* N-doped, W-doped, and WN-codoped photoactive TiO_2 photoanodes. The N-doped and WN-codoped ones were sensitive to visible light. This work has pointed out that TiO_2:WN codoped films (at optimal doping levels) are the most appropriate for water decontamination under sunlight.

(ii) We were able establish fundamental correlations between dopant nature/content and the relevant properties of the RF-MS deposited films. This enables us to optimize their visible light photoactivity.

(iii) The key characteristics of the TiO_2:N, TiO_2:W, and TiO_2:WN thin films were directly related to their visible light driven EPC ability to degrade real water pollutants. The EPC part on this work was done in collaboration with Prof. Drogui's group (INRS-ETE).

That being said, many features of this complex system would need further investigations. From a technical perspective, the effect of some RF-MS parameters on the resulting TiO_2:WN films remain to be explored. For instance, it is likely that the substrate deposition bias could be used to control the exact proportion of the dopant nature and location in the films (*e.g.* interstitial *vs* substitutional) as this would benefit stronger bonded species during deposition. Additionally, other permutations of sputter targets and reactive gases could be used for a similar purpose. Ideally, these studies would allow for the synthesis of TiO_2:WN films with exclusively substitutional nitrogen and hexavalent tungsten.

From a material perspective, a detailed E_g-structure and photocurrent study as a function of relative codopant concentrations would provide further insight into the WN-codoping system. Such optimization studies would likely result in further gains in per-photon efficiency of TiO_2:WN for visible light driven EPC applications. Electrochemical characterization of these optimized photoanodes would provide insight into working EPC parameters that would maximize the material's lifetime and establish economic viability for niche applications (*i.e.* allow for dopant dependent redox level adjustment for specific applications).

From a more fundamental viewpoint, quantitative FP-TRMC studies with variable laser wavelength would not only provide insight into the photocharge generation efficiency as a function of doping scheme and content, but would allow to more accurately pinpoint the energy band states responsible for generating/trapping/annihilating excitons. These fundamental studies would pave the way for integrating codoped TiO_2 (with specifically tailored dopant contents for these architectures and applications) onto carbon nanotubes, graphene, and other 1D/2D materials. Forming next generation systems that would take advantage of TiO_2's visible-light harvesting and tailored redox levels while benefiting from the exceptional photocharge transport separation/conduction properties of the scaffolding material. The tunability of the CBM/VBM levels would allow TiO_2:WN's use for

a wide range of EPC processes, such as CO_2/H_2 reduction. Finally, the use of visible-light sensitive TiO_2:WN (especially 1D TiO_2:WN) could replace the TiO_2/dye electrodes in modern DSSCs, providing an avenue for new solar cell architectures.

Part II

Résumé de la thèse en français

Le dopage *in-situ* de films de dioxyde de titane par pulvérisation-magnétron pour leur exploitation efficace dans les processus électrophotocatalytiques de dégradation de polluants sous lumière visible

La section suivante sert d'un résumé de la thèse en français selon les normes linguistiques de l'INRS. Se distinguant d'un "abstract", ce résumé vise aussi à présenter le contexte et la structure de cette thèse.

Mots-clés: Pulvérisation-magnétron en mode RF, dopage *in-situ*, codopage à l'azote et au tungstène, TiO_2:WN, photoanode, rétrécissement de la bande interdite, passivation électronique donneur-accepteur, électro-photocatalyse sous lumière solaire, dégradation des polluants.

5.1 Introduction, motivations, et méthodologie

La pollution environnementale jumelée avec un manque de sources d'énergie renouvelables est parmi les plus grands défis de l'ère moderne. En conséquence, l'objectif de ce travail de thèse est de

développer des couches minces à base de TiO_2 pour la dégradation électrophotocatalytique sous lumière visible des polluants dans l'eau.

L'exploitation du TiO_2 pour l'électrophotocatalyse est déclenchée par l'absorption d'un photon d'énergie suffisante (3.2 eV dans le cas de l'anatase). Ce photon peut promouvoir un électron de la bande de valence à la bande de conduction; l'électron (e^-) et le trou (h^+) qui en résultent (aussi appelé exciton) peuvent ensuite retrouver leur état d'équilibre en se recombinant, ou en agissant comme donneur et/ou accepteur de charge avec une molécule/atome qui est en contact avec le système. Ainsi, l'électron et le trou peuvent participer à des réactions de réduction et d'oxydation respectivement. Les probabilités de ces réactions sont guidées par le temps de vie, les défauts et les probabilités de recombinaison de ces photocharges. Hélas, on peut établir quelques critères requis pour un processus électrophotocatalytique efficace:

(i) L'amplitude de la bande interdite (E_g) dicte le nombre de photons qui peuvent participer dans les processus photocatalytiques (et électrophotocatalytique).

(ii) Les limites de la bande interdite définissent l'énergie potentielle chimique des électrons et trous dans les réactions de réduction et d'oxydation respectivement. Spécifiquement, le minimum de la bande de conduction doit être par-dessus l'énergie de réduction et le maximum de la bande de valence doit être en dessous de l'énergie d'oxydation visée (voir figure 1.1).

(iii) Les photocharges doivent avoir des temps de vie suffisamment longs pour entamer les réactions désirées. En d'autres mots, il faut que le libre parcours moyen leur permette de se rendre aux molécules des réactifs.

Fondamentalement, le TiO_2 est un semi-conducteur de type-n avec une bande interdire intrinsèque (E_g) de 3.0 eV et 3.0 eV dans le cas des polymorphes rutile et anatase respectivement. Le TiO_2 est donc un semi-conducteur à large bande interdite directe pour le rutile et indirecte pour l'anatase. Dans le choix des polymorphes du TiO_2, l'anatase est le candidat par excellence pour des applications photocatalytiques, étant donné la nature indirecte de sa bande interdite qui permet un temps de vie plus long aux photocharges. La large bande interdite du TiO_2 limite l'absorption du matériau à des longueurs d'onde de l'UV. Or, les radiations UV ne représentent que $\approx$4 % du

flux énergétique total solaire à la surface terrestre, tel qu'illustré à la figure 5.1. Le maximum du flux énergétique des rayons solaires se situe autour de 550 nm correspondant à une E_g théorique d'environ 2.2 eV.

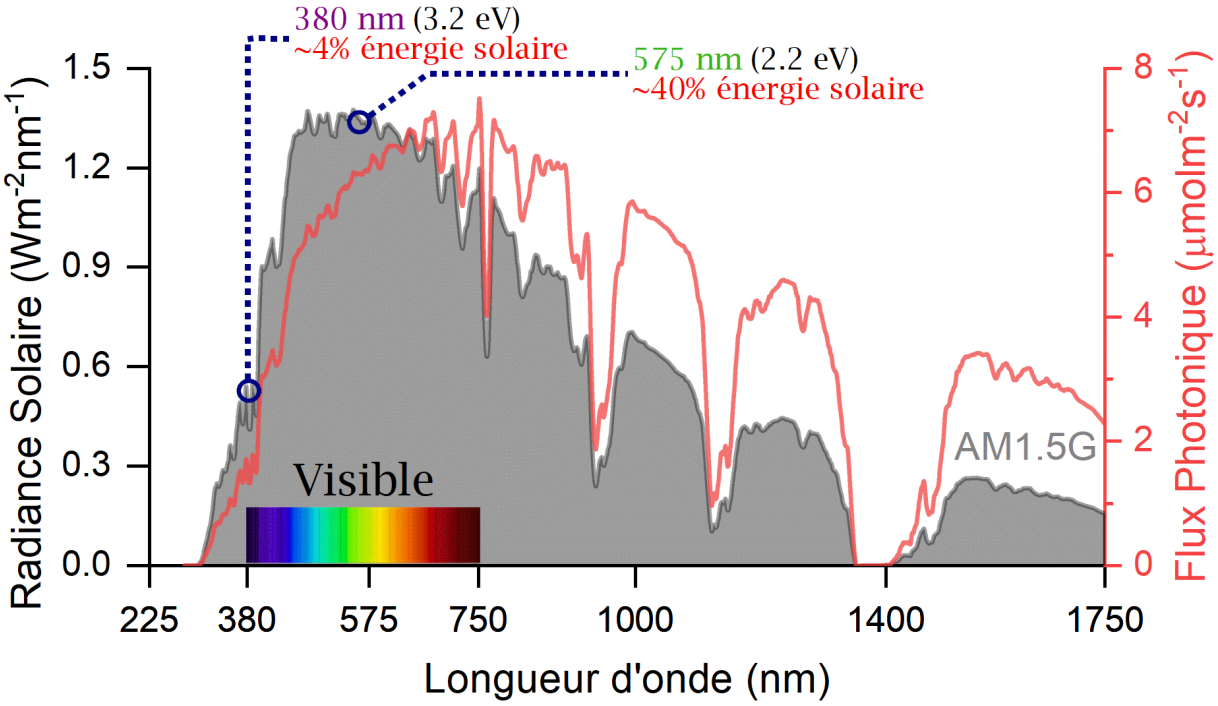

Figure 5.1 – Spectre solaire AM 1.5G (ligne noire, axe vertical de gauche) et flux photonique à AM 1.5G (ligne rouge, axe vertical de droite). On remarque les démarcations à 3.2 eV et 2.2 eV représentant ≈4 % et ≈40 % respectivement de l'énergie totale solaire. Pris de la base de données de NREL.

Les limitations du TiO_2 telles que la largeur significative de la bande interdite et le temps de vie des excitons dictent les efforts de recherche (et les défis de ce projet) sur l'optimisation de la photoactivité de ce matériau. De plus, les processus électrophotocatalytiques efficaces requièrent une localisation des limites de l'E_g proche des énergies potentielles nécessaires pour la formation des espèces réduction-oxydation visées. Dans un cas idéal, la bande interdite du matériau devrait être proche du maximum solaire, *i.e.* 2.2 eV, préserver les alignements des bandes énergétiques désirés (voir figure 1.1) tout en préservant les propriétés avantageuses du TiO_2 (*e.g.* photostabilité, compatibilité environnementale, etc.).

Dans le but d'étendre la zone spectrale de photoactivité du TiO_2 à la lumière visible, plusieurs approches ont été rapportées dans la littérature tels l'autodopage, le dopage cationique, le dopage anionique, la sensibilisation avec des colorants, etc[34, 35, 6]. Cependant, plusieurs de ces ap-

proches sont de synthèse chimique, non-systématiques dans les concentrations de dopants explorées et rapportent des conclusions contradictoires sur les effets des dopants dans la matrice du TiO_2.

Asahi et al. ont proposé que le dopage anionique de TiO_2 avec de l'azote puisse être utilisé pour contourner plusieurs de ces limitations[33]. Néanmoins, il y a des aspects de cette approche qui sont encore débattus dans la littérature, tels que le rôle optoélectrotechnique exact des dopants (*e.g.* interstitiels *vs* substitutionels), les propriétés des photocharges en fonction des dopants, etc[34, 35, 113]. Autrement dit, si le dopage du TiO_2 doit être étudié, une méthode de synthèse hautement flexible, de très haute pureté et reproductible doit être mise en place. Toutes ces conditions sont atteignables en utilisant la pulvérisation-magnétron radiofréquence, la technique de synthèse utilisée pour la préparation des films électrophotocatalytiques tout le long de ce projet de thèse.

5.1.1 Objectifs

Cette thèse vise donc à développer un procédé de déposition et dopage *in-situ* des films de TiO_2 par pulvérisation-magnétron pour étendre leur photoactivité au spectre visible. Même si l'emphase principale va porter sur le rétrécissement de la bande interdite des films de TiO_2 dopés, une attention particulière va être attribuée au maintien des énergies chimiques potentielles des photocharges (*i.e.* le minimum de la bande de conduction et le maximum de la bande de valence). La microstructure et les propriétés optoélectroniques de ces films seront optimisées pour les utiliser dans des applications de dégradation de contaminants réels (*e.g.* l'atrazine, la chlortetracycline, etc.) par électrophotocatalyse. Spécifiquement, ce travail doctoral a les objectifs suivants:

(i) Développer une approche à base de la pulvérisation-magnétron radiofréquence pour la déposition des couches minces de TiO_2 dopées *in-situ* pour leur application en électrophotocatalyse sous lumière visible.

(ii) Caractériser et optimiser les propriétés optoélectroniques des couches minces de TiO_2 en fonction des paramètres de déposition (*e.g.* puissance de pulvérisation-magnétron, température des substrats, niveau de dopage, etc.). Une attention particulière va être portée au rétrécissement de la bande interdite du matériau et le temps de vie des photocharges.

(iii) Agencer les résultats des objectifs (i) et (ii) en intégrant le TiO_2 en tant que photoanodes dans un processus électrophotocatalytique pour la dégradation de polluants dans l'eau. Cet objectif vais être réalisé en collaboration avec nos collègues au centre INRS-ETE (sous la supervision du Prof. Patrick Drogui).

(iv) Combiner les résultats et observations des objectifs (ii) et (iii) pour mieux comprendre les relations entre les caractéristiques physiques des photoanodes et leurs performances en électrophotocatalyse pour la dégradation des polluants tels la chlortetracycline et l'atrazine.

5.1.2 Méthodologie

Déposition des couches minces de TiO_2

La pulvérisation magnétron est une méthode de dépôts de couches minces qui consiste à pulvériser une cible de métal ou semi-conducteur en présence d'un gaz porteur neutre (chimiquement inerte) ionisé, accéléré et confiné par un champ électromagnétique, le tout dans une chambre à base pression (pression interdéposition de 1×10^{-8} Torr et pression de dépôt 1.4×10^{-3} Torr)[14, 36]. Ainsi, un plasma est créé au niveau de la cible soit par une décharge de courant direct (DC, dans le cas des cibles métalliques) ou en radiofréquence (RF, dans le cas des diélectriques) en présence d'ions d'argon (du gaz porteur). Les ions d'Ar viennent pulvériser la cible (accéléré et dirigé par ledit champ magnétron) créant ainsi un flux atomique, qui par condensation se dépose sur le substrat. Le plasma de pulvérisation est confiné vers la cible suivant les lois d'interaction des particules chargées et les champs électromagnétiques tels que schématisés sur la figure A.1. De plus, il est possible de faire une pulvérisation dite réactive en introduisant des gaz réactifs en plus du gaz porteur d'énergie. L'utilisation simultanée de deux ou plusieurs cibles dans le processus de pulvérisation permettent également de déposer des films aux compositions atomiques diverses résultant des mélanges atomiques produits dans le plasma de déposition. Dans le processus de déposition par pulvérisation, les paramètres de dépôt influencent directement le plasma de déposition et par conséquent, les propriétés des films déposés. Par exemple, la température du substrat a un effet sur la structure cristalline du TiO_2. Le rapport des flux des gaz permet le dopage des films de TiO_2 et le potentiel d'accélération au substrat permet de densifier le matériau. Cette méthode de

déposition physique permet d'avoir des films d'une pureté inégalée et surtout un contrôle très précis du dopage. Une description élaborée de la pulvérisation-magnétron radiofréquence est présentée dans l'annexe A.1.

Méthodes de caractérisation

Les effets de plusieurs paramètres clés doivent être étudiés lors du processus d'optimisation des couches minces de TiO_2. Notre objectif ultime est de réduire la largeur de la bande interdite du matériau, garder une cristallinité de type anatase et assurer des propriétés optoélectroniques permettant un transport efficace des charges photogénérées avec une longue durée de vie. Plusieurs méthodes de caractérisation des matériaux seront donc utilisées pour avancer ce travail incrémental d'optimisation de la structure et des propriétés optoélectroniques des films de TiO_2. Les observations à l'aide un microscope à balayage électronique (SEM) nous permettent de vérifier l'épaisseur et la morphologie des films; des paramètres critiquent pour la caractérisation du processus de dépôt et certaines analyses à base de modélisation telles: l'ellipsométrie spectroscopique et les mesures diélectriques à haute fréquence. La cristallinité des couches préparées est déterminée par la diffraction des rayons X à angle rasant (XRD). La nature des liens chimiques et la composition élémentaire sont obtenues à l'aide des analyses spectroscopie à photoélectrons X (XPS). Ces mesures XPS sont, au besoin, complémentées par la spectroscopie infrarouge à transformer de Fourier (FTIR) et l'analyse par détection de collisions atomiques de nature élastiques (ERD-TOF). Les propriétés optiques sont étudiées à l'aide de la spectroscopie d'absorption dans l'ultraviolet et visible en transmission et réflexion (UV-Vis); ces spectres sont ensuite analysés à l'aide du modèle de Tauc pour extraire la valeur de la bande interdite optique. Dans certains cas, l'E_g a été également déduite des mesures d'ellipsométrie spectroscopique (SE). La SE permet d'obtenir des informations intrinsèques au matériau (*e.g.* l'E_g) avec des modèles qui considèrent des paramètres tels: la rugosité, l'épaisseur et l'uniformité des films. Dans le but d'étudier les performances électrophotocatalytiques de couches minces optimisées, elles sont utilisées comme photoanodes dans un réacteur EPC développé par nos collaborateurs de l'INRS-ETE (voir section suivante). De plus, il y a des méthodes d'analyse spécifiques aux propriétés optoélectroniques, telle la spectroscopie à réflexion microondes (TRMC), qui seront utilisées dans le cadre de ce doctorat pour mieux cerner la capacité de photogénération de nos films et de la durée de vie des photocharges générées. Finalement, les études diélectriques à haute fréquence (HF-DS) seront utilisées pour sonder le comportement électronique (dipôles élec-

troniques) des défauts dans les couches minces de TiO_2 déposés par pulvérisation-magnétron. Les détails techniques des méthodes de caractérisation utilisés lors de ce projet de thèse sont détaillés dans l'annexe A.

Études électrophotocatalytiques

Dans le but d'étudier les performances électrophotocatalytiques des couches minces de TiO_2 déposées, un réacteur électrophotocatalytique a été développé avec nos collaborateurs à l'INRS-ETE (groupe du Prof. Drogui). Pour ces buts, les couches minces optimisées de TiO_2 sont déposées sur des grilles de Ti déployés. Le réacteur EPC se compose principalement d'un contenant inerte, une pompe péristaltique et un simulateur solaire pour l'illumination. Dans le contenant sont placées les photoanodes (TiO_2) et la cathode (carbone vitreux, BDD, etc.). Le système est suffisamment adaptable pour explorer l'impact de plusieurs facteurs de dégradation tels le débit, la puissance solaire, le potentiel appliqué, la distance inter-électrode, l'effet du barbotage d'air, etc. Ces études ont été effectuées au laboratoire du Prof. Drogui è l'INRS-ETE. Une description détaillée du réacteur et des études électrophotocatalytiques se trouvent à l'annexe A.3.

5.1.3 Plan de la thèse

Ce travail de thèse est présenté sous format d'une thèse par article. Le chapitre 2 présente le contexte scientifique relié à la photocatalyse à base de TiO_2. Le tout débute avec un survol des principes qui guident les réactions électrophotocatalytiques à la surface du TiO_2 (section 2.2). Une compréhension du processus électrophotocatalytique nous permet ensuite d'établir les caractéristiques d'intérêt du photocatalyseur. En conséquence, les propriétés cristallographiques et optoélectroniques du TiO_2 sont présentées dans la section 2.3. À titre informatif, ce texte va utiliser la notation de défauts Kröger–Vink. Cette notation décrit d'une manière précise et concise la charge électrique et le lieu d'un défaut dans un cristal; *e.g.* atome de tungstène substitutionel dans un emplacement d'un atome de Ti avec une double charge négative de plus s'écrit W''_{Ti} et atome d'azote substitutionel dans un emplacement d'oxygène avec une charge positive nette est noté $N^{\bullet}_{O}$. Le chapitre 2 se termine avec un survol des méthodes de synthèse du TiO_2 (voir section 2.4) et quelques avenues d'application pour le matériel (voir section 2.5).

Les résultats obtenus lors de ce projet de thèse sont présentés dans le chapitre 3. Ce chapitre est séparé en trois sections initialisé avec (i) le dopage du TiO_2 à l'azote (section 3.1) qui vise à photosensibiliser les couches minces de TiO_2:N dans le visible. Les diverses propriétés des films de TiO_2:N y sont discutées avec une attention particulière attribuée au rétrécissement de la bande interdite. Les bienfaits du dopage à l'azote sont démontrés à travers l'exploitation des photoanodes de TiO_2:N pour la dégradation électrophotocatalytique de la chlortetracycline (polluant dans l'eau) sous lumière visible. Cette section se termine avec une identification de certains inconvénients du dopage à l'azote. Par la suite, (ii) la section 3.2 présente les avantages du dopage au tungstène du TiO_2 avec une attention particulière sur la passivation des défauts de charge avec l'incorporation des W''_{Ti}. Finalement, (iii) la section 3.3 présente une solution aux inconvénients et limitations du monodopage via la passivation induite par le codopage au tungstène et azote, *i.e.* couches minces de TiO_2:WN. Les résultats de cette thèse servent à supporter les divers papiers scientifiques publiés sur le sujet (voir section IV). L'objectif de cette thèse est de complimenter et consolider les résultats des articles sans répétition superflus.

Ce travail de thèse est conclu au chapitre 4. Les contributions scientifiques du projet de thèse sont mises en valeur et une ouverture scientifique pour les travaux futurs est offerte.

Dans le cadre de ce résumé, la section suivante va servir d'un exposé des résultats intéressants obtenus lors de ce projet de thèse.

5.2 Sommaire des résultats

Le dopage à l'azote du TiO_2

Le dopage anionique surpasse le dopage métallique grâce à une meilleure stabilité thermique, simplicité d'intégration et un décalage (vers le visible) du seuil d'absorption plus prononcé. Suite à une revue de la littérature sur les avantages et désavantages de différents dopants pour la photosensibilisation du TiO_2 dans le visible, le dopage à l'azote est ressorti comme le candidat de choix par le mérite de la compatibilité énergétique de ses orbitales N_{2p} avec celles de O_{2p} (qui composent la bande de valence du TiO_2). Pour préparer les couches minces de TiO_2:N, un réacteur de pulvérisation-magnétron utilisant une décharge radiofréquence à 13.56 MHz a été utilisé. Ces dépôts ont été faits

à une pression partielle de 1.4×10^{-3} Torr avec des rapports de débits massiques R_{N2} variant entre 0 % et 25 %, *i.e.* le ratio $R_{N2} = 100\% \times [N_2] \div ([N_2] + [Ar]) = 0 \rightarrow 25\%$ (dans le but de contrôler l'incorporation d'azote dans les couches minces de TiO_2:N). Le reste des détails techniques de dépôt incluant une description plus détaillée de la méthode de déposition par pulvérisation-magnétron se trouve à l'annexe A.1.

La variation du ratio d'azote-à-argon dans la chambre de dépôt a permis la synthèse de films de TiO_2:N avec une grande plage de dopage allant de 0 at.% à 13 at.%. Les analyses par XPS (voir les figures 1 & 5 dans l'article 1) ont dévoilé que la majorité des dopants d'azote sont à des emplacements substitutionels désirés (*i.e.* $N_O^{\bullet}$). De plus, les analyses d'UV-Vis et d'ellipsométrie spectroscopique ont permis de quantifier l'ampleur de la bande interdite en fonction du contenu d'azote dans les couches de TiO_2:N tel qu'illustré à la figure 5.2(a) (voir aussi figures 6 & 7 de l'article 1). Ces études ont révélé un point optimal de dopage N qui résulte à un rétrécissement de l'E_g de 3.2 eV pour le TiO_2 à 2.2 eV pour le TiO_2:N avec ∼3.5 at.% d'azote.

Ce gain en absorptivité de lumière visible a été mis à l'épreuve et exploité vers la dégradation électrophotocatalytique de la chlortetracycline sous lumière 1.5AM. Tel qu'illustré à la figure 5.2(b), les photoanodes de TiO_2:N ont pu dégrader 98 % (en 2 h du CTC sous lumière visible simulée). Critiquement, on remarque que l'augmentation de la cinétique de dégradation est directement corrélée avec la réduction de l'E_g. En effet, le point de dopage optimal pour la réduction de la bande interdite a aussi prouvé d'être le dopage optimal pour la dégradation du CTC.

Cependant, une analyse de l'augmentation de l'efficacité de dégradation électrophotocatalytique en fonction de la photosensibilisation apportée par le rétrécissement de la bande interdite a dévoilé qu'une grande partie des photocharges sont perdues. Des études subséquentes en tandem avec les résultats rapportés dans la littérature ont dévoilé que le dopage à l'azote était synonyme avec la formation des lacunes d'oxygène (*i.e.* V_O) dans le TiO_2. Ces défauts étaient responsables de la réduction en efficacité des photocharges en agissant comme des centres de recombinaison, réduisant l'efficacité du matériau.

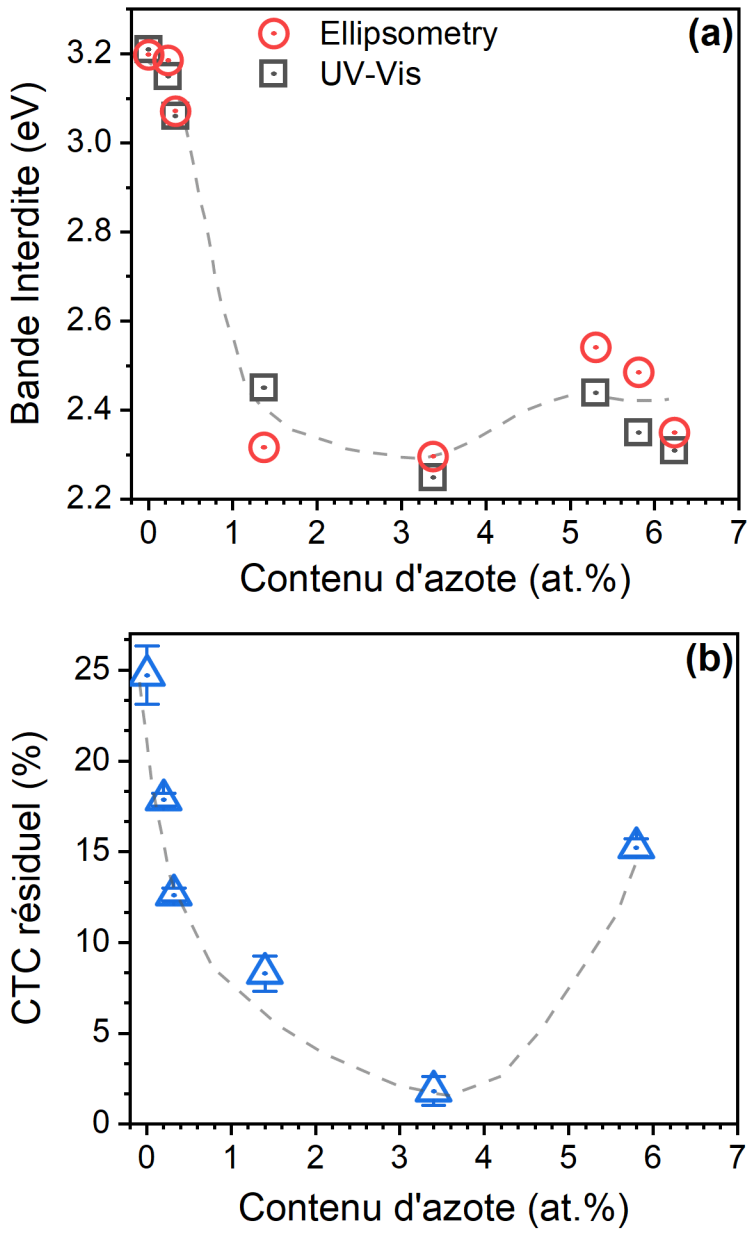

Figure 5.2 – (a) Comparaison des valeurs pour la bande interdite obtenue par Uv-Vis. et par ellipsométrie spectroscopique. (b) Taux de dégradation du CTC en fonction du taux d'incorporation d'azote dans les couches minces de TiO_2:N déposées sur des grilles de Ti. Les lignes grises servent de guide visuel.

Le dopage au tungstène du TiO_2

Dans le but de contourner les limitations présentées par le dopage à l'azote, des couches minces de TiO_2 dopé au tungstène ont été développées et fabriqués. Le tout a été poussé principalement par les résultats théoriques indiquant que l'intégration du tungstène dans la matrice du dioxyde de

titane mènerait à l'augmentation de l'énergie de formation des V_O. À cette fin, la pulvérisation-magnétron RF a été utilisée pour fabriquer des couches minces non-dopés (TiO_2), dopés au V_O (TiO_{2-x}), et dopés au tungstène (TiO_2:W). Les paramètres de dépôt sont présentés dans l'annexe A.1. Critiquement, l'incorporation du W a été assurée par la copulvérisation d'une cible de WO_3 en parallèle à la cible principale de TiO_2. Le contrôle de l'incorporation du tungstène dans le TiO_2 est assuré via l'ajustement de la puissance cathodique appliqué sur la cible d'oxyde de tungstène, *i.e.* W_{power} de $0.10\,W\,cm^{-2}$ à $0.70\,W\,cm^{-2}$.

Les analyses par XPS (voir figure 3 de l'article 3) ont dévoilé que les dopants de tungstène étaient présents sous deux formes substitutionelles: W^{VI} (W''_{Ti}) et W^{IV} ($W^{\times}_{Ti}$). De plus, le dopage total au tungstène pouvait être contrôlé entre 0 at.% et 10 at.%. De plus, ces analyses compositionnelles ont indiqué une harmonisation de la stœchiométrie suite à l'incorporation de W''_{Ti} tel que présenté dans le tableau 1 de l'article 3. Le tout a été renforcé par des observations diélectriques à haute fréquence (voir figure 5.3(a)) qui ont confirmé une concentration optimale du dopant W de ≈2.5 at.%. À ce point de dopage, on observe la plus petite contribution des défauts stœchiométriques V_O (*i.e.* contribution de ϵ_{dipole} provenant des $2\,Ti^{III}{-}V''_O$) au signal diélectrique total ϵ'. On peut voir dans la figure 5.3(b) qu'il y a une réduction de deux ordres de grandeur de la contribution diélectrique provenant des V_O suite pour le dopage optimal de tungstène.

Suite à ces observations du rétablissement de stœchiométrie, les films optimaux de TiO_2:W ont été intégrés en tant que photoanodes pour la dégradation électrophotocatalytique de l'atrazine sous lumière visible. Les constantes cinétiques de dégradation observées ont augmenté de $0.027\,min^{-1}$ pour le TiO_2 non-dopé (et dopé au V_O, TiO_{2-x}) à $0.053\,min^{-1}$ pour le TiO_2:W optimal. Cette augmentation d'efficacité était directement attribuée à la réduction des V_O dans les couches. Ce qui était le plus surprenant est que les photoanodes de TiO_2:W ont démontré des constantes de dégradation presque identiques aux photoanodes de TiO_2:N. Cette observation confirme que l'optimisation des temps de vie des photocharges est d'une importance égale à la photosensibilisation dans le cadre des applications électrophotocatalytiques. L'intérêt est donc de jumeler l'absorption dans le visible du TiO_2:N avec la réduction des V_O associée avec le TiO_2:W.

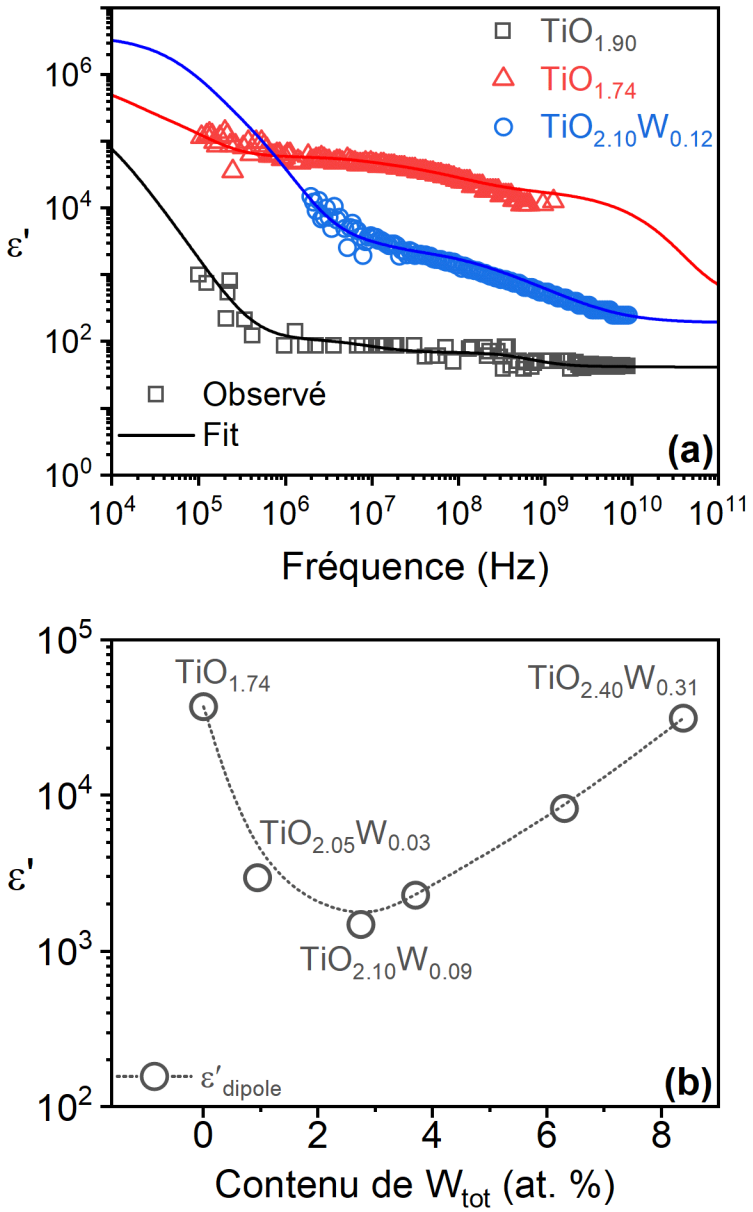

Figure 5.3 – (a) Constance diélectrique réelle ϵ' pour divers configuration de dopage; on remarque la contribution des défauts $\mathbf{V_O}$ (ϵ_{dipole}) dans la zone spectrale entre les MHz et GHz , (b) ϵ_{dipole} en fonction du contenu de tungstène des couches minces de $\mathbf{TiO_2}$:W.

Le codopage du TiO_2

Dans le but de combiner les bienfaits du monodopage à l'azote avec ceux au tungstène guidé par des modèles théoriques, la pulvérisation-magnétron RF a été utilisée pour synthétiser des couches minces de TiO_2:WN *in-situ* codopé. Les paramètres exacts de dépôt sont présentés à l'annexe A.1.

Critiquement, la variation des paramètres R_{N2} et W_{power} ont permis la déposition de couches minces de TiO_2:WN avec une large latitude de chaque dopant. L'objectif du codopage était double: (i) rétrécir la bande interdite du TiO_2:WN via l'introduction des dopants d'azote substitutionels et (ii) passiver les défauts de charge qui mènent à la formation des V_O via l'introduction de tungstène.

Des analyses systématiques des spectres XPS et XRD ont dévoilé que la majorité des dopants de W et N étaient dans des emplacements substitutionels dans la matrice de TiO_2:WN (voir figures 3 et 4 de l'article 6). De plus, le rôle de l'azote dans le rétrécissement de la bande interdite a été explicitement démontré avec les couches minces de TiO_2:N et TiO_2:WN qui ont montré des E_g de 2.3 eV. Critiquement, les études XPS ont indiqué que l'approche de codopage semblait réduire significativement la présence des V_O dans le TiO_2:WN à comparer des couches minces de TiO_2:N similairement dopées. Ce rétablissement stœchiométrique a engendré des améliorations de la structure cristalline et une augmentation des limites de solubilité de chaque dopant. La réduction des V_O engendrée par l'approche de codopage a été directement affirmée via des études diélectriques à haute fréquence. Ces mesures HF-DS ont dévoilé une réduction drastique des dipôles de $2\,Ti^{III}-V_O''$ dans les couches minces de TiO_2:WN à comparer avec des échantillons monodopés à l'azote. Comme illustré dans la figure 5.4(a), cette réduction des défauts s'est directement traduite en augmentation des constantes de temps de vie caractéristiques (τ) des photocharges (sondé par FP-TRMC). L'analyse quantitative de ces constantes de temps de vie a dévoilé trois processus d'extermination de photocharges: le piégeage de charges, la recombinaison des photocharges et les réactions de surface. Les temps de vie caractéristiques des couches minces de TiO_2:WN (*i.e.* 0.08 µs, 0.75 µs, et 11.5 µs, respectivement) ont été démontrés d'être environ trois fois plus longs que ceux du TiO_2:N (*i.e.* 0.03 µs, 0.35 µs, et 6.8 µs). Ces mesures de TRMC ont confirmé quantitativement les bienfaits de la passivation suite au codopage WN du TiO_2.

Dans le but d'exploiter les bienfaits de cette approche, les couches minces de TiO_2:WN (et ceux de TiO_2, TiO_2:N, et TiO_2:W) ont été intégrées en tant que photoanodes pour la dégradation électrophotocatalytique de l'atrazine sous lumière visible. Les résultats obtenus sont présentés dans la figure 5.4(b). Une augmentation significative de la constante de dégradation k a été observée pour les photoanodes de TiO_2:WN ($k = 0.106\,min^{-1}$) en comparaison des photoanodes de TiO_2 et TiO_{2-x} ($k = 0.026\,min^{-1}$ pour les deux). Critiquement, les photoanodes de TiO_2:WN ont dégradé le polluant environ deux fois plus rapidement que les photoanodes de TiO_2:W ($k = 0.057\,min^{-1}$) et TiO_2:N ($k = 0.047\,min^{-1}$). Cette augmentation significative des caractéristiques électrophoto-

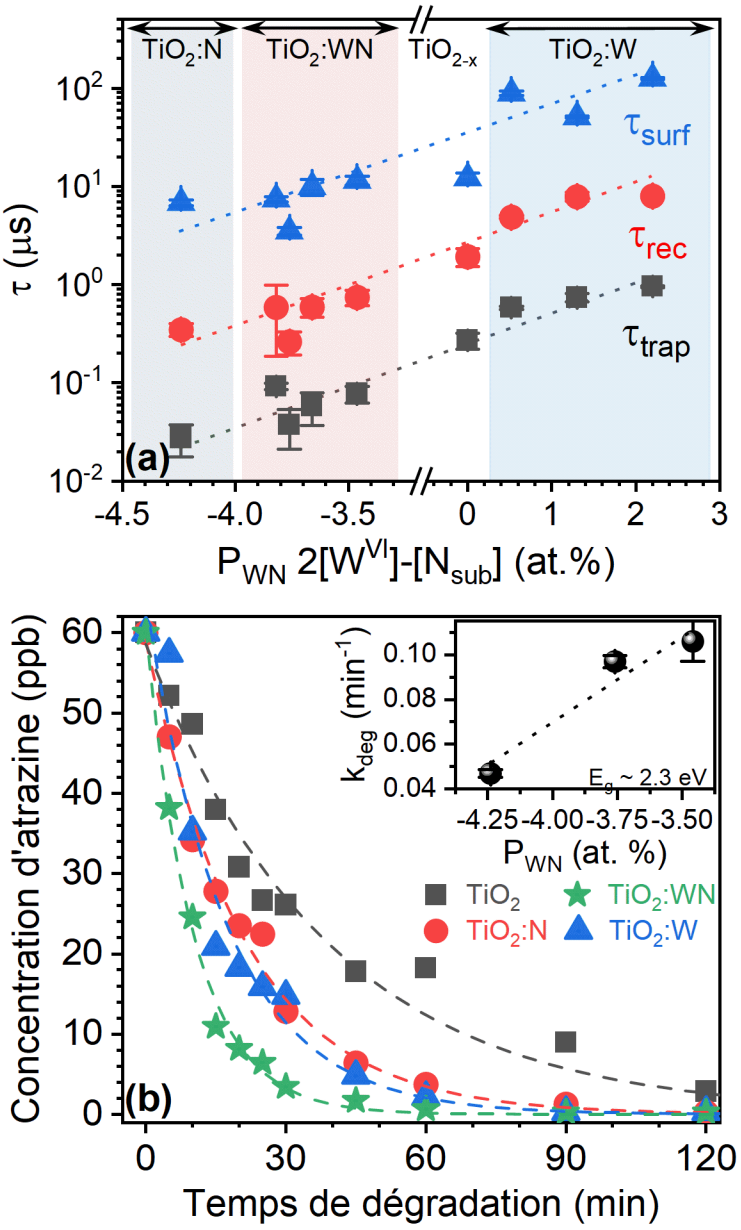

Figure 5.4 – (a) Variation des temps de vie caractéristiques des photocharges en fonction du paramètre de passivation P_{WN}. (b) Performances électrophotocatalytiques des meilleures photoanodes de TiO_{2-x} (performance identique à TiO_2), TiO_2:N, TiO_2:W et TiO_2:WN sous lumière visible simulé de 1.5AM. L'encart montre les constantes de dégradation pour des photoanodes à E_g identique (*i.e.* de 2.3 eV) en fonction du paramètre de passivation.

catalytiques a été directement attribuée à l'augmentation des temps de vie des photocharges tout en gardant la photosensibilité à la lumière visible. L'encart de la figure 5.4(b) souligne l'effet de la passivation (et par extension de la réduction des V_O) sur les performances électrophotocatalytiques du TiO_2:WN à E_g fixe.

5.3 Conclusion

Nous avons réussi à élaborer des couches minces de TiO_2:WN dopés in-situ à l'azote et au tungstène avec la technique de pulvérisation-magnétron RF. Le procédé que nous avons développé permet d'obtenir des films de TiO_2:WN (et de TiO_2, TiO_{2-x}, TiO_2:N, TiO_2:W) d'excellente qualité, de façon contrôlable et reproductible. Les diverses analyses ont clairement montré des structures denses de nature anatase tout en ayant une bande interdite réduite au spectre visible solaire, *i.e.* 2.3 eV. De plus, le codopage a permis de minimiser la présence des V_O augmentant ainsi les temps de vie des photocharges. Ces améliorations se sont traduit par une augmentation (quatre fois plus) des performances électrophotocatalytiques des photoanodes de type TiO_2:WN comparées aux photoanodes non dopées de TiO_2.

Suite à ces résultats, on peut confirmer que les objectifs de cette thèse doctorale ont été atteints. Spécifiquement, les objectifs suivants ont été accomplis:

(i) On a mis en place un procédé de déposition par pulvérisation magnétron à radiofréquence pour la synthèse des films in−situ dopés à l'azote, le tungstène et codopés tungstène-azote. Les films contenant de l'azote étaient tous photosensibilité au spectre visible solaire. Ce travail a démontré que les films TiO_2:WN sont les plus appropriés pour les applications électrophotocatalytiques sous lumière visible.

(ii) On a pu souligner et établir des corrélations fondamentales entre les dopants et les diverses propriétés des couches minces de TiO_2 déposées par pulvérisation-magnétron. Ceci nous a permis d'optimiser davantage la photoactivité sous lumière visible des photoanodes en question.

(iii) Les caractérisations clés des couches minces de TiO_2:N, TiO_2:W et TiO_2:WN ont été corrélées avec leurs performances électrophotocatalytiques dans la dégradation de polluants réels tels l'atrazine et la chlortetracycline. Les aspects électrophotocatalytiques de ce travail de thèse ont été accomplis en collaboration avec le groupe du Prof. Drogui de l'INRS-ETE.

Part III

Appendices and References

Appendices

Appendix A

Experimental methods

A.1 RF-magnetron sputtering

The principles governing sputter deposition were first practically demonstrated in the 19th century, and were used for the fabrication of mirrors[205]. However, modern sputtering traces it's origins back to the 1970s where is was first applied and continues to be a deposition method of choice for the fabrication of microelectronic/optoelectronic devices and thin films[206, 207, 14, 36].

As the name implies, the method involves ejecting material (*i.e.* sputtering) from a target (source of material to deposit) onto a substrate of choice. The most rudimentary of such methods is cathodic sputtering which involved the formation of an atomic plasma in a vacuum chamber between a negative potential cathode (sputtering target at $\approx -500\,\mathrm{V}$) and an anode (typically a grounded component nearby). A small amount of inert sputtering gas (*e.g.* Ar) is injected into the chamber, which, when near the cathode surface is ionized and accelerated towards it. This results in a continuous ionic bombardment, ensuring a constant ejecting flux of atoms from the target. Efficient momentum transfer is ensured when the sputtering gas is of similar atomic weight to that of the target atoms. In the case of poly-atomic targets, one can therefore expect varying sputtering yields for each atomic species involved.

Most often however, sputtering sources are coupled with a magnetron that applies a strong electromagnetic field as to confine and accelerate the charged plasma atoms near the target's surface. In this electromagnetic field, charged particles follow helical magnetic field lines as seen in figure

A.1. This increases ionizing collisions with the sputtering gas, increasing the yield considerably (ten-fold increase is typical) and allowing the plasma to be maintained at very low pressures (*e.g.* 1×10^{-3} Torr). Magnetron sputtering targets are therefore typically marked with a depleted ring erosion profile at their surface due to the sputtering plasma shape as can be seen in figure A.2 (also seen in figure A.1 and titled the "erosion trench"). Critically, the sputtered atoms are neutral (only around 1% are ionized), and therefore are mostly unaffected by this electromagnetic trap. These sputtered atoms can have a wide energy distributions, from ≈0 eV to ≈10 eV. The entire range of post sputtering impacts, ranging from ballistic to low-energy diffusion-like motion is varied by changing the ambient sputtering gas pressure[14, 36].

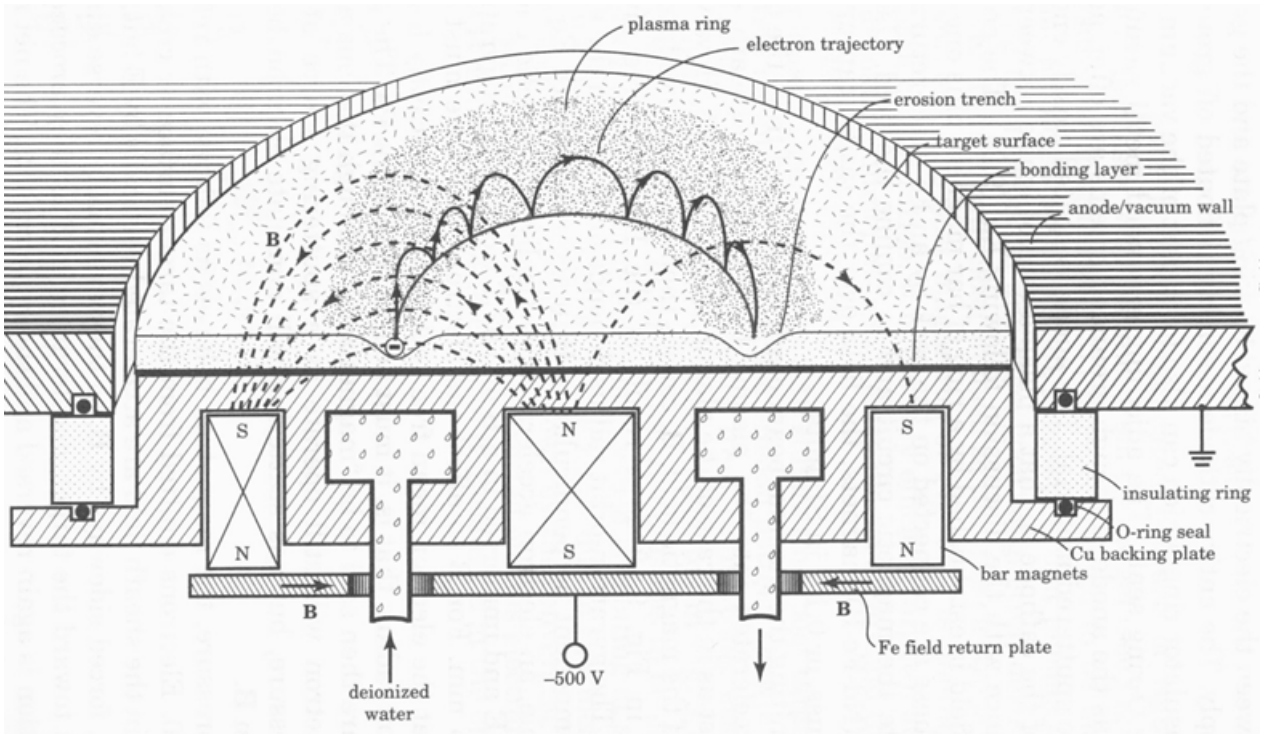

Figure A.1 – Cross-sectional view of a magnetron sputtering gun. Adapted from D.L.Smith, "Thin-Film Deposition: Principles Practice", McGrawHill (1995), ISBN 0-07-058502-4[14].

To the neutral sputtering gas, a controlled amount of a reactive gas can be added. This gas can then react with the atomic species within the plasma, forming desired compounds. These can be formed in-flight, on the substrate, or on the target (or a combination of these locations). Typically, by controlling the relative mass flow ratios of the reactive gas to the sputtering gas, one can control the deposited film stoichiometry regarding the reactive gas atomic species.

Figure A.2 – View of a toroidal plasma plume produced by a running magnetron-sputtering gun in a vacuum chamber. Adapted from Wikimedia Commons (following CC BY-SA 3.0).

DC current magnetron set-ups depend on a high electric flux being able to pass through the cathode, limiting this method to conductive sputtering targets. In order to avoid damaging charge build-up on, and generalize the technique to insulating targets an RF (radio frequency) sputtering scheme is used. This approach relies on the sign (direction) of the anode-cathode bias to oscillate at a high rate, with the industry standard being 13.56 MHz. Given that the electrons have significantly higher mobility than the ions involved, the RF discharge allows for significantly reduced surface charge buildup, while maintaining an effective negatively charged cathode.

Most modern systems also allows the application of a RF bias to the sputter holder, allowing for further control. Locally, this can behave as a cathode, attracting Ar^+ ions which in-turn bombard the substrate surface during deposition. This bombardment can displace loosely bonded atoms, increasing their surface mobility, and therefore the film density. If the applied sputtering power to the substrate is increased, it can behave as a secondary source, typically used to etch-clean the substrate pre-deposition.

Naturally, such intricate impedance matching networks and RF capable power supplies tend to greatly increase the technical and economic costs of such setups. These costs are often burdened for the advantages that RF-MS provides as compared to other deposition methods [14, 36]:

(i) High sputtered atom energy which is crucial for the condensation of smooth and dense thin films.

(ii) Impurity free deposition with a high level of compositional control making the technique suitable for ultrahigh-vacuum applications.

(iii) High melting point materials can be easily sputtered (*e.g.* W).

(iv) With optimization, sputter deposited films have a relatively close composition to that of the source material. Any difference is due to different elements diffusing differently due to varying masses in a constant sputtering gas environment (see A.1).

(v) Good substrate adhesion and step coverage.

(vi) No hot parts, allowing compatibility with oxidizing reactive gases as most deposition critical components are water cooled. Substrates can however vary in temperature if this is desired.

(vii) Sputtering process is iso-directional, allowing for design flexibility (top-down, bottom-up, and sideways)

(viii) Compatible with epitaxial growth processes.

However, no technique is perfect, and the sputtering process comes with some key disadvantages that need to be considered [14, 36]:

(i) Incompatible with lift-off procedures due to diffusion like behavior of deposited atoms.

(ii) Layer-by-layer growth is difficult.

(iii) Target poisoning possible, experimental caution needs to be taken to prevent/remedy this.

(iv) Reactor "memory" needs to be taken into account.

(v) If uncompensated for, preferential sputtering effects can lead to non-stoichiometric deposition. This happens because of two major effects: (i) sputtering effective cross-sections vary between atomic species and binding energy strength leading to uneven sputtering of poly-atomic targets, and (ii) sputter ejected atomic species have different mean free paths (effective collisions with ambient gas), leading to uneven rates of effective condensation (this is exacerbated by the chemical reactivity of some atoms during their displacement form the target to the substrate).

A critical 1974 Thornton study applied the structure zone model (an extension of a Movchan & Demchishin model previously proposed) to describe the sputter deposited thin film morphologies as shown in figure A.3[15]. Thornton introduced the structure zone T, at low argon pressures, characterized by dense and fibrous grains. Most of the depositions in this work were performed in this zone. Critically, this revealed that both the deposition pressure P and substrate temperature T were paramount in describing any sputtering process. This is mainly due to the fact that pressure governs the mean free path and energy distribution followed of sputtered species and by extension, the deposited thin film morphology.

The many parameters that control sputter deposition make it a complex process, but also allow for an unparalleled control over the thin film growth. This doctoral project required precise, contaminant free, flexible, and consistent deposition process. Naturally, magnetron sputtering became the synthesis method of choice. Figure A.4 shows a schematic of the RF-MS system used for the deposition of TiO_2:WN thin film studied in this thesis work. While up to three sputtering targets can be simultaneously used, for our purposes, two were sufficient.

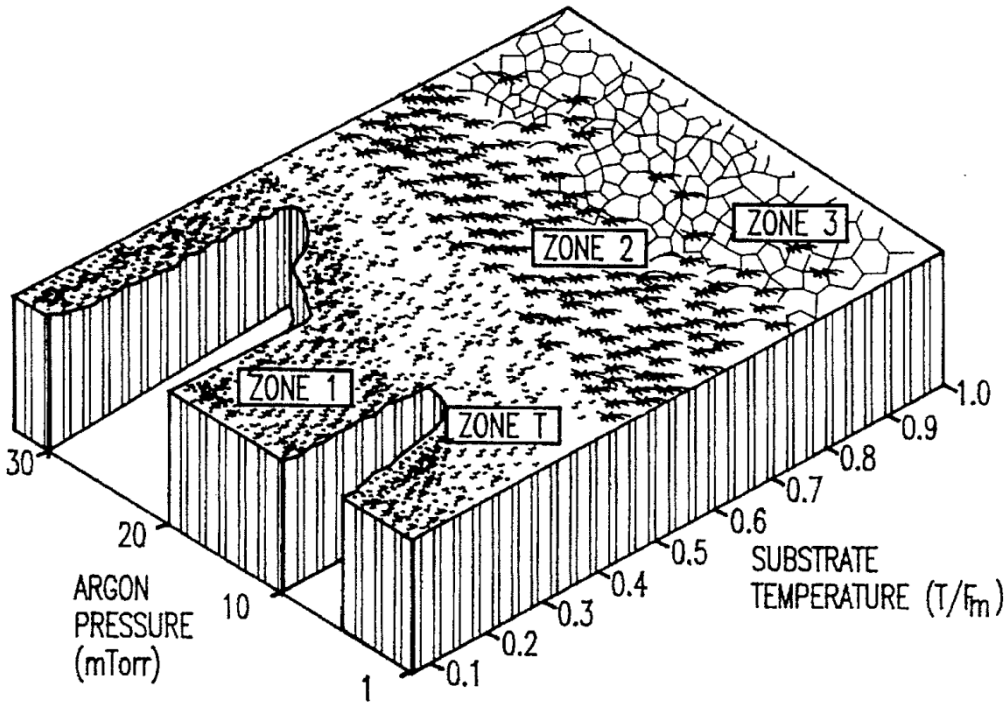

Figure A.3 – Thornton zone model at a function of two critical sputtering parameters: T the substrate temperature (divided by melting point F_m) and P the deposition pressure in mTorr. We can note the zone T which is characteristic of dense and fibrous grains in the sputter deposited films[15].

Typically, all the thin films were sputter-deposited from a 7.62 cm diameter TiO_2 target (99.99% purity) with a constant power density of $5.5\,W\,cm^{-2}$ applied to the target. The chamber was cryo-pumped to a base pressure of 2×10^{-8} Torr prior to deposition. Thereafter, high purity Ar (99.999%) was introduced in the chamber with the gas flow rates monitored as to maintain a constant pressure of 1.45 mTorr during the sputter-deposition process. Nitrogen and tungsten incorporations were accomplished by injecting N_2 gas (99.995%) into the chamber and by concomitant 7.62 cm diameter WO_3 target (99.95% purity) sputtering, respectively. The N incorporation in the TiO_2:WN films was controlled by adjusting the relative nitrogen mass flow rate ratio R_{N2} (*i.e.* $100\% \times [N_2] \div ([N_2] + [Ar])$ between 0 and 20%. The W incorporation was controlled by varying the WO_3 target power density (W_{power}) from $0.1\,W\,cm^{-2}$ to $0.7\,W\,cm^{-2}$. The TiO_2:WN films could be concomitantly deposited onto silicon, quartz, Ti, and ITO substrates. These were mounted on a rotating substrate holder located off-axis at a distance of 20 cm from the sputtering target and heated during deposition by a quartz lamp heater to an on-substrate temperature of ≈470 °C. Prior to film deposition, the substrates and targets were systematically sputter-cleaned with Ar ions for 15 min with the

shutters closed. No post acceleration bias was applied to the substrates during the sputtering process. However, a built-in plasma sheath bias of around $-15\,\mathrm{V}$ was detected. The thickness of the TiO_2:WN films could be *in-situ* monitored by means of a calibrated quartz-crystal micro-balance. In some situations, the base power of the TiO_2 sputtering power was increased as to allow for better ocntrol of W incorporation. This was critical when trying to deposit thin films from a metallic W target, as it's sputter rates were much higher than the oxide target. Such technical details are presented in the main text whenever they become relevant.

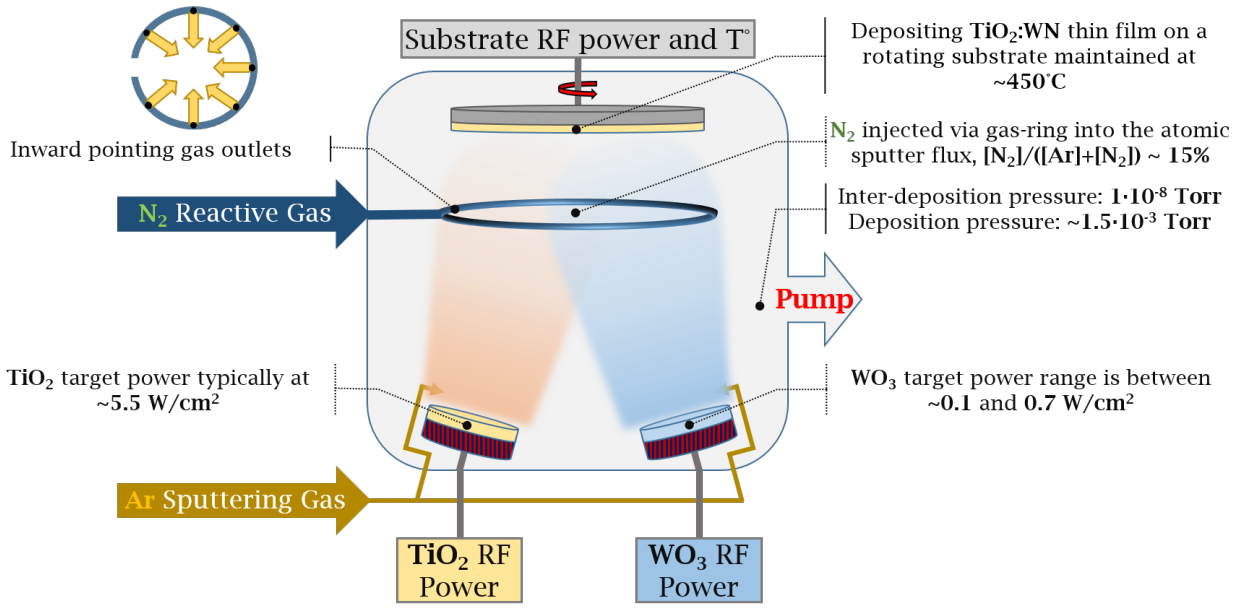

Figure A.4 – Schematic representation of the RF-MS (13.56 MHz) sputtering system used for most depositions in this thesis work. Typical codoping deposition parameters are presented. Specifically, the system used is an MS-13 RF-Magnetron Sputtering system from the Kurt. J. Lesker Company.

A.2 Characterization methods

A.2.1 Photoelectron spectroscopy

X-ray photoelectron spectroscopy

X-ray photoelectron spectroscopy (XPS), also known as electron spectroscopy for chemical analysis (ESCA) is a surface sensitive spectroscopy technique used to measure the elemental composition (and chemical states) of elements within a material. It is based on the photoelectric effect first

explained by Einstein in 1905, and experimentally first demonstrated by Innes around 2 years later. This foundation was improved upon by several groups thereafter, culminating in Siegbahn receiving a Nobel Prize for Physics in 1981 to acknowledge his extensive efforts to develop XPS into what had become a useful analytical tool.

XPS binding energy (BE) spectra is obtained by irradiating a material with an X-ray beam while collecting the ejected electrons (minus the apparatus extraction work function θ) and their kinetic energy (KE) resulting from the photoelectric as such:

$$BE = h\nu - (KE + \theta) \tag{A.1}$$

Typically, $Al_{K\alpha}$ X-rays are used ($h\nu = 1486.7\,\text{eV}$), resulting in a characteristic penetration depth of about 0 nm to 10 nm (*i.e.* $\approx 3 \cdot \lambda$). Ideally, measurements are performed in high vacuum conditions as to minimize X-ray and electron collisions with ambient molecules *i.e.* anywhere between 1×10^{-10} Torr to 1×10^{-8} Torr.

For analysis purposes, the electron counts (Y-axis) are plotted *vs* the BE values (X-axis), stemming from the fact that each element has characteristic orbital BE signatures. These peaks correspond to the various electron configurations the atomic orbitals. Critically, the relative number of detected electrons in each configuration is directly related (via their relative X-ray sensitivity factors (RSF)) to the proportion of said element within the XPS sampling volume (except for H).

In our experiments, high resolution binding energy O_{1s}, Ti_{2p}, N_{1s}, W_{4d}, and W_{4f} core level spectra were collected by using the ESCALAB 220i-XL spectrophotometer (Thermo VG Scientific Ltd., UK), equipped with a monochromatized $Al_{K\alpha}$ (1486.6 eV) twin-anode source after a systematic *in-situ* surface cleaning by means of 5 keV Ar^+ ion sputtering gun with an average 0.15 mA current. Given the overlapped nature of the tungsten spectra, both the W_{4f} and W_{4d} binding energy windows were used to ensure appropriate quantification. Also, the Ar_{2p} energy window is superimposed with the W_{4d} BE window. The collected spectra were fitted using the CasaXPS software (ver. 2.3.15). A Shirley background was approximated on all spectra. Surface charge effects were controlled for by verifying the location of the pre-sputter cleaned C_{1s} peak (C−C bond at 284.8 eV. Typically, this shift was in the 0.6 eV to 3.0 eV range, increasing with a decrease in sample surface conductivity. All atomic species were fitted using fixed intrinsic properties such as peak shape, and the doublet

area/separation relationships taken from the NIST Standard Reference Database 20, Version 4.1. Atomic concentrations were quantified via relative peak areas with corresponding RSF taken from the NIST database. Thin films deposited on quartz substrates were preferentially measured, in case of doubt, those deposited on Si(001) were used. Figure A.5 shows the raw fitting results from a typical WN-codoped sample, with table A.1 detailing the fit parameters for all elemental orbitals considered.

Peak	Position $\pm\delta$ (eV)	FWHM (eV)	Area Constraint	R.S.F.
$Ti^{IV}_{2p\ 3/2}$	458.6 ± 0.1	$0.8 - 2.0$	-	5.22
$Ti^{IV}_{2p\ 1/2}$	$Ti^{IV}_{2p\ 3/2} + 5.6$	$0.8 - 3.0$	$Ti^{IV}_{2p3/2} \cdot \frac{1}{2}$	0
$Ti^{III}_{2p\ 3/2}$	456.9 ± 0.1	$0.8 - 2.0$	-	5.22
$Ti^{III}_{2p\ 1/2}$	$Ti^{III}_{2p\ 3/2} + 5.6$	$0.8 - 3.0$	$Ti^{III}_{2p\ 3/2} \cdot \frac{1}{2}$	0
$Ti^{II}_{2p\ 3/2}$	455.0 ± 0.3	$0.8 - 2.0$	-	5.22
$Ti^{II}_{2p\ 1/2}$	$Ti^{II}_{2p\ 3/2} + 5.6$	$0.8 - 3.0$	$Ti^{II}_{2p\ 3/2} \cdot \frac{1}{2}$	0
N^{sub}_{1s}	396.2 ± 0.2	$0.8 - 2.0$	-	1.80
N^{int}_{1s}	397.2 ± 0.2	$0.8 - 2.0$	-	1.80
$W_{4d\ 5/2}$	246.4 ± 0.5	$5.0 - 6.0$	-	9.65
$W_{4d\ 3/2}$	$W_{4d\ 5/2} + 12.4$	$5.0 - 6.0$	$W_{4d\ 5/2} \cdot \frac{2}{3}$	0
$Ar_{2p\ 3/2}$	241.1 ± 0.2	$0.8 - 2.0$	-	2.01
$Ar_{2p\ 1/2}$	$Ar_{2p\ 3/2} + 2.05$	$0.8 - 3.0$	$Ar_{2p\ 3/2} \cdot \frac{1}{2}$	0
$W^{VI}_{4f\ 7/2}$	34.9 ± 0.2	$0.8 - 2.0$	-	5.48
$W^{VI}_{4f\ 5/2}$	$W^{VI}_{4f\ 7/2} + 2.2$	$W^{VI}_{4f\ 7/2} \cdot 1$	$W_{4d\ 5/2} \cdot \frac{3}{4}$	0
$W^{IV}_{4f\ 7/2}$	33.1 ± 0.2	$0.8 - 2.0$	-	5.48
$W^{IV}_{4f\ 5/2}$	$W^{IV}_{4f\ 7/2} + 2.2$	$W^{IV}_{4f\ 7/2} \cdot 1$	$W_{4d\ 5/2} \cdot \frac{3}{4}$	0
Ti^{IV}_{3p}	37.2 ± 0.4	$1.0 - 2.5$	-	0.81
Ti^{III}_{3p}	$Ti^{IV}_{3p} - 1.2$	$1.0 - 2.5$	-	0.81
Ti^{II}_{3p}	$Ti^{IV}_{3p} - 2.4$	$1.0 - 2.5$	-	0.81
$O^{Ti(IV)}_{1s}$	529.9 ± 0.2	$0.8 - 2.0$	-	2.93
$O^{Ti(III)}_{1s}$	$O^{Ti(IV)} + 0.5$	$0.8 - 2.0$	-	2.93
$O^{Ti(II)}_{1s}$	$O^{Ti(III)} + 0.5$	$0.8 - 2.0$	-	2.93
O^{def}_{1s}	530.8 ± 0.5	$1.0 - 3.0$	-	2.93

Table A.1 – Fitting parameters used for analysis of XPS spectra.

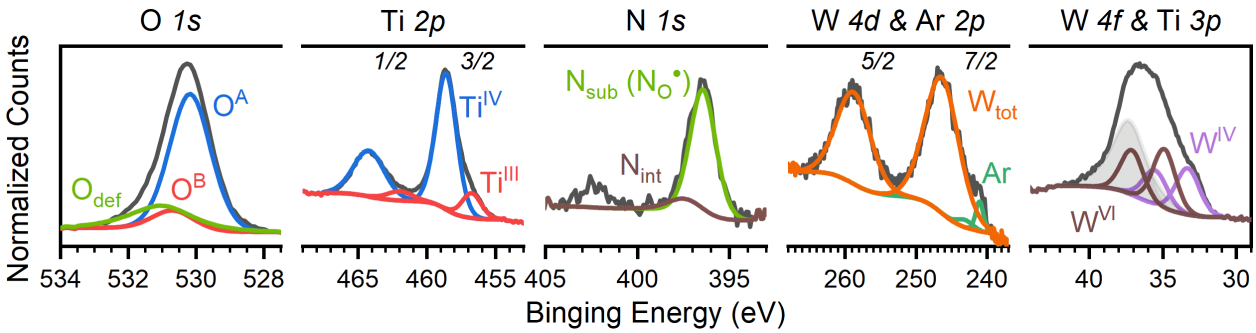

Figure A.5 – O_{1s}, Ti_{2p}, N_{1s}, W_{4d}, and W_{4f} core level spectra from left-to-right for the TiO_2:WN (R_{N2} = 13 % & WO_3 target W_{power} = 0.26 W cm^{-2}) type films. The Ti_{3p} species are grayed out when there is overlap with W_{4f} signatures as to ease visibility.

Ultraviolet and valence-band photoelectron spectroscopy

In parallel with Siegbahn's work on XPS, David Turner in the UK developed ultraviolet photoelectron spectroscopy (UPS). UPS operates on the same principles as XPS, the only difference being that ionising radiation with energies in the 10 eV range are used, typically produced by He gas lamps (*e.g.* 21.2 eV for He_I, and 40.8 eV for He_{II}). This low energy of UPS probing photons made most core level photo-emission inaccessible, limiting this technique to valence band acquisition and electronic work function (Φ) measurement. While the combination of both XPS and UPS to investigate this spectral region might seem redundant, it is in fact complementary. The orbital ionization cross section is strongly dependent on incident radiation energy, allowing for different electronic transitions and states to have better resolutions under varying incident photon energies.

The electronic work function (Φ) is defined as the difference between E_F and the vacuum level (E_{VAC}) measured as the cutoff at the low kinetic energy end of the spectrum while substracting from the incident photon energy:

$$\Phi(\text{eV}) = h\nu - (E_{VAC} - E_F) \tag{A.2}$$

Typically a small bias (3 V) is applied as to counteract the measurement apparatus work function. Finally, these measurements are extremely sensitive to surface properties such as contaminants, much care must be attributed in order to compare varying samples on equal grounds. For our purposes, photoemission studies were performed with an ESCALAB 220iXL spectrophotometer (Thermo VG Scientific Ltd., UK) with at base pressure of 1.5×10^{-9} Torr using the He_I line at

($h\nu = 21.2\,\text{eV}$) as the excitation source in normal emission with a resolution of 0.06 eV. The E_F position was calibrated using an Au reference with a known $\Phi = 5.0\,\text{eV}$ (with an applied $-3\,\text{V}$ bias as to offset the intrinsic detector work function barrier of 3 eV). An Ar ion gun was used to surface clean all samples at an ion energy of 3 keV for 200 s (optimized as to be barely sufficient in removing the surface carbonaceous contaminants). Figure A.6 shows typical acquired UPS spectra per doping type with the key parameters of interest. For comparison, a figure showing the XPS derived VB spectra and deconvolution can be found in article 2, figure 4.

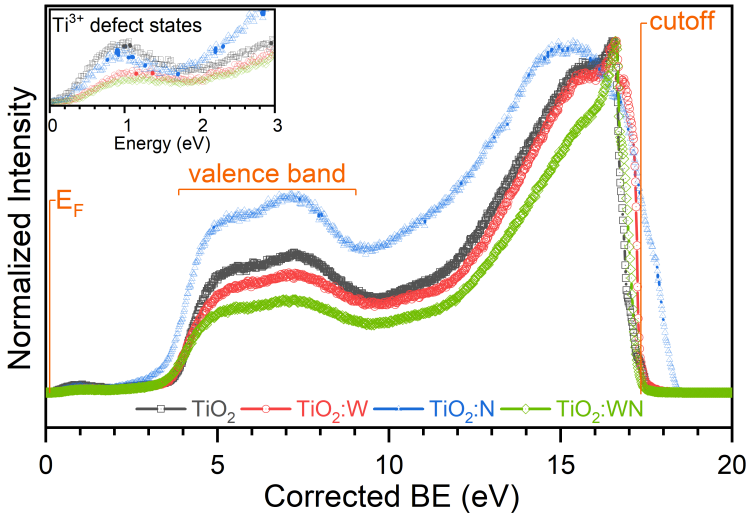

Figure A.6 – Typical UPS spectra of the TiO_2, TiO_2:W (2.3 at.% of W), TiO_2:N (5.7 at.% of N), and TiO_2:WN (1.6 at.% of W & 7.2 at.% of N) prepared with a metallic co-sputtering W target. Inset shows zoom at low energy region depicting the Ti^{III} defect states (*i.e.* V_O).

A.2.2 UV-Visible spectroscopy

Ultraviolet-visible spectroscopy (UV-Vis) refers to absorption or reflectance spectroscopies using the UV or visible spectral regions. A spectrophotometer is used to measure these spectra using a light source, a diffraction grating (in a monochromator or a prism as to separate the different wavelengths of light), and a detector. The detector, measures the intensity of light passing through a sample $I^t(\omega)$ as a function of wavelength, and compares it to the initial light intensity $I_0^t(\omega)$. This $I^t(\omega)/I_0^t(\omega)$ ratio is called the transmittance T (sometimes expressed as the absorbance $A = -\log(T)$). With the help of an integration sphere, the spectrophotometer can also be configured to measure the reflectance spectra. In these cases, a scan of the reflected light $I^r(\omega)$ intensity is measured from the sample and compared to the intensity of light reflected from a ≈100 % reflective calibration material

$I_0^r(\omega)$ *i.e.* $R = I^r(\omega)/I_0^r(\omega)$. While perfectly flat samples can be measured without the use of an integration sphere, surface scattering and roughness effects make it preferable to use an integration sphere which captures both the direct and diffuse reflectance components. For our purposes the UV-Vis spectra were collected using an Agilent (Varian Cary) 5000 UV-vis-NIR spectrophotometer in the 250 nm to 1800 nm range. Figure A.7 shows typical collected T and R UV-Vis spectra.

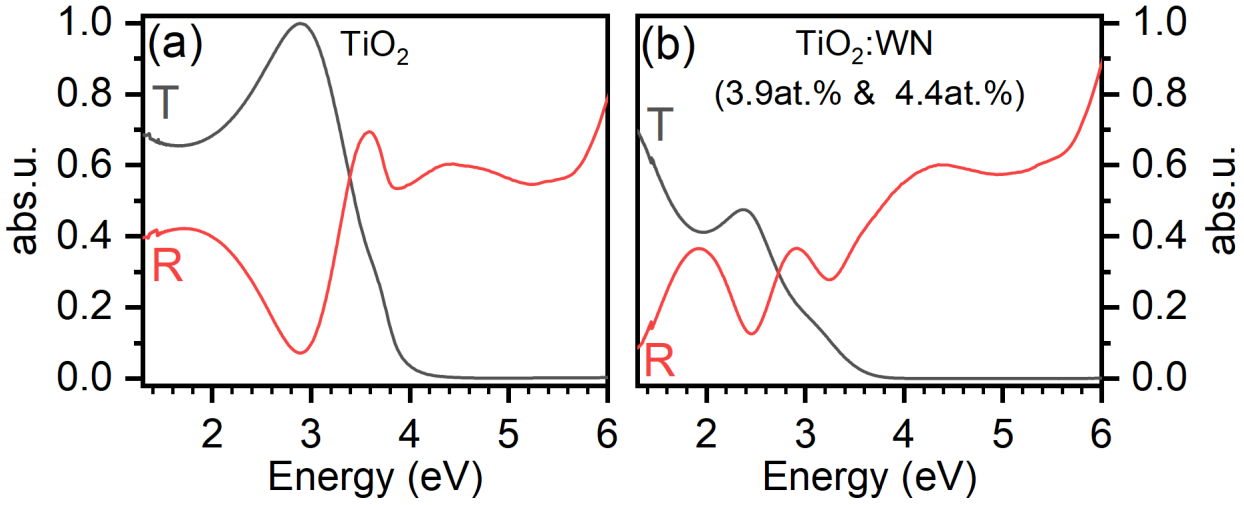

Figure A.7 – Typical R & T UV-Vis spectra for the TiO_2 (a), and TiO_2:WN (b) (3.9 at.% of W & 4.4 at.% of N) prepared with an oxide co-sputtering WO_3 target.

While these spectra provide a slew of information about our thin films such as the absorption edge, and film thickness (from the inter-fringe spacing), Tauc analysis was used to extract quantified values for the optical E_g of the material. These were obtained by extrapolating the linear region of the Tauc plot for indirect E_g transitions to the intersection with the horizontal x-axis:

$$(\alpha \cdot h \cdot \nu)^{\frac{1}{r}} = h\nu \tag{A.3}$$

In equation A.3, r represents the optical transition nature ($r = 2$ for indirect allowed transitions), h the Planck constant, and α the absorption coefficient of the material. The absorption coefficient α can be obtained from the UV-Vis spectra near the absorption edge using relationship A.4 (film thicknesses obtained from direct SEM observations).

$$\alpha = \frac{1}{thickness} \ln\left(\frac{2 \cdot (1 - R)}{T}\right) \tag{A.4}$$

The resulting plot has a distinct linear regime which denotes the onset of absorption. Thus, extrapolating this linear region to the abscissa yields the energy of the optical band gap of the material as shown in figure A.8 for our sputter-deposited TiO_2 thin films.

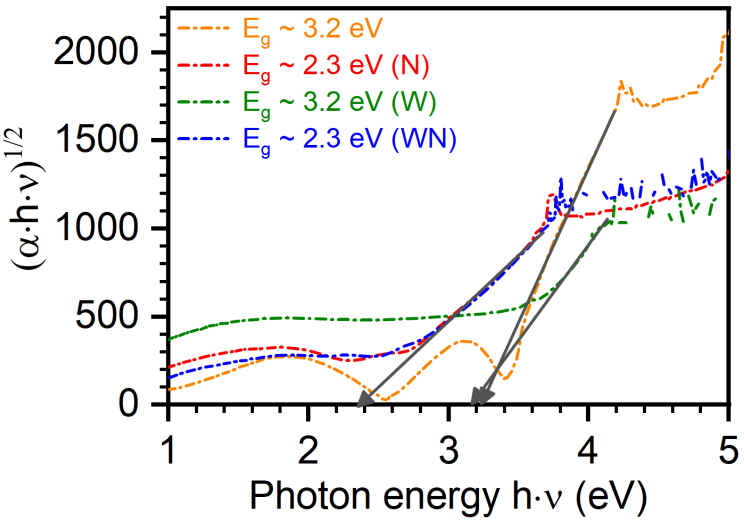

Figure A.8 – Typical Tauc plots for TiO_2, TiO_2:N, TiO_2:W, and TiO_2:WN thin films prepared with a metallic co-sputtering W target.

A.2.3 Spectroscopic ellipsometry

Parallel to the UV-Vis characterizations, spectroscopic ellipsometry (SE) measurements were also performed in order to alternatively discern the thin-films' E_g as a function of dopant loading. Ellipsometry is an optical technique that measures the change of polarization (elliptical polarization, hence the name) upon reflection or transmission of a sample and compares said changes to those predicted by a material model. The spectroscopic part stems from the wavelength dependent nature of the approach. Given that SE exploits the phase information, it can achieve sub-nm resolution and is therefore perfectly suited for thin-film science. SE models typically assume the sample is composed of well-defined homogeneous and isotropic layers (advanced effective medium models can be used otherwise) while accounting for composition, roughness, thickness, crystalline nature, dielectric properties, etc. Because SE measures the relative ratio of the two polarization components, it is very robust, as it does not require a reference signal.

Technically, SE measures the complex reflectance ratio ρ, described by the amplitude component Ψ ($\tan\Psi$ is teh amplitude ratio upon reflection) and the observed phase difference Δ. This can also be expressed from the reflected amplitudes r_s (reflection in the s polarization direction) and

r_p (reflection in the p polarization direction) after normalization to their initial value. These are measured at their Brewster angle of incidence as to maximize the difference between these s & p components:

$$\rho = \frac{r_p}{r_s} = \tan(\Psi)e^{i\Delta} \tag{A.5}$$

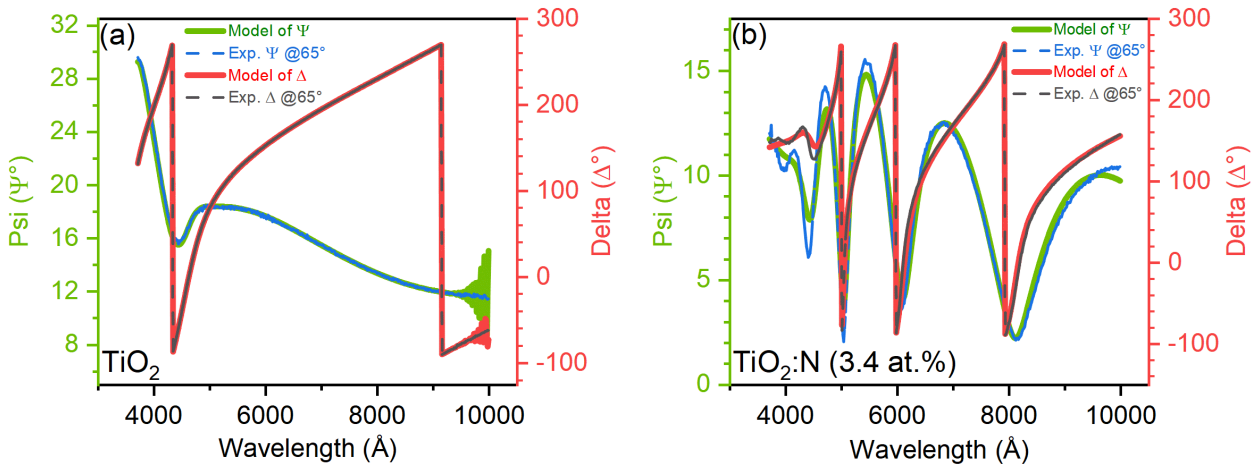

Figure A.9 – Typical SE Ψ & Δ fit plots for TiO_2 (a), and TiO_2:N (b) (3.4 at.%) thin films.

Real-material parameters are extracted by matching a material model on the collected data. This is typically accomplished via an iterative procedure (least-squares minimization) for unknown optical model parameters with the Ψ and Δ parameters calculated using the Fresnel equations.

For our purposes, the SE spectra were acquired using a J.A. Woollam M-2000 ellipsometer from 350 nm to 1000 nm at 65 ° incidence with ≈10 Å spectral resolution. The experimentally acquired SE spectra were analyzed using a composite model with three main components: (i) a Tauc-Lorentz (TL) contribution (see equation A.6 with C being the broadening factor, A the Tauc coefficient times the peak strength, and E_0 being the peak central energy), (ii) a Cody-Lorentz (CL) dispersion contribution (see equation A.7 with E_t the Urbach tail start energy, E_p the Cody/Lorentz model weighting factor, E_μ the Urbach tail decrease rate, and A_L the Lorentz oscillator strength), and

(iii) a Drude free-carriers contribution (see equation A.8 where Γ is the charge collision frequency in eV).

$$\epsilon''(h\omega) = \frac{A \cdot E_0 \cdot C\,(h\omega - E_g)^2}{h\omega \cdot \left((h\omega)^2 - E_0^2\right)^2 + C^2 \cdot (h\omega)^2} \text{ for } h\omega > E_g \tag{A.6}$$

$$\epsilon''(h\omega) = \frac{(E_t - E_g)^2 \cdot A_L \cdot E_0 \cdot C \cdot E_t^2}{\left((E_t - E_g)^2 + E_p^2\right) \cdot h\omega \cdot \left(E_t^2 - E_0^2\right)^2 + C^2 \cdot E_t^2} \exp\left(\frac{h\omega - E_g}{E_\mu}\right) \text{ for } 0 < h\omega \leq E_g \tag{A.7}$$

$$\epsilon''(\omega) = \frac{\omega_p^2 \cdot \Gamma}{\omega \cdot (\omega^2 + \Gamma^2)} \text{ where } \omega_p = \sqrt{\frac{N \cdot e^2}{m \cdot \epsilon_0}} \tag{A.8}$$

This model takes into account the TL dispersion in determining the imaginary dielectric function ϵ'' for all energies above the E_g. This TL dispersion, however, has restricts the ϵ'' to 0 above the band edge. This is compensated for by the CL component used to describe ϵ'' above E_g by parameterizing the transition energies in the transparent and inter-band regions. Both models derive the real dielectric function ϵ' from the Kramers-Kronig relations (shown in equation A.9) and have an explicit expression for the E_g as part of their formalism (transition region between the two in their complex component).

$$\epsilon'(\omega) = \frac{-2\omega}{\pi} \int_0^\infty \frac{\omega' \cdot \epsilon''(\omega')}{\omega'^2 - \omega^2}\, d\omega' \tag{A.9}$$

Finally, to account for the increase in free charge carriers brought on by the N-doping and intrinsic deficiencies, a Drude free-carrier contribution was added to the total dielectric function. The material layer described by the above-mentioned composite model was completed by imposing a surface roughness component (accounting for light scattering). Typically, the roughness values obtained for the best fits were in the 2 nm to 5 nm range, in agreement with SEM observations. Figure A.9 shows typical satisfactory fits for the TiO_2 and TiO_2:N (3.4 at.%) thin films. From figure A.9 (b), we can note a slight mismatch between the experimental and modeled spectra in teh oscillation amplitudes for the high energy part. This is attributed to the heavy doping of the semi-conducting films. While the Drude free-carrier model is accurate in the 1.5 eV to 2.5 eV

to describe carrier lifetimes determined by scattering from lattice vibrations, in the high energy (>2.5 eV) region, the screening of excitonic responses and the band edge shift become non-negligible affecting the modeled absorption coefficients' accuracy. Luckily, such discrepancies in the oscillatory amplitudes would have little effect on the extracted E_g values (main information extracted from said models) which is mainly determined by the energy point where both TL and CL components complete each other. Figure A.10 shows the SE derived E_g values as compared to the Tauc plot derived ones.

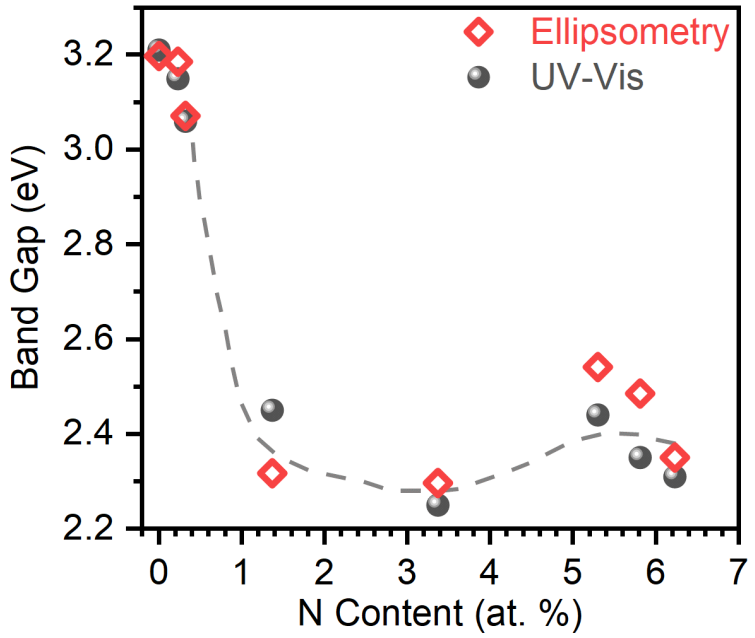

Figure A.10 – Variation of the E_g of the sputter-deposited TiO_2:N films as a function of their N content. E_g values derived from both UV-Vis/Tauc and SE measurements are compared.

A.2.4 X-ray diffraction

The idea that crystals could be used as a diffraction grating for X-rays arose in 1912 in a conversation between Paul Peter Ewald and Max von Laue. This, with time and input form many researchers evolved into what is now knows as X-ray diffraction (XRD). XRD crystallography is an ubiquitous technique used for determining the atomic and molecular structure of crystals. Regularly arranged atoms in a crystal form electron density plains, which can scatter oncoming radiation (such as X-rays). A regular arrangement of scatterers produces an ordered array of spherical scattered

waves which can then interfere constructively or destructively as a function of incident angle ϕ and inter-n-plane spacing d:

$$2d\sin\theta = n\lambda \tag{A.10}$$

X-rays are typically used as their wavelengths λ are on the order of magnitude of the crystallographic d spacing (*i.e.* 1 Å to 100 Å). Samples are mounted on a goniometer with multiple angles of freedom where the detector and/or X-ray source can be moved progressively. This, as its most basic produces a series of X-ray count peaks (Bragg diffraction peaks) in the y-axis as a function of angle in the x-axis (typically 2θ for grazing angle and 2θ type scans). For our experiments the crystalline structure of the on-quartz deposited films was investigated by means of a PANalytical X-Pert Pro XRD system using $Cu_{K\alpha}$ radiation (1.5418 Å) at a grazing incident angle of 0.75 °. Figure A.11 shown typical XRD spectra collected (0.02 ° 2θ step with a 10 s acquisition time per step).

Qualitatively, such scans ar useful as they allow us to identify the crystalline nature of the films, for our purposes this mainly implied either the anatase (ICDD card #00-021-1272) or rutile (ICDD card #00-021-1276) phases of TiO_2; although, high nitrogen containing thin-films showed a Magneli-like oxynitride phase of titania; ICDD card #01-076-9463. This can be accomplished as a group of (hkl) crystallographic peaks of a given crystal have a unique 2θ signature as seen in figure A.11. Quantitatively, such spectra can be used in conjunction with the Debye-Scherrer formula (equation A.11) relating the peak broadening to the sub-micrometer crystallite size:

$$D = \frac{0.9 \cdot \lambda}{\beta \cdot \cos\theta} \tag{A.11}$$

Where β is the peak broadening in rad at half the maximum intensity (FWHM), θ is the Bragg angle, λ is the X-ray wavelength, and D is the crystalline size (0.9 is a constant related to the shape factor, this value can vary, but for most of our situations it's fixed at the present value). The broadening β is corrected as to account for the inherent instrumental broadening, *i.e.* $\beta_{hkl} = \sqrt{(\beta_{hkl}^{Measured})^2 + (\beta_{hkl}^{Instrumental})^2}$. Unfortunately, the Debye-Scherrer formula only provides a lower bound on the particle size (does not account for inhomogeneous strain and imperfections), and

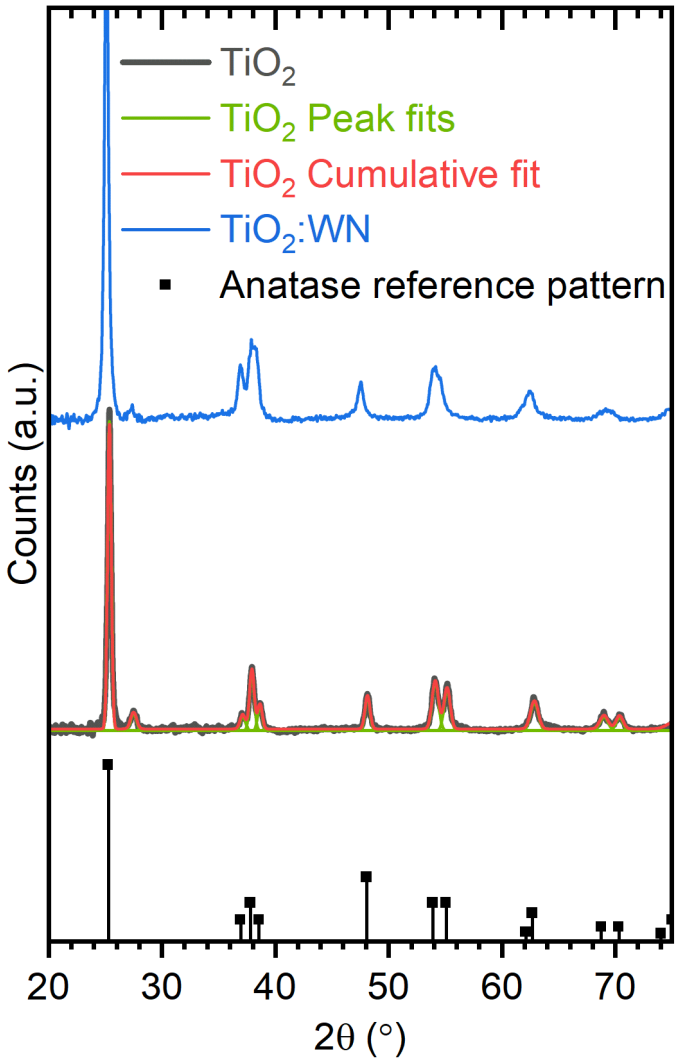

Figure A.11 – From bottom to top we see: (i) an anatase polymorph reference pattern, (ii) a raw signal from a 180 nm thick TiO_2 sample obtained at typical scan conditions showed in gray, with peak fits shows in green, and a total fit shown in red, and (iii) in blue we see the signature of a WN-codoped sample prepared with WO_3 $W_{power} = 26\,W\,cm^{-2}$ & $R_{N2} = 10\%$ with a thickness of 320 nm.

gives little information about the lattice strain. To remedy this, a more complete Williamson-Hall (W-H) analysis was also performed, which approximates the lattice strain ϵ as:

$$\epsilon = \frac{\beta_{hkl}}{4 \cdot \tan\theta} \tag{A.12}$$

By combining and rearranging equations A.11 & A.12, we are able to write out the Williamson-Hall equation:

$$\beta_{hkl}\cos\theta = \frac{0.9\lambda}{D} + 4\epsilon\sin\theta \tag{A.13}$$

This is, in essence a linear equation with $4\sin\theta$ along the x-axis and $\beta_{hkl}\cos\theta$ along the y-axis. Upon linear fitting, we can extract the lattice strain from the slope and the crystallite size from the y-intercept. Finally, the lattice parameters a & c can be derived by taking the θ position of the corresponding peaks in conjunction with the Bragg formula (equation A.10) *e.g.* using the $A(200)$ (anatase (200) peak location) position to determine a, then using the $A(101)$ position to determine c. From this final step, we can derive the lattice size, and therefore approximated strain, as to once again have a secondary source of information which can in turn be compared and contrasted to the W-H derived results.

A.2.5 Flash-photolysis time-resolved microwave conductivity

Flash-photolysis time-resolved microwave conductivity (FP-TRMC) is a technique allowing quantitative and qualitative detection of radiation induced charge separation (photolysis). This is accomplished via the time-resolved measurement of the changes in microwave absorption resulting from the variation of charged entities. The time dependent decay of these conductivity signals reveals the lifetimes of said photocharges. Specifically, the relative change $\Delta P(t)/P$ of the reflected microwave power results from a change in the photoconductivity $\Delta\sigma(t)$ and is proportional via a sensitivity factor A (frequency and conductivity dependent constant), so that:

$$\frac{\Delta P(t)}{P} = A\cdot\Delta\sigma(t) = A\cdot e\sum_i(\Delta N_i(t)\cdot\mu_i) \tag{A.14}$$

Where $N_i(t)$ is the number of charge-carrier type i with a mobility of μ_i. For our purposes it is reasonable to approximate that the main charge-carrier species upon photolysis in TiO_2 are electrons, resulting in the simplification : $\Delta\sigma(t) \approx \mu{\cdot}N(t)$. Therefore, the time evolution of $\Delta P(t)/P$ reveals the timescales of recombination and trapping mechanisms, resulting in annihilation of charge carriers. For our purposes, TRMC experiments were performed using a microwave generator (μwave)

operating at either 7 GHz or 20 GHz as to probe the photoconductive decay in the sample cavity. The pulsed light excitation causing photolysis was produced using an yttrium aluminum garnet (YAG) optical parametric oscillator as to provide light pulses at 10 Hz with a wavelength of 420 nm with an intensity of 1 mW cm^{-2}. These pulses were 3 ns to 5 ns wide with a 5 ns detector response time. The microwave transmission coefficient change was modulated by the photogenerated carriers and was transformed into a change in voltage using a PIN diode. Figure A.12 shows typical TRMC $\Delta P(t)/P$ decay curves of the TiO_{2-x}, TiO_2:N, TiO_2:W, and TiO_2:WN sputter deposited thin films.

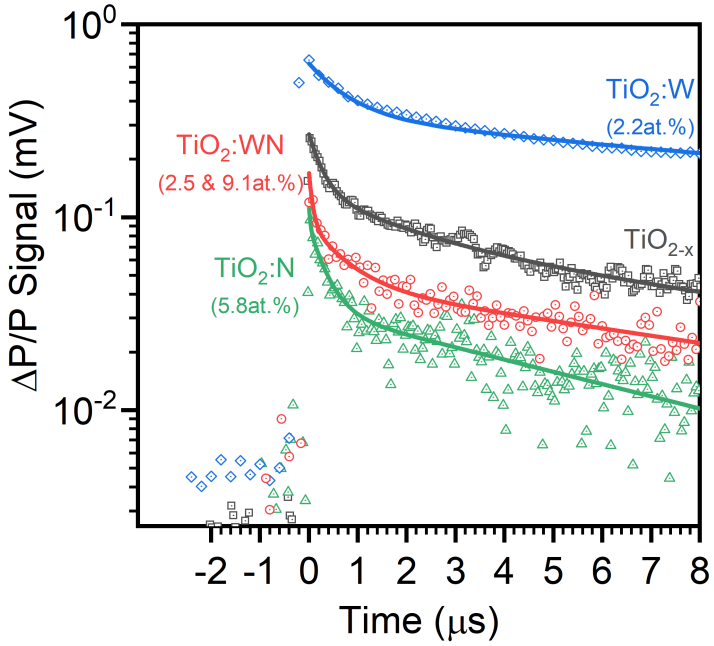

Figure A.12 – Representative FP-TRMC signals of the TiO_{2-x}, TiO_2:N, TiO_2:W, and TiO_2:WN thin films. These were excited with a 3 ns to 5 ns wide, 420 nm laser pulse. The prepulse baseline was $\approx 10 \times 10^{-2}$ µV.

It can be clearly seen that the signal amplitudes vary immensely. it is known that the $\Delta P(t)/P$ signal is not purely determined by the excitation light intensity I_{ex}, typically three main material factors influence it (this is excluding film thickness and density): (i) trap filling effects at low excitation energy, (ii) recombination effects at high excitation energy, and (iii) dopant induced donor and/or acceptor populations. For our purposes, we focused on the lifetime extraction, as this does not depend on the signal intensity, but decay time. To accomplish this, the $\Delta P(t)/P$ decay curves were fitted using a standard exponential decay function:

$$\sum_{n=1}^{i} A_n \cdot \exp\left(\frac{-t}{\tau_n}\right) \tag{A.15}$$

Where A_n and τ_n are the respective proportionality and time constants of each of the i decay processes. From this, and by using the TiO_{2-x} thin films as references, it was determined that three main decay regimes are in play, each with their characteristic time constant τ_{trap}, τ_{rec}, and τ_{surf} (τ on the order of 0.05 µs, 1 µs, and 10 µs, respectively)[5]. These are each associated with photocharge decay via charge trapping ($e^-|h^+ \rightarrow e-_{tr}|h^+_{tr}$), charge annihilation ($e^- + h^+|e-_{tr} + h^+|e^- + h^+_{tr} \rightarrow h\nu$), and surface reactions ($e^- + O_2 \rightarrow O_2^-$), respectively. The quality of these fits almost perfectly describe our system as seen by the full lines in figure A.12.

A.2.6 Dielectric spectroscopy

Figure A.13 A presents a simple dielectric material, placed between two parallel and infinite conductive electrodes with an applied electric field E. Naturally, the material in question will present a polarization P in response to the extrinsic field based on it's dielectric constant ϵ as presented in equation A.16.

$$P(\omega) = \epsilon_0 \left(\epsilon_r(\omega) - 1\right) E(\omega) \tag{A.16}$$

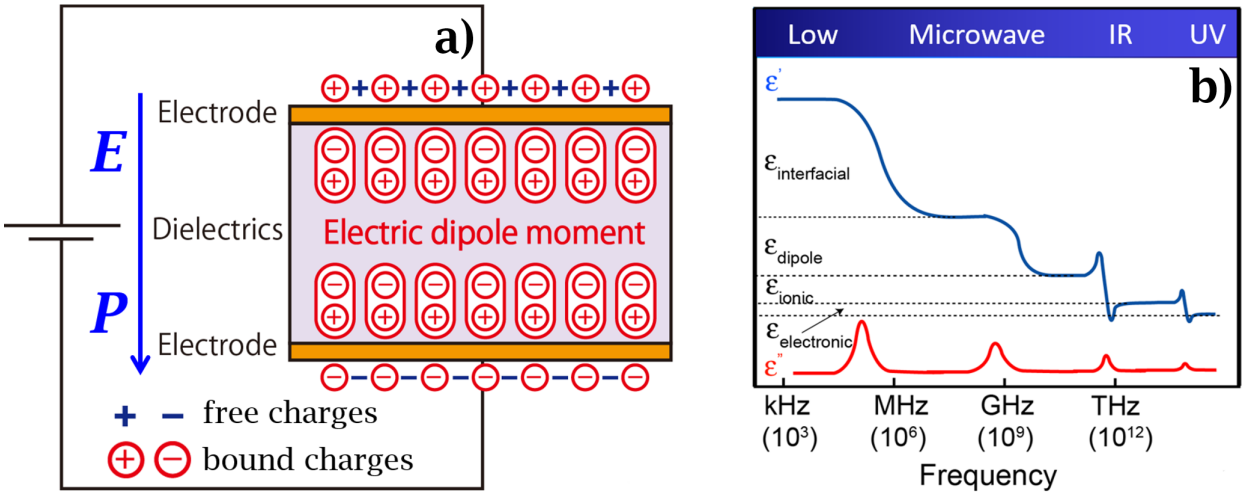

Figure A.13 – a) Model dielectric material placed between two parallel conductive plates with an applied electric field E. b) Various contributions to ϵ_r as a function of vibrational frequency.

The dielectric constant $\epsilon_r(\omega) = \epsilon'(w) + i\epsilon''(w)$ of the material is determined by various intrinsic and extrinsic properties of the device. Roughly speaking, the various effects contributing to ϵ_r can

be segregated based on frequency of excitation ω as shown in figure A.13 B. These contributions to the dielectric properties of the material can be discerned based on the frequency range in which they are active. It can be approximated that the total dielectric constant in the case of typical dielectric materials is a sum of interfacial effects, intrinsic dipoles, ionic contributions, and electronic oscillations as shown in figure A.14 A, B, C, and D respectively[191].

$$\epsilon \approx \epsilon_{interfacial} + \epsilon_{dipole} + \epsilon_{ionic} + \epsilon_{electronic} \tag{A.17}$$

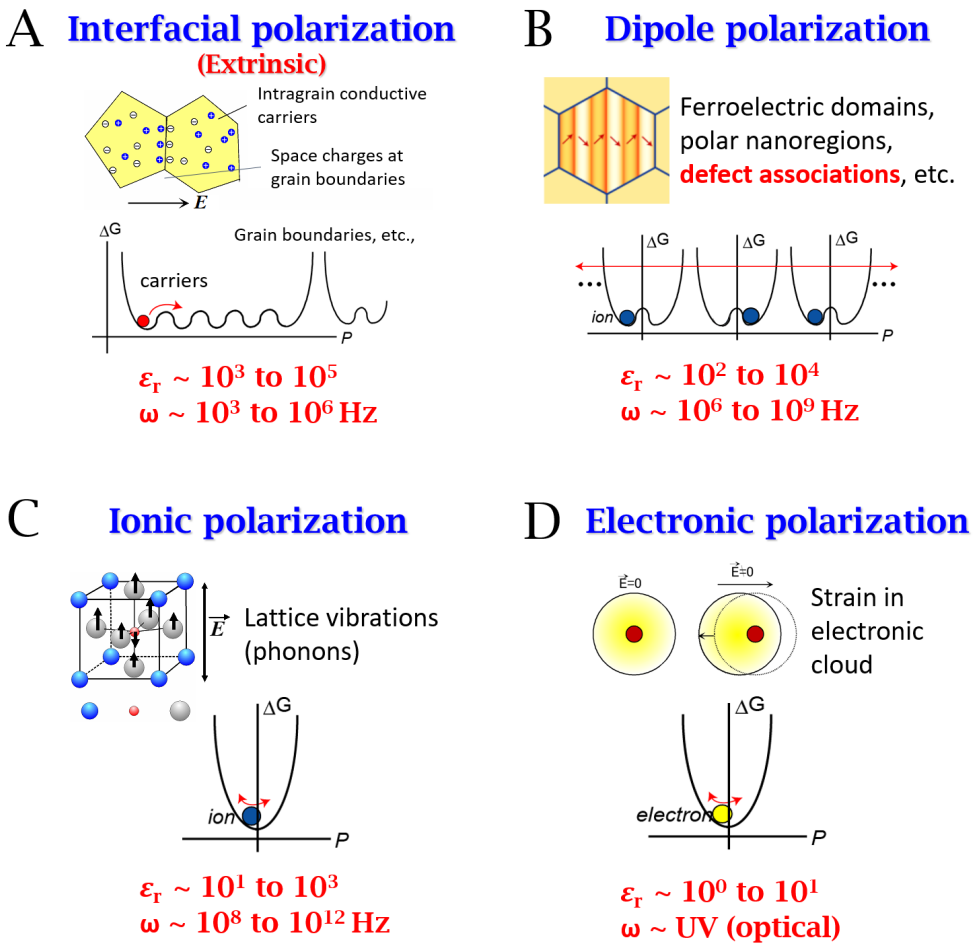

Figure A.14 – Examples of material phenomenon leading to various dielectric contributions as described by equation A.17 with their expected ϵ_r magnitudes and ω resonance frequencies.

It is fairly well understood that certain types of doping should induce defect pairs in TiO_2, whether these are due to intrinsic doping (such as V_O) or extrinsic doping. If such defects form

association pairs between which carriers can oscillate, they will behave like dipoles and therefore contribute to the dielectric signature of the material accordingly. It is expected that such signatures are present in the MHz to GHz range. Therefore, by studying the dielectric behavior of the material in this frequency window, we should be able to track how these defect dipoles behave as a function of the various dopant concentrations present within undoped (TiO_2), substoichiometric (TiO_{2-x}), monodoped (TiO_2:N & TiO_2:W), and codoped (TiO_2:WN) titania thin films.

It is important to note that this will be the tailing region for the dielectric signature of unavoidable extrinsic phenomenon (see figure A.14 A). Additionally, the low GHz region is expected to show only partial relaxation features for the various dipole contributions. Therefore, in order to accurately extract any meaningful information, precise dielectric models of the materials will have to be built and fitted onto the experimental data as to discern each of these contributions.

In preparation for the dielectric experiments, TiO_2 thin films with varying dopant concentrations were prepared via radio frequency magnetron sputtering as shown in table A.2. These samples varied in thickness from 150 nm to 1150 nm and were deposited on quartz substrates as to minimize any parasitic dielectric contributions from the substrate.

	Nitrogen (at.%)	**Tungsten (at.%)**	**Number of Samples**
TiO_2	0	0	2
TiO_2:N	0 - 12.6	0	5
TiO_2:W	0	0 - 8.4	6
TiO_2:WN	0 - 8	0 - 8	8

Table A.2 – Summary of RF-MS samples prepared for dielectric characterization at Okayama University.

Given that the TiO_2 thin films were deposited onto quartz, a parallel plate setup would have been difficult, a planar electrode approach had to be adopted. In other words, instead of using a parallel plate capacitor setup as presented in figure A.13, planar electrodes were deposited onto the thin films to be measured via micro-probe. Figure A.15 A shows the experimental setup used for these measurements. In order to ensure maximum signal fidelity and to be within the network analyzer's sensitivity (E4991A Network Analyzer, Agilent Tech.), an inter-electrode gap of 20 µm was required with a total electrode thickness of 200 nm. Such electrodes were deposited using DC sputtering of an Au target using a Sanuy Denshi DC-701 quick coater. The electrode shape was

ensured via mechanical fixing of a laser etched stainless steel mask mirroring the desired pattern. Sputtering time (1 h) and DC current (10 mA) were maintained as to ensure a consistent 200 nm Au deposition thickness. Figure A.15 B shows a typical planar electrode obtained on a TiO_2:WN thin film.

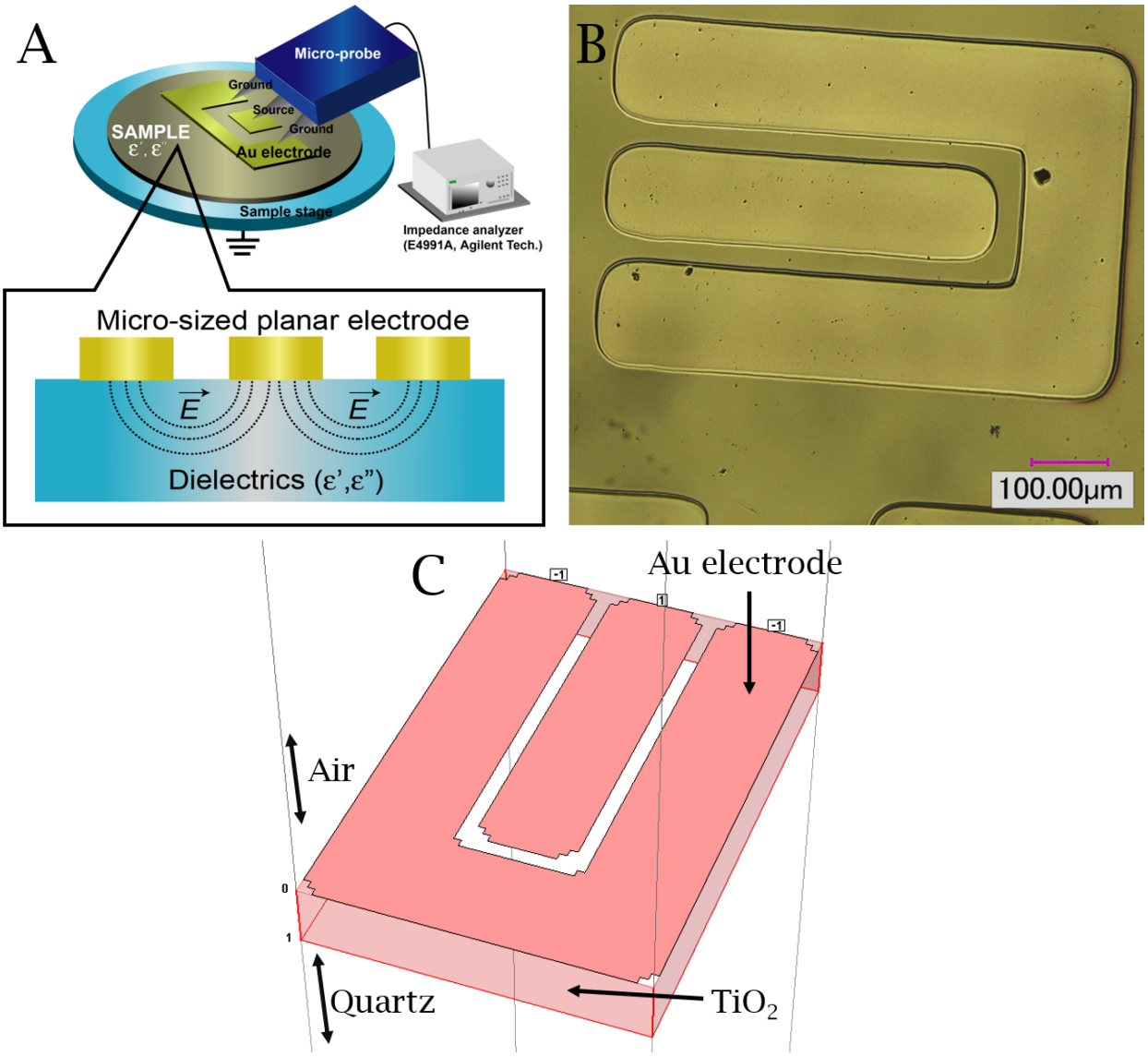

Figure A.15 – A - The planar electrode measurement setup. B - Typical sputter deposited planar electrode with ≈20 µm inter-electrode gap. C - An example of a Sonnet spatial model used to calculate the dielectric response of the samples.

Given the electrode planar geometry, the electric field generated by an excitation $V(\omega)$ in such an experimental setup is expected to create cylindrical field lines that traverse the dielectric film, substrate, electrodes, and air (above) (see figure A.15 A). In order to distinguish these contributions

from the intrinsic material signal, accurate spatial models (thickness, size, and shape) of each measured thin film were built and simulated using the Sonnet 13 software suite (see figure A.15 C)[191]. The dielectric properties of the quartz substrates and Au electrodes used were measured independently as to be accurately incorporated into said models. During measurement, the micro-probe dielectric signature (and that of the measurement device) was accounted for via OSL calibration using high-precision micro-fabricated reference circuits. The measured data (real and imaginary admittance) values were then fitted onto the simulated data to determine ϵ' and the $\tan(\delta)$ (ϵ'') as shown in figure A.16. It is to be noted that the simulated $\tan(\delta)$ spectra were based of Cole-Cole parameters obtained from the ϵ' measurements and are therefore expected to diverge slightly from experimental data in complex situations (such as heavily codoped systems with multiple sources of foreign charge carriers).

It is to be noted that this approach is extremely demanding from a computational stand point (≈60 h of calculations required per sample). While the Sonnet software suit is an off-the-shelf product, the data management and fitting software had to be programmed in-house using MatLab and Fortran respectively.

The experimental dielectric data was fitted using a standard dielectric empirical relation:

$$\frac{\epsilon(\omega) - \epsilon_\infty}{\epsilon_0 - \epsilon_\infty} = \sum_{n=1}^{m} g_n \cdot \left(\frac{1}{1 + i\omega\tau_n} \right) \tag{A.18}$$

Where ϵ_∞ is the permittivity contribution from ionic and electronic resonances, ϵ_0 the low-frequency permittivity, with g_n and τ_n being the proportionality coefficient and characteristic relation time of contributions n respectively[192, 193]. Figure A.17 presents typical fitted ϵ' & ϵ'' spectra as a function of doping type, *i.e.* undoped TiO_2 (a), V_O heavy TiO_{2-x} (b), TiO_2:W (c), TiO_2:N (d), and TiO_2:WN (e). While a detailed discussion of the features revealed by such spectra will be developed in the appropriate sections of the results discussion, for now, a few common features can be noted: (i) an interfacial contribution leading up to the MHz range, and (ii) a dipole contribution in the MHz to GHz range. Additionally, we note that pure TiO_2 has a slightly lower dielectric value than expected, $\epsilon_\infty \approx 42$ (expected ≈ 42), which could be due to the thin film nature of our samples[208].

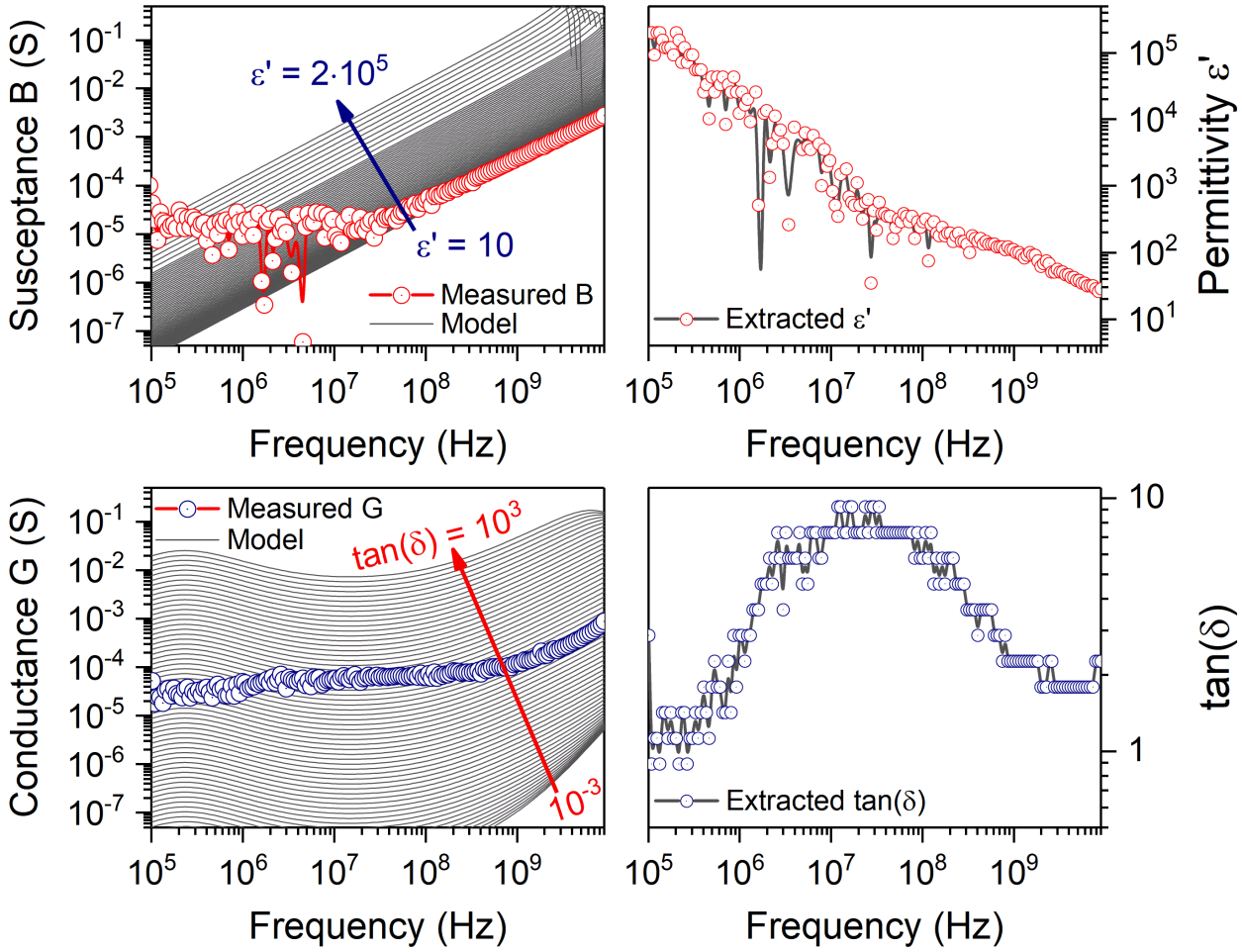

Figure A.16 – Example of data analysis for a TiO_2:WN sample. Top left shows matching of the measured susceptance B onto the modeled values with the extracted ϵ' shown in the top right graph. This data is then used to create a $\tan(\delta)$ model used to match the conductance G data as seen in the bottom left graph. Finally, the extracted $\tan(\delta)$ values are shown in the bottom right figure.

Finally, it can be noted that the incorporation of various intrinsic and extrinsic dopants directly affects the dipole contribution in the high frequency regime. Therefore, we can propose that $\epsilon_{dipole} \approx \epsilon_{doped} - \epsilon_{\infty intrinsic}$ as shown in figure A.18. For some samples, all these values can be directly ascertained from the dielectric fit, for others a reference sample is needed to set a baseline, typically these things are left for discussion in the appropriate sections[191].

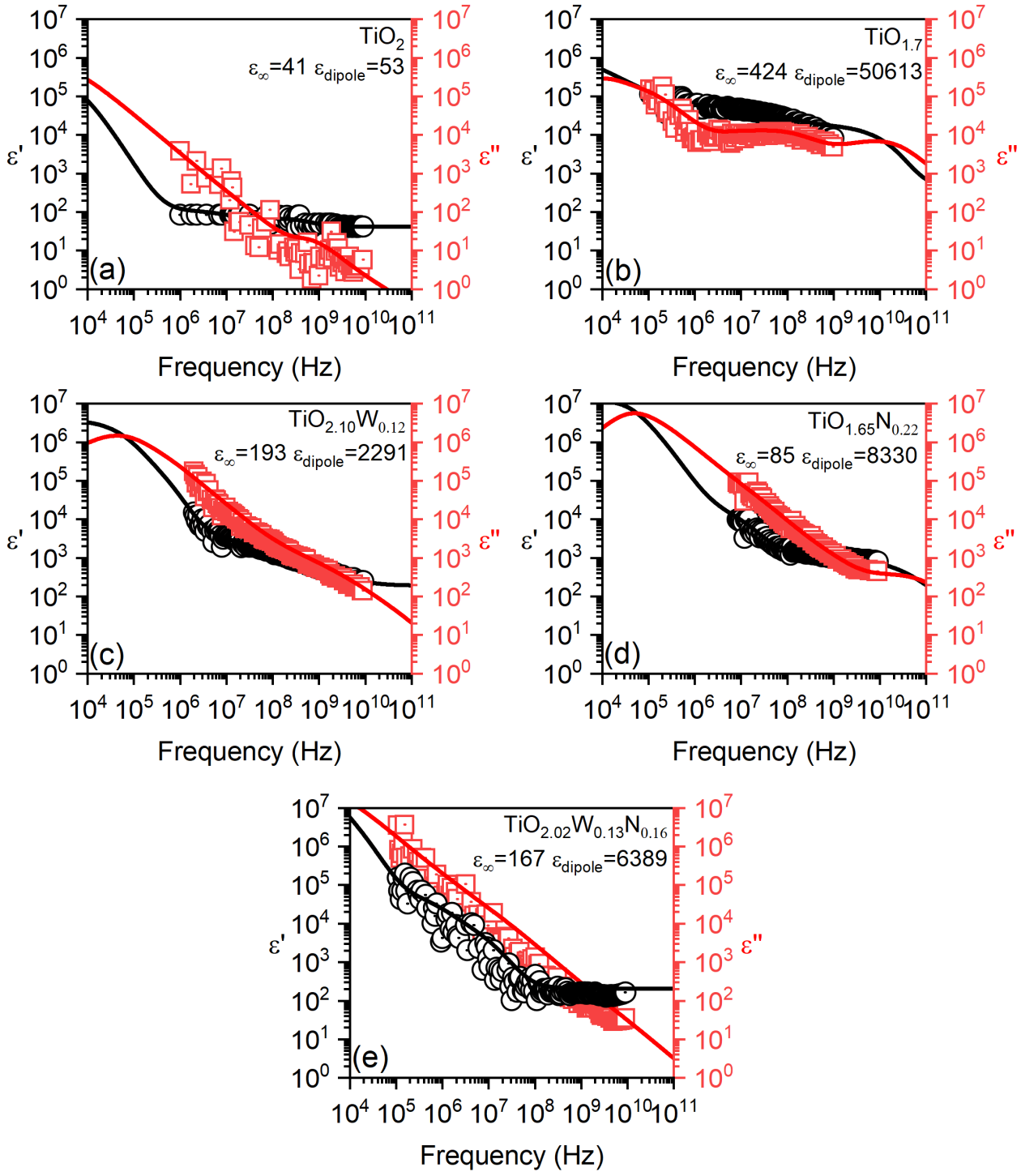

Figure A.17 – Typical fitted ϵ' & ϵ'' spectra as a function of doping type, *i.e.* undoped TiO_2 (a), V_O heavy TiO_{2-x} (b), TiO_2:W (c), TiO_2:N (d), and TiO_2:WN (e).

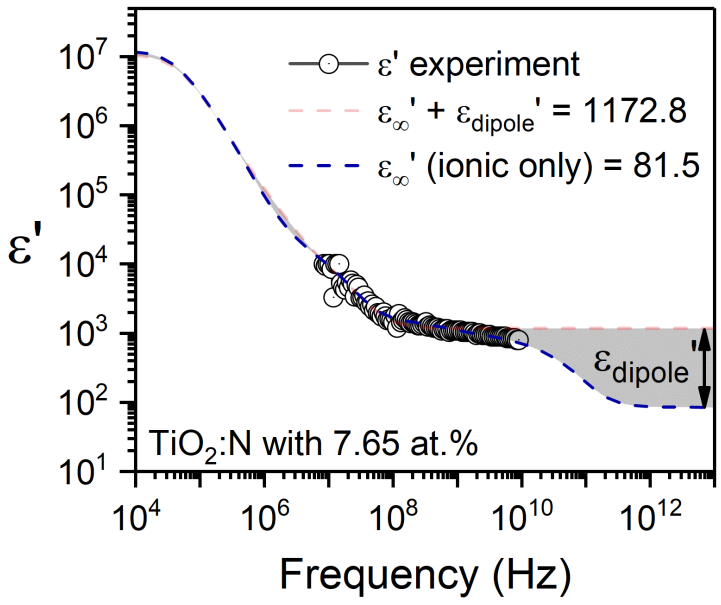

Figure A.18 – Dipole contribution component displayed for a TiO_2:N sample with 7.65 at.% of nitrogen.

A.3 Electro-photocatalytic degradation and voltammetry measurements

Electro-photocatalytic degradation and characterization were performed in a 1 L EPC reactor as shown in figure A.19 with the full setup shown in figure A.20 (a) (other, similar iterations of this set-up were used in earlier EPC tests [182]). The studies were carried out in a closed loop by continuously circulating the synthetic solutions with a peristaltic pump (Master flex, Model 77200-50, USA) with flow rates from 0.1 L min^{-1} to 0.5 L min^{-1}. The EPC reactor functioning components were comprised of two parallel 10 cm by 11 cm electrodes as shown in figure A.21 (a) (later iterations had 15.24 cm diameter electrodes to increase surface area as shown in figure A.21 (b)). The photoanodes were comprised of TiO_2 based thin films (varying doping schemes), deposited onto deployed Ti-grids as shown in figure A.21. The inter-electrode distance could be varied, but was typically left at 1 cm. Synthetic solutions of pollutants were typically complemented with 0.07 mol L^{-1} or less of sodium sulfate (Na_2SO_4) as to allow for increased solution conductivity. The EPC cell was operated under galvanostatic conditions with varying current intensities in the range of 0.1 A to 0.8 A imposed during treatment via a PS3030D, Circuit-Test Electronics (Burnaby, BC, Canada) DC power source. AM 1.5 solar illumination was assured via a SS50AAA 150W Xenon

lap equipped (Photo emission Tech., INC, Camarillo, USA), and later Oriel's Sol2A solar simulator. Figure A.20 (b) shows the EPC setup used for the prototype reactor.

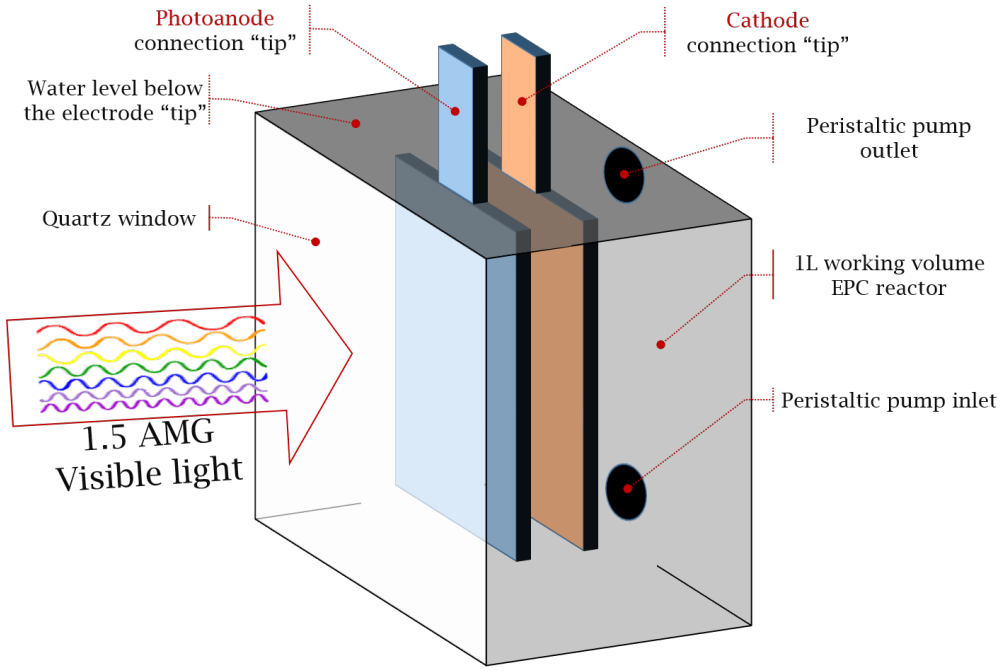

Figure A.19 – Schematic diagram of the experimental EPC reactor.

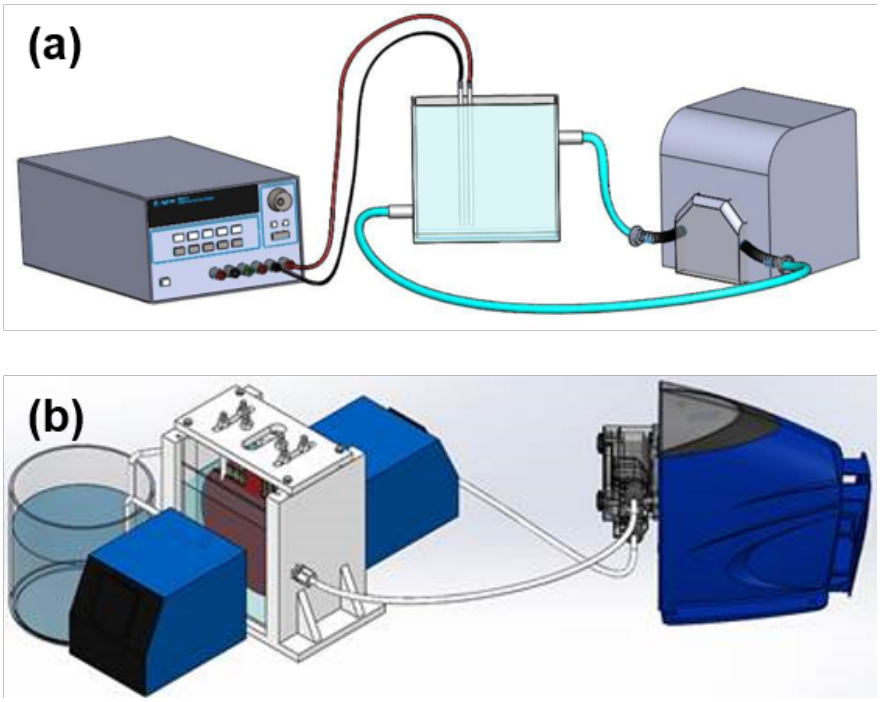

Figure A.20 – Schematic diagram of the experimental EPC setup with the experimental reactor (a) and prototype reactor (b).

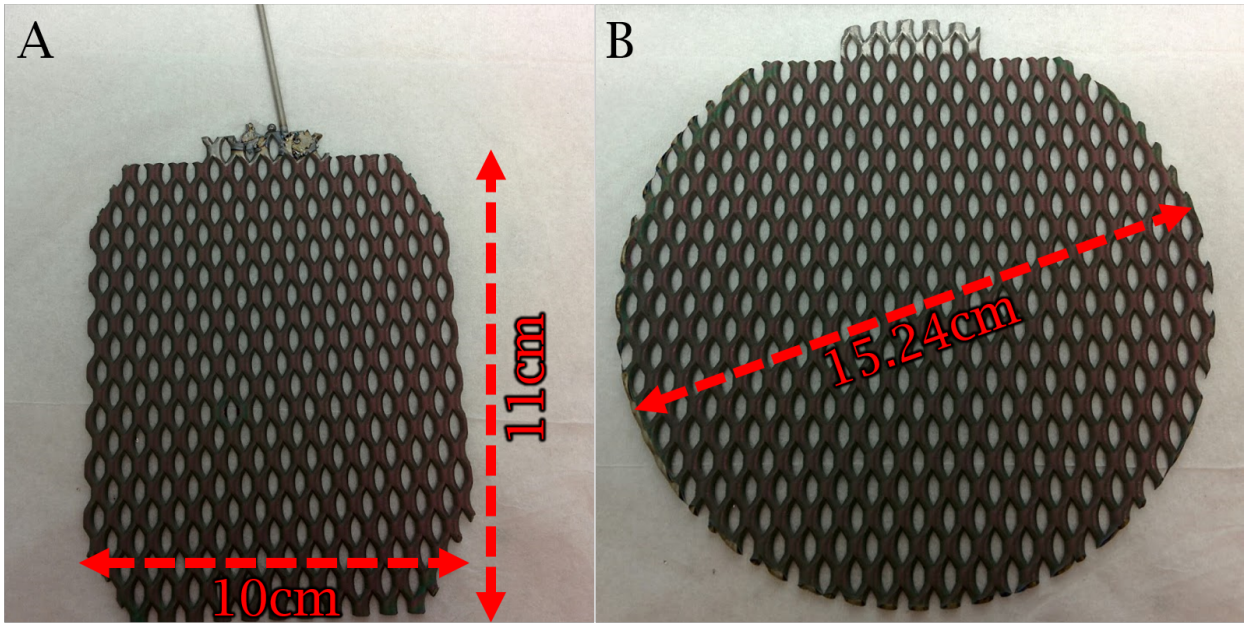

Figure A.21 – Photos of TiO_2 based photoanodes in two commonly used formats. Note the connection tips at top that are not sputter-coated as to allow electrical connectivity of the electrodes.

References

[1] M. Grätzel, "Photoelectrochemical cells," *Nature*, vol. 414, pp. 338–344, nov 2001.

[2] P. Kanhere and Z. Chen, "A Review on Visible Light Active Perovskite-Based Photocatalysts," *Molecules*, vol. 19, pp. 19995–20022, dec 2014.

[3] W. Wu, C. Jiang, and V. A. L. Roy, "Recent Progress in Magnetic Iron Oxide Semiconductor Composite Nanomaterials as Promising Photocatalysts," *Nanoscale*, pp. 38–58, oct 2014.

[4] A. Fujishima and K. Honda, "Electrochemical Photolysis of Water at a Semiconductor Electrode," *Nature*, vol. 238, pp. 37–38, jul 1972.

[5] A. Fujishima, X. Zhang, and D. Tryk, "TiO_2 photocatalysis and related surface phenomena," *Surface Science Reports*, vol. 63, pp. 515–582, dec 2008.

[6] J. Schneider, M. Matsuoka, M. Takeuchi, J. Zhang, Y. Horiuchi, M. Anpo, and D. W. Bahnemann, "Understanding TiO_2 Photocatalysis: Mechanisms and Materials," *Chemical Reviews*, vol. 114, pp. 9919–9986, oct 2014.

[7] E. P. Meagher and G. A. Lager, "Polyhedral thermal expansion in the TiO_2 polymorphs: refinement of the crystal structures of rutile and brookite at high temperature," *Canadian Mineralogist*, vol. 17, pp. 77–85, 1979.

[8] C. J. Howard, T. M. Sabine, and F. Dickson, "Structural and thermal parameters for rutile and anatase," *Acta Crystallographica Section B Structural Science*, vol. 47, pp. 462–468, aug 1991.

[9] R. Asahi, Y. Taga, W. Mannstadt, and A. J. Freeman, "Electronic and optical properties of anatase TiO_2," *Physical Review B*, vol. 61, pp. 7459–7465, mar 2000.

[10] X. Chen and S. S. Mao, "Titanium Dioxide Nanomaterials: Synthesis, Properties, Modifications, and Applications," *Chemical Reviews*, vol. 107, pp. 2891–2959, jul 2007.

[11] P. I. Sorantin and K. Schwarz, "Chemical bonding in rutile-type compounds," *Inorganic Chemistry*, vol. 31, no. 4, pp. 567–576, 1992.

[12] J. Tian, Z. Zhao, A. Kumar, R. I. Boughton, and H. Liu, "Recent progress in design, synthesis, and applications of one-dimensional TiO_2 nanostructured surface heterostructures: a review," *Chem. Soc. Rev.*, vol. 43, pp. 6920–6937, jul 2014.

[13] D. Cronemeyer, "Infrared absorption of reduced rutile TiO_2 single crystals," *Physical review*, vol. 113, no. 5, p. 1222, 1959.

[14] D. Smith, *Thin-Film Deposition: Principles and Practice*. McGraw-Hill Education, 1995.

[15] J. A. Thornton, "Influence of apparatus geometry and deposition conditions on the structure and topography of thick sputtered coatings," *Journal of Vacuum Science and Technology*, vol. 11, no. 4, pp. 666–670, 1974.

[16] H. Tang, K. Prasad, R. Sanjines, P. Schmid, and F. Levy, "Electrical and optical properties of TiO_2 anatase thin films," *Journal of Applied Physics*, vol. 75, no. 4, pp. 2042–2047, 1994.

[17] M. Li, J. Zhang, and Y. Zhang, "First-principles calculation of compensated (2N, W) codoping impacts on band gap engineering in anatase TiO_2," *Chemical Physics Letters*, vol. 527, pp. 63–66, feb 2012.

[18] R. Long and N. J. English, "First-principles calculation of nitrogen-tungsten codoping effects on the band structure of anatase-titania," *Applied Physics Letters*, vol. 94, no. 13, p. 132102, 2009.

[19] C. Renz, "Photoreduktionen von metalloxyden," *Helvetica Chimica Acta*, vol. 15, no. 1, pp. 839–842, 1932.

[20] E. Baur and A. Perret, "Über die einwirkung von licht auf gelöste silbersalze in gegenwart von zinkoxyd," *Helvetica Chimica Acta*, vol. 7, no. 1, pp. 910–915, 1924.

[21] C. Renz, "Lichtreaktionen der oxyde des titans, cers und der erdsäuren," *Helvetica Chimica Acta*, vol. 4, no. 1, pp. 961–968, 1921.

[22] N. S. Ezio Pelizzetti, *Homogeneous and Heterogeneous Photocatalysis*, vol. 8. Dordrecht: Springer Netherlands, 1986.

[23] N. Serpone and E. Pelizzetti, *Photocatalysis : fundamentals and applications*. New York: Wiley, 1989.

[24] D. F. Ollis and H. H. Al-Ekabi, *Photocatalytic purification and treatment of water and air*. Elsevier, 1993.

[25] E. Pelizzetti, M. Borgarello, C. Minero, E. Pramauro, E. Borgarello, and N. Serpone, "Photocatalytic degradation of polychlorinated dioxins and polychlorinated biphenyls in aqueous suspensions of semiconductors irradiated with simulated solar light," *Chemosphere*, vol. 17, pp. 499–510, jan 1988.

[26] R. I. Bickley, T. Gonzalez-Carreno, J. S. Lees, L. Palmisano, and R. J. Tilley, "A structural investigation of titanium dioxide photocatalysts," *Journal of Solid State Chemistry*, vol. 92, pp. 178–190, may 1991.

[27] L. A. Dibble and G. B. Raupp, "Fluidized-bed photocatalytic oxidation of trichloroethylene in contaminated air streams," *Environmental Science & Technology*, vol. 26, pp. 492–495, mar 1992.

[28] J. Peral and D. Ollis, "Heterogeneous photocatalytic oxidation of gas-phase organics for air purification: Acetone, 1-butanol, butyraldehyde, formaldehyde, and m-xylene oxidation," *Journal of Catalysis*, vol. 136, pp. 554–565, aug 1992.

[29] G. B. Raupp and C. T. Junio, "Photocatalytic oxidation of oxygenated air toxics," *Applied Surface Science*, vol. 72, pp. 321–327, dec 1993.

[30] O. Carp, C. Huisman, and A. Reller, "Photoinduced reactivity of titanium dioxide," *Progress in Solid State Chemistry*, vol. 32, no. 1-2, pp. 33–177, 2004.

[31] M. Anpo and P. V. Kamat, *Environmentally benign photocatalysts: applications of titanium oxide-based materials*. Springer Science & Business Media, 2010.

[32] M. Xu, Y. Gao, E. M. Moreno, M. Kunst, M. Muhler, Y. Wang, H. Idriss, and C. Wöll, "Photocatalytic Activity of Bulk TiO_2 Anatase and Rutile Single Crystals Using Infrared Absorption Spectroscopy," *Physical Review Letters*, vol. 106, p. 138302, mar 2011.

[33] R. Asahi, "Visible-Light Photocatalysis in Nitrogen-Doped Titanium Oxides," *Science*, vol. 293, pp. 269–271, jul 2001.

[34] A. V. Emeline, V. N. Kuznetsov, V. K. Rybchuk, and N. Serpone, "Visible-Light-Active Titania Photocatalysts: The Case of N-Doped TiO_2 — Properties and Some Fundamental Issues," *International Journal of Photoenergy*, vol. 2008, pp. 1–19, 2008.

[35] Y. Ma, X. L. Wang, Y. S. Jia, X. B. Chen, H. X. Han, and C. Li, "Titanium Dioxide-Based Nanomaterials for Photocatalytic Fuel Generations," *Chemical Reviews*, vol. 114, no. 19, pp. 9987–10043, 2014.

[36] M. Ohring, *Materials Science of Thin Films, Second Edition*. Academic Press, 2001.

[37] E. Baur and C. Neuweiler, "Über photolytische bildung von hydroperoxyd," *Helvetica Chimica Acta*, vol. 10, no. 1, pp. 901–907, 1927.

[38] C. F. Goodeve and J. A. Kitchener, "Photosensitisation by titanium dioxide," *Trans. Faraday Soc.*, vol. 34, pp. 570–579, 1938.

[39] C. F. Goodeve and J. A. Kitchener, "The mechanism of photosensitisation by solids," *Trans. Faraday Soc.*, vol. 34, pp. 902–908, 1938.

[40] C. Wagner and W. Traud, "Über die deutung von korrosionsvorgängen durch Überlagerung von elektrochemischen teilvorgängen und über die potentialbildung an mischelektroden," *Zeitschrift für Elektrochemie und angewandte physikalische Chemie*, vol. 44, no. 7, pp. 391–402, 1938.

[41] A. E. Jacobsen, "Titanium dioxide pigments: Correlation between photochemical reactivity and chalking.," *Industrial & Engineering Chemistry*, vol. 41, no. 3, pp. 523–526, 1949.

[42] M. C. Markham and K. J. Laidler, "A kinetic study of photo-oxidations on the surface of zinc oxide in aqueous suspensions," *The Journal of Physical Chemistry*, vol. 57, no. 3, pp. 363–369, 1953.

[43] T. R. Rubin, J. G. Calvert, G. T. Rankin, and W. MacNevin, "Photochemical synthesis of hydrogen peroxide at zinc oxide surfaces1," *Journal of the American Chemical Society*, vol. 75, no. 12, pp. 2850–2853, 1953.

[44] M. C. Markham, M. C. Hannan, R. M. Paternostro, and C. B. Rose, "Oxidation of alcohols catalyzed by zinc oxide and light," *Journal of the American Chemical Society*, vol. 80, no. 20, pp. 5394–5397, 1958.

[45] R. E. Stephens, B. Ke, and D. Trivich, "The efficiencies of some solids as catalysts for the photosynthesis of hydrogen peroxide," *The Journal of Physical Chemistry*, vol. 59, no. 9, pp. 966–969, 1955.

[46] C. B. Vail, J. P. Holmquist, and L. White, "Function of organic material in the photochemical formation of hydrogen peroxide at zinc oxide surfaces1," *Journal of the American Chemical Society*, vol. 76, no. 2, pp. 624–625, 1954.

[47] M. Markham and M. C. Upreti, "Photoelectric effects at semiconductor electrodes," *Journal of Catalysis*, vol. 4, no. 2, pp. 229 – 238, 1965.

[48] D. R. Kennedy, M. Ritchie, and J. Mackenzie, "The photosorption of oxygen and nitric oxide on titanium dioxide," *Trans. Faraday Soc.*, vol. 54, pp. 119–129, 1958.

[49] A. Terenin and Y. Solonitzin, "Action of light on the gas adsorption by solids," *Discuss. Faraday Soc.*, vol. 28, pp. 28–35, 1959.

[50] V. Filimonov, "Photocatalytic oxidation of gaseous isopropanol on ZnO + TiO_2," *Doklady Akademii Nauk SSSR*, vol. 154, pp. 922–925, 1964.

[51] S. Kato and F. Mashio, "Titanium dioxide-photocatalyzed liquid phase oxidation of tetralin," *The Journal of the Society of Chemical Industry, Japan*, vol. 67, no. 8, pp. 1136–1140, 1964.

[52] I. S. McLintock and M. Ritchie, "Reactions on titanium dioxide; photo-adsorption and oxidation of ethylene and propylene," *Trans. Faraday Soc.*, vol. 61, pp. 1007–1016, 1965.

[53] F. Lohmann, "Elektrochemische reaktionen an uv-bestrahlten zinkoxidelektroden," *Berichte der Bunsengesellschaft für physikalische Chemie*, vol. 70, no. 1, pp. 87–92, 1966.

[54] S. R. Morrison and T. Freund, "Chemical role of holes and electrons in ZnO photocatalysis," *The Journal of Chemical Physics*, vol. 47, no. 4, pp. 1543–1551, 1967.

[55] K.-i. H. Akira FUJISHIMA and S.-I. KIKUCHI, "Photosensitized electrolytic oxidation on semiconducting n-type TiO_2 electrode," *The Journal of Chemical Physics*, vol. 72, pp. 108–113, 1969.

[56] A. Fujishima and K. Honda, "Verification of the photo senitized electrolytic oxidation of TiO_2 electrode by ph measurement," *J Chem Soc Japan*, vol. 74, pp. 355–360, 1971.

[57] S. N. Frank and A. J. Bard, "Heterogeneous photocatalytic oxidation of cyanide ion in aqueous solutions at titanium dioxide powder," *Journal of the American Chemical Society*, vol. 99, no. 1, pp. 303–304, 1977.

[58] S. N. Frank and A. J. Bard, "Heterogeneous photocatalytic oxidation of cyanide and sulfite in aqueous solutions at semiconductor powders," *The Journal of Physical Chemistry*, vol. 81, no. 15, pp. 1484–1488, 1977.

[59] S. N. Frank and A. J. Bard, "Semiconductor electrodes. 12. photoassisted oxidations and photoelectrosynthesis at polycrystalline titanium dioxide electrodes," *Journal of the American Chemical Society*, vol. 99, no. 14, pp. 4667–4675, 1977.

[60] B. Kraeutler and A. J. Bard, "Heterogeneous photocatalytic synthesis of methane from acetic acid - new kolbe reaction pathway," *Journal of the American Chemical Society*, vol. 100, no. 7, pp. 2239–2240, 1978.

[61] N. Negishi, T. Iyoda, K. Hashimoto, and A. Fujishima, "Preparation of Transparent TiO_2 Thin Film Photocatalyst and Its Photocatalytic Activity," *Chemistry Letters*, vol. 24, pp. 841–842, sep 1995.

[62] A. L. Linsebigler, G. Lu, and J. T. Yates, "Photocatalysis on TiO_2 Surfaces: Principles, Mechanisms, and Selected Results," *Chemical Reviews*, vol. 95, pp. 735–758, may 1995.

[63] E. Borgarello, J. Kiwi, M. Graetzel, E. Pelizzetti, and M. Visca, "Visible light induced water cleavage in colloidal solutions of chromium-doped titanium dioxide particles," *Journal of the American chemical society*, vol. 104, no. 11, pp. 2996–3002, 1982.

[64] M. Anpo, Y. Ichihashi, M. Takeuchi, and H. Yamashita, "Design of unique titanium oxide photocatalysts by an advanced metal ion-implantation method and photocatalytic reactions under visible light irradiation," *Research on Chemical Intermediates*, vol. 24, no. 2, pp. 143–149, 1998.

[65] M. Anpo and M. Takeuchi, "The design and development of highly reactive titanium oxide photocatalysts operating under visible light irradiation," *Journal of catalysis*, vol. 216, no. 1, pp. 505–516, 2003.

[66] W. Choi, A. Termin, and M. R. Hoffmann, "The role of metal ion dopants in quantum-sized tio2: correlation between photoreactivity and charge carrier recombination dynamics," *The Journal of Physical Chemistry*, vol. 98, no. 51, pp. 13669–13679, 1994.

[67] R. Dholam, N. Patel, M. Adami, and A. Miotello, "Hydrogen production by photocatalytic water-splitting using cr-or fe-doped TiO_2 composite thin films photocatalyst," *International Journal of Hydrogen Energy*, vol. 34, no. 13, pp. 5337–5346, 2009.

[68] M. A. Khan, S. I. Woo, and O.-B. Yang, "Hydrothermally stabilized fe (iii) doped titania active under visible light for water splitting reaction," *International Journal of Hydrogen Energy*, vol. 33, no. 20, pp. 5345–5351, 2008.

[69] A. A. Gribb and J. F. Banfield, "Particle size effects on transformation kinetics and phase stability in nanocrystalline TiO_2," *American Mineralogist*, vol. 82, no. 7-8, pp. 717–728, 1997.

[70] H. Zhang and J. F. Banfield, "Thermodynamic analysis of phase stability of nanocrystalline titania," *J. Mater. Chem.*, vol. 8, pp. 2073–2076, 1998.

[71] K.-N. P. Kumar, K. Keizer, A. J. Burggraaf, T. Okubo, H. Nagamoto, and S. Morooka, "Densification of nanostructured titania assisted by a phase transformation," *Nature*, vol. 358, pp. 48–51, jul 1992.

[72] X. Ye, J. Sha, Z. Jiao, and L. Zhang, "Thermoanalytical characteristic of nanocrystalline brookite-based titanium dioxide," *Nanostructured Materials*, vol. 8, no. 7, pp. 919 – 927, 1997.

[73] H. Kominami, M. Kohno, and Y. Kera, "Synthesis of brookite-type titanium oxide nanocrystals in organic media," *J. Mater. Chem.*, vol. 10, pp. 1151–1156, 2000.

[74] M. Ramamoorthy, D. Vanderbilt, and R. D. King-Smith, "First-principles calculations of the energetics of stoichiometric TiO_2 surfaces," *Physical Review B*, vol. 49, pp. 16721–16727, jun 1994.

[75] V. Shklover, M.-K. Nazeeruddin, S. M. Zakeeruddin, C. Barbé, A. Kay, T. Haibach, W. Steurer, R. Hermann, H.-U. Nissen, and M. Grätzel, "Structure of nanocrystalline TiO_2 powders and precursor to their highly efficient photosensitizer," *Chemistry of Materials*, vol. 9, no. 2, pp. 430–439, 1997.

[76] Y. Liang, S. Gan, S. A. Chambers, and E. I. Altman, "Surface structure of anatase $tio_2(001)$: reconstruction, atomic steps, and domains," *Phys. Rev. B*, vol. 63, p. 235402, May 2001.

[77] S. D. Burnside, V. Shklover, C. Barbé, P. Comte, F. Arendse, K. Brooks, and M. Grätzel, "Self-organization of TiO_2 nanoparticles in thin films," *Chemistry of Materials*, vol. 10, no. 9, pp. 2419–2425, 1998.

[78] A. Di Paola, M. Bellardita, and L. Palmisano, "Brookite, the Least Known TiO_2 Photocatalyst," *Catalysts*, vol. 3, pp. 36–73, jan 2013.

[79] A. Beltrán, L. Gracia, and J. Andrés, "Density functional theory study of the brookite surfaces and phase transitions between natural titania polymorphs," *The Journal of Physical Chemistry B*, vol. 110, no. 46, pp. 23417–23423, 2006. PMID: 17107193.

[80] T. P. Feist and P. K. Davies, "The soft chemical synthesis of TiO_2 (b) from layered titanates," *Journal of solid state chemistry*, vol. 101, no. 2, pp. 275–295, 1992.

[81] L. S. Dubrovinsky, N. A. Dubrovinskaia, V. Swamy, J. Muscat, N. M. Harrison, R. Ahuja, B. Holm, and B. Johansson, "Materials science: The hardest known oxide," *Nature*, vol. 410, pp. 653–654, apr 2001.

[82] M. Mattesini, J. S. de Almeida, L. Dubrovinsky, N. Dubrovinskaia, B. Johansson, and R. Ahuja, "Cubic TiO_2 as a potential light absorber in solar-energy conversion," *Phys. Rev. B*, vol. 70, p. 115101, Sep 2004.

[83] S. Andersson and A. Magnéli, "Diskrete titanoxydphasen im zusammensetzungsbereich $TiO_{1.75}TiO_{1.90}$," *Naturwissenschaften*, vol. 43, no. 21, pp. 495–496, 1956.

[84] L. Bursill and B. Hyde, "Crystallographic shear in the higher titanium oxides: Structure, texture, mechanisms and thermodynamics," *Progress in solid state chemistry*, vol. 7, pp. 177–253, 1972.

[85] Y. Le Page and P. Strobel, "'structural chemistry of magnéli phases Ti_nO_{2n-1} $(4 \leq n \leq 9)$. iii. valence ordering of titanium in Ti_6O_{11} at 130 k'," *Journal of Solid State Chemistry*, vol. 47, pp. 6–15, mar 1983.

[86] J. B. Goodenough, "Direct cation- -cation interactions in several oxides," *Phys. Rev.*, vol. 117, pp. 1442–1451, Mar 1960.

[87] J. Zhang, P. Zhou, J. Liu, and J. Yu, "New understanding of the difference of photocatalytic activity among anatase, rutile and brookite TiO_2," *Phys. Chem. Chem. Phys.*, vol. 16, pp. 20382–20386, aug 2014.

[88] C. Colbeau-Justin, "Structural influence on charge-carrier lifetimes in TiO_2 powders studied by microwave absorption," *Journal of Materials Science*, vol. 38, no. 11, pp. 2429–2437, 2003.

[89] M. D. Earle, "The electrical conductivity of titanium dioxide," *Physical Review*, vol. 61, no. 1-2, p. 56, 1942.

[90] L. Forro, O. Chauvet, D. Emin, L. Zuppiroli, H. Berger, and F. Lévy, "High mobility n -type charge carriers in large single crystals of anatase (TiO_2)," *Journal of Applied Physics*, vol. 75, pp. 633–635, jan 1994.

[91] D. C. Cronemeyer and M. A. Gilleo, "The optical absorption and photoconductivity of rutile," *Phys. Rev.*, vol. 82, pp. 975–976, Jun 1951.

[92] D. C. Cronemeyer, "Electrical and optical properties of rutile single crystals," *Phys. Rev.*, vol. 87, pp. 876–886, Sep 1952.

[93] R. G. Breckenridge and W. R. Hosler, "Electrical properties of titanium dioxide semiconductors," *Phys. Rev.*, vol. 91, pp. 793–802, Aug 1953.

[94] F. Zuo, L. Wang, T. Wu, Z. Zhang, D. Borchardt, and P. Feng, "Self-doped Ti^{3+} enhanced photocatalyst for hydrogen production under visible light," *Journal of the American Chemical Society*, vol. 132, no. 34, pp. 11856–11857, 2010.

[95] R. Dholam, N. Patel, M. Adami, and A. Miotello, "Physically and chemically synthesized TiO_2 composite thin films for hydrogen production by photocatalytic water splitting," *International journal of hydrogen energy*, vol. 33, no. 23, pp. 6896–6903, 2008.

[96] M. Kitano, M. Takeuchi, M. Matsuoka, J. M. Thomas, and M. Anpo, "Photocatalytic water splitting using pt-loaded visible light-responsive TiO_2 thin film photocatalysts," *Catalysis Today*, vol. 120, no. 2, pp. 133–138, 2007.

[97] D. O. Scanlon, C. W. Dunnill, J. Buckeridge, S. a. Shevlin, A. J. Logsdail, S. M. Woodley, C. R. a. Catlow, M. J. Powell, R. G. Palgrave, I. P. Parkin, G. W. Watson, T. W. Keal, P. Sherwood, A. Walsh, and A. a. Sokol, "Band alignment of rutile and anatase TiO_2," *Nature materials*, vol. 12, pp. 798–801, sep 2013.

[98] P. Hoyer and R. Könenkamp, "Photoconduction in porous TiO_2 sensitized by PbS quantum dots," *Applied Physics Letters*, vol. 66, no. 3, pp. 349–351, 1995.

[99] D. Fitzmaurice, H. Frei, and J. Rabani, "Time-resolved optical study on the charge carrier dynamics in a TiO_2/AgI sandwich colloid," *The Journal of Physical Chemistry*, vol. 99, no. 22, pp. 9176–9181, 1995.

[100] R. Vogel, P. Hoyer, and H. Weller, "Quantum-sized PbS, CdS, Ag_2S, Sb_2S_3, and Bi_2S_3 particles as sensitizers for various nanoporous wide-bandgap semiconductors," *The Journal of Physical Chemistry*, vol. 98, no. 12, pp. 3183–3188, 1994.

[101] P. A. Sant and P. V. Kamat, "Interparticle electron transfer between size-quantized CdS and TiO_2 semiconductor nanoclusters," *Physical Chemistry Chemical Physics*, vol. 4, no. 2, pp. 198–203, 2002.

[102] Q. Xiang, J. Yu, and M. Jaroniec, "Enhanced photocatalytic H_2-production activity of graphene-modified titania nanosheets," *Nanoscale*, vol. 3, no. 9, pp. 3670–3678, 2011.

[103] Q. Xiang, J. Yu, and M. Jaroniec, "Synergetic effect of mos2 and graphene as cocatalysts for enhanced photocatalytic h2 production activity of tio2 nanoparticles," *Journal of the American Chemical Society*, vol. 134, no. 15, pp. 6575–6578, 2012.

[104] B. O'Regan and M. Grätzel, "A low-cost, high-efficiency solar cell based on dye-sensitized colloidal TiO_2 films," *Nature*, vol. 353, pp. 737–740, oct 1991.

[105] M. Zukalová, A. Zukal, L. Kavan, M. K. Nazeeruddin, P. Liska, and M. Grätzel, "Organized mesoporous TiO_2 films exhibiting greatly enhanced performance in dye-sensitized solar cells," *Nano Letters*, vol. 5, no. 9, pp. 1789–1792, 2005.

[106] G. J. Meyer, "Molecular approaches to solar energy conversion with coordination compounds anchored to semiconductor surfaces," *Inorganic chemistry*, vol. 44, no. 20, pp. 6852–6864, 2005.

[107] K. Schwarzburg, R. Ernstorfer, S. Felber, and F. Willig, "Primary and final charge separation in the nano-structured dye-sensitized electrochemical solar cell," *Coordination chemistry reviews*, vol. 248, no. 13, pp. 1259–1270, 2004.

[108] Y. Ohko, T. Tatsuma, T. Fujii, K. Naoi, C. Niwa, Y. Kubota, and A. Fujishima, "Multicolour photochromism of TiO_2 films loaded with silver nanoparticles," *Nature Materials*, vol. 2, no. 1, pp. 29–31, 2003.

[109] Y. Tian and T. Tatsuma, "Plasmon-induced photoelectrochemistry at metal nanoparticles supported on nanoporous TiO_2," *Chemical Communications*, vol. 16, pp. 1810–1811, 2004.

[110] Y. Tian and T. Tatsuma, "Mechanisms and applications of plasmon-induced charge separation at TiO_2 films loaded with gold nanoparticles," *Journal of the American Chemical Society*, vol. 127, no. 20, pp. 7632–7637, 2005.

[111] P. D. Cozzoli, M. L. Curri, and A. Agostiano, "Efficient charge storage in photoexcited TiO_2 nanorod-noble metal nanoparticle composite systems," *Chemical communications*, vol. 25, pp. 3186–3188, 2005.

[112] Z. W. Seh, S. Liu, M. Low, S.-Y. Zhang, Z. Liu, A. Mlayah, and M.-Y. Han, "Janus au-TiO_2 photocatalysts with strong localization of plasmonic near-fields for efficient visible-light hydrogen generation," *Advanced Materials*, vol. 24, no. 17, pp. 2310–2314, 2012.

[113] R. Asahi, T. Morikawa, H. Irie, and T. Ohwaki, "Nitrogen-Doped Titanium Dioxide as Visible-Light-Sensitive Photocatalyst: Designs, Developments, and Prospects," *Chemical Reviews*, vol. 114, pp. 9824–9852, oct 2014.

[114] T. Umebayashi, T. Yamaki, H. Itoh, and K. Asai, "Analysis of electronic structures of 3d transition metal-doped TiO_2 based on band calculations," *Journal of Physics and Chemistry of Solids*, vol. 63, no. 10, pp. 1909–1920, 2002.

[115] R. Dholam, N. Patel, A. Santini, and A. Miotello, "Efficient indium tin oxide/cr-doped-TiO_2 multilayer thin films for H_2 production by photocatalytic water-splitting," *international journal of hydrogen energy*, vol. 35, no. 18, pp. 9581–9590, 2010.

[116] R. Niishiro, H. Kato, and A. Kudo, "Nickel and either tantalum or niobium-codoped TiO_2 and $SrTiO_3$ photocatalysts with visible-light response for H_2 or O_2 evolution from aqueous solutions," *Physical Chemistry Chemical Physics*, vol. 7, no. 10, pp. 2241–2245, 2005.

[117] T. Sun, J. Fan, E. Liu, L. Liu, Y. Wang, H. Dai, Y. Yang, W. Hou, X. Hu, and Z. Jiang, "Fe and ni co-doped TiO_2 nanoparticles prepared by alcohol-thermal method: application in hydrogen evolution by water splitting under visible light irradiation," *Powder technology*, vol. 228, pp. 210–218, 2012.

[118] T. Ohno, M. Akiyoshi, T. Umebayashi, K. Asai, T. Mitsui, and M. Matsumura, "Preparation of s-doped TiO_2 photocatalysts and their photocatalytic activities under visible light," *Applied Catalysis A: General*, vol. 265, no. 1, pp. 115–121, 2004.

[119] Y. Nakano, T. Morikawa, T. Ohwaki, and Y. Taga, "Electrical characterization of band gap states in c-doped TiO_2 films," *Applied Physics Letters*, vol. 87, no. 5, p. 052111, 2005.

[120] S. U. M. Khan, M. Al-Shahry, and W. B. Ingler, "Efficient photochemical water splitting by a chemically modified n-TiO_2.," *Science (New York, N.Y.)*, vol. 297, pp. 2243–5, sep 2002.

[121] W. Krengvirat, S. Sreekantan, A.-F. M. Noor, N. Negishi, S. Y. Oh, G. Kawamura, H. Muto, and A. Matsuda, "Carbon-incorporated TiO_2 photoelectrodes prepared via rapid-anodic oxidation for efficient visible-light hydrogen generation," *international journal of hydrogen energy*, vol. 37, no. 13, pp. 10046–10056, 2012.

[122] C. Di Valentin, G. Pacchioni, and A. Selloni, "Origin of the different photoactivity of N-doped anatase and rutile TiO_2," *Physical Review B*, vol. 70, p. 085116, aug 2004.

[123] J. Yuan, M. Chen, J. Shi, and W. Shangguan, "Preparations and photocatalytic hydrogen evolution of n-doped TiO_2 from urea and titanium tetrachloride," *International Journal of Hydrogen Energy*, vol. 31, no. 10, pp. 1326–1331, 2006.

[124] Y. Nakano, T. Morikawa, T. Ohwaki, and Y. Taga, "Deep-level optical spectroscopy investigation of n-doped TiO_2 films," *Applied Physics Letters*, vol. 86, no. 13, p. 132104, 2005.

[125] T. Okato, T. Sakano, and M. Obara, "Suppression of photocatalytic efficiency in highly n-doped anatase films," *Physical Review B*, vol. 72, no. 11, p. 115124, 2005.

[126] X. Zhou, F. Peng, H. Wang, H. Yu, and J. Yang, "Effect of nitrogen-doping temperature on the structure and photocatalytic activity of the b, n-doped TiO_2," *Journal of Solid State Chemistry*, vol. 184, no. 1, pp. 134–140, 2011.

[127] J. Yuan, E. Wang, Y. Chen, W. Yang, J. Yao, and Y. Cao, "Doping mode, band structure and photocatalytic mechanism of b–n-codoped TiO_2," *Applied Surface Science*, vol. 257, no. 16, pp. 7335–7342, 2011.

[128] Y. Gai, J. Li, S.-S. Li, J.-B. Xia, and S.-H. Wei, "Design of Narrow-Gap TiO_2: A Passivated Codoping Approach for Enhanced Photoelectrochemical Activity," *Physical Review Letters*, vol. 102, p. 036402, jan 2009.

[129] R. Long and N. J. English, "Synergistic Effects on Band Gap-Narrowing in Titania by Codoping from First-Principles Calculations," *Chemistry of Materials*, vol. 22, pp. 1616–1623, mar 2010.

[130] D. Wang, Y. Zou, S. Wen, and D. Fan, "A passivated codoping approach to tailor the band edges of TiO_2 for efficient photocatalytic degradation of organic pollutants," *Applied Physics Letters*, vol. 95, no. 1, p. 012106, 2009.

[131] W.-J. Yin, H. Tang, S.-H. Wei, M. M. Al-Jassim, J. Turner, and Y. Yan, "Band structure engineering of semiconductors for enhanced photoelectrochemical water splitting: The case of TiO_2," *Physical Review B*, vol. 82, p. 045106, jul 2010.

[132] R. Sasikala, A. Shirole, V. Sudarsan, C. Sudakar, R. Naik, R. Rao, S. Bharadwaj, *et al.*, "Enhanced photocatalytic activity of indium and nitrogen co-doped TiO_2–pd nanocomposites for hydrogen generation," *Applied Catalysis A: General*, vol. 377, no. 1, pp. 47–54, 2010.

[133] X. Sun, H. Liu, J. Dong, J. Wei, and Y. Zhang, "Preparation and characterization of ce/n-codoped TiO_2 particles for production of h2 by photocatalytic splitting water under visible light," *Catalysis letters*, vol. 135, no. 3-4, pp. 219–225, 2010.

[134] X. Li, Q. Liu, X. Jiang, and J. Huang, "Enhanced Photocatalytic Activity of Ga-N Co-doped Anatase TiO_2 for Water Decomposition to Hydrogen," *Int. J. Electrochem. Sci.*, vol. 7, pp. 11519–11527, 2012.

[135] J. Zhang, J. Xi, and Z. Ji, "Mo + N Codoped TiO_2 sheets with dominant {001} facets for enhancing visible-light photocatalytic activity," *Journal of Materials Chemistry*, vol. 22, no. 34, p. 17700, 2012.

[136] J. Low, B. Cheng, and J. Yu, "Surface modification and enhanced photocatalytic CO_2 reduction performance of TiO_2 : a review," *Applied Surface Science*, vol. 392, pp. 658–686, jan 2017.

[137] M. Ge, C. Cao, J. Huang, S. Li, Z. Chen, K.-Q. Zhang, S. S. Al-Deyab, and Y. Lai, "A review of one-dimensional TiO_2 nanostructured materials for environmental and energy applications," *Journal of Materials Chemistry A*, vol. 4, no. 18, pp. 6772–6801, 2016.

[138] J. Livage, M. Henry, and C. Sanchez, "Sol-gel chemistry of transition metal oxides," *Progress in solid state chemistry*, vol. 18, no. 4, pp. 259–341, 1988.

[139] F. Pedraza and A. Vazquez, "Obtention of TiO_2 rutile at room temperature through direct oxidation of $TiCl_3$," *Journal of Physics and Chemistry of Solids*, vol. 60, no. 4, pp. 445–448, 1999.

[140] K. Nagaveni, M. S. Hegde, and G. Madras, "Structure and Photocatalytic Activity of $Ti_{1-x}M_xO_{2\pm\delta}$ (M = W, V, Ce, Zr, Fe, and Cu) Synthesized by Solution Combustion Method," *The Journal of Physical Chemistry B*, vol. 108, pp. 20204–20212, dec 2004.

[141] I. Zhitomirsky, "Cathodic electrosynthesis of titanium and ruthenium oxides," *Materials Letters*, vol. 33, no. 5-6, pp. 305–310, 1998.

[142] C. W. Dunnill, A. Kafizas, and I. P. Parkin, "CVD Production of Doped Titanium Dioxide Thin Films," *Chemical Vapor Deposition*, vol. 18, pp. 89–101, jun 2012.

[143] G. Li Puma, A. Bono, D. Krishnaiah, and J. G. Collin, "Preparation of titanium dioxide photocatalyst loaded onto activated carbon support using chemical vapor deposition: A review paper," *Journal of Hazardous Materials*, vol. 157, pp. 209–219, sep 2008.

[144] Y. Bessekhouad, D. Robert, J.-V. Weber, and N. Chaoui, "Effect of alkaline-doped TiO_2 on photocatalytic efficiency," *Journal of Photochemistry and Photobiology A: Chemistry*, vol. 167, no. 1, pp. 49–57, 2004.

[145] F. Gracia, J. Holgado, A. Caballero, and A. Gonzalez-Elipe, "Structural, optical, and photoelectrochemical properties of M^{n+}-TiO_2 model thin film photocatalysts," *The Journal of Physical Chemistry B*, vol. 108, no. 45, pp. 17466–17476, 2004.

[146] Y. Cao, W. Yang, W. Zhang, G. Liu, and P. Yue, "Improved photocatalytic activity of Sn^{4+} doped TiO_2 nanoparticulate films prepared by plasma-enhanced chemical vapor deposition," *New Journal of Chemistry*, vol. 28, no. 2, pp. 218–222, 2004.

[147] J. H. Park, S. Kim, and A. J. Bard, "Novel carbon-doped TiO_2 nanotube arrays with high aspect ratios for efficient solar water splitting," *Nano letters*, vol. 6, no. 1, pp. 24–28, 2006.

[148] M. Shen, Z. Wu, H. Huang, Y. Du, Z. Zou, and P. Yang, "Carbon-doped anatase TiO_2 obtained from TiC for photocatalysis under visible light irradiation," *Materials Letters*, vol. 60, no. 5, pp. 693–697, 2006.

[149] T. Umebayashi, T. Yamaki, S. Tanaka, and K. Asai, "Visible light-induced degradation of methylene blue on s-doped TiO_2," *Chemistry Letters*, vol. 32, no. 4, pp. 330–331, 2003.

[150] T. Umebayashi, T. Yamaki, S. Yamamoto, A. Miyashita, S. Tanaka, T. Sumita, and K. Asai, "Sulfur-doping of rutile-titanium dioxide by ion implantation: photocurrent spectroscopy and first-principles band calculation studies," *Journal of Applied Physics*, vol. 93, no. 9, pp. 5156–5160, 2003.

[151] A. Hattori, M. Yamamoto, H. Tada, and S. Ito, "A promoting effect of nh4f addition on the photocatalytic activity of sol-gel TiO_2 films," *Chemistry Letters*, vol. 27, no. 8, pp. 707–708, 1998.

[152] C. Burda, Y. Lou, X. Chen, A. C. Samia, J. Stout, and J. L. Gole, "Enhanced nitrogen doping in TiO_2 nanoparticles," *Nano letters*, vol. 3, no. 8, pp. 1049–1051, 2003.

[153] X. Chen, Y.-B. Lou, A. C. Samia, C. Burda, and J. L. Gole, "Formation of oxynitride as the photocatalytic enhancing site in nitrogen-doped titania nanocatalysts: Comparison to a commercial nanopowder," *Advanced Functional Materials*, vol. 15, no. 1, pp. 41–49, 2005.

[154] S. Sakthivel and H. Kisch, "Photocatalytic and photoelectrochemical properties of nitrogen-doped titanium dioxide," *ChemPhysChem*, vol. 4, no. 5, pp. 487–490, 2003.

[155] S. M. Prokes, J. L. Gole, X. Chen, C. Burda, and W. E. Carlos, "Defect-related optical behavior in surface modified TiO_2 nanostructures," *Advanced Functional Materials*, vol. 15, no. 1, pp. 161–167, 2005.

[156] H. Irie, Y. Watanabe, and K. Hashimoto, "Nitrogen-concentration dependence on photocatalytic activity of $TiO_{2-x}N_x$ powders," *The Journal of Physical Chemistry B*, vol. 107, no. 23, pp. 5483–5486, 2003.

[157] C. Shifu, C. Lei, G. Shen, and C. Gengyu, "The preparation of nitrogen-doped photocatalyst by ball milling," *Chemical Physics Letters*, vol. 413, no. 4, pp. 404–409, 2005.

[158] O. Diwald, T. L. Thompson, T. Zubkov, E. G. Goralski, S. D. Walck, and J. T. Yates, "Photochemical activity of nitrogen-doped rutile TiO_2 (110) in visible light," *The journal of physical chemistry B*, vol. 108, no. 19, pp. 6004–6008, 2004.

[159] X.-h. Huang, C. HU, *et al.*, "Preparation and characterization of visible-light-active nitrogen-doped TiO_2 photocatalyst," *Journal of Environmental Sciences*, vol. 17, no. 4, pp. 562–565, 2005.

[160] Y. C. Hong, C. U. Bang, D. H. Shin, and H. S. Uhm, "Band gap narrowing of TiO_2 by nitrogen doping in atmospheric microwave plasma," *Chemical Physics Letters*, vol. 413, no. 4, pp. 454–457, 2005.

[161] F. Gao, Y. Wang, J. Zhang, D. Shi, M. Wang, R. Humphry-Baker, P. Wang, S. M. Zakeeruddin, and M. Grätzel, "A new heteroleptic ruthenium sensitizer enhances the absorptivity of mesoporous titania film for a high efficiency dye-sensitized solar cell," *Chemical Communications*, 2008.

[162] S. Mathew, A. Yella, P. Gao, R. Humphry-Baker, B. F. Curchod, N. Ashari-Astani, I. Tavernelli, U. Rothlisberger, M. K. Nazeeruddin, and M. Grätzel, "Dye-sensitized solar cells with 13% efficiency achieved through the molecular engineering of porphyrin sensitizers," *Nature Chemistry*, 2014.

[163] J. Burschka, N. Pellet, S. J. Moon, R. Humphry-Baker, P. Gao, M. K. Nazeeruddin, and M. Grätzel, "Sequential deposition as a route to high-performance perovskite-sensitized solar cells," *Nature*, 2013.

[164] H.-S. Rao, W.-Q. Wu, Y. Liu, Y.-F. Xu, B.-X. Chen, H.-Y. Chen, D.-B. Kuang, and C.-Y. Su, "CdS/CdSe co-sensitized vertically aligned anatase TiO_2 nanowire arrays for efficient solar cells," *Nano Energy*, 2014.

[165] Y.-S. Lee, C. V. V. M. Gopi, A. Eswar Reddy, C. Nagaraju, and H.-J. Kim, "High performance of TiO_2/CdS quantum dot sensitized solar cells with a Cu−ZnS passivation layer," *New Journal of Chemistry*, vol. 41, no. 5, pp. 1914–1917, 2017.

[166] G. Shen, Z. Du, Z. Pan, J. Du, and X. Zhong, "Solar Paint from TiO_2 Particles Supported Quantum Dots for Photoanodes in Quantum Dot–Sensitized Solar Cells," *ACS Omega*, 2018.

[167] Z. Zhu, J. Y. Chen, K. Y. Su, and R. J. Wu, "Efficient hydrogen production by water-splitting over Pt-deposited C-HS-TiO_2 hollow spheres under visible light," *Journal of the Taiwan Institute of Chemical Engineers*, 2016.

[168] J. Zhang, X. Jin, P. I. Morales-Guzman, X. Yu, H. Liu, H. Zhang, L. Razzari, and J. P. Claverie, "Engineering the Absorption and Field Enhancement Properties of Au-TiO_2 Nanohybrids via Whispering Gallery Mode Resonances for Photocatalytic Water Splitting," *ACS Nano*, 2016.

[169] C. Wang, Q. Hu, J. Huang, L. Wu, Z. Deng, Z. Liu, Y. Liu, and Y. Cao, "Efficient hydrogen production by photocatalytic water splitting using N-doped TiO_2 film," *Applied Surface Science*, 2013.

[170] C. Han, Y. Wang, Y. Lei, B. Wang, N. Wu, Q. Shi, and Q. Li, "In situ synthesis of graphitic-C_3N_4 nanosheet hybridized N-doped TiO_2 nanofibers for efficient photocatalytic H_2 production and degradation," *Nano Research*, 2015.

[171] T. Inoue, A. Fujishima, S. Konishi, and K. Honda, "Photoelectrocatalytic reduction of carbon dioxide in aqueous suspensions of semiconductor powders," *Nature*, 1979.

[172] Y. Wang, Q. Lai, F. Zhang, X. Shen, M. Fan, Y. He, and S. Ren, "High efficiency photocatalytic conversion of CO_2 with H_2O over Pt/TiO_2 nanoparticles," *RSC Adv.*, vol. 4, pp. 44442–44451, dec 2014.

[173] Z. Zhang, Z. Huang, X. Cheng, Q. Wang, Y. Chen, P. Dong, and X. Zhang, "Product selectivity of visible-light photocatalytic reduction of carbon dioxide using titanium dioxide doped by different nitrogen-sources," *Applied Surface Science*, vol. 355, pp. 45–51, nov 2015.

[174] C. M. Teh and A. R. Mohamed, "Roles of titanium dioxide and ion-doped titanium dioxide on photocatalytic degradation of organic pollutants (phenolic compounds and dyes) in aqueous solutions: A review," *Journal of Alloys and Compounds*, vol. 509, pp. 1648–1660, feb 2011.

[175] Z. Shayegan, C.-S. Lee, and F. Haghighat, "TiO_2 photocatalyst for removal of volatile organic compounds in gas phase – A review," *Chemical Engineering Journal*, vol. 334, pp. 2408–2439, feb 2018.

[176] I. S. Cho, C. H. Lee, Y. Feng, M. Logar, P. M. Rao, L. Cai, D. R. Kim, R. Sinclair, and X. Zheng, "Codoping titanium dioxide nanowires with tungsten and carbon for enhanced photoelectrochemical performance," *Nature Communications*, vol. 4, p. 1723, apr 2013.

[177] N. Delegan, R. Daghrir, P. Drogui, and M. El Khakani, "Bandgap tailoring of in-situ nitrogen-doped TiO_2 sputtered films intended for electrophotocatalytic applications under solar light," *Journal of Applied Physics*, vol. 116, p. 153510, oct 2014.

[178] S. Liu, J. Yu, and W. Wang, "Effects of annealing on the microstructures and photoactivity of fluorinated N-doped TiO_2.," *Physical chemistry chemical physics : PCCP*, vol. 12, pp. 12308–15, oct 2010.

[179] R. Pandiyan, N. Delegan, A. Dirany, P. Drogui, and M. El Khakani, "Probing the Electronic Surface Properties and Bandgap Narrowing of in situ N, W, and (W,N) Doped Magnetron-Sputtered TiO_2 Films Intended for Electro-Photocatalytic Applications," *The Journal of Physical Chemistry C*, vol. 120, pp. 631–638, jan 2016.

[180] G. Hyett, M. A. Green, and I. P. Parkin, "The Use of Combinatorial Chemical Vapor Deposition in the Synthesis of $Ti_{3-\delta}O_4N$ with $0.06 < \delta < 0.25$: A Titanium Oxynitride Phase Isostructural to Anosovite," *Journal of the American Chemical Society*, vol. 129, pp. 15541–15548, dec 2007.

[181] R. Daghrir, P. Drogui, N. Delegan, and M. A. El Khakani, "Electrochemical degradation of chlortetracycline using N-doped Ti/TiO_2 photoanode under sunlight irradiations," *Water Research*, vol. 47, pp. 6801–6810, nov 2013.

[182] R. Daghrir, P. Drogui, N. Delegan, and M. A. El Khakani, "Removal of chlortetracycline from spiked municipal wastewater using a photoelectrocatalytic process operated under sunlight irradiations.," *The Science of the total environment*, vol. 466-467, pp. 300–5, jan 2014.

[183] L. H. Santos, A. Araújo, A. Fachini, A. Pena, C. Delerue-Matos, and M. Montenegro, "Ecotoxicological aspects related to the presence of pharmaceuticals in the aquatic environment," *Journal of Hazardous Materials*, vol. 175, pp. 45–95, mar 2010.

[184] M. D'Arienzo, N. Siedl, A. Sternig, R. Scotti, F. Morazzoni, J. Bernardi, and O. Diwald, "Solar Light and Dopant-Induced Recombination Effects: Photoactive Nitrogen in TiO_2 as a Case Study," *The Journal of Physical Chemistry C*, vol. 114, pp. 18067–18072, oct 2010.

[185] R. Katoh, A. Furube, K.-i. Yamanaka, and T. Morikawa, "Charge Separation and Trapping in N-Doped TiO_2 Photocatalysts: A Time-Resolved Microwave Conductivity Study," *The Journal of Physical Chemistry Letters*, vol. 1, pp. 3261–3265, nov 2010.

[186] S. Sathasivam, D. S. Bhachu, Y. Lu, N. Chadwick, S. a. Althabaiti, A. O. Alyoubi, S. N. Basahel, C. J. Carmalt, and I. P. Parkin, "Tungsten Doped TiO_2 with Enhanced Photocatalytic and Optoelectrical Properties via Aerosol Assisted Chemical Vapor Deposition," *Scientific Reports*, vol. 5, p. 10952, jun 2015.

[187] A. Kubacka, G. Colón, and M. Fernández-García, "Cationic (V, Mo, Nb, W) doping of TiO_2–anatase: A real alternative for visible light-driven photocatalysts," *Catalysis Today*, vol. 143, pp. 286–292, may 2009.

[188] O. Lorret, D. Francová, G. Waldner, and N. Stelzer, "W-doped titania nanoparticles for UV and visible-light photocatalytic reactions," *Applied Catalysis B: Environmental*, vol. 91, pp. 39–46, sep 2009.

[189] J. Li, J. Xu, W. L. Dai, H. Li, and K. Fan, "One-pot synthesis of twist-like helix tungsten-nitrogen-codoped titania photocatalysts with highly improved visible light activity in the abatement of phenol," *Applied Catalysis B: Environmental*, vol. 82, no. 3-4, pp. 233–243, 2008.

[190] T. Mishra, M. Mahato, N. Aman, J. N. Patel, and R. K. Sahu, "A mesoporous WN co-doped titania nanomaterial with enhanced photocatalytic aqueous nitrate removal activity under visible light," *Catalysis Science & Technology*, vol. 1, no. 4, p. 609, 2011.

[191] T. TERANISHI, "Broadband spectroscopy of dielectrics and oxygen-ion conductors," *Journal of the Ceramic Society of Japan*, vol. 125, no. 7, pp. 547–551, 2017.

[192] T. Teranishi, H. Hayashi, A. Kishimoto, and T. Tsurumi, "Broadband spectroscopy of the complex conductivity of polycrystalline yttria-stabilized zirconia," *Materials Science and Engineering: B*, vol. 177, pp. 69–73, jan 2012.

[193] T. Teranishi, N. Akiyama, K. Ayano, H. Hayashi, A. Kishimoto, K. Fujimori, T. Hoshina, H. Takeda, and T. Tsurumi, "Quasi-millimeter-wave absorption behavior in Y/Yb-stabilized zirconia ceramics," *Applied Physics Letters*, vol. 100, p. 242903, jun 2012.

[194] V. Çelik and E. Mete, "Range-separated hybrid exchange-correlation functional analyses of anatase TiO_2 doped with W, N, S, W/N, or W/S," *Physical Review B*, vol. 86, p. 205112, nov 2012.

[195] X. Cui, S. Rong, Y. Cao, Y. Yin, S. Li, and M. Li, "One-step hydrothermal synthesis of nitrogen and tungsten codoped TiO_2 nanorods with high visible light photocatalytic activity," *Applied Physics A*, vol. 113, pp. 47–51, oct 2013.

[196] S. S. Thind, G. Wu, and A. Chen, "Synthesis of mesoporous nitrogen–tungsten co-doped TiO_2 photocatalysts with high visible light activity," *Applied Catalysis B: Environmental*, vol. 111-112, pp. 38–45, jan 2012.

[197] A. Kubacka, B. Bachiller-Baeza, G. Colón, and M. Fernández-García, "Doping level effect on sunlight-driven W,N-co-doped TiO_2-anatase photo-catalysts for aromatic hydrocarbon partial oxidation," *Applied Catalysis B: Environmental*, vol. 93, pp. 274–281, jan 2010.

[198] A. Folli, J. Z. Bloh, E.-P. Beukes, R. F. Howe, and D. E. Macphee, "Photogenerated Charge Carriers and Paramagnetic Species in (W,N)-Codoped TiO_2 Photocatalysts under Visible-Light Irradiation: An EPR Study," *The Journal of Physical Chemistry C*, vol. 117, pp. 22149–22155, oct 2013.

[199] J. Z. Bloh, A. Folli, and D. E. Macphee, "Adjusting Nitrogen Doping Level in Titanium Dioxide by Codoping with Tungsten: Properties and Band Structure of the Resulting Materials," *The Journal of Physical Chemistry C*, vol. 118, pp. 21281–21292, sep 2014.

[200] M. C. Biesinger, B. P. Payne, A. P. Grosvenor, L. W. Lau, A. R. Gerson, and R. S. Smart, "Resolving surface chemical states in XPS analysis of first row transition metals, oxides and hydroxides: Cr, Mn, Fe, Co and Ni," *Applied Surface Science*, vol. 257, pp. 2717–2730, jan 2011.

[201] A. K. Rumaiz, J. C. Woicik, E. Cockayne, H. Y. Lin, G. H. Jaffari, and S. I. Shah, "Oxygen vacancies in N doped anatase TiO_2: Experiment and first-principles calculations," *Applied Physics Letters*, vol. 95, p. 262111, dec 2009.

[202] M. J. Jackman, A. G. Thomas, and C. Muryn, "Photoelectron Spectroscopy Study of Stoichiometric and Reduced Anatase TiO_2 (101) Surfaces: The Effect of Subsurface Defects on Water Adsorption at Near-Ambient Pressures," *The Journal of Physical Chemistry C*, vol. 119, pp. 13682–13690, jun 2015.

[203] J. Lynch, C. Giannini, J. K. Cooper, A. Loiudice, I. D. Sharp, and R. Buonsanti, "Substitutional or Interstitial Site-Selective Nitrogen Doping in TiO_2 Nanostructures," *The Journal of Physical Chemistry C*, vol. 119, pp. 7443–7452, apr 2015.

[204] N. Laidani, P. Cheyssac, J. Perrière, R. Bartali, G. Gottardi, I. Luciu, and V. Micheli, "Intrinsic defects and their influence on the chemical and optical properties of TiO_{2-x} films," *Journal of Physics D: Applied Physics*, vol. 43, no. 48, p. 485402, 2010.

[205] D. M. Mattox, *The Foundations of Vacuum Coating Technology*. Berlin, Heidelberg: Springer Berlin Heidelberg, 2003.

[206] S. M. Rossnagel, "Sputter deposition for semiconductor manufacturing," *IBM Journal of Research and Development*, vol. 43, pp. 163–179, Jan 1999.

[207] S. M. Rossnagel, "Thin film deposition with physical vapor deposition and related technologies," *Journal of Vacuum Science & Technology A: Vacuum, Surfaces, and Films*, vol. 21, no. 5, pp. S74–S87, 2003.

[208] P. Walke, R. Bouregba, A. Lefevre, G. Parat, F. Lallemand, F. Voiron, B. Mercey, and U. Lüders, "Giant dielectric constant in TiO_2/Al_2O_3 nanolaminates grown on doped silicon substrate by pulsed laser deposition," *Journal of Applied Physics*, vol. 115, p. 094103, mar 2014.

Part IV

Articles

Article 1

Bandgap tailoring of *in-situ* nitrogen-doped TiO_2 sputtered films intended for electrophotocatalytic applications under solar light; N. Delegan, R. Daghrir, P. Drogui, and M. A. El Khakani; Journal of Applied Physics 116, 153510 (2014)

Bandgap tailoring of *in-situ* nitrogen-doped TiO_2 sputtered films intended for electrophotocatalytic applications under solar light

N. Delegan,[1] R. Daghrir,[2] P. Drogui,[2] and M. A. El Khakani[1,a)]
[1]*Institut National de la Recherche Scientifique, Centre Énergie, Matériaux et Télécommunications, 1650, Boulevard Lionel-Boulet, Varennes, Québec J3X-1S2, Canada*
[2]*Institut National de la Recherche Scientifique, Centre Eau, Terre et Environnement, 490 Rue de la Couronne, Québec G1K-9A9, Canada*

(Received 11 July 2014; accepted 7 October 2014; published online 20 October 2014)

We report on a reactive RF-sputtering process permitting the *in-situ* nitrogen doping of TiO_2 films in order to shift their photoactivity from UV to visible range. By carefully controlling the relative nitrogen-to-argon mass flow rate ratio (within the 0%–25% range) in the sputter deposition chamber, TiO_2:N films were grown with nitrogen contents ranging from 0 to 6.2 at. %, as determined by high-resolution X-ray spectroscopy measurements. A systematic investigation of the crystalline structure of the TiO_2:N films, as a function of their N content, revealed that low N contents (0.2–0.3 at. %) induce crystallization in the rutile phase while higher N contents ($\geq$1.4 at. %) were accompanied with the recovery of the anatase structure with an average crystallite size of ~35 nm. By using both UV-Vis absorption and spectroscopic ellipsometry measurements, we were able to quantitatively determine the bandgap (E_g) variation of the TiO_2:N films as a function of their N content. Thus, we have demonstrated that the E_g of the TiO_2:N films effectively narrows from 3.2 eV down to a value as low as ~2.3 eV for the optimal N doping concentration of 3.4 at. % (higher N incorporation does not translate into further red shifting of the TiO_2:N films' E_g). The photoactivity of the TiO_2:N films under visible light was confirmed through electro-photocatalytic decomposition of chlortetracycline (CTC, an emerging water pollutant) under standard 1.5AM solar radiation. Thus, CTC degradation efficiencies of up to 98% were achieved with 2 hours process cycles under simulated solar light. Moreover, the electro-photocatalytic performance of the TiO_2:N films is shown to be directly correlated to their optoelectronic properties (namely their bandgap narrowing). © *2014 AIP Publishing LLC*. [http://dx.doi.org/10.1063/1.4898589]

I. INTRODUCTION

Titanium dioxide (TiO_2) continues to attract high interest as a semiconducting photoactive material for different applications such as solar energy conversion,[1,2] self-cleaning,[1] and waste-water purification through photoelectrochemical processing.[1,3] Its widespread use in many technological sectors is mainly motivated by its UV-photoabsorbance, high optochemical stability, non-toxicity, low cost, and abundance.[1,4,5] From an optoelectronic point of view, TiO_2 is an n-type semiconductor with a wide intrinsic bandgap (E_g) in the UV, namely 3.0 eV and 3.2 eV for rutile and anatase polymorphs, respectively. Since the UV light represents only ~4% of the solar spectral irradiance, it is highly desirable to extend the photoactivity of TiO_2 to the visible range (which represents ~40% of the solar spectrum). In this context, among the strategies proposed to narrow the band-gap of TiO_2, atomic doping arises as the approach of choice as it preserves the intrinsic photocatalytic properties of TiO_2 while potentially extending its photosensitivity in the visible.[1,4–7] Anions have been outlined to be the best doping candidates because non-metals have been reported to provide greater thermal stability, integration simplicity, and lower rates of charge carrier recombination as compared to cationic doping.[1,4] Among possible anion dopants of TiO_2, nitrogen stands out as the most effective candidate because of its easier incorporation in the TiO_2 lattice and the energetic compatibility for the mixing of its p states with the O_{2p} ones.[1,4,5,7] The N doping induced bandgap narrowing of TiO_2 mainly occurs through the insertion of defect associated states in the gap above the O_{2p} states, as proposed by theoretical calculations and confirmed by recent experimental work.[1,4–11] More specifically, it has been demonstrated that two deep levels are formed in the doped TiO_2 films at ~1.0 and ~2.5 eV below the conduction band associated with O vacancies and N doping (E_g narrowing), respectively.[10,12,13] Although some authors have used physical vapor deposition methods to investigate the N doping of TiO_2,[7,9,10,14–16] most of the experimental work on this subject has focused on the use of chemical processing routes (such as sol-gel and hydrothermal methods)[1,4,6,11,13,17–20] mainly because of their low cost and ease of implementation. However, the chemically processed films generally suffer from both the reproducibility issues and the inherent presence of residual contaminants, which could hinder a precise control of the doping levels and thereby a better understanding of the effect of dopants on the optoelectronic properties of the N doped TiO_2 films.[1,4] Moreover, although some reduced E_g values of N doped TiO_2 films have been sparsely reported,[4,9,15] thorough studies on the quantitative measurement of this key parameter and its systematic variation with the N-doping level are still lacking.

a)Author to whom correspondence should be addressed. Eletronic mail: elkhakani@emt.inrs.ca

In this paper, we report on the development of a reactive magnetron-sputtering process for the *in-situ* incorporation of nitrogen atoms into highly pure TiO_2 films. By controlling the N_2-to-Ar gas flow ratio in the RF-sputtering plasma source, we were able to tune at will the N incorporation rate into the films, and achieve N doped TiO_2 (TiO_2:N) films with N contents varying from 0 to 6.2 at.%. The effect of N doping of the TiO_2 lattice on both the microstructural and optoelectronic properties of the sputter-deposited TiO_2:N films was systematically investigated as a function of their N doping level. A particular attention was given to the quantitative determination of the bandgap of the TiO_2:N films. This has permitted in particular to access, for the first time, the systematic variation of E_g of TiO_2:N films as a function of their N doping level. We were thus able to pinpoint the existence of an optimal N content which yields the narrowest E_g value of 2.25 eV. This significant bandgap reduction (by ~1 eV) of the initial 3.2 eV of undoped anatase TiO_2 films is directly related to the introduction of N bonding states in the TiO_2:N films. Finally, the developed TiO_2:N films were shown to be very effective for the electro-photocatalytic (EPC) degradation of chlorotetracycline (an antibiotic residual contaminant in water) under simulated solar light. More interestingly, the highest degradation rate (~98.5%) of chlortetracycline (CTC) was achieved with the TiO_2:N photoanodes possessing the narrowest E_g value of 2.25 eV, highlighting a direct correlation between bandgap narrowing and photocatalytic efficiencies.

II. EXPERIMENTAL

The TiO_2:N films were sputter-deposited from a 3″-diameter TiO_2 target (99.995% purity) using an RF (13.56 MHz) magnetron sputtering system at a constant power density of 7.7 W/cm^2. Prior to deposition, the chamber was cryo-pumped to a base pressure of 2×10^{-8} Torr. High purity Ar (99.999%) and N_2 (99.995%) gases were then introduced in the chamber. The gas flow rates were monitored to keep a constant pressure of 1.44 mTorr in the chamber during the sputter-deposition process. In order to control the N incorporation in the TiO_2:N films, the relative nitrogen mass flow rate ratio R (i.e., $[N_2]/([N_2]+[Ar])$ was varied between 0 and 25%. The TiO_2:N films were simultaneously deposited onto different substrates, including: (i) undoped and double side-polished Si(100), (ii) quartz, and (iii) deployed (10 cm × 11 cm) Ti-grids. The substrates were mounted on a holder located off-axis at a distance of 20 cm from the target, and heated by a quartz lamp heater of which temperature was kept constant at 650 °C during deposition (which corresponds to an on-substrate temperature of ~470 °C). Prior to film deposition, the target was systematically sputter-cleaned with Ar ions for ~15 min with the shutters closed. The thickness of the TiO_2:N films was *in-situ* monitored by means of a calibrated quartz-crystal microbalance and *ex-situ* measured through cross-section scanning electron microscopy (SEM) observations by means of a Jeol JSM-6300F SEM system. No post acceleration voltage was intentionally applied to the substrates during the sputter-deposition process (they were nonetheless subjected to a built-in plasma sheath bias of ~−13 V during their growth).

The atomic composition and chemical bonding states of the films were systematically investigated by means of X-ray photoelectron spectroscopy (XPS) and Fourier-transform infrared (FTIR) spectroscopy. The XPS spectra were collected by using the ESCALAB 220I-XL spectrophotometer, equipped with an $Al_{K\alpha}$ (1486.6 eV) monochromatic source, after a systematic *in-situ* surface cleaning by means of 5 keV Ar^+ ion sputtering gun. The in-depth composition of the films was determined by performing elastic recoil detection with time of flight (ERD-TOF) measurements using a Ge^{9+} ion beam with an incident energy of 55 MeV and beam current of 1 nA. The FTIR spectra were acquired by using a Thermo Electron Corp Nicolet-6700 spectrometer. The crystalline structure of the films was characterized by means of a Panalytical X-Pert Pro X-ray diffractometer (XRD) system using $Cu_{K\alpha}$ radiation of 1.5418 *i*. The optical properties of the TiO_2:N films were systematically characterized by measuring both their UV-Vis spectra (using an Agilent/Varian Cary 5000 system) and their ellipsometric spectra (using a J.A. Woollam M-2000 ellipsometer). Thus, their E_g values were independently derived from both UV-Vis Tauc plot modeling and ellipsometry data analysis. The EPC properties of the TiO_2:N films deposited onto deployed titanium-grid substrates (used as photoanodes) were evaluated in an EPC reactor of which details are described elsewhere.[3]

III. RESULTS AND DISCUSSION

Figure 1(a) (left-hand Y-axis) shows the nitrogen incorporation effectiveness of our magnetron sputter process as a function of the $[N_2]/([N_2]+[Ar])$ flow rate ratio (R). The N content of the films was determined by means of XPS analysis of the N1s, Ti2p, and O1s core level XPS spectra while using their corresponding sensitivity factors.[21] In Figure 1(a), three N incorporation regimes can be distinguished: (i) for the initial regime ($0\% \le R \le 5\%$), a very low incorporation (low slope) is observed because of the rather limited amount of present and dissociated N atoms in the plasma; (ii) in the intermediate regime ($5 \le R \le 15\%$), the N incorporation is seen to increase steadily (with a much steeper slope) with R to reach a maximum N content value of 6.2 at. %. In this regime, interaction between Ar ions and N_2 molecules in the plasma is more effective and leads to an increasing production of atomic N as the N_2 gas flow in increased; and (iii) finally, in the saturation regime ($R \ge 15\%$), further increasing of R does not translate into higher N incorporation rates. In contrast, the N content of the TiO_2:N films tends to slightly decrease from 6.2 to ~5 at. % when R is increased from 15% to 25%. This is highly likely a consequence of the balance of the energy available in the plasma to ionize and accelerate Ar atoms, on one hand, and to dissociate N_2 molecules into N atoms on the other hand. Thus, as the N_2 proportion in increased in the carrier gas, an increasing part of the energy available in the plasma serves to dissociate the N_2 molecules, leaving thereby less energy to produce Ar ions, which in turn, translates into less efficient sputtering process. This is consistently reflected from the variation of the sputter-deposition rate with the increase of the relative proportion of N_2 in the sputtering gas (right hand side Y-axis of

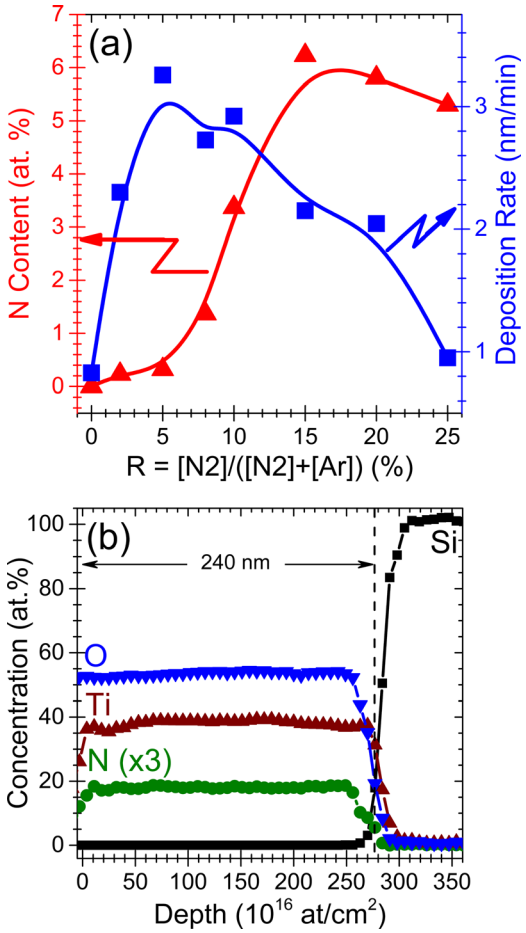

FIG. 1. (a) Nitrogen incorporation efficiency and deposition rate as a function of the nitrogen flow rate ratio (R) in the sputter-deposition process of TiO_2:N; (b) typical ERD-TOF depth profiles of Ti, O and N of the TiO_2:N films deposited on a silicon substrate.

Fig. 1). Figure 1(a) clearly shows that while the deposition rate increases in the low flow ratio regime ($0 \le R \le 5\%$) up to a maximum of ~3.3 nm/min at $R = 5\%$, it continuously drops with higher R values to reach a value of ~1 nm/min at $R = 25\%$. In terms of N incorporation, our results point out the existence of a maximum N content of ~6.2 at. % that can be achieved at $R = 15\%$. This maximum value results from a trade-off between the abundance of N_2 molecules in the plasma gas and their effective dissociation into atomic N without compromising the sputtering rate of the target. On the other hand, the in-depth compositional uniformity of the TiO_2:N films was investigated by means of ERD-TOF measurements. Figure 1(b) shows typical Ti, O, and O elemental profiles as a function of the film thickness for $R = 15\%$. The N depth profile confirms that the N doping is fairly uniform through all the thickness of the TiO_2:N film. This compositional uniformity of the films is important to simplify the modeling (the film is considered as one layer with a constant N content) used to extract the bandgap values from the ellipsometry spectra analysis.

By examining the morphology of the sputter-deposited TiO_2:N films, via SEM observations, as a function of their N content, no significant differences have been observed. Indeed, the TiO_2:N films were generally found to exhibit a

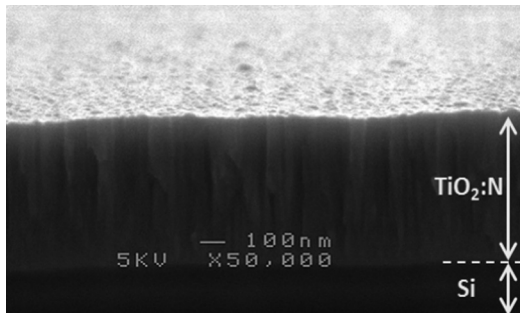

FIG. 2. Typical cross-sectional SEM micrograph of the sputter-deposited TiO_2:N films. The image shown here is for a film with a N doping content of 3.4 at. %.

relatively dense columnar microstructure and certain intercolumnar nanoporosity, regardless of their N content. This nanoporosity remains nonetheless very low (of the order of few % at most), and would have a little effect on the overall dielectric constant of the films. Figure 2 shows a typical cross-sectional SEM image of the 3.4 at. % N doped TiO_2 films; where the film is seen to have a thickness is of ~540 nm and consists of densely packed TiO_2 columns with an average diameter of ~40 nm. Figure 3 shows the XRD

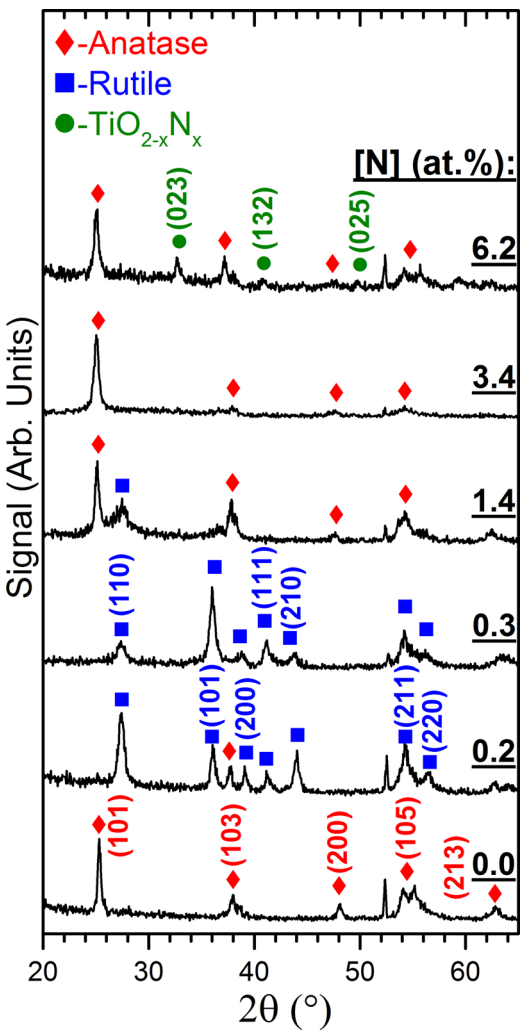

FIG. 3. Typical XRD spectra of the sputter-deposited TiO_2:N films as a function of their N content.

patterns of the sputter-deposited TiO_2:N films on Si(100) substrates. The undoped TiO_2 films expectedly crystallize in the anatase phase with its (101), (103), (200), and (105) characteristic diffraction peaks.[22] As soon as a small amount of N (i.e., 0.2 and 0.3 at. %) is incorporated in the TiO_2:N films, their crystalline structure undergoes a transition into the denser rutile phase. For higher N contents ($\geq$1.4 at. %), the TiO_2:N films recover their anatase crystalline structure with an average crystallite size of ~35 nm, as determined via the Scherrer equation[22] from the full width at half maximum (FWHM) of the (101) diffraction peak. Incidentally, this crystallite size is rather comparable to the feature size of 40 nm directly observed in the SEM micrographs. For the highest N content of 6.2 at. %, although weak in intensity, some additional XRD peaks were also detected and could be associated most probably with the presence of $TiO_{2-x}N_x$ titanium oxynitride phase.[23] It is worth recalling that the anatase phase is more appropriate for EPC applications because of its indirect bandgap which is associated with longer lifetime of the photocharges, as compared to the rutile phase.[5,24] The anatase-rutile-anatase transition revealed by the XRD measurements, as the N content of the TiO_2:N films is increased, was also confirmed by the FTIR absorption spectra. Indeed, Figure 4 clearly shows that the position of the main absorption band associated with Ti-O stretching vibrations shifts from the rutile position of ~505 cm^{-1} (for the low N contents of 0.2 and 0.3 at. %) to the anatase characteristic wavenumber of 440 cm^{-1} (Ref. 19) (for N contents $\geq$ 1.4 at. %). It is also worth noting the slight shift of the anatase band position towards slightly higher wavenumbers (from ~440 to 480 cm^{-1}) as the N content is increased (Fig. 4). This shift has been interpreted as a consequence of a progressive substitution of oxygen atoms by N ones in the TiO_2 lattice.[25] Moreover, a small shoulder centered around 620 cm^{-1} can be noticed particularly for the TiO_2:N films doped at 6.2 at. %; this feature is thought to be due to the presence of Ti-N bonds.[26] The presence of such Ti-N bonds is in accordance with the XRD spectra where a titanium oxynitride phase was detected for the 6.2 at. % N-doped films, suggesting an increasing substitution of O atoms by the incorporated N ones in the TiO_2 lattice. The observed anatase-to-rutile phase transition (occurring at 0.2–0.3 at. %) is believed to be due to oxygen vacancies,[24] which result from a lack of oxygen in the sputtering gas (mainly composed of Argon and a small amount of N_2). At higher nitrogen incorporation levels (at N contents $\geq$ 1.4 at. %), most of the oxygen vacancies are filled with the increasingly available nitrogen atoms allowing thereby the recovery of the anatase polymorph. This progressive predominance of substitutional doping as the N content of the TiO_2:N films is increased will be also confirmed by the XPS analysis.

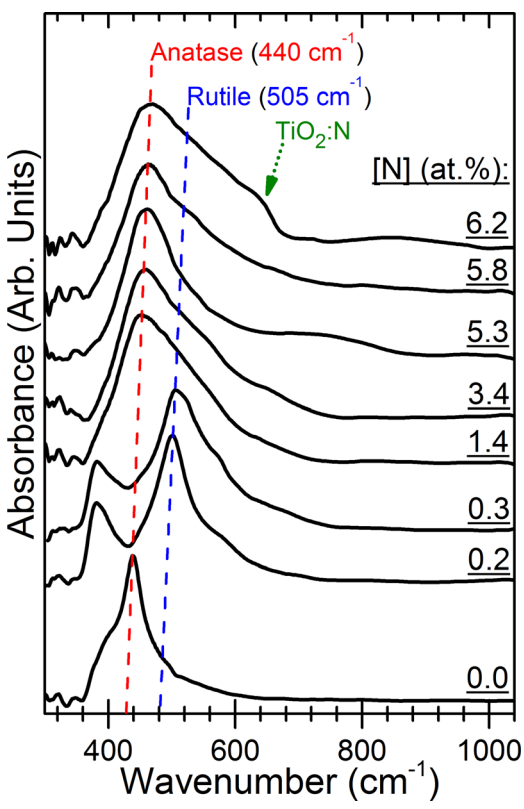

FIG. 4. FTIR absorption spectra of the sputter-deposited TiO_2:N films as a function of their N content.

Figure 5 shows the high resolution XPS spectra of the O1s, Ti2p, and N1s core levels of the TiO_2:N films as a function of their N contents. These spectra were deconvoluted into different components corresponding to different possible local environments. For the undoped TiO_2 films, the Ti2p peak (Fig. 5(b)) can be decomposed into two main components corresponding to two oxidation states of Ti, namely Ti^{III} and Ti^{IV} (centered around 457.5 eV and 459.6 eV for $Ti2p_{1/2}$, respectively[13,16,20]). These bonding states can also be mirror-derived from the analysis of the O1s core level (Fig. 5(a)), which also consists of two chemical states (located around 531.7 eV and 530.8 eV corresponding to O in TiO_{2-x} and TiO_2, respectively[16]). The deconvolution of the O1s peak suggests that the undoped TiO_2 films is mostly composed of stoichiometric TiO_2 (~62%) with the presence of certain amount of oxygen vacancies in the films that would correspond to TiO_{2-x} local environments. The presence of oxygen vacancies is known to originate from the preferential sputtering of oxygen atoms by argon ions in the sputter-deposition process[27] and subsequently from the N doping process in itself.[8] As nitrogen is introduced into the films, the N1s peak is seen to increase in intensity (Fig. 5(c)). Concomitantly, a $Ti2p_{3/2}$ shoulder (located around 455.6 eV) becomes more and more noticeable in the Ti2p peak as the N content of the films is increased. This component indicates the existence of Ti-O bonds with N atoms in their surrounding (leading to a slightly lower binding energy), as result of the substitution of N for O atoms in the TiO_2 lattice. Likewise, the N1s peak can be also deconvoluted into 2 main components centered on 397.0 eV and 398.4 eV, which can be attributed to two main different local environments of the N atoms. While the main component centered around 397.0 eV is generally attributed to N^- anions in substitutional N-Ti bondings (a binding energy almost identical to that of N-Ti bonds in TiN of ~396.9 eV)[7,14,16,18] the second component located at 398.4 eV has been attributed to N-O-Ti type of bindings as the N^- anions would be in a state of higher binding

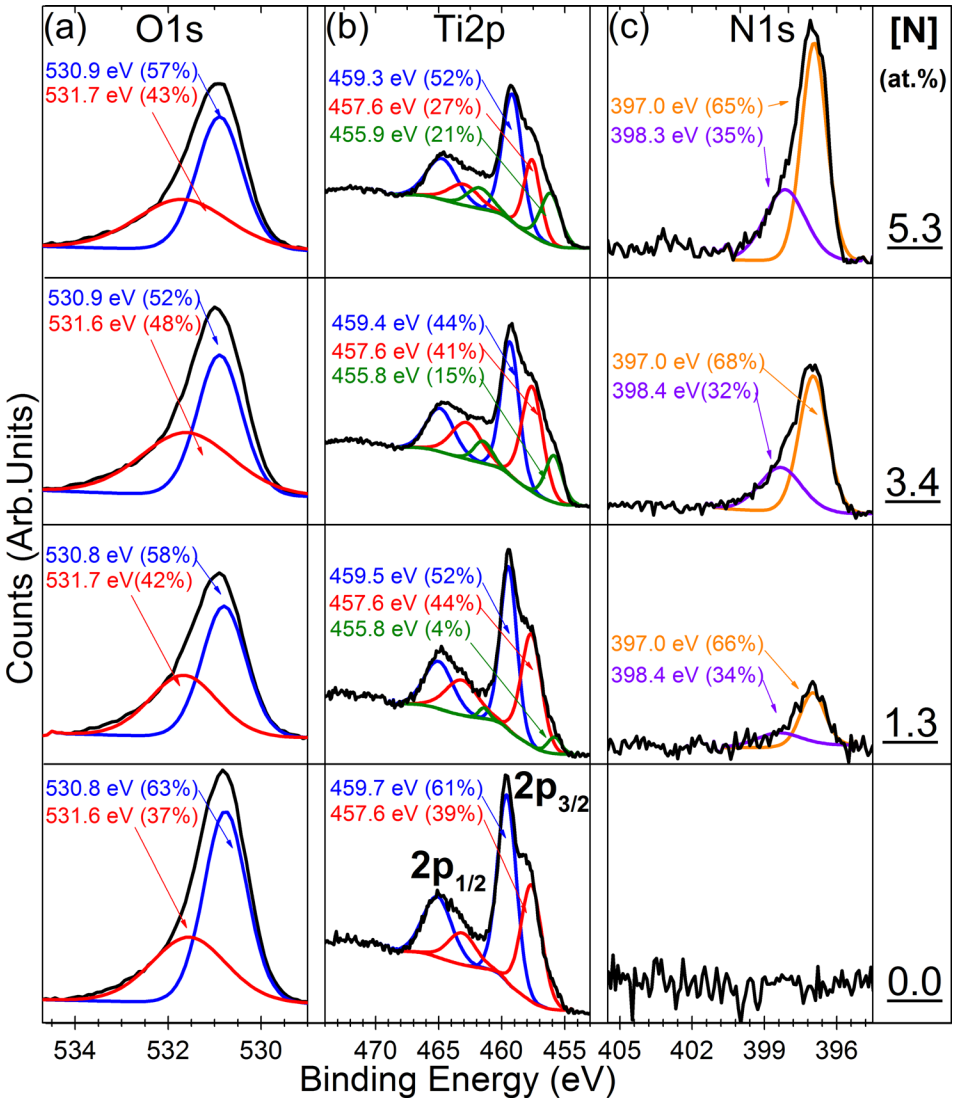

FIG. 5. High-resolution XPS spectra of the O1s (a), Ti2p (b), and N1s (c) core levels of the TiO_2:N films as a function of their N content.

energy.[5,18] Consistently, the O1s peak was also found to contain two main following components: (i) the first one located at 530.8 eV is known to be due to O-Ti bonds in TiO_2; and (ii) the second component located at 531.7 eV for undoped TiO_2, of which position slightly shifts to higher energies, and increases in width as the N content is increased (to reach 532.0 eV for the 5.3 at. % N-doped films), is most likely due to O-Ti bonds in oxygen-deficient TiO_{2-x} (Ref. 16) and in Ti-O-N oxynitride type of bonding.[20]

The effect of doping on the optical absorption properties of the TiO_2:N films was systematically investigated as a function of their N content. Figure 6(a) shows UV-VIS transmission spectra of TiO_2:N films, deposited on quartz substrates, for different increasing N contents. The most striking feature shown by Figure 6(a) is the evident red shift of the absorption edge of the spectra from about 320 nm for undoped TiO_2 films to ~480 nm for TiO_2:N films with N contents $\geq$ 3.4 at. %. This optical properties change of the TiO_2:N films as their N content is increased can be visually noticed from their color, which is found to change significantly from a transparent very light bluish (for undoped-TiO_2 films) to more absorbing greenish-yellow (for the 3.4 at. % N-doped films), as illustrated by the photos shown at the top of Fig. 6(a). Interestingly, our results show that further increasing the N content beyond 3.4 at. % does not translate into further red shifting of the absorption edge. Actually, the highest N content of 6.2 at. % is even seen to lead to a slight blue shift as compared to the 3.4 at. % doped film. This suggests the existence of an optimal N content that leads to the largest red shift (i.e., the narrower bandgap). In order to derive a quantitative value of the E_g of the TiO_2:N films, their corresponding UV-Vis spectra were analyzed according to the Tauc formula:[9,15,28] $(\alpha h\upsilon)^{\frac{1}{r}} = A(h\upsilon - E_g)$, where α is the absorption coefficient of the material, E_g is its optical energy gap, A is a proportionality constant, $h\upsilon$ is the photon energy, and r is a power factor which equals 2 for indirect band gap semiconductors. Figure 6(b) shows typical Tauc plots of the TiO_2:N films where the E_g value can be deduced from the x-intercept of the tangential extrapolation of the curves.[9,15,28] Thus, the E_g values, deduced from Tauc plots, are found to decrease from 3.18 eV for undoped TiO_2 films, in accordance with literature values,[4,5] to (2.25 ± 0.05) eV for the 3.4 at. % N-doped ones. Further increasing the N content of the films up to 6.2 at. % was found to lead to slightly higher E_g values of $\sim 2.35 \pm 0.05$ eV, confirming that the narrowest E_g value is effectively reached at the optimal N content of 3.4

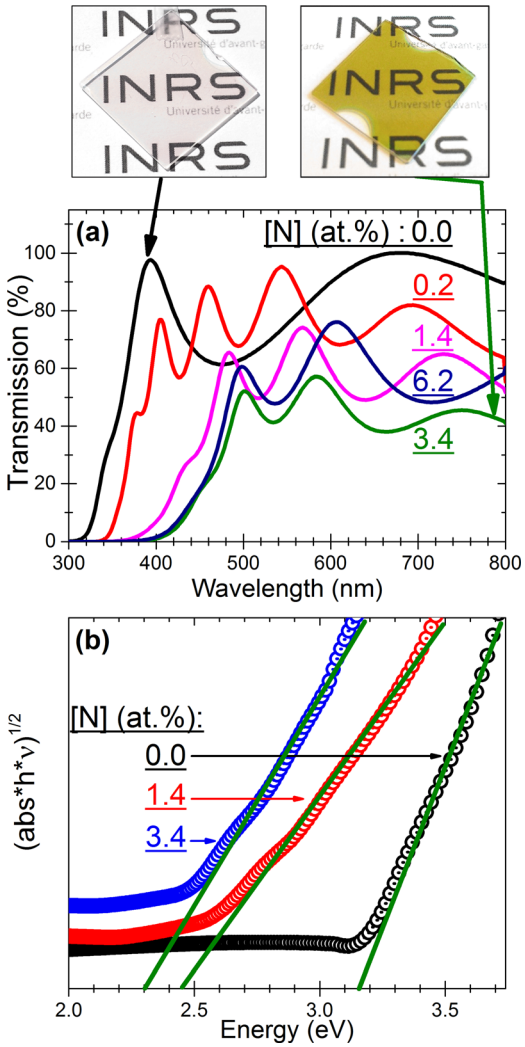

FIG. 6. (a) UV-Vis spectra of the sputter-deposited TiO_2:N films with different N doping levels ranging from 0 (undoped) to 6.2 at. %; (b) Selected Tauc plots of TiO_2:N films with different N contents (0, 1.4, and 3.4 at. %).

at. %. It is worth noting here that the E_g value of 2.25 eV achieved at 3.4 at. % is, to the best of our knowledge, the narrowest bandgap achieved so far for N doped TiO_2 films.[4,5] These results show that the N doping used here was effective in achieving a significant reduction of the bandgap by as much as ~1 eV from the initial value for the anatase of 3.2 eV.

Parallel to the UV-Vis absorption measurements, we have also performed systematic spectroscopic ellipsometry measurements in order to have an alternative and more direct access to the bandgap of the TiO_2:N films as a function of their N content. To this end, the experimentally acquired ellipsometry spectra were analyzed by using a "composite" model composed of three main components, namely (i) the Tauc-Lorentz (T-L)[29] contribution, (ii) the Cody-Lorentz (C-L) dispersion contribution,[30] and (iii) the Drude free-carriers contribution.[31] Thus, our global model takes into account the T-L dispersion in determining the imaginary dielectric function ε_2 for all energies above the Band Edge (E_g). The T-L dispersion, however, has explicit restriction for the ε_2 above the band edge to be zero. Therefore, the Cody-Lorentz component is used to describe ε_2 for contributions above the band edge as it parameterizes transition energy in the transparent and inter-band transition regions. Both the T-L and C-L contributions derive the real dielectric function ε_1 from the Kramers-Kronig relations and have an explicit expression for the E_g as part of their formalism (to dictate the transition regions). Finally, to account for the increase in free charge carries brought on by the N doping, a Drude free-carrier contribution was added to the total dielectric function.[31,32] As the surface roughness can increase light scattering in the ellipsometry measurements, it was accounted for by inserting a shallow surface layer of which roughness is a fitting parameter in the model. The roughness values obtained for the best fits of the various films were found to be the 2–5 nm range, in agreement with the very smooth TiO_2:N surfaces as observed by SEM. Figure 7(a) shows a typical satisfactory fit of the experimental data (for the 3.4 at. % N doped films for instance) by the above-discussed "composite" model. One can note nonetheless a slight mismatch between experimental and modeled spectra (Fig. 7(a)) in the oscillation amplitudes in the high energy part (below 450 nm). Such a mismatch can be attributed directly to the heavy doping (above 1–2 at. %) of the semiconducting films.[35] Indeed, for energy levels (1.5–2.5 eV range), the effects of heavy doping are well described and accounted for by the Drude free-carrier model with lifetimes determined by scattering from lattice vibrations. However, for high energy regions (≥2.5 eV), the screening of excitonic responses and the shift of the band edges become non-negligible, and affect the accuracy of the modeled absorption coefficients' values. This results in a mismatch that is mainly represented by a

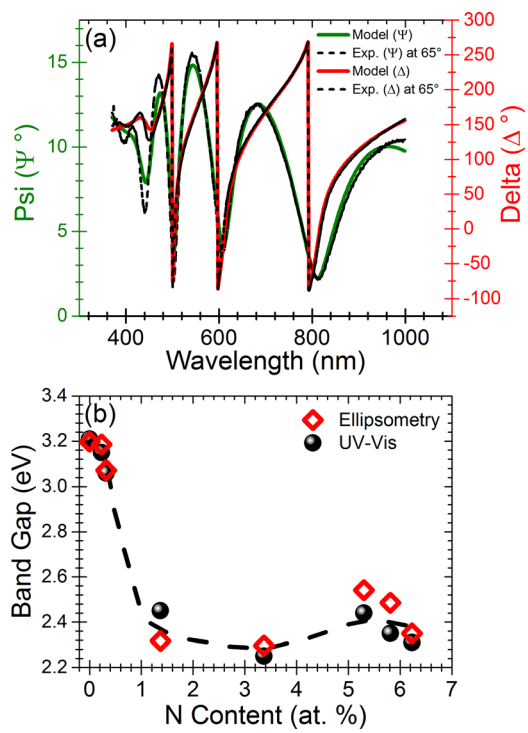

FIG. 7. (a) Typical fitting of ellipsometric data by the proposed theoretical model in the case of a TiO_2:N film doped with 3.4 at.% of N; (b) Variation of the bandgap (E_g) of the sputter-deposited TiO_2:N films as a function of their N content. Eg values derived from both UV-Vis (filed black spheres) and ellipsometric measurements (open red diamonds) are compared.

discrepancy of the oscillation amplitudes, as seen in Fig. 7(a). However, such amplitude discrepancies would have a very little effect of the extracted E_g value, which is rather determined by the energy point where both T-L and C-L model components complete each other. Thus, by fitting the ellipsometry spectra of the different TiO_2:N films, we were able to extract the E_g values for the films with various N doping levels. The E_g values, independently determined from both the ellipsometry and the UV-Vis measurements, are plotted against the N content of the TiO_2:N films (Fig. 7(b)). First of all, one can note that a satisfactory agreement between E_g values derived from both methods is obtained. These results of Fig. 7(b) constitute, to the best of our knowledge, the first ever-reported systematic N-content dependence of the Eg of TiO_2:N films while comparing two different and independent approaches (UV-Vis and ellipsometry). Second, Figure 7(b) clearly shows that as the N content is increased, the E_g of the TiO_2:N films significantly decreases to reach a value as low as 2.25 eV at the optimal N concentration of 3.4 at. %, and then slightly increases for higher N contents (>5 at. %). Such limitation in further narrowing E_g is likely due to the fact that beyond 5 at. % of N, the energy bands associated with the E_g narrowing are saturated, and any further doping will simply increase the concentration of oxygen vacancies and other defects. The latters act as trap/recombination centers which directly counteract the nitrogen induced E_g reduction.[10,12,13] Finally, Figure 7(b) clearly highlights the latitude of our magnetron-sputtering process to tailor, at will, the bandgap of the TiO_2:N films, over all the (2.25–3.2) eV range, by varying their N content, which in turn is precisely monitored through the relative gas flow ratio (R) during the plasma deposition process.

Finally, the effectiveness of the achieved E_g narrowing in improving the EPC properties of the TiO_2:N films was assessed by integrating them as photoanodes (i.e., TiO_2:N films deposited on both sides of deployed (10 cm × 11 cm) Ti-grids) in a home-built electrochemical reactor, of which details can be found elsewhere[3]). Most often the photocatalytic activity of TiO_2 or N-doped TiO_2 films is evaluated by using standard colorants, such as methylene blue (MB),[13,17] methyl orange (MO),[19] or RhB dye,[18] which give a generic assessment of their photocatalytic performance. Here, the EPC performance of our TiO_2:N photoanodes was directly assessed towards the degradation of a real emerging contaminant, namely CTC. The CTC is a widely used antibiotic in the agricultural industry[33] which is neither filtered by current water treatment plants nor significantly decomposed in the biosphere. Thus, CTC arises as an emerging contaminant that increases the hazard should it seep into the drinkable water supply of rural and even urban communities.[34] For the purpose of the present study, synthetic solutions containing CTC concentrations of 100 μg/L were prepared and treated in our EPC reactor under 1.5 AM solar simulator while continuously circulating them for 2 h treatment time. A more detailed study on the EPC treatment conditions and associated data analysis were reported elsewhere[3]). First of all, our TiO_2:N photoanodes have been shown to be very effective in degrading CTC under the optimal EPC conditions.[3] However, their degradation effectiveness under sun illumination conditions is clearly found to be dependent on the N content of the TiO_2:N photoanodes. To highlight this latter fact, Figure 8 shows the residual amount of CTC following its degradation with the TiO_2:N photoanodes as a function of their N content. It is clearly seen that the higher degradation efficiency of CTC is reached for the TiO_2:N films having the N content of 3.4 at. % (98.5% of the CTC molecules were degraded). Interestingly, this optimal N content was also shown to lead to TiO_2:N films with the narrowest bandgap of 2.25 eV, confirming thereby the most efficient harvesting of photons in the visible and UV range for their contribution to the EPC process. In fact, the N content dependence of E_g (Fig. 7(b)) is seen to resemble to a large extent that of the EPC degradation efficiency of CTC (Fig. 8). These results show that the narrowest is the bandgap of the TiO_2:N films, the highest is their ability to degrade CTC. The higher CTC degradation capacity at $E_g = 2.25$ eV is a direct consequence of increased absorption in the visible portion of the solar spectrum, leading thereby to the increased creation of oxidative species in the EPC reactor. These results are highly promising as they open up immediate prospects for the EPC degradation of emerging contaminant such as CTC under visible solar light radiation.

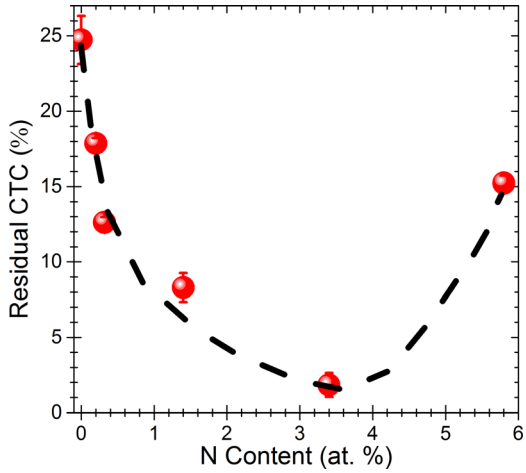

FIG. 8. Electro-photocatalytic degradation efficiency of CTC, under 1.5 AM solar irradiation, as a function of N content of the TiO_2:N photoanodes.

IV. CONCLUSION

We have successfully developed a magnetron sputter-deposition process that permits the controlled incorporation of N into TiO_2 films over all the (0–6.3) at. % range. The TiO_2:N films were found to crystallize in the desired anatase phase for all N contents in excess of 1.4 at. %, while the rutile phase was found to be predominant at low N contents (0.2 and 0.3 at. %). A detailed analysis of the chemical bonding states of the films revealed that N atoms are incorporated into the films through substitution of oxygen atoms in the TiO_2 lattice (for N contents $\geq$ 1.4 at. %). The ellipsometry and UV-Vis characterizations allowed to clearly demonstrate the progressive narrowing of the bandgap of TiO_2:N films as a function of their N content. We were thus able to point up the existence of an optimal N content of 3.4 at. % corresponding to the narrowest bandgap of 2.25 eV. This significant bandgap narrowing (close to the sun peak power located

at about ~2.2 eV) makes our TiO_2:N films highly suitable for efficient photoconversion of sunlight. Finally, the EPC performance of our sputter-deposited TiO_2:N films, towards CTC degradation under solar illumination conditions, is shown to be correlated to their bandgap, with the highest degradation rate being achieved with the narrowest bandgap of 2.25 eV. The use of such optimised TiO_2:N photoanodes opens up new prospects for the effective degradation of emerging contaminants in water under direct sunlight irradiation.

ACKNOWLEDGMENTS

The authors acknowledge the financial support from NSERC (the Natural Science and Engineering Research Council of Canada), Nano-Québec (the Québec Organization for the promotion of nanoscience and nanotechnologies), Produits Chimiques Magnus Ltée, and the FRQNT (Le Fonds de Recherche du Québec-Nature et Technologies) through its strategic Network "Plasma-Québec."

[1]O. Carp, C. Huisman, and A. Reller, Prog. Solid State Chem. **32**, 33 (2004).
[2]B. O'Regan and M. Grätzel, Nature **353**, 737 (1991).
[3]R. Daghrir, P. Drogui, N. Delegan, and M. A. El Khakani, Water Res. **47**, 6801 (2013).
[4]N. Serpone, A. V. Emeline, V. N. Kuznetsov, and V. K. Ryabchuk, in *Environ. Benign Photocatal.* (2010), pp. 35–111.
[5]A. V. Emeline, V. N. Kuznetsov, V. K. Rybchuk, and N. Serpone, Int. J. Photoenergy **2008**, 1.
[6]D. N. Tafen, J. Wang, N. Wu, and J. P. Lewis, Appl. Phys. Lett. **94**, 093101 (2009).
[7]R. Asahi, T. Morikawa, T. Ohwaki, K. Aoki, and Y. Taga, Science **293**, 269 (2001).
[8]A. K. Rumaiz, J. C. Woicik, E. Cockayne, H. Y. Lin, G. H. Jaffari, and S. I. Shah, Appl. Phys. Lett. **95**, 262111 (2009).
[9]P.-G. Wu, C.-H. Ma, and J. K. Shang, Appl. Phys. A **81**, 1411 (2005).
[10]G. R. Torres, T. Lindgren, J. Lu, C.-G. Granqvist, and S.-E. Lindquist, J. Phys. Chem. B **108**, 5995 (2004).
[11]R. Nakamura, T. Tanaka, and Y. Nakato, J. Phys. Chem. B **108**, 10617 (2004).
[12]Y. Nakano, T. Morikawa, T. Ohwaki, and Y. Taga, Appl. Phys. Lett. **86**, 132104 (2005).
[13]L. Zhao, Q. Jiang, and J. Lian, Appl. Surf. Sci. **254**, 4620 (2008).
[14]M. Kitano, K. Funatsu, M. Matsuoka, M. Ueshima, and M. Anpo, J. Phys. Chem. B **110**, 25266 (2006).
[15]K. G. Grigorov, I. C. Oliveira, H. S. Maciel, M. Massi, M. S. Oliveira, J. Amorim, and C. A. Cunha, Surf. Sci. **605**, 775 (2011).
[16]M.-S. Wong, H. Pang Chou, and T.-S. Yang, Thin Solid Films **494**, 244 (2006).
[17]D.-L. Shieh, Y.-S. Lin, J.-H. Yeh, S.-C. Chen, B.-C. Lin, and J.-L. Lin, Chem. Commun. (Camb). **48**, 2528 (2012).
[18]S. Liu, J. Yu, and W. Wang, Phys. Chem. Chem. Phys. **12**, 12308 (2010).
[19]N. Arconada, Y. Castro, and A. Durán, Appl. Catal. A Gen. **385**, 101 (2010).
[20]Y. Cong, J. Zhang, F. Chen, and M. Anpo, J. Phys. Chem. C **111**, 6976 (2007).
[21]J. H. Scofield, J. Electron Spectros. Relat. Phenomena **8**, 129 (1976).
[22]Y. Djaoued, S. Badilescu, and P. Ashrit, J. Sol-Gel Sci. Technol. **24**, 255 (2002).
[23]G. Hyett, M. a Green, and I. P. Parkin, J. Am. Chem. Soc. **129**, 15541 (2007).
[24]M. Batzill, E. Morales, and U. Diebold, Phys. Rev. Lett. **96**, 026103 (2006).
[25]J.-Y. Zhang, I. W. Boyd, B. O'Sullivan, P. K. Hurley, P. V. Kelly, and J.-P. Sénateur, J. Non. Cryst. Solids **303**, 134 (2002).
[26]S. Sedira, S. Achour, A. Avci, and V. Eskizeybek, Appl. Surf. Sci. **295**, 81 (2014).
[27]D. Brassard, M. A. El Khakani, and L. Ouellet, J. Appl. Phys. **102**, 034106 (2007).
[28]J. Tauc, R. Grigorovici, and A. Vancu, Phys. Status Solidi **15**, 627 (1966).
[29]G. E. Jellison and F. A. Modine, Appl. Phys. Lett. **69**, 371 (1996).
[30]A. S. Ferlauto, G. M. Ferreira, J. M. Pearce, C. R. Wronski, R. W. Collins, X. Deng, and G. Ganguly, J. Appl. Phys. **92**, 2424 (2002).
[31]W. Su, K. Song, D. Huo, and B. Li, Curr. Appl. Phys. **13**, 556 (2013).
[32]N. White, A. L. Campbell, J. T. Grant, R. Pachter, K. Eyink, R. Jakubiak, G. Martinez, and C. V. Ramana, Appl. Surf. Sci. **292**, 74 (2014).
[33]R. Daghrir, P. Drogui, I. Ka, and M. A. El Khakani, J. Hazard. Mater. **199–200**, 15 (2012).
[34]R. Daghrir and P. Drogui, Environ. Chem. Lett. **11**, 209 (2013).
[35]D. Aspnes, A. Studna, and E. Kinsbron, Phys. Rev. B **29**, 768 (1984).

Article 2

Probing the Electronic Surface Properties and Bandgap Narrowing of in situ N, W, and (W,N) Doped Magnetron-Sputtered TiO_2 Films Intended for Electro-Photocatalytic Applications; Rajesh Pandiyan, Nazar Delegan, Ahmad Dirany, Patrick Drogui, and My Ali El Khakani; J. Phys. Chem. C 2016, 120, 631-638

THE JOURNAL OF PHYSICAL CHEMISTRY C

Article

pubs.acs.org/JPCC

Probing the Electronic Surface Properties and Bandgap Narrowing of in situ N, W, and (W,N) Doped Magnetron-Sputtered TiO_2 Films Intended for Electro-Photocatalytic Applications

Rajesh Pandiyan,[†] Nazar Delegan,[†] Ahmad Dirany,[‡] Patrick Drogui,[‡] and My Ali El Khakani*[,†]

[†]Institut National de la Recherche Scientifique, Centre-Énergie, Matériaux et Télécommunications, 1650 Blvd. Lionel−Boulet, Varennes, QC J3X-1S2, Canada

[‡]Institut National de la Recherche Scientifique, Centre Eau, Terre et Environnement, 490 Rue de la Couronne, Québec, QC G1K-9A9, Canada

ABSTRACT: We report on the optical and electronic properties of undoped, nitrogen (N) doped, tungsten (W) doped, and (W,N) doped TiO_2 films deposited by RF magnetron sputtering process. The optical absorption edge of the N doped TiO_2 films is shown to red-shift significantly as compared to the undoped TiO_2 films. This tendency was found to continue with the codoped films, as their absorption edge substantially red-shifted to ∼420 nm. This red-shifting is due to the effective narrowing of the band gap of the doped films as determined via Tauc plot analysis, which confirmed a reduction of the bandgap of the (W,N) codoped TiO_2 films to a value as low as 2.2 eV (in comparison with the 3.2 eV value of the undoped TiO_2 films). From X-ray photoelectron spectroscopy (XPS) analysis, it is shown that the N and W atoms were incorporated into the O and Ti lattice sites of TiO_2 respectively. On the other hand, valence band spectra of these films suggest that it primarily consists of O 2*p* derived states and the maximum upshift of surface position of valence band maximum (0.8 eV) with respect to the Fermi level was observed for (W,N) doped films, which, in turn, is in accordance with the narrowing of the bandgap revealed by UV−vis spectra analysis. Finally, by quantitatively measuring the work function of undoped, monodoped, and codoped TiO_2 films, by means of UV-photoelectron spectroscopy (UPS), we were able to achieve a complete reconstruction of their one-dimensional energy band structure. This fundamental information is highly valuable for the efficient use of doped TiO_2 films in electro-photocatalytic and/or optoelectronic applications.

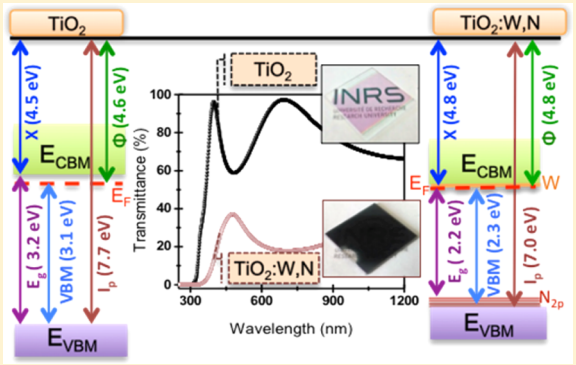

1. INTRODUCTION

Titanium dioxide (TiO_2) continues to receive considerable attention as a promising photocatalyst material[1] due to its high oxidative power combined with its charge transport properties for the remediation of organic and inorganic pollutants in water and air.[2−5] However, the photoreaction efficiency of TiO_2 is rather limited due to its wide intrinsic band gap (3.2 and 3.0 eV for the anatase and rutile polymorph, respectively), which confines its photon absorption solely to the ultraviolet fraction of the solar spectrum (∼4% of the total solar energy flux).[6] In recent years, great efforts have been made to tailor the bandgap (E_g) of TiO_2 to photosensitize it in the visible light region (∼40% of total solar energy) while ensuring significant quantum yields.[6−9] For this purpose, many attempts have been made to reduce the bandgap by doping with nonmetal anionic elements (N, C, and S)[10−12] or transition-metal cations (W, Mo, V, and Cr).[13−16] Anionic and cationic type monodoping in TiO_2 forms acceptor or donor levels in the energy gap of the material, the former usually creates 2p states just above the valence band maximum (VBM) while the latter creates the localized d states below the conduction band minimum (CBM). Such localized states result in an apparent decrease of the bandgap to some extent, but may also create recombination centers within the bandgap (deep gap states), which affect the lifetimes of photoexcited charge carriers.[17] For this purpose, substitutional codoping of anions at O sites and metal cations at Ti sites, not only narrows the band gap significantly, but also serves to counteract the presence of carrier recombination centers (achieving a sort of electronic passivation). Gai et al.[17] and Long et al.[18] have theoretically predicted that codoping with specific anion/cation pairs can result in gap state passivation of dopant induced defects, while maintaining a significant bandgap (E_g) reduction. Among the possible codoping couples, some of the recent studies have demonstrated that simultaneous (W,N) codoping of TiO_2 induces substantial bandgap narrowing while providing electronic passivation, improving thereby their overall photocatalytic activity under visible light irradiation.[19−24] Although a few papers have reported W and N codoping (achieved exclusively by wet chemical synthesis routes),[19−21,23−25] there is

Received: August 18, 2015
Revised: December 2, 2015
Published: December 2, 2015

DOI: 10.1021/acs.jpcc.5b08057
J. Phys. Chem. C 2016, 120, 631−638

still a significant lack of complete and direct comparative study of the effect of various doping schemes in the TiO_2 films, based on their associated valence band structure, the Fermi level position and local work function values. In recent reports,[23,24] electrochemical impedance spectroscopy (EIS) measurements have been used in order to depict the band structure of chemically synthesized TiO_2 powders with different doping conditions, but without being able to track directly the position of the VB edge and/or to determine the Fermi level position. From a fundamental point of view, the in situ physical doping process (as in the sputter deposition investigated here) leads to a more substitutional type of doping as opposed to the interstitial doping generally obtained by chemical synthesis routes. In the case of nitrogen doping, wet chemistry routes have yielded mainly interstitials, which were responsible for the insertion of deep and isolated levels in the TiO_2 band gap.[26−30] In the case of the substitutional W−N codoping, theoretical studies[17,31−33] have predicted that not only the uncompensated isolated N defects will be electronically passivated but also the E_g will concomitantly shrink via the valence band energy increase. It is thus desirable to experimentally access the valence band position through direct measurements. The UPS technique (used here) is very appropriate and straightforward to measure directly the work function, which accurately defines the position of the Fermi level. In combination with XPS measurements, the position of the VB edge can be determined.

In this paper, we report on the optical and electronic structure properties of undoped, nitrogen (N) doped, tungsten (W) doped, and (W,N) codoped TiO_2 films deposited by means of an in situ doping, purely physical reactive-magnetron sputtering (RF-MS) process. To achieve a better understanding of the electronic band structure of TiO_2 under various doping configurations, we have combined different and complementary spectroscopy techniques, namely UV−vis-NIR, XPS, and UPS. We were thus able to not only elucidate the exact location of the band edges but also to access all the experimental physical values needed to derive a complete picture of the electronic band structure of both in situ mono- and codoped sputtered-TiO_2 films. Interestingly, our results pointed out that the shift in the valence band edge position is dopant dependent, which is in apparent contradiction with the EIS derived results from chemically doped TiO_2 powder.[24,34] This is probably due to the different doping configurations (substitutional in our sputtered films versus interstitial in chemically processed TiO_2). This highlights the relevance of tracking the VB edge, which revealed not only the presence of defect states in the lower part of the gap (providing hints of passivation, in accordance with theoretical predictions,[17,31−33] but also that the large reduction of the bandgap (by ∼1 eV) is mainly due to the VBM upward shifting. As a result, the (W,N) doping is shown to lead to a significant bandgap narrowing (down to a value as low as 2.2 eV) and a higher visible light absorption as a consequence of the synergetic influence of anion−cation doping species.

2. EXPERIMENTAL SECTION

The undoped (TiO_2) and nitrogen doped (TiO_2:N) films were sputter-deposited from a TiO_2 target (3″ in diameter, 99.995% purity) by radio frequency (RF, 13.56 MHz) magnetron sputtering process in a pure argon (Ar) plasma and mixed gas plasma with nitrogen mass flow ratio R (i.e., $[N_2]/([N_2] + [Ar])$) varying between 0 and 10%. In both cases, the sputtering deposition was carried out with a constant power density of 8.8 W/cm^2 applied to the TiO_2 target. The W atom incorporation for the TiO_2:W and TiO_2:W,N films was achieved through concomitant cosputtering of a W target. The W content of the TiO_2:W films was controlled by varying the RF power density applied to the W target between 0.15 and 0.22 W/cm^2. Initial N doping concentrations and working parameters were set based on optimal parameters from our previous work on TiO_2:N films;[35] the initial W doping concentration levels were derived based on desired W-to-N ratios from predicted optimal theoretical concentrations.[31,32] The targets were systematically sputter-cleaned with Ar ions for ∼15 min with the shutters closed in order to remove the surface target contamination. The films were deposited onto a group of silicon, quartz, and titanium substrates in a chamber evacuated to an interdeposition base pressure of 10^{-8} Torr. The gas flow rates were monitored to keep a constant working pressure of 1.44 mTorr during the sputter-deposition process. The target to substrate distance was fixed at 20 cm, while the substrates were rotated and heated to a constant temperature of 475 °C by means of a quartz lamp heater. The crystalline structure of the films was characterized using an X'Pert Pro (PANalytical Inc.) X-ray diffractometer employing a Cu Kα (λ = 1.5418 Å) source at a grazing incident angle of 0.75°. Their optical bandgaps were systematically determined by measuring the UV−vis transmittance and reflectance spectra, using an Agilent/Varian Cary 5000 UV−vis-NIR spectrophotometer in the 250−1800 nm range. The surface atomic composition, chemical bonding states, and valence band of the films were explored by ex-situ method using both XPS and UPS spectroscopies. Photoemission studies are performed with an ESCALAB 220iXL spectrophotometer (Thermo VG Scientific Ltd., UK) with a base pressure of 2×10^{-9} mbar, using a standard Al Kα twin anode X-ray source (exciting photon energy of 1486.6 eV, Power =400 W) for XPS analysis and while the UPS spectra were recorded using the He I line at $h\nu$ = 21.2 eV as the excitation source in normal emission with a resolution of 0.06 eV. The Fermi level position was calibrated using a gold reference (work function of 5.0 eV) with a −3 V bias applied to eliminate the intrinsic detector work function barrier of 3 eV. The XPS spectrometer is also equipped with an argon ion gun that allows the sample surface to be cleaned. High-resolution XPS core level spectra of all the samples were acquired after a systematic in situ surface cleaning by means of Ar^+ ion sputtering of ion energy of 3 keV for 200 s, optimized as to be barely sufficient to remove the carbon contamination surface layer due to air exposure.

3. RESULTS AND DISCUSSION

X-ray diffraction studies were carried out to compare and investigate the modifications to the phase structure, crystallinity of TiO_2 films resulting from the various doping configurations. The XRD patterns of sputter deposited TiO_2, TiO_2:N, TiO_2:W, and TiO_2:W,N films are shown in Figure 1. From the structural analysis, the undoped TiO_2 film exhibits a crystalline structure with dominant anatase phase with its (101), (103), (004), (200), (105), and (211) crystallographic planes (ICDD card, #21-1272). A significant loss in the crystallinity accompanied by a phase transformation from anatase (A) to rutile (R) is observed while going from undoped to N, W, and (W,N) doped films.

In the TiO_2:N doped system, incorporation of N dopant into the crystal lattice of TiO_2 via either substitutional or interstitial mode slightly hindered the crystallization of titania films resulting in the main anatase (101) peak fwhm broadening. It

DOI: 10.1021/acs.jpcc.5b08057
J. Phys. Chem. C 2016, 120, 631−638

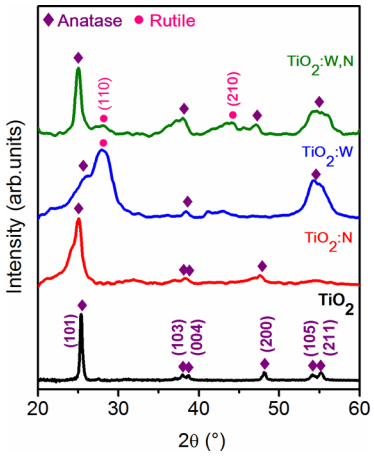

Figure 1. Typical X-ray diffraction patterns of the sputter-deposited undoped TiO_2, TiO_2:N, TiO_2:W, and TiO_2:W,N doped films.

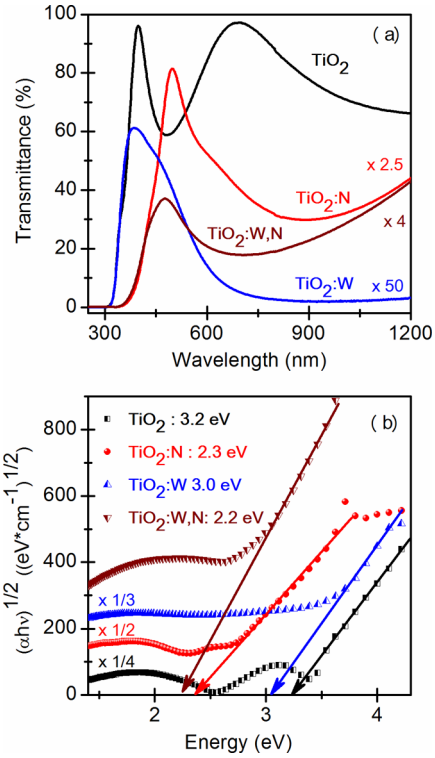

Figure 2. (a) UV−vis transmittance spectra of the sputter-deposited films (b) Tauc plots used to derive the bandgap for the undoped TiO_2, TiO_2:N, TiO_2:W, and TiO_2:W,N doped films.

can be proposed that this is due to N atoms reducing the size of TiO_2 domains via the introduction of crystal lattice impurities such as Ti−O−N type bonds.[31] In the case of W and (W,N) doped films, incorporation of W atoms into the titania lattice leads to two main changes in the crystallographic structure of the films: (i) appearance of both anatase and rutile (R:(110) and (210) planes) phases with the latter mainly present in samples with no N in the deposition process, and (ii) a broadening of the peaks. The appearance of rutile may originate from O vacancies, as we have previously observed that due to preferential sputtering effects, TiO_2 films tend to transition into a rutile structure when deprived of O atoms in the sputter deposition process. As noted for the TiO_2:N films (this work and previously published results), the addition of nitrogen seems to partially fill these vacancies, allowing the structure to regain its anatase form in the TiO_2:W,N films.[35] Tungsten incorporation into the TiO_2 matrix leads to a small shift and significant broadening in the anatase peak position (101). This is indicative of internal strain and lattice distortion induced by W size mismatch during substitutional incorporation. This broadening is significantly reduced during codoping (TiO_2:W,N) indicative of strain relaxation via codoping. The ionic radius of W^{VI} (∼60−62 pm) as compared to Ti^{IV} (∼62−68 pm) ions restricts tungsten mostly into a substitutional doping regime, forming Ti−O−W type bonds.[36,37] Insights into the impact of doping on the electronic structure of TiO_2 films can be obtained from the optical characteristics. Figure 2a shows the UV−vis transmittance spectra of the undoped TiO_2, TiO_2:N, TiO_2:W, and TiO_2:W,N doped films, deposited on quartz substrates. TiO_2 exhibits a strong absorption onset around 320 nm, which can be related to the intrinsic band-to-band transition. The most striking feature of Figure 2a is the evident red-shift of the absorption band edge of the spectra from about 320 nm for TiO_2 film to ∼400 nm for TiO_2:N films. Furthermore, the effect of codoping (W,N) on the visible light absorption shows the largest redshift (i.e., the narrowest E_g) of the absorption band edge toward longer wavelengths as compared to the pristine TiO_2. Figure 2b shows the typical Tauc plots of the undoped N, W, and (W,N) doped films where the quantitative band gap energy value can be extrapolated. The optical band gap (E_g) of the films was calculated by Tauc's relation and the absorption coefficient (α) can be determined near the absorption edge using the relationship $\alpha = (1/t)\ln[(1 - R)^2/T]$, where t is the film thickness and T and R are the corresponding transmittance and reflectance, respectively.

The thickness of the undoped TiO_2, TiO_2:N, TiO_2:W, and TiO_2:W,N doped films was in situ monitored by means of a calibrated quartz-crystal microbalance during the sputter deposition process, and ex-situ measured by means of cross-sectional scanning electron microscopy (SEM) images. The thickness was measured on the films deposited onto silicon substrates and was found to be of ∼130, 250, 530, and 300 nm for undoped-TiO_2, TiO_2:N, TiO_2:W, and TiO_2:W,N doped films, respectively. For the UV−vis measurements, the same films were concomitantly deposited onto quartz substrates. The effective optical band gap energies for the films were obtained by extrapolating the linear region of the Tauc plot [i.e., $(\alpha h\nu)^{1/2} = f(h\nu)$ formula for indirect E_g transitions] to the intersection with the horizontal x-axis.[38] The estimated E_g of about 3.2 eV was determined for undoped anatase TiO_2, in agreement with literature.[13,24,39] A clear red-shift of the absorption edge toward the longer wavelength is observed for all the doped samples, which indicates effective optical E_g narrowing. After monodoping, the band gap value decreases to 3.0 and 2.3 eV for the W and N dopants at 2.3 at. % and 5.7 at. %, respectively. In the case of W doping, one can notice that only a small reduction in the band gap (0.2 eV) is occurring. Since the Tauc plot formula used here is the one for indirect transitions, this slight E_g narrowing can be attributed to the substitution of W at Ti sites in the TiO_2 anatase indirect bandgap phase, generating thereby isolated impurity energy levels below the CBM within the gap (W 5d states are below Ti 3d ones). Nevertheless, one can also notice the coexistence of both rutile (with a direct bandgap of 3.0 eV) and anatase phases. Thus, we cannot exclude a possible slight contribution from the rutile phase to the observed overall shrinkage of the bandgap of TiO_2:W films. In the case of N

DOI: 10.1021/acs.jpcc.5b08057
J. Phys. Chem. C 2016, 120, 631−638

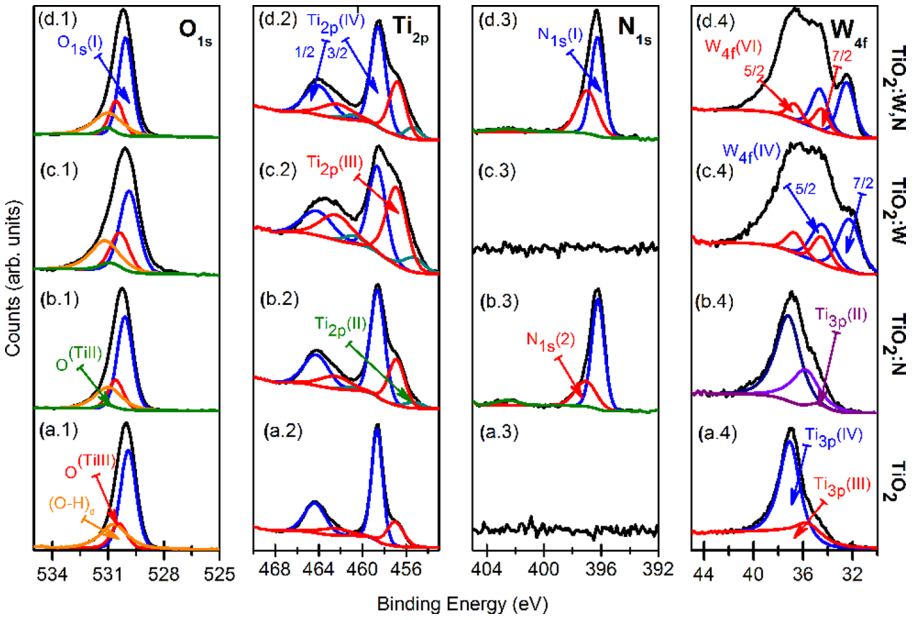

Figure 3. Chemical states and film surface stoichiometry deconvolution of O 1s (0.1), Ti 2p (0.2), N 1s (0.3), W 4f (0.4), and high-resolution core level XPS spectra of undoped (a), N doped (b), W doped (c), and (W,N) doped TiO_2 (d).

doping of TiO_2, the strong reduction of E_g is due to the introduction of isolated N 2p states with within the gap, which are located above the mainly O 2p state composed valence band of TiO_2.[35]

Finally, the (W,N) doping of TiO_2 films was found to lead to the highest absorption of photons (Figure 2a) along with the largest bandgap reduction with an E_g value as low as 2.2 eV. This significant bandgap narrowing (by 1 eV in comparison with undoped anatase TiO_2) is due to the synergetic effects of the acceptor electronic states above the valence band maximum (VBM) via N substitutional doping of TiO_2 (p type-doping) combined with the partially occupied electron states below the CBM due to W ions (n type-doping) in substitutional sites. The synergy of the codopants is predicted to lower the formation energy of the dopants as compared to undesired defects (such as oxygen vacancies), to electronically passivate the impurity states (allowing for greater charge mobility), and to shrink the E_g by allowing for easier hybridization of the N 2p and O 2p states (vs inserting discrete energy states deep into the E_g structure as in the case of monodoping).[18,32,33]

To gain more insights on the observed E_g narrowing as a function of dopant incorporation, photoelectron spectroscopy was used to probe the structure of core level and valence electronic band structures of the undoped and doped TiO_2 films. Figure 3 illustrates the high-resolution Ti 2p, O 1s, N 1s, and W 4f core level XPS spectra acquired on undoped, N, W, and (W,N) doped TiO_2 with deconvolutions after a Shirley background subtraction. The XPS wide scan spectra (not shown) confirmed the presence of Ti, O, N, and W XPS peaks. The Ti 2p core level spectrum of undoped TiO_2 (Figure 3a.2) is deconvoluted using two distinct doublets centered at binding energy (BE) 458.6 and 464.3 eV assigned to Ti $2p_{3/2}$ and Ti $2p_{1/2}$ for Ti^{IV} oxidation states (TiO_2),[21] while peaks located at lower BE 456.9 and 462.4 eV attributed to Ti^{III} states (substoichiometric oxides, i.e., Ti_2O_3),[35,40] respectively. The reduction of TiO_2 to Ti_2O_3 (i.e., oxidation state below IV) indicates the presence of positively charged oxygen vacancies shared by the titanium cations adjacent to the defect sites arising from the preferential sputtering of O atoms.[35,41] Furthermore, Ti 2p core level spectra of mono and (W,N) doped films is slightly altered exhibiting a contribution of the Ti^{II} oxidation state (substoichiometric, i.e., TiO) centered at lower BE 455.3 and 460.9 eV for the $2p_{3/2}$ and $2p_{1/2}$ peaks, respectively.[40] It is to be noted that some Ti^{III} species can be created during the XPS etch-cleaning of the sample surface. This leads to an unavoidable overestimation of the Ti^{III} defect states, as compared to the actual bulk Ti^{III} content. Nevertheless, it is still safe to study the different samples on a comparative basis given that they all were subjected to an identical in situ Ar^+ cleaning procedure. On the other hand, the O 1s core level spectra can be decomposed into two peaks for all the films. The O 1*s* XPS spectra of all the films reveal a well-defined major peak (O1s (1)) located at 529.9 eV attributed to the O^{2-} ions in TiO_2 (O−Ti−O bond) and the other O_{1s} (2) at 530.4 eV is associated with the substoichiometric lattice oxygen and it is denoted as $O^{(TiIII)}$ at ∼0.5 eV higher binding energy. In addition, one can note the presence of a third component under the O 1s peak, denoted as $(O-H)_d$ at 530.7 eV, which is due the adsorbed defective hydroxide groups, as it is generally reported for metal oxide surfaces.[42,43]

In the case of N and (W,N) doped TiO_2 (Figures 3b.3 and d.3 respectively), the N 1s core level, was further deconvoluted into three main components centered on 396.2 eV $N_{1s}(1)$, 397.1 eV $N_{1s}(2)$, and 402.5 eV $N_{1s}(3)$, which can be attributed to different local environments of N atoms. The former component at 396.2 eV arises from N^- anions in substitutional N−Ti bondings (similar to that of N−Ti bonds in TiN of ∼396.9 eV),[6,35,44] while the second component located at 397.1 eV resulted from the N−O−Ti and/or Ti−N−O linkage[45] (electron transfer from Ti to N). The latter component of N 1s at 402.5 eV is of debated nature and is sometimes given contradictory assignments in the literature.[46−49] Given the very low intensity of this component, and the relative uncertainty on its assignment, we prefer not to speculate about its origin. From the tungsten atoms' viewpoint, the W 4f core level spectra are decomposed into two doublets. The first doublet, appearing at

DOI: 10.1021/acs.jpcc.5b08057
J. Phys. Chem. C 2016, 120, 631−638

Table 1. Bandgap, Position of the Energy Levels, Work Function, and Elemental Composition (Ti, O, W, and N) for Monodoped and Codoped TiO_2 Films as Derived from the XPS and UPS Spectra Analysis

films	E_g (eV)	Ti (at. %)	O (at. %)	W (at. %)	N (at. %)	N 1s (1) (at. %)	N 1s (2) (at. %)	VBM edge (eV)	Φ (eV)
TiO_2	3.2	34.5	64.6					3.1	4.6
TiO_2:N	2.3	34.2	59.0		5.7	4.1	1.6	2.4	3.7
TiO_2:W	3.0	35.3	60.5	2.3				2.8	4.7
TiO_2:W,N	2.2	33.8	56.2	1.6	7.2	4.3	2.9	2.3	4.8

binding energies 34.5 and 36.7 eV, is due to W $4f_{7/2}$ and W $4f_{5/2}$ in the W^{VI} oxidation state corresponding to the WO_3 phase.[50] The second doublet (at 32.3 and 34.5 eV) is attributed to W^{IV}-like oxidation states in more oxygen deficient phases.[51] One can also note the presence of other peaks in this spectral window (at 37.1 (IV), 35.7 (III) and 34.8 (II) eV) originating from Ti 3p states. Given the superposition of Ti 3p and W 4f orbital energies, extra precautions were taken to ensure proper W 4f deconvolution. For this purpose, three main restrictions were imposed based on electronic properties of the materials: (i) Ti 3p IV, III, and II oxidation state ratios were allowed to reflect those of the Ti 2p orbital; (ii) Ti to W ratios were locked with accordance with Ti 2p and W 4d derived concentrations (W 4d window not shown); (iii) W $4f_{7/2}$ and W $4f_{5/2}$ doublet separation and characteristics were set from a survey of NIST database spectra for the W 4f in WO_3 and WO_{3-x} oxidative species. These restrictions allowed us to get the most accurate picture possible of the W 4f species in the TiO_2:W,N films. Upon W doping there is a formation of occupied W 5d states below the mainly Ti 3d CBM which leads to the effective downshift of the CBM.[22] Due to size constraints W and N are mostly expected to substitute into Ti and O sites respectively and it is likely that nitrogen species coordinated to tungsten loaded to form the O−W−N linkage along with coexistence of N−Ti, N−O−Ti, and/or Ti−N−O type bonds.[25] The binding energies and chemical compositions, as derived from XPS analysis, of doped and codoped TiO_2 are presented in Table 1. The atomic concentration of elements was evaluated with relative sensitivity factors (RSF) defined in the standard table in the CasaXPS software.[52] In our case, we have used the RSF value from the default CasaXPS element library. The RSF values are 7.81 (for Ti 2p), 2.93 (for O 1s), 1.8 (for N 1s), and 9.8 (W 4f).

To observe the effect of doping on the TiO_2 valence band electronic structure, we carried out XPS measurements at low binding energies varying between 0 and 12 eV. Figure 4a shows the pile up of XPS valence band spectra of undoped TiO_2, TiO_2:N, TiO_2:W, and TiO_2:W,N films; Figure 4b shows the extrapolation of valence band maximum energy and chemical states observed above the VBM energy of TiO_2:W,N film. We could note that the top of the VB of TiO_2 is comprised of O 2p nonbonding states. The t_{2g} states are bonded in π orbitals and lie higher in energy than the σ states. The e_g states are σ bonded and are located in the deeper binding energy region of the VB.[53,54] A very weak Ti 3d defect state intensities located at BE 1.2 and 1.1 eV appeared for both W and (W,N) doped films below the Fermi level (E_F). This defect state comes from the surface oxygen vacancies, V_o,[54] which results in partially filled Ti 3d nonbonding states within the gap. The VBM energy is determined as the zero-intensity energy of the lower binding region of the spectrum and the VBM value relative to the Fermi level (E_F) is found by extrapolating the linear portion of the lower energy side of the VB to the spectral baseline. Thus, the

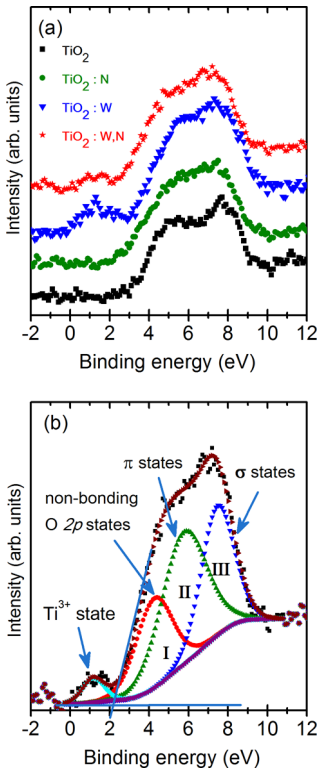

Figure 4. (a) Pile up of XPS valence band using O2p spectra of undoped TiO_2, TiO_2:N, TiO_2:W, and TiO_2:W,N films (b) extrapolation of valence band maximum energy and chemical states observed above the VBM energy of (W,N) doped TiO_2 film.

deduced VBM values for the four different TiO_2 based films are reported in Table 1.

The valence band onset for undoped TiO_2 is found around 3.1 eV. For the doped films, significant changes in the peak shape and position of the VBM edge within the bandgap were observed, and the corresponding VBM value relative to E_F is determined to be 2.8, 2.4, and 2.3 eV for W, N, and (W,N) doped TiO_2 films. Therefore, as predicted theoretically,[18,32] we note a large upshift of the VBM toward the Fermi level (by 0.7 and 0.8 eV for the respective N and (W,N) doped films), as compared to the undoped TiO_2. This substantial shifting up of the VBM toward the conduction band (well illustrated in the band diagrams hereafter) is mainly responsible for the observed band gap narrowing. It is seen that (W,N) codoping is more effective in narrowing the E_g as compared to N or W monodoping. It is possible that the predicted lower formation energy of desired impurities (substitutional N and W versus other types of defects) allows for easier hybridization of N 2p with the O 2p states, resulting thus in a continuous increase in the VBM energy as compared to discrete levels within the E_g for N or W doped samples.[32] To further investigate the doping effects on the energy band, the work function (Φ) of the films was characterized by ultraviolet photoelectron spectroscopy

DOI: 10.1021/acs.jpcc.5b08057
J. Phys. Chem. C 2016, 120, 631−638

(UPS). Figure 5 shows typical UPS spectra of the TiO_2 films with the different doping schemes. The work function of the

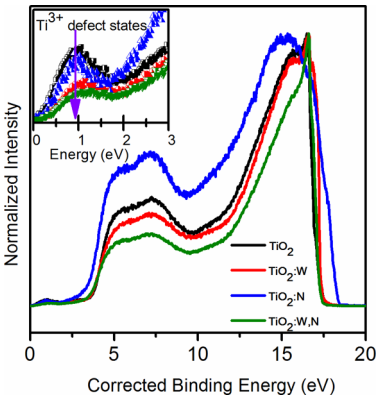

Figure 5. Comparison of UPS spectra (shows detailed spectra of secondary electron cutoff region) of undoped TiO_2, W doped, N doped, and (W,N) doped TiO_2. The expanded inset view shows the shallow valence features.

films was calculated using the Fermi edge (E_{Fermi}) and the half height of secondary electron cutoff region (E_{cutoff}) while subtracting the He I energy of 21.2 eV. Therefore, the Φ can be expressed as, Φ (eV) = $hv - (E_{cutoff} - E_{Fermi})$.[55] The UPS measurements were calibrated via the acquisition of the UPS spectrum of a gold reference sample and found its work function to be 5.0 eV, in accordance with literature values.[56]

From Figure 5, it is interesting to note that W, N, and (W,N) doping significantly changes the vacuum level of the TiO_2 films (i.e., Φ), which in turn is reflected as a variation in the secondary cutoff energy region of the UPS spectra. The work function of undoped TiO_2 thin film was found to be 4.6 eV, while that of TiO_2:N decreased to 3.7 eV. This significant reduction is due to the substitution of oxygen by nitrogen atoms in the oxygen lattice sites, thus creating defect states such as oxygen vacancies (in the form of donor energy states), formed below the conduction band. We also know that substitution of oxygen by nitrogen atoms in TiO_2 creates the isolated N 2p states, located just above the VBM. Thus, the presence of donor levels below the CBM and the shallow acceptor states near the VBM will rise the position of Fermi level, and thereby lowering the work function.[57,58] Doping with cations of which valence is different from that of the host location will result in the alteration of Fermi level and work function. The Φ value of the TiO_2:W films was found to be 4.6 eV, while the (W,N) doping increased Φ to 4.8 eV (which is 0.2 eV higher than that of TiO_2). Substitutional replacement of Ti with W ions in the TiO_2 lattice results in a slight change in the work function, due to the formation of impurity states below CBM, indicating that W 5d states are below Ti 3d states. Since the surface work function is directly related to the Fermi level, tungsten doping might enhance the effective positive charge density, lowering the Fermi level toward the valence band. It is well recognized that the effective work function value depends upon many critical factors, including the level of crystallinity, film morphology, defects, chemicals state, surface roughness and stoichiometry ratio. Finally, by combining the XPS and UPS results along with the bandgap information derived from UV−vis absorption measurements, we were able to access other electronic properties of the films, such as ionization potential and electron affinity. Accessing this complete array of experimentally derived physical characteristics of the TiO_2 films (under various doping schemes) is essential to come up with their most accurately possible energy level band diagrams. The ionization potential (I_p) and the electron affinity (χ) with respect to the vacuum level were calculated using the two following respective expressions: I_p = Φ + VBM and $\chi = I_p - E_g$. Accordingly, I_p (and χ) values were estimated to 7.7, 6.1, 7.4, and 7.0 eV (4.5, 3.8, 4.4, and 4.8 eV) for the respective undoped, N, W, and (W,N) doped TiO_2 films. Figure 6 shows the schematic energy level diagrams of

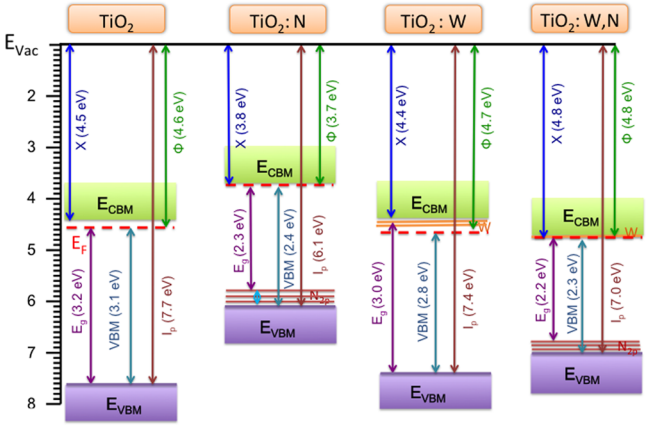

Figure 6. Energy band diagrams of undoped TiO_2, TiO_2:N, TiO_2:W, and (W,N) doped TiO_2 films.

undoped, N, W, and (W,N) doped TiO_2. From the lower binding energy region of UPS spectra (0 to 3 eV), an intriguing observation shows that the Ti^{III} defect states due to the oxygen vacancies close to the Fermi edge forms a peak symmetrically distributed around a binding energy of 0.9 eV. However, this defect induced signal intensity was found to vanish monotonically upon W and (W,N) doping of TiO_2. Also, from the inset of Figure 5, it is important to note that in the case of N doped films, the intensity of this defect states associated peak (while being less than that of undoped films) is much higher than the case of (W,N) doping.

This would infer that the defect states are being passivated by the (W,N) codoping approach, which leads to the suppression of recombination centers (especially Ti^{III} defect states) and yet maintaining the effective reduced bandgap.

4. CONCLUSION

In summary, by developing a reliable RF cosputtering process for the deposition of in situ doped TiO_2 films, we were able to achieve both monodoped (by N or W) and (W,N) doped films with accurately controlled doping levels. The doped TiO_2 films were shown to exhibit a significant redshift of their absorption band edge, indicating thereby the progressive narrowing of their bandgap into the visible (as compared to the UV bandgap of 3.2 eV of undoped films). Indeed, a maximum bandgap reduction of up to 1.0 eV was achieved for the (W,N) codoped TiO_2 film. A detailed analysis of the chemical bonding states of the films revealed that the N and W were incorporated into the TiO_2 lattice through their respective substitution of O and Ti in the TiO_2 lattice. The apparent upshift of valence band edge toward the conduction band deduced from the VB spectra and directly correlated to the decrease of the observed band gap energy. The observed variation in work function values of these

DOI: 10.1021/acs.jpcc.5b08057
J. Phys. Chem. C 2016, 120, 631−638

films indicates the shifting of Fermi level with the introduction of defects states within the bandgap. A careful integration of all the XPS, UPS, and UV−vis derived results enabled us to schematize/map out the electronic structure of these doped structures through their respective band energy diagrams. This is of prime importance for the optimized integration of these doped TiO_2 films in optoelectronic or electro-photocatalytic devices. Work is underway to integrate these differently doped TiO_2 films as photoanodes and compare their performance for the electrophotocatalytic degradation of emerging contaminants in water.

AUTHOR INFORMATION

Corresponding Author

*E-mail: elkhakani@emt.inrs.ca. Tel: 514 228-6922.

Notes

The authors declare no competing financial interest.

ACKNOWLEDGMENTS

The authors would like to acknowledge the financial support from NSERC (the Natural Science and Engineering Research Council of Canada), Nano-Québec (the Québec Organization for the promotion of nanoscience and nanotechnologies), and the FRQNT (Le Fonds de Recherche du Québec-Nature et Technologies) through its strategic Network "Plasma-Québec".

REFERENCES

(1) Fujishima, A.; Honda, K. Electrochemical photolysis of water at a semiconductor electrode. *Nature* **1972**, *238*, 37−38.

(2) Mills, A.; Hunte, S. L. An overview of semiconductor photocatalysis. *J. Photochem. Photobiol., A* **1997**, *108*, 1−35.

(3) Linsebigler, L.; Lu, G. Q.; Yates, J. T. Photocatalysis on TiO_2 surfaces: principles, mechanisms, and selected results. *Chem. Rev.* **1995**, *95*, 735−738.

(4) Fujishima, A.; Rao, T. N.; Tryk, D. A. Titanium dioxide photocatalysis. *J. Photochem. Photobiol., C* **2000**, *1*, 1−21.

(5) Luo, H.; Takata, T.; Lee, Y.; Zhao, J.; Domen, K.; Yan, Y. Photocatalytic activity enhancing for titanium dioxide by co-doping with bromine and chlorine. *Chem. Mater.* **2004**, *16*, 846−849.

(6) Asahi, R.; Morikawa, T.; Ohwaki, T.; Aoki, K.; Taga, Y. Visible-light photocatalysis in nitrogen-doped titanium oxides. *Science* **2001**, *293*, 269−271.

(7) Yin, W. J.; Wei, S. H.; Al-Jassim, M. M.; Yan, Y. Double-hole-mediated coupling of dopants and its impact on band gap engineering in TiO_2. *Phys. Rev. Lett.* **2011**, *106*, 066801−4.

(8) Yu, H.; Irie, H.; Hashimoto, K. Conduction band energy level control of titanium dioxide: toward an efficient visible-light-sensitive photocatalyst. *J. Am. Chem. Soc.* **2010**, *132*, 6898−6899.

(9) Zhu, W.; Qiu, X.; Iancu, V.; Chen, X.; Pan, H.; Wang, W.; Dimitrijevic, N. M.; Rajh, T.; Meyer, H. M.; Paranthaman, M. P.; et al. Band gap narrowing of titanium oxide semiconductors by non-compensated anion-cation codoping for enhanced visible-light photoactivity. *Phys. Rev. Lett.* **2009**, *103*, 226401−4.

(10) Nishijima, K.; Ohtani, B.; Yan, X.; Kamai, T. A.; Chiyoya, T.; Tsubota, T.; Murakami, N.; Ohno, T. Incident light dependence for photocatalytic degradation of acetaldehyde and acetic acid on S-doped and N-doped TiO_2 photocatalysts. *Chem. Phys.* **2007**, *339*, 64−72.

(11) Batzill, M.; Morales, E. H.; Diebold, U. Influence of nitrogen doping on the defect formation and surface properties of TiO_2 rutile and anatase. *Phys. Rev. Lett.* **2006**, *96*, 026103−4.

(12) Park, J. H.; Kim, S.; Bard, A. J. Novel carbon-doped TiO_2 nanotube arrays with high aspect ratios for efficient solar water splitting. *Nano Lett.* **2006**, *6*, 24−28.

(13) Li, Y.; Zhou, X.; Chen, W.; Li, L.; Zen, M.; Qin, S.; Sun, S. Photodecolorization of rhodamine B on tungsten-doped TiO_2/activated carbon under visible-light irradiation. *J. Hazard. Mater.* **2012**, *227*, 25−33.

(14) Devi, L. G.; Murthy, B. N. Characterization of Mo doped TiO_2 and its enhanced photocatalytic activity under visible light. *Catal. Lett.* **2008**, *125*, 320−330.

(15) Bhattacharyya, K.; Varma, S.; Tripathi, A. K.; Bharadwaj, S. R.; Tyagi, A. K. Effect of vanadia doping and its oxidation state on the photocatalytic activity of TiO_2 for gas-phase oxidation of ethene. *J. Phys. Chem. C* **2008**, *112*, 19102−19112.

(16) Dholam, R.; Patel, N.; Adami, M.; Miotello, A. Hydrogen production by photocatalytic water-splitting using Cr- or Fe-doped TiO_2 composite thin films photocatalyst. *Int. J. Hydrogen Energy* **2009**, *34*, 5337−5346.

(17) Gai, Y.; Li, J.; Li, S. S.; Xia, J. B.; Wei, S. H. Design of narrow-gap TiO_2: a passivated codoping approach for enhanced photoelectrochemical activity. *Phys. Rev. Lett.* **2009**, *102*, 036402−4.

(18) Long, R.; English, N. J. First-principles calculation of nitrogen-tungsten codoping effects on the band structure of anatase-titania. *Appl. Phys. Lett.* **2009**, *94*, 132102−3.

(19) Kubacka, A.; Colon, G.; Garcia, M. F. N- and/or W-(co)doped TiO_2-anatase catalysts: effect of the calcination treatment on photoactivity. *Appl. Catal., B* **2010**, *95*, 238−244.

(20) Kubacka, A.; Baeza, B. B.; Colon, G.; Garcia, M. F. Doping level effect on sunlight-driven W,N-codoped TiO_2-anatase photo-catalysts for aromatic hydrocarbon partial oxidation. *Appl. Catal., B* **2010**, *93*, 274−281.

(21) Thind, S. S.; Wu, G.; Tian, M.; Chen, A. Significant enhancement in the photocatalytic activity of N, W co-doped TiO_2 nanomaterials for promising environmental applications. *Nanotechnology* **2012**, *23*, 475706−8.

(22) Celik, V.; Mete, E. Range-separated hybrid exchange-correlation functional analyses of Anatase TiO_2 doped with W, N, S, W/N, or W/S. *Phys. Rev. B: Condens. Matter Mater. Phys.* **2012**, *86*, 205112−9.

(23) Folli, A.; Bloh, J. Z.; Beukes, E. P.; Howe, F.; Macphee, D. E. Photogenerated charge carriers and paramagnetic species in (W,N)-codoped TiO_2 photocatalysts under visible-light irradiation: an EPR study. *J. Phys. Chem. C* **2013**, *117*, 22149−22155.

(24) Bloh, J. Z.; Folli, A.; Macphee, D. E. Adjusting nitrogen doping level in titanium dioxide by codoping with tungsten: properties and band structure of the resulting materials. *J. Phys. Chem. C* **2014**, *118*, 21281−21292.

(25) Gao, B.; Ma, Y.; Cao, Y.; Yang, W.; Yao, J. Great enhancement of photocatalytic activity of nitrogen-doped titania by coupling with tungsten oxide. *J. Phys. Chem. B* **2006**, *110*, 14391−14397.

(26) Di Valentin, C.; Finazzi, E.; Pacchioni, G.; Selloni, A.; Livraghi, S.; Paganini, M. C.; Giamello, E. N-doped TiO_2: theory and experiment. *Chem. Phys.* **2007**, *339*, 44−56.

(27) Barolo, G.; Livraghi, S.; Chiesa, M.; Paganini, M. C.; Giamello, E. Mechanism of the photoactivity under visible light of N-doped titanium dioxide. Charge carriers migration in irradiated N-TiO_2 investigated by electron paramagnetic resonance. *J. Phys. Chem. C* **2012**, *116*, 20887−20894.

(28) Lee, S.; Cho, I. S.; Lee, D. K.; Kim, D. W.; Noh, T. H.; Kwak, C. H.; Park, S.; Hong, K. S.; Lee, J. K.; Jung, H. S. Influence of nitrogen chemical states on photocatalytic activities of nitrogen-doped TiO_2 nanoparticles under visible light. *J. Photochem. Photobiol., A* **2010**, *213*, 129−135.

(29) Chen, X.; Burda, C. The electronic origin of the visible-light absorption properties of C-, N-and S-doped TiO_2 nanomaterials. *J. Am. Chem. Soc.* **2008**, *130*, 5018−5019.

(30) Napoli, F.; Chiesa, M.; Livraghi, S.; Giamello, E.; Agnoli, S.; Granozzi, G.; Pacchioni, G.; Di Valentin, C. The nitrogen photoactive centre in N-doped titanium dioxide formed via interaction of N atoms with the solid. Nature and energy level of the species. *Chem. Phys. Lett.* **2009**, *477*, 135−138.

(31) Wang, D.; Zou, Y.; Wen, S.; Fan, D. A. Passivated codoping approach to tailor the band edges of TiO_2 for efficient photocatalytic degradation of organic pollutants. *Appl. Phys. Lett.* **2009**, *95*, 012106−3.

DOI: 10.1021/acs.jpcc.5b08057
J. Phys. Chem. C 2016, 120, 631−638

(32) Li, M.; Zhang, J.; Zhang, Y. First-principles calculation of compensated (2N, W) codoping impacts on bandgap engineering in anatase TiO_2. *Chem. Phys. Lett.* **2012**, *527*, 63−66.
(33) Long, R.; English, N. J. Synergistic effects on bandgap-narrowing in titania by codoping from first-principles calculations. *Chem. Mater.* **2010**, *22*, 1616−1623.
(34) Sakthivel, S.; Kisch, H. Photocatalytic and photoelectrochemical properties of nitrogen-doped titanium dioxide. *ChemPhysChem* **2003**, *4*, 487−490.
(35) Delegan, N.; Daghrir, R.; Drogui, P.; El Khakani, M. A. Bandgap tailoring of in-situ nitrogen doped TiO_2 sputtered films intended for electrophotocatalytic applications under solar light. *J. Appl. Phys.* **2014**, *116*, 153510−8.
(36) Li, J.; Xu, J.; Dai, W. L.; Li, H.; Fan, K. One-pot synthesis of twist-like helix tungsten-nitrogen-codoped titania photocatalysts with highly improved visible light activity in the abatement of phenol. *Appl. Catal., B* **2008**, *82*, 233−243.
(37) Mishra, T.; Mahato, M.; Aman, N.; Patel, J. N.; Sahu, R. K. A mesoporous WN co-doped titania nanomaterial with enhanced photocatalytic aqueous nitrate removal activity under visible light. *Catal. Sci. Technol.* **2011**, *1*, 609−615.
(38) Tauc, J. Optical properties and electronic structure of amorphous Ge and Si. *Mater. Res. Bull.* **1968**, *3*, 37−46.
(39) Scanlon, D. O.; Dunnill, C. W.; Buckeridge, J.; Shevlin, S. A.; Logsdail, A. J.; Woodley, S. M.; Catlow, C. R. A.; Powell, M. J.; Palgrave, R. G.; Parkin, I. P.; et al. Band alignment of rutile and anatase TiO_2. *Nat. Mater.* **2013**, *12*, 798−801.
(40) Wong, M.-S.; Chou, H. P.; Yang, T.-S. Reactively sputtered N-doped titanium oxide film as visible-light photocatalyst. *Thin Solid Films* **2006**, *494*, 244−249.
(41) Price, N. J.; Reitz, J. B.; Madix, R. J.; Solomon, E. I. A synchrotron XPS study of the vanadia-titania system as a model for monolayer oxide catalysts. *J. Electron Spectrosc. Relat. Phenom.* **1999**, *98*, 257−266.
(42) Biesinger, M. C.; Payne, B. P.; Grosvenor, A. P.; Lau, L. W. M.; Gerson, A. R.; Smart, R. S. C. Resolving surface chemical states in XPS analysis of first row transition metals, oxides and hydroxides: Sc, Ti, V, Cu and Zn. *Appl. Surf. Sci.* **2010**, *257*, 887−898.
(43) Jackman, M. J.; Thomas, A. G.; Muryn, C. Photoelectron spectroscopy study of stoichiometric and reduced anatase TiO_2(101) surfaces: the effect of subsurface defects on water adsorption at near-ambient pressures. *J. Phys. Chem. C* **2015**, *119*, 13682−13690.
(44) Kitano, M.; Funatsu, K.; Matsuoka, M.; Ueshima, M.; Anpo, M. Preparation of nitrogen-substituted TiO_2 thin film photocatalysts by the radio frequency magnetron sputtering deposition method and their photocatalytic reactivity under visible light irradiation. *J. Phys. Chem. B* **2006**, *110*, 25266−25272.
(45) Emeline, A. V.; Kuznetsov, V. N.; Rybchuk, V. K.; Serpone, N. Visible-light-active titania photocatalysts: the case of N-doped TiO_2-properties and some fundamental issues. *Int. J. Photoenergy* **2008**, *1* (ID 258394), 1−19.
(46) Viswanathan, B.; Krishnamurthy, K. R. Nitrogen incorporation in TiO_2: does it make a visible light photo-active material. *Int. J. Photoenergy* **2012**, *2012* (ID 269654), 1−10.
(47) Guo, X.; Dai, J.; Zhang, K.; Wang, X.; Cui, Z.; Xiang, J. Fabrication of N-doped TiO_2/activated carbon fiber composites with enhanced photocatalytic Activity. *Text. Res. J.* **2014**, *84*, 1891−1900.
(48) Zhang, Z.; Wang, X.; Long, J.; Gu, Q.; Ding, Z.; Fu, X. Nitrogen-doped titanium dioxide visible light photocatalyst: spectroscopic identification of photoactive centers. *J. Catal.* **2010**, *276*, 201−214.
(49) Duarte, D. A.; Massi, M.; da Silva Sobrinho, A. S. Development of dye-sensitized solar cells with sputtered N-doped TiO_2 thin films: from modelling the growth mechanism of the films to fabrication of the solar cells. *Int. J. Photoenergy* **2014**, *2014* (ID 839757), 1−13.
(50) Cortes- Jacome, M. A.; Morales, M.; Chavez, C. A.; Ramirez-Verduzco, L. F.; Lopez-Salinas, E.; Toledo-Antonio, J. A. WO_x/TiO_2 catalysts via titania nanotubes for the oxidation of dibenzothiophene. *Chem. Mater.* **2007**, *19*, 6605−6614.
(51) Sun, M.; Xu, N.; Cao, Y. W.; Yao, J. N.; Wang, E. G. Nanocrystalline tungsten oxide thin film: preparation, microstructure, and photochromic behavior. *J. Mater. Res.* **2000**, *15*, 927−933.
(52) CasaXPS software version 2.3.16 PR 1.6, Casa software Ltd.
(53) Fischer, D. W. X-ray band spectra and molecular-orbital structure of rutile TiO_2. *Phys. Rev. B* **1972**, *5*, 4219−4226.
(54) Laidani, N.; Cheyssac, P.; Perrière, J.; Bartali, R.; Gottardi, G.; Luciu, I.; Micheli, V. Intrinsic defects and their influence on the chemical and optical properties of TiO_{2-X} films. *J. Phys. D: Appl. Phys.* **2010**, *43* (485402), 1−11.
(55) Gutmann, S.; Wolak, M. A.; Conrad, M.; Beerbom, M. M.; Schlaf, R. Effect of ultraviolet and X-ray radiation on the work function of TiO_2 surfaces. *J. Appl. Phys.* **2010**, *107* (103705), 1−8.
(56) Kim, J. S.; Lagel, B.; Moons, E.; Johansson, N.; Baikie, I. D.; Salaneck, W. R.; Friend, R. H.; Cacialli, F. Kelvin probe and ultraviolet photoemission measurements of indium tin oxide work function: a comparison. *Synth. Met.* **2000**, *111*, 311−314.
(57) Kumar, A.; Mohanty, T. Electro-optic modulation induced enhancement in photocatalytic activity of N-doped TiO_2 thin films. *J. Phys. Chem. C* **2014**, *118*, 7130−7138.
(58) Raut, N. C.; Mathews, T.; Panda, K.; Sundaravel, B.; Dash, S.; Tyagi, A. K. Enhancement of electron field emission properties of TiO_{2-x} nanoplatelets by N-doping. *RSC Adv.* **2012**, *2*, 812−815.

DOI: 10.1021/acs.jpcc.5b08057
J. Phys. Chem. C 2016, 120, 631−638

Article 3

Direct evidence of defect pair reduction in magnetron sputtered TiO_2:W films leading to improved electro-photocatalytic performance – a dielectric spectroscopic study; N. Delegan,1 T. Teranishi,2 and M. A. El Khakani; Submitted to Journal of Applied Physics (Oct 2018)

Direct evidence of oxygen vacancy defects reduction in RF-magnetron sputtered TiO_2:W – a high frequency dielectric spectroscopy study

N. Delegan,[1] T. Teranishi,[2] and M. A. El Khakani*,[1]

[1]Institut National de la Recherche Scientifique, Centre-Énergie, Matériaux et Télécommunications, 1650 Blvd. Lionel-Boulet, Varennes, QC, J3X-1S2, Canada

[2]Okayama University, 3-1-1 Tsushima-naka, Kita-ku, Okayama 700-8530, Japan

Corresponding author: elkhakani@emt.inrs.ca

Abstract

Tungsten doped titanium dioxide (TiO_2:W) has been reported to have increased photocatalytic performance as compared to undoped TiO_2. The exact mechanisms behind this remain debated. Consequently, the purpose of this work is to refine the understanding of optoelectronic changes brought on via TiO_2 tungsten doping. An *in-situ* radio frequency magnetron-sputtering deposition process was used to fabricate undoped (TiO_2), oxygen deficient (TiO_{2-x}), and tungsten doped (TiO_2:W) films with varying dopant levels. X-ray photoelectron spectroscopy measurements showed the presence of both W_{Ti}'' and W_{Ti}^{x} type dopants that led to significantly reduced oxygen vacancy (V_O) densities. These observations were corroborated by X-ray diffraction analysis which revealed that the improved stoichiometry resulted in a marked enhancement of the rutile phase as compared to the sub-stoichiometric (V_O doped) samples. Critically, high frequency dielectric spectroscopy measurements revealed an optimal tungsten doping level of ~2.5 at.%. This point showed the greatest tungsten induced reduction in the $2[Ti^{III}]$-$[V_O'']$ defect pair ε' contribution, *i.e.* almost two orders of magnitude. Finally, this dielectrically observed reduction in V_O was correlated to an increase in photocharge decay

lifetimes. In other words, photocharge lifetimes increased in accordance with the reduction of V_O defects brought on by tungsten doping.

Introduction

Titanium dioxide (TiO_2) has been widely studied in the field of photocatalysis. With much of the recent research efforts targeted at either increasing its visible light photosensitivity or charge separation efficiency.[1–5] On the visible light absorption front, TiO_2 doping with anionic elements has shown much promise.[2–4,6–10] It was successful in reducing the band gap (E_g) of TiO_2 well into the visible light absorption range (*i.e.* E_g ~2.3 eV). However, such approaches suffered from a marked increase in oxygen vacancy defects (V_O). Leading to a reduction of the material's per-photon photocatalytic efficiency, due to poor carrier transport properties.[10–17] On the other hand, cationic type doping of TiO_2, most notably tungsten doping (TiO_2:W), has been shown to drastically increase the materials photocatalytic performance. This was achieved even while minimal visible light photosensitisation (*i.e.* a maximal ~0.2 eV red-shift of the E_g) was reported.[18–20] The exact mechanisms behind this remain debated. The proposed hypothesis for this improvement being that tungsten doping could increase the surface roughness (active area), grain size, carrier mobility, or assist charge carrier separation.[18–20]

The purpose of this work is to refine the understanding of the structural and optoelectronic changes brought on by tungsten doping of TiO_2 (TiO_2:W). All the while showing practical applicability of these thin films for electro-photocatalytic (EPC) applications. In this context, we report on a one-step, ultra-pure reactive RF-magnetron sputtering process used to prepare undoped (TiO_2), oxygen deficient (TiO_{2-x}), and tungsten doped (TiO_2:W) films with varying

doping levels. These were subjected to different characterization techniques such as X-ray photoelectron spectroscopy (XPS), Scanning Electron Microscopy (SEM), and X-ray diffraction (XRD). These characterizations served to qualify their chemical composition, dopant oxidation states, morphology, and structure. In parallel, high frequency dielectric spectroscopy (HF-DS) measurements of the sputtered samples were performed. HF-DS analysis revealed the defect dielectric contributions, distinguishing them from structural effects such as grain and domain boundaries.[21–23] This was critical in thinning down the aforementioned hypothesis for the observed improved EPC properties of TiO_2:W.

Specifically, we were able to elaborate on the dopant dependent electronic defect states of TiO_2:W. Most notably, we noted a sharp variation of V_O charge recombination centers because of tungsten loading and demonstrated an optimal tungsten loading point. These results help clarify the beneficial photocatalytic performances reported for TiO_2:W based photoanodes. Finally, the added benefits of tungsten doping were reiterated by demonstrating a perfect correlation between the reduction in the defect dipole ε' contribution and characteristic photocharge lifetimes of the TiO_2:W films.

Experimental

The TiO_2:W films were sputter-deposited from a 7.62 cm-diameter TiO_2 target (99.99% purity) using an RF (13.56 MHz) magnetron sputtering process with a constant power density of $W \cdot cm^{-2}$ applied to the target. Prior to deposition, the sputtering chamber was cryo-pumped to a $2 \cdot 10^{-8}$ Torr base pressure. During sputter-deposition, high purity Ar gas (99.999%) was introduced in the chamber with monitored gas flow rates as to maintain a $1.44 \cdot 10^{-3}$ Torr working pressure. For the deposition of stoichiometric TiO_2 thin films, high purity O_2 gas (99.995% purity) at a ratio of

15% (*i.e.* 100%·[O_2]/([O_2]+[Ar])) was maintained in the sputtering gas as to offset the naturally occurring preferential oxygen sputtering. Tungsten incorporation was accomplished via concomitant 7.62 cm-diameter WO_3 target (99.95% purity) sputtering parallel to the main TiO_2 target sputtering. The W incorporation into the TiO_2:W films was controlled by varying the WO_3 target power density (W_{power}) from 0.11 W·cm^{-2} to 0.66 W·cm^{-2}. The sputter-deposited films were deposited onto silicon, quartz, and Ti substrates mounted on an off-axis holder 20 cm from the sputtering target. Prior to film deposition, the targets were systematically sputter-cleaned with Ar ions for ~15 min with the shutters closed. No post acceleration bias was applied to the substrates during the sputtering process. However, a built-in plasma sheath bias of ~ -15 V was detected. During deposition, the substrates were heated by a quartz lamp heater to an on-substrate temperature of ~470 °C.

The thicknesses of the TiO_2:W films were *in-situ* monitored by means of a calibrated quartz-crystal microbalance and *ex-situ* measured through cross-sectional high-resolution SEM images obtained using a Jeol JSM-6300F microscope. The crystalline structure of the on-quartz deposited films was investigated by means of a PANalytical X-Pert Pro X-ray diffractometer (XRD) system using CuKα radiation (1.5418 Å) at a grazing incidence angle of 0.75°. Williamson-Hall plot values were fitted using the standard $\beta_{hkl}\cdot\cos\theta = 4\varepsilon\cdot\sin\theta + K\lambda/D$ relationship (where β_{hkl}, θ, ε, K, λ, and D are the peak broadening (in rad), peak position, strain, shape factor (~0.9), the CuKα wavelength, and crystallite size, respectively).[24] The dopant bonding states and atomic composition of the films were systematically characterized by means of X-ray photoelectron spectroscopy (XPS). The spectra were collected by using the ESCALAB 220i-XL spectrophotometer (Thermo VG Scientific Ltd., UK), equipped with an AlKα (1486.6 eV) twin-anode X-ray source, after a systematic *in-situ* surface cleaning by means of 5 keV Ar^+

ion sputtering. The obtained spectra were fitted using the CasaXPS *ver. 2.3.15* software with Shirley background approximation. Surface charge effects were controlled for by verifying the location of the pre-sputter cleaned C *1s* peak (C-C bond). All atomic species were fitted using fixed values for intrinsic properties such as peak shape (*i.e.* GL(30)), and the doublet area/separation relationships taken from the NIST Standard Reference Database 20, Version 4.1. Given the overlapped nature of the tungsten spectra, both the W *4f* and W *4d* binding energy windows were used as to assure appropriate quantification.

In order to perform high-frequency dielectric measurements, planar top electrodes with a 20 μm gap and 200 nm thickness were sputter-deposited onto the TiO_2:W thin films by DC sputtering of an Gold (Au) target through a laser etched stainless-steel mask using a Sanuy Denshi DC-701 quick coater. The sputtering current and time was maintained at 10 mA and 1 h, respectively as to obtain the desired thickness. The thin film's dielectric signal was measured via microscope-aligned micro-probe using an E4991A Agilent Tech. network analyser. Accurate spatial models of the sample, electrode, and substrate environment were developed and calculated via electromagnetic field simulations using the Sonnet 13 software suite. The complex permittivity of the sputter deposited thin films in the low MHz to GHz range was determined by fitting measured susceptance onto that calculated data as to extract the TiO_2:W thin film ε' and $\tan(\delta)$ (*i.e.* $\tan(\delta) = \varepsilon''/\varepsilon'$ and measured $\varepsilon = \varepsilon' + i\varepsilon''$). The dielectric dispersion caused by the interfacial contributions and dipole polarisations was fitted using the empirical relation: $\frac{\varepsilon(\omega)-\varepsilon_\infty}{\varepsilon_0-\varepsilon_\infty} = \sum_{i=1}^{contributions} g_i \left(\frac{1}{1+i\omega\tau_i}\right)$ where ε_∞ is the permittivity contribution from ionic and electronic resonances, ε_0 the low-frequency permittivity, with g_i and τ_i being the proportionality coefficient

and characteristic relaxation time of contributions *I*, respectively. A more detailed description of the experimental procedure can be found elsewhere.[21]

Results and Discussion

A typical (Au) top electrode with contact micro-probe is shown in Figure 1 (a). Figure 1 (b) shows across-sectional SEM micrograph of 455 nm thick TiO_2:W thin film on an Si substrate. Film thicknesses for all deposited TiO_2:W were maintained in the 400-500 nm range. The sputter-deposited thin films were all dense, smooth, and had few structural features. No significant differences in morphology were observed for varying dopant-loading levels.

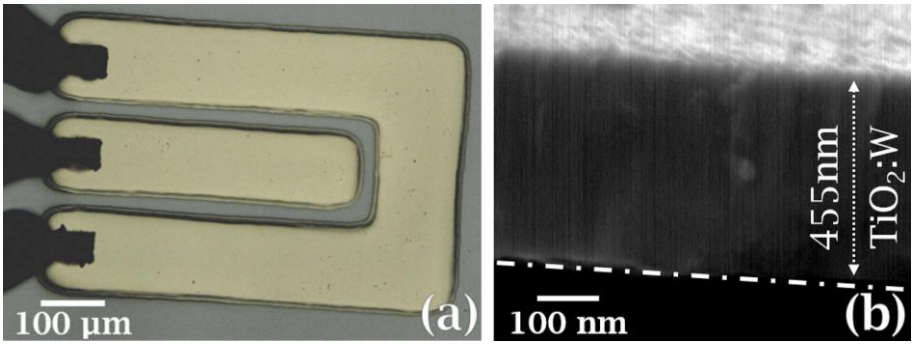

Figure 1: (a) top-view of an Au planar electrode with micro-probe in contact on a TiO_2:W sample. (b) typical cross-section SEM micrograph of a 455nm thick TiO_2:W thin film on a Si substrate.

The dopant incorporation efficiency of our sputtering approach was tracked as a function of tungsten target power (W_{power}) via quantitative XPS analysis. The derived quantifications are presented in Figure 2. We can note a steady quasi-linear increase in the total tungsten content (W_{tot}) of the sputtered thin films as a function of applied W_{power}. Due to size constraints, the W atoms are restricted only substitute the Ti atoms within the titania matrix.[18] Moreover, tungsten can adopt two distinct oxidation states in response to its local environment, *i.e.* W^{IV} and W^{VI}. We

note from Figure 2 that while W^{IV} also follows a quasi-linear dependence, the W^{VI} component tends to quickly saturate at the ~2 at.% mark. This saturation limit is a direct consequence of the local charge disparities brought up in the W_{Ti}'' doping configuration (W^{VI} substituting for Ti^{IV}) while not observed for W_{Ti}^{x} type doping (W^{IV} substituting for Ti^{IV}).

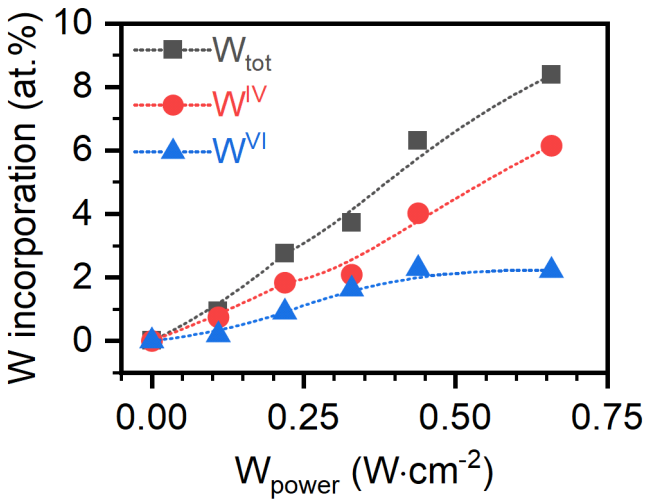

Figure 2: Tungsten (W) dopant incorporation efficiency differentiated by it's two main oxidative states W^{IV} and W^{VI} (with their total W_{tot}) in the sputter deposited TiO_2:W thin films as a function of variable WO_3 target power (W_{power}).

The quantifications for each dopant state and the overall chemical composition of the deposited thin films were derived from the O *1s*, Ti *2p*, W *4d* (also Ar *2p*), and W *4f* (also Ti *3p*) high-resolution XPS core level spectra. The redundant tungsten orbital quantifications were performed as to ensure proper deconvolution of the W *4f* spectra (*i.e.* use of W *4d* and Ti *2p* quantifications to ensure proper W *4f* and Ti *3p* deconvolution). Figure 3 shows the typical high-resolution XPS spectra for the above-mentioned energy windows in order of decreasing binding energy (BE) from left to right. For all sputtered samples, the Ti $2p_{3/2}$ peak can be split into two components: the Ti^{IV} and Ti^{III} oxidation states at 458.6 eV and 456.9 eV, respectively. With their

corresponding Ti $2p_{1/2}$ energy levels at ~5.6 eV higher BE.[7,18,25–27] These chemical states can be mirror derived from the Ti *3p* spectra. However, for visual clarity, the Ti *3p* peaks are greyed-out under the W *4f* & Ti *3p* envelope in Figure 3. The reduced Ti^{III} states are coherent with sub-stoichiometric TiO_{2-x} structures (Magneli phases). These are synonymous with oxygen vacancy (V_O) defect pairs, *i.e.* 2[Ti^{III}]-[V''_O]. All of the Ti *2p* derived states are mirrored in the O *1s* spectra. The TiO_2 lattice oxygen main peak O^A can be seen at 529.9 eV, with the sub-stoichiometric O^B at ~0.5 eV higher binding energy.[25,26] A third signature O_{def} is seen at slightly higher BE and is associated with defective oxygen species and surface hydroxides.[25,26,28] Samples prepared with sputtering of a WO_3 target showed the presence of W *4f* and W *4d* features in their corresponding BE windows. The two doublets observed in the W *4f* window are representative of the W^{VI} and W^{IV} oxidative states of tungsten in an oxide environment with the main $4f_{7/2}$ components at 34.5 eV and 32.3 eV, respectively. The corresponding $4f_{5/2}$ doublets are found at ~2.2 eV higher BE.[18,29–32]

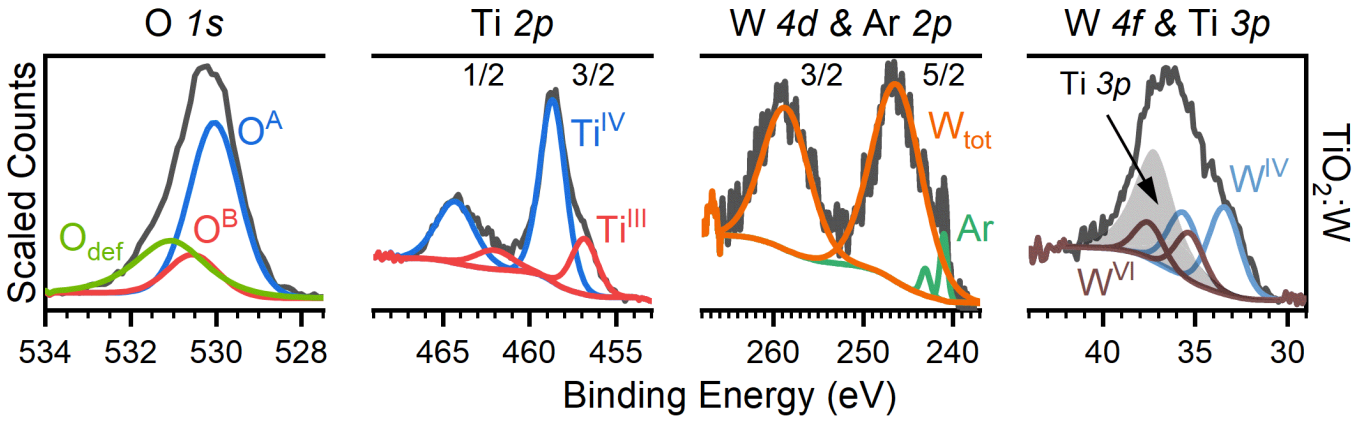

Figure 3: X-ray photoelectron spectroscopy spectra with deconvoluted chemical bonding states for the W_{power} = 0.22 W·cm^{-2} deposited TiO_2:W. From left to right we see the BE energy windows of the O *1s*, Ti *2p*, W *4d* (also Ar *2p*) and W *4f* (also Ti *3p*) orbitals. The Ti *3p*

signatures within the W *4f* BE window are greyed out to visually lighten the figure. Normalised (scaled) counts used as the Y-axis for display purposes.

A summary of the TiO_2:W film's chemical quantifications and stoichiometry is presented in Table 1. From this, we can confirm that the addition of O_2 in the sputtering gas negates the formation of 2[Ti^{III}]-[V''_O] defect pairs (caused by preferential sputtering).[7,8] Quantitatively, we note that the stoichiometry improved from $TiO_{1.74}$ to $TiO_{1.90}$ for the Ar-gas and O_2/Ar-gas sputtered samples, respectively. The control of these defects is key as they are known photocharge recombination sites. While they contribute to some visible light absorption (through the formation of defect bands below the conduction band minimum (CBM)). Overall, they greatly hinder the charge transport efficacy of the material in PEC applications.[8,10–17,33] Interestingly, the incorporation of tungsten results in the suppression of Vo defects. We note that while under a 100% pure Ar sputtering gas environment we observe a drastic stoichiometric shift from $TiO_{1.74}$ to $TiO_{2.05}W_{0.03}$ for W_{power} = 0.11 $W{\cdot}cm^{-2}$, indicating a colossal reduction of V_O density. While some of this is due to the co-sputtering target acting as a source of atomic O. Most of the effect is a direct consequence of W_{Ti}'' incorporation raising the formation energy of V_O defects.[34,35] This was further reiterated by swapping the WO_3-target for a metallic W-target as a co-sputtering tungsten source (*i.e.* not a source of atomic O). This was done with an applied W_{power} of 0.09 $W{\cdot}cm^{-2}$ to the W-target. XPS analysis showed a marked improvement of stoichiometry from $TiO_{1.74}$ to $TiO_{1.96}W_{0.02}$. This confirms the benefits of tungsten incorporation on the reduction of oxygen vacancy defects in TiO_2:W. However, this effect seems to diminish upon higher W loading due to the heavy cationic load. Hinting at the presence of an optimal point between heavy cationic load and V_O decrease.

W_{power} ($W \cdot cm^{-2}$)		O (at.%)	Ti_{tot} (at.%)	W^{VI} (at.%)	W^{IV} (at.%)	W_{tot} (at.%)	Stoichiometry
	O_2	65.6	34.4	0.0	0.0	0.0	$TiO_{1.90}$
	Ar	62.9	37.0	0.0	0.0	0.0	$TiO_{1.74}$
0.11		66.6	32.5	0.2	0.7	0.9	$TiO_{2.05}W_{0.03}$
0.22		65.8	31.4	0.9	1.8	2.7	$TiO_{2.10}W_{0.09}$
0.33		65.2	31.1	1.6	2.1	3.7	$TiO_{2.10}W_{0.12}$
0.44		64.8	28.9	2.3	4.0	6.3	$TiO_{2.24}W_{0.22}$
0.66		64.7	27.0	2.2	6.2	8.4	$TiO_{2.40}W_{0.31}$

Table 1: TiO_2:W thin film stoichiometry derived from quantitative XPS analysis as a function of deposition conditions such as the addition of 15% O_2 in the sputtering gas and applied WO_3 target sputtering power (W_{power}).

X-ray diffraction measurements were performed, and are presented as a function of tungsten loading in Figure 4 (with doping levels in ascending order from bottom to top). A well crystallised anatase phase can be detected for the $TiO_{1.90}$ thin films with a weak shoulder on its main peak indicative of trace amounts of rutile.[7,8] Samples with a high V_O density (*e.g.* $TiO_{1.74}$) show a poorly crystallised rutile phase. This is an expected consequence of TiO_2 sputter-deposition near the anatase-rutile transition point (*i.e.* ~500-600°C) with no extra O sources present.[7,36] Once tungsten is introduced into the lattice, we note that a well crystallised rutile phase becomes dominant. This is in alignment with previously noted XPS observations showing a higher content of W^{IV} as compared to W^{IV} in the TiO_2:W. Substitutional W^{VI} doping is expected to favor anatase formation due to dopant size compatibility, *i.e.* W_{Ti}'' (0.600 Å atomic radii) fits better into anatase lattice Ti_{Ti}^{x} (0.605 Å) locations as compared to W_{Ti}^{x} (0.660 Å atomic radii).[18] However, the W^{IV} species naturally form in a rutile-like structure, pushing the TiO_2:W to crystalize as such.[37] At higher doping levels (*i.e.* around the W^{VI} dopant saturation point), both the anatase and rutile phases are present. This is likely a result of two main factors:

(i) the anatase favoring W^{VI} content is at its highest, and (ii) the lattice strain is minimised upon the formation of the mostly W^{VI} containing anatase and mostly W^{IV} containing rutile phases. To verify these hypotheses, Williamson-Hall (W-H) analysis was performed on the obtained XRD signals. The inset in Figure 4 shows the Williamson-Hall derived strain η as a function of total tungsten content W_{tot}. Indeed, we note that up to ~2.5 at.% of incorporated tungsten, there is a steady build-up of lattice expansion strain in the rutile structure; specifically through stretching of the *a* lattice constant. This culminates in the formation of a bi-phase polycrystalline thin films as a relaxation mechanism. Past this point, the W^{VI} loading no longer increases, whereas W^{IV} continues to build up. Favoring the rutile phase formation with the strain continuing to build up. This change in strain is accompanied with changes in domain sizes. The $TiO_{1.90}$ films showed domains of ~130 nm, decreasing to their lowest size of ~15 nm upon the introduction of V_O (*i.e.* $TiO_{1.74}$) and then holding quasi-unchanged with W loading at about ~40 nm ($TiO_{2.10}W_{0.09}$). Most importantly, we note that for all samples, a clear dominant TiO_2 phase is present with no signs of WO_2 or WO_3 clustering.

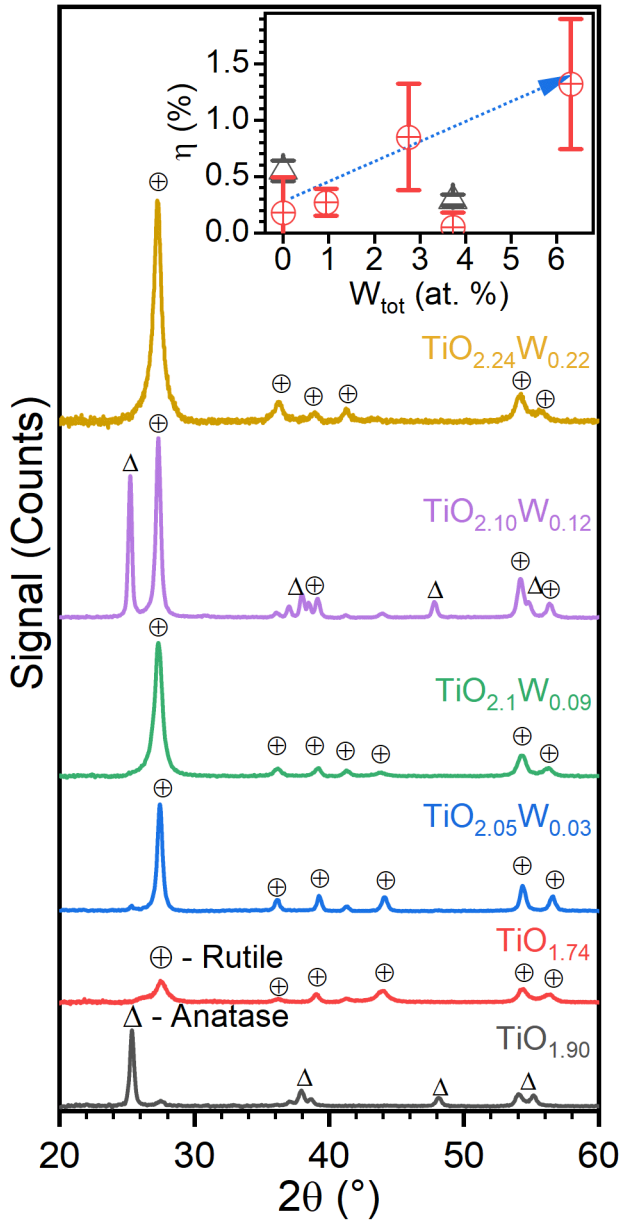

Figure 4: X-ray diffraction spectra of the TiO_2:W as a function of increasing W loading. The reference undoped $TiO_{1.90}$ and sub-stoichiometric $TiO_{1.74}$ spectra included for comparison. Inset shows the Williamson-Hall derived strain η as a function of total tungsten content W_{tot}.

In order to study the intrinsic benefits provided by W loading while distinguishing these from the structural relaxation effects, high frequency dielectric spectroscopy (HF-DS) measurements of the sputter deposited TiO_2:W thin films were performed. HF-DS allows the differentiation of

various dielectric contributions based on the frequency range in which they respond. The total dielectric constant of the material being the combined contribution of interfacial effects, intrinsic dipoles, ionic contributions, and electronic oscillations, *i.e.* $\varepsilon_{total} \approx \varepsilon_{interface} + \varepsilon_{dipole} + \varepsilon_{ionic} + \varepsilon_{electronic}$. The $\varepsilon_{interface}$ contributions manifest themselves as dielectric relaxations in ε' at the MHz range and lower. Whereas ε_{dipole} contributions such as defect association pairs (*e.g.* $2[Ti^{III}]$-$[V''_O]$) are expected to resonate in the MHz-GHz range.[22] Therefore, by studying the ε' behavior of the material in this spectral range, both the contributions from the grain interfaces and lattice dipoles should manifest, yet be distinguishable. Permittivity in the THz and far-infrared is dictated by resonant ionic polarisation and soft-phonon modes, respectively (*i.e.* $\varepsilon'_\infty \sim \varepsilon_{ionic} + \varepsilon_{electronic}$). In sum, we can safely approximate that past the MHz range, the dielectric relaxation contribution due to interfacial domain polarisation will be negligible, leaving us with $\varepsilon'_{dipole} \approx \varepsilon' - \varepsilon'_\infty$.[21,38]

Figures 5 (a) and (b) present typical ε' and ε'' HF-DS experimental and fitted spectra for the undoped ($TiO_{1.90}$), oxygen deficient ($TiO_{1.74}$), and tungsten doped ($TiO_{2.10}W_{0.12}$) samples. As predicted, all of the samples showed a significant interfacial ε' contribution tapering off in the MHz range (with its corresponding ε'' relaxation peak). To better understand this, Figure 6 (a) presents the ε' and tanδ ($\varepsilon''/\varepsilon'$) as a function of W-doping taken at 1 MHz (data point left of 0 at.% represents O_2-gas sputter-deposited $TiO_{1.90}$). We note that both ε' and tanδ remain mostly unchanged for all but the undoped $TiO_{1.90}$ sample. Indeed, given that all of samples have crystal grain sizes in the ~15-40 nm range (as determined by Williamson-Hall analysis), their interfacial ε' contribution remains relatively similar. This is contrasted by the $TiO_{1.90}$ samples with significantly larger crystal domains of ~130 nm. Confirming that up to the MHz range, the dielectric contributions arise from domain interfaces.

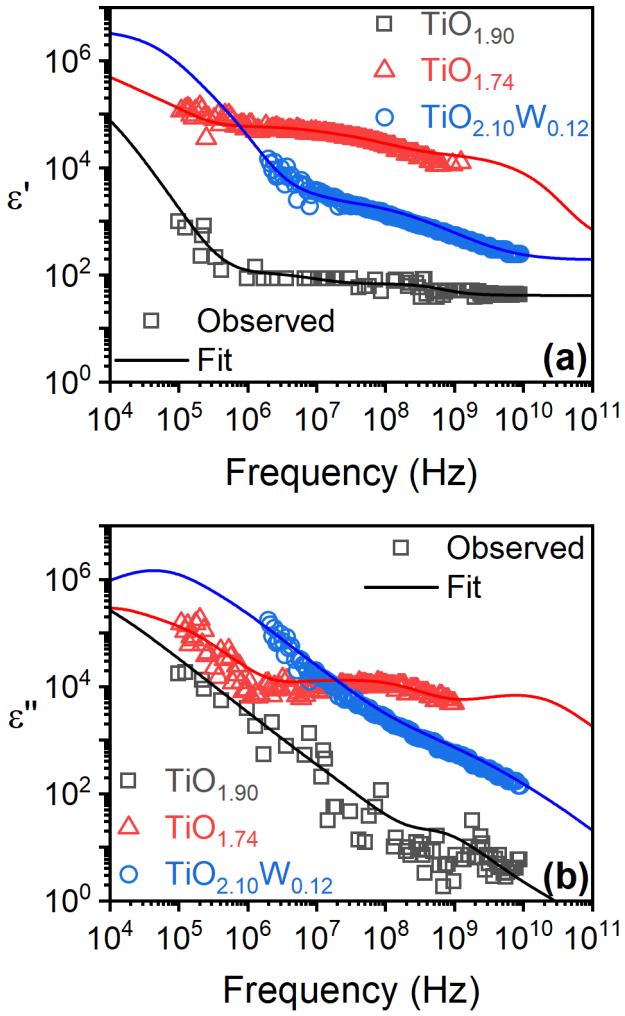

Figure 5: (a) ε′ and (b) ε″ HF-DS spectra for the undoped ($TiO_{1.90}$), oxygen deficient ($TiO_{1.74}$), and tungsten doped ($TiO_{2.10}W_{0.12}$).

In comparison, Figure 6 (b) shows the ε′ and tanδ as a function of W-doping, taken at 1 GHz. We note that tanδ slowly increases with W_{tot} as a result of increased overall n-type doping of the material. Interestingly, the ε′ contribution is seen to be dictated by the tungsten and V_O content, in contrast to what was observed in the MHz regime. Specifically, we note that the dielectric contribution is highest for the heavily sub-stoichiometric samples, and decreases steadily with additional tungsten doping. This is corroborated by the clearly visible contribution in the MHz to GHz range as seen in Figures 5 (a) and (b). By comparing the $TiO_{1.90}$ and $TiO_{1.74}$ samples, it can

be proposed that this MHz to GHz ε'_{dipole} contribution arises from $2[Ti^{III}]$-$[V''_O]$ defect association dipoles.

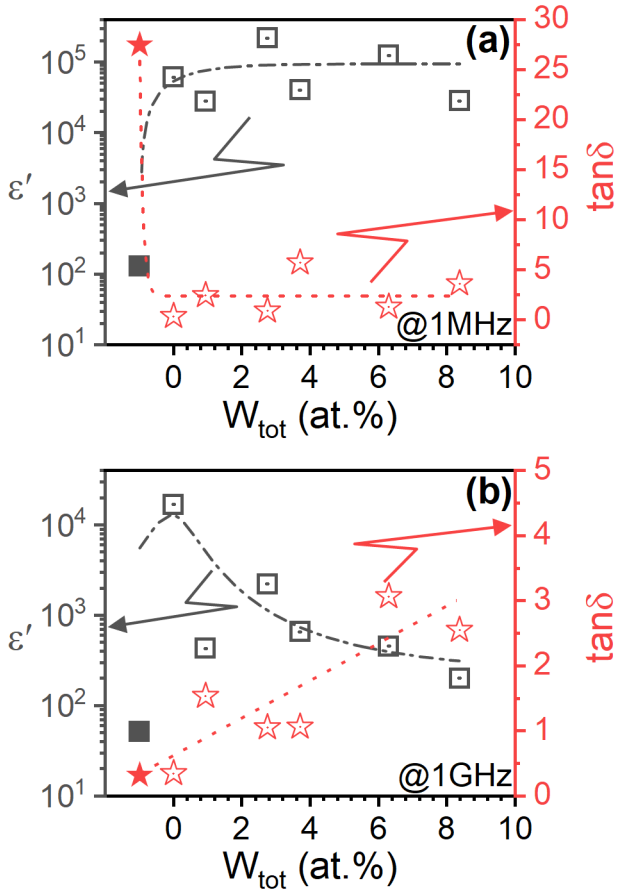

Figure 6: ε′ and tanδ as a function of tungsten loading (W_{tot}) taken at (a) 1 MHz and (b) 1 GHz. For comparison, the undoped, O_2 sputter-deposited $TiO_{1.90}$ sample is shown to the left of the 0 at.% mark with a filled symbol.

This defect dielectric contribution was isolated, *i.e.* $\varepsilon'_{dipole} \approx \varepsilon' - \varepsilon'_{\infty}$. Visually, the V_O dielectric contribution in the MHz-GHz range is shown in Figure 7 (a). Figure 7 (b) plots the isolated ε'_{dipole} as a function of W_{tot}. Indeed, we note about a four orders of magnitude increase in the ε'_{dipole} between the reference $TiO_{1.90}$ (ε'_{dipole} ~ 20) and the heavily sub-stoichiometric (V_O doped) $TiO_{1.74}$ films. Such V_O act as charge trapping and recombination centers, reducing the per-photon photocatalytic efficiency of the material.[10–17] Interestingly, tungsten loading significantly passivates the V_O defect contribution to the dielectric signature. All the while, no major variation

is observed in the ionic and electronic contributions as demonstrated by the almost constant ε'_{∞}. These observations are corroborated by the XPS results, which indicated a significant recovery of stoichiometry in the TiO_2:W samples. Figure 7 (b) shows that this effect has an optimal tungsten loading point of about ~2.5 at.%, at which we find minimized V_O defect electronic contributions. Past this point, the decrease in V_O formation from W^{VI} incorporation is offset by the heavy cationic load.[34,35]

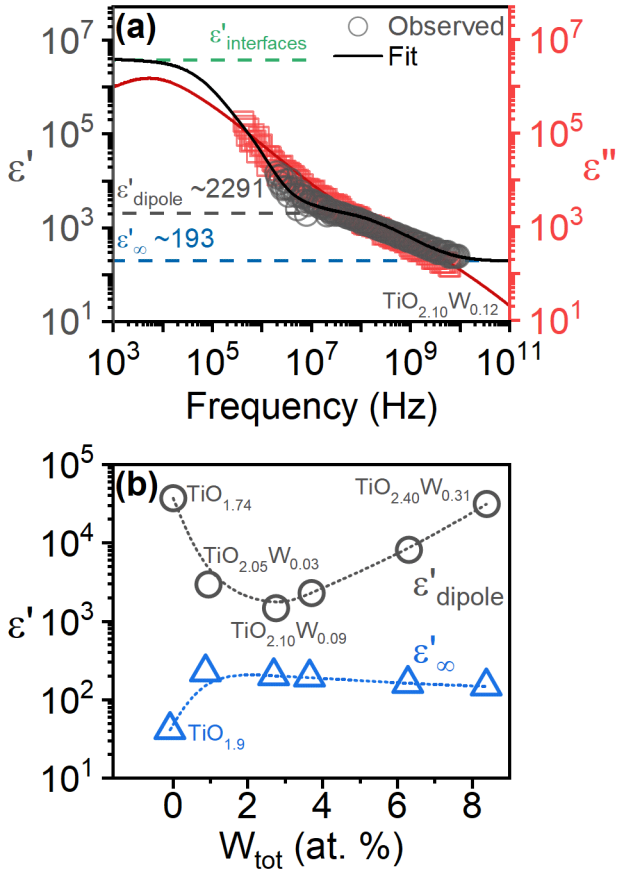

Figure 7: (a) V_O dielectric contribution ε'_{dipole} in the MHz-GHz range isolated from ε'_{∞} for the $TiO_{2.10}W_{0.12}$ sample (b) Isolated ε'_{dipole} plotted alongside ε'_{∞} as a function of W_{tot}.

Based on the observation of this optimal point, we would predict that TiO_2:W should perform better than any V_O doped or undoped titania when used as photoanodes in electro-photocatalytic

processes. In a separate study, we investigated the effect of W-doping on photocharge lifetime constants of TiO_2:W.[39] It was observed that the photocharge trapping decay constants within titania increased from 0.3 ± 0.06 μs for $TiO_{1.7}$ up to 1 ± 0.1 μs for optimally doped TiO_2:W.[39] This improvement translated to increased efficiency of exciton transport within the doped material as compared to the sub-stoichiometric one. It was proposed that this was due to a reduction in V_O defect trapping and recombination states brought on via W-doping. Figure 8 shows the V_O ε'_{dipole} contribution *versus* the photochange decay trapping lifetime constants (samples with similar tungsten incorporations). Indeed, we note a direct relationship between the electronic activity of V_O defects as tracked by HF-DS measurements, and photocharge lifetimes. This relationship confirms that tungsten doping is effective in directly reducing the formation V_O defects (*i.e.* the $2[Ti^{III}]$-$[V_O{''}]$ defect pair dipole) and therefore improving photocharge transport properties of TiO_2:W.

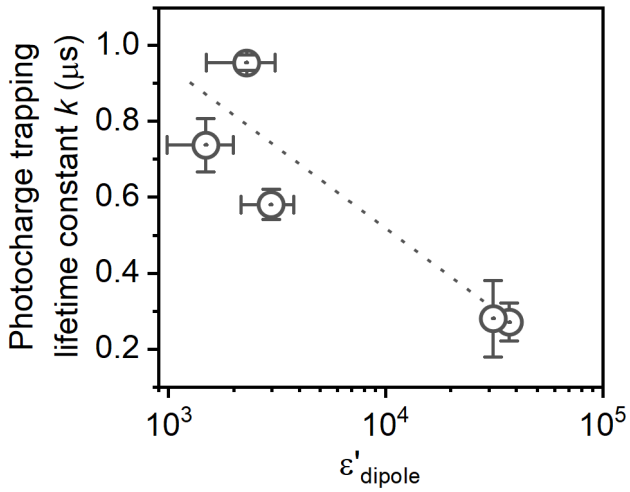

Figure 8: Photocharge trapping lifetime decay constant *k* (μs) as a function of V_O ε'_{dipole} contribution in TiO_2:W (both undoped and tungsten doped).

Conclusion

In summary, we have successfully synthesised *in-situ* V_O doped, and W doped thin films via a reliable RF magnetron sputtering process. The tungsten was shown to be incorporated in both W''_{Ti} and W_{Ti}^{x} type doping configurations. More importantly, as compared to $TiO_{1.74}$ thin films, the W doped thin films showed significant improvements in stoichiometry mainly due to an increase in the formation energy of V_O defects. These observations were corroborated by the improved stoichiometry, resulting in a marked improvement of the rutile phase as compared to the heavily V_O loaded samples. Additionally, the uneven lattice geometry and total incorporation of the W^{IV} and W^{VI} species culminated in the appearance of an anatase-rutile bi-phase polycrystalline structure. High frequency dielectric spectroscopy measurements revealed an optimal doping level ~2.5 at.% of W tungsten showing the biggest reduction of the $2[Ti^{III}]$-$[V_O{''}]$ defect pair ε' contribution. These observations were in direct alignment with XPS observed improvements in stoichiometry. Finally, a direct relationship between the electronic activity of V_O defects as tracked by HF-DS measurements, and photocharge lifetimes was confirmed. Reiterating that tungsten doping is effective in directly reducing the formation V_O defects (*i.e.* the $2[Ti^{III}]$-$[V_O{''}]$ defect pair dipole), and therefore improving the photocatalytic properties of TiO_2:W

Acknowledgements

The authors would like to acknowledge the financial support from NSERC (the Natural Science and Engineering Research Council of Canada) and the FRQNT (Le Fonds de Recherche du Québec-Nature et Technologies) through its strategic Network “Plasma-Québec”.

References

1. O'Regan, B. & Grätzel, M. A low-cost, high-efficiency solar cell based on dye-sensitized colloidal TiO2 films. *Nature* **353,** 737–740 (1991).

2. Khan, S. U. M., Al-Shahry, M. & Ingler, W. B. Efficient photochemical water splitting by a chemically modified n-TiO2. *Science* **297,** 2243–5 (2002).

3. Emeline, A. V., Kuznetsov, V. N., Rybchuk, V. K. & Serpone, N. Visible-Light-Active Titania Photocatalysts: The Case of N-Doped TiO 2 s—Properties and Some Fundamental Issues. *Int. J. Photoenergy* **2008,** 1–19 (2008).

4. FUJISHIMA, A., ZHANG, X. & TRYK, D. TiO2 photocatalysis and related surface phenomena. *Surf. Sci. Rep.* **63,** 515–582 (2008).

5. Hashimoto, K., Irie, H. & Fujishima, A. TiO 2 Photocatalysis: A Historical Overview and Future Prospects. *Jpn. J. Appl. Phys.* **44,** 8269–8285 (2005).

6. Asahi, R. Visible-Light Photocatalysis in Nitrogen-Doped Titanium Oxides. *Science (80-.).* **293,** 269–271 (2001).

7. Delegan, N., Daghrir, R., Drogui, P. & El Khakani, M. A. Bandgap tailoring of in-situ nitrogen-doped TiO 2 sputtered films intended for electrophotocatalytic applications under solar light. *J. Appl. Phys.* **116,** 153510 (2014).

8. Pandiyan, R., Delegan, N., Dirany, A., Drogui, P. & El Khakani, M. A. Probing the Electronic Surface Properties and Bandgap Narrowing of in situ N, W, and (W,N) Doped Magnetron-Sputtered TiO 2 Films Intended for Electro-Photocatalytic Applications. *J. Phys. Chem. C* **120,** 631–638 (2016).

9. Scanlon, D. O. *et al.* Band alignment of rutile and anatase TiO2. *Nat. Mater.* **12,** 798–801

(2013).

10. Di Valentin, C., Pacchioni, G. & Selloni, A. Origin of the different photoactivity of N-doped anatase and rutile TiO2. *Phys. Rev. B* **70,** 085116 (2004).

11. Di Valentin, C., Pacchioni, G., Selloni, A., Livraghi, S. & Giamello, E. Characterization of Paramagnetic Species in N-Doped TiO 2 Powders by EPR Spectroscopy and DFT Calculations. *J. Phys. Chem. B* **109,** 11414–11419 (2005).

12. Lynch, J. *et al.* Substitutional or Interstitial Site-Selective Nitrogen Doping in TiO 2 Nanostructures. *J. Phys. Chem. C* **119,** 7443–7452 (2015).

13. Peng, F., Cai, L., Yu, H., Wang, H. & Yang, J. Synthesis and characterization of substitutional and interstitial nitrogen-doped titanium dioxides with visible light photocatalytic activity. *J. Solid State Chem.* **181,** 130–136 (2008).

14. Torres, G. R., Lindgren, T., Lu, J., Granqvist, C.-G. & Lindquist, S.-E. Photoelectrochemical Study of Nitrogen-Doped Titanium Dioxide for Water Oxidation. *J. Phys. Chem. B* **108,** 5995–6003 (2004).

15. D'Arienzo, M. *et al.* Solar Light and Dopant-Induced Recombination Effects: Photoactive Nitrogen in TiO 2 as a Case Study. *J. Phys. Chem. C* **114,** 18067–18072 (2010).

16. Liu, B., Wen, L. & Zhao, X. The photoluminescence spectroscopic study of anatase TiO 2 prepared by magnetron sputtering. *Mater. Chem. Phys.* **106,** 350–353 (2007).

17. Katoh, R., Furube, A., Yamanaka, K. & Morikawa, T. Charge Separation and Trapping in N-Doped TiO 2 Photocatalysts: A Time-Resolved Microwave Conductivity Study. *J. Phys. Chem. Lett.* **1,** 3261–3265 (2010).

18. Sathasivam, S. *et al.* Tungsten Doped TiO2 with Enhanced Photocatalytic and Optoelectrical Properties via Aerosol Assisted Chemical Vapor Deposition. *Sci. Rep.* **5,** 10952 (2015).

19. Kubacka, A., Colón, G. & Fernández-García, M. Cationic (V, Mo, Nb, W) doping of TiO2–anatase: A real alternative for visible light-driven photocatalysts. *Catal. Today* **143,** 286–292 (2009).

20. Lorret, O., Francová, D., Waldner, G. & Stelzer, N. W-doped titania nanoparticles for UV and visible-light photocatalytic reactions. *Appl. Catal. B Environ.* **91,** 39–46 (2009).

21. Teranishi, T. *et al.* Quasi-millimeter-wave absorption behavior in Y/Yb-stabilized zirconia ceramics. *Appl. Phys. Lett.* **100,** 242903 (2012).

22. Teranishi, T., Kanemoto, R., Hayashi, H. & Kishimoto, A. Effect of the (Ba + Sr)/Ti ratio on the microwave-tunable properties of Ba 0.6 Sr 0.4 TiO 3 ceramics. *J. Am. Ceram. Soc.* **100,** 1037–1043 (2017).

23. Teranishi, T., Hoshina, T., Takeda, H. & Tsurumi, T. Analysis of polarization behavior in relaxation of BaTiO 3 -based ferroelectrics using wideband dielectric spectroscopy. *IEEE Trans. Ultrason. Ferroelectr. Freq. Control* **57,** 2118–2126 (2010).

24. Williamson, G. . & Hall, W. . X-ray line broadening from filed aluminium and wolfram. *Acta Metall.* **1,** 22–31 (1953).

25. Biesinger, M. C. *et al.* Resolving surface chemical states in XPS analysis of first row transition metals, oxides and hydroxides: Cr, Mn, Fe, Co and Ni. *Appl. Surf. Sci.* **257,** 2717–2730 (2011).

26. Jackman, M. J., Thomas, A. G. & Muryn, C. Photoelectron Spectroscopy Study of Stoichiometric and Reduced Anatase TiO 2 (101) Surfaces: The Effect of Subsurface Defects on Water Adsorption at Near-Ambient Pressures. *J. Phys. Chem. C* **119,** 13682–13690 (2015).

27. Thind, S. S., Wu, G., Tian, M. & Chen, A. Significant enhancement in the photocatalytic activity of N, W co-doped TiO 2 nanomaterials for promising environmental applications. *Nanotechnology* **23,** 475706 (2012).

28. Kitano, M., Funatsu, K., Matsuoka, M., Ueshima, M. & Anpo, M. Preparation of nitrogen-substituted TiO2 thin film photocatalysts by the radio frequency magnetron sputtering deposition method and their photocatalytic reactivity under visible light irradiation. *J. Phys. Chem. B* **110,** 25266–72 (2006).

29. Mishra, T., Mahato, M., Aman, N., Patel, J. N. & Sahu, R. K. A mesoporous WN co-doped titania nanomaterial with enhanced photocatalytic aqueous nitrate removal activity under visible light. *Catal. Sci. Technol.* **1,** 609 (2011).

30. Li, J., Xu, J., Dai, W. L., Li, H. & Fan, K. One-pot synthesis of twist-like helix tungsten-nitrogen-codoped titania photocatalysts with highly improved visible light activity in the abatement of phenol. *Appl. Catal. B Environ.* **82,** 233–243 (2008).

31. Ng, K. T. & Hercules, D. M. Studies of nickel-tungsten-alumina catalysts by x-ray photoelectron spectroscopy. *J. Phys. Chem.* **80,** 2094–2102 (1976).

32. Sun, M., Xu, N., Cao, Y. W., Yao, J. N. & Wang, E. G. Nanocrystalline Tungsten Oxide Thin Film: Preparation, Microstructure, and Photochromic Behavior. *J. Mater. Res.* **15,** 927–933 (2000).

33. Rumaiz, A. K. *et al.* Oxygen vacancies in N doped anatase TiO2: Experiment and first-principles calculations. *Appl. Phys. Lett.* **95,** 262111 (2009).

34. Long, R. & English, N. J. First-principles calculation of nitrogen-tungsten codoping effects on the band structure of anatase-titania. *Appl. Phys. Lett.* **94,** 132102 (2009).

35. Long, R. & English, N. J. Synergistic Effects on Band Gap-Narrowing in Titania by Codoping from First-Principles Calculations. *Chem. Mater.* **22,** 1616–1623 (2010).

36. Brassard, D., El Khakani, M. a. & Ouellet, L. Substrate biasing effect on the electrical properties of magnetron-sputtered high-k titanium silicate thin films. *J. Appl. Phys.* **102,** 034106 (2007).

37. Wong, F. J. & Ramanathan, S. Heteroepitaxy of distorted rutile-structure WO2 and NbO2 thin films. *J. Mater. Res.* **28,** 2555–2563 (2013).

38. Teranishi, T., Hayashi, H., Kishimoto, A. & Tsurumi, T. Broadband spectroscopy of the complex conductivity of polycrystalline yttria-stabilized zirconia. *Mater. Sci. Eng. B* **177,** 69–73 (2012).

39. Delegan, N. *et al.* Lifetime Enhancement of Visible Light Induced Photocharges in Tungsten and Nitrogen in situ Codoped TiO 2 :WN Thin Films. *J. Phys. Chem. C* **122,** 5411–5419 (2018).

Article 4

Lifetime Enhancement of Visible Light Induced Photocharges in Tungsten and Nitrogen in situ Codoped TiO_2:WN Thin Films; N. Delegan, R. Pandiyan, S. Johnston, A. Dirany, S. Komtchou, P. Drogui, and M. A. El Khakani; J. Phys. Chem. C 2018, 122, 10, 5411-5419

THE JOURNAL OF PHYSICAL CHEMISTRY C

Article

Cite This: J. Phys. Chem. C XXXX, XXX, XXX–XXX

pubs.acs.org/JPCC

Lifetime Enhancement of Visible Light Induced Photocharges in Tungsten and Nitrogen *in situ* Codoped TiO_2:WN Thin Films

N. Delegan,[†] R. Pandiyan,[†] S. Johnston,[‡] A. Dirany,[§] S. Komtchou,[§] P. Drogui,[§] and M. A. El Khakani*[,†]

[†]Centre-Énergie, Matériaux et Télécommunications, Institut National de la Recherche Scientifique, 1650 Blvd. Lionel-Boulet, Varennes, QC J3X-1S2, Canada

[‡]National Renewable Energy Laboratory, 1617 Cole Boulevard, Golden, Colorado 80401-3393, United States

[§]Centre-Eau, Terre et Environnement, Institut National de la Recherche Scientifique, 490 Rue de la Couronne, Québec City, QC G1K-9A9, Canada

ABSTRACT: We report on one-step in situ codoped TiO_2 thin films synthesized by cosputtering. The purpose of this acceptor–donor passivated codoping approach is to overcome the optoelectronic limitations that arise for monodoped TiO_2 in photocatalytic applications. To evaluate these added benefits, the TiO_2:WN thin films were characterized by different techniques. X-ray diffraction patterns and X-ray photoelectron spectral analysis revealed that both N and W dopants are mostly present in the desired substitutional locations. Additionally, the codoping approach was found to reduce the internal strain and defect density of the TiO_2:WN films as compared to their monodoped TiO_2:N counterparts. This defect reduction is confirmed via photocharge lifetime variation obtained using visible light flash photolysis time-resolved microwave conductivity measurements (FP-TRMC). Photocharge lifetime analysis indicated the presence of three distinct decay processes: charge trapping, recombination, and surface reactions. These characteristic lifetimes of the codoped TiO_2:WN films (i.e., 0.08, 0.75, and 11.5 μs, respectively) were found to be about double those of their nitrogen monodoped TiO_2:N counterparts (i.e., 0.03, 0.35, and 6.8 μs), quantitatively confirming the effective passivating outcome of the tungsten–nitrogen codoping approach developed here. The practicality of this method was confirmed by integrating the TiO_2:WN films as photoanodes for the electro-photocatalytic, solar light driven degradation of a real pollutant (i.e., atrazine). A significant increase in the degradation kinetics, leading to a 4-fold increase in the pseudo-first-order degradation constant for the optimally doped TiO_2:WN photoanodes (0.106 min^{-1}) from the undoped TiO_{2-x} ones (0.026 min^{-1}), is a direct consequence of the increased photocharge lifetimes in tandem with visible light photosensitivity.

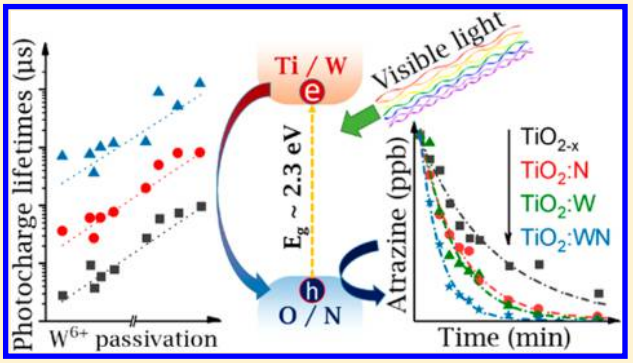

INTRODUCTION

Titanium dioxide (TiO_2) based photocatalysts continue to be extensively studied due to their high photoreactivity in water splitting reactions and in decomposing environmental pollutants. This interest is compounded by the material's availability, stability, and energy band positioning.[1−5] Fundamentally, TiO_2 is an n-type semiconductor with a wide intrinsic bandgap (E_g). The exact E_g value depends on the polymorph, with rutile (R) and anatase (A) having a 3.0 and 3.2 eV band gap, respectively. Its large E_g limits the use of pure TiO_2 driven photocatalytic applications to the UV portion of the solar spectrum, which represent only ~4% of the total energy flux at AM1.5G.[1−5] This limitation has led to substantial research efforts aimed at narrowing the E_g of the material to photosensitize it in the visible. To this end, various methods (such as self-doping, dye sensitization, cationic and/or anionic doping, etc.[2−4,6−10]) have been attempted. Substitutional nitrogen (N) doping has shown promising results as the formation for discrete N 2p acceptor states within the TiO_2 E_g has been reported to photosensitize the material well into the visible spectrum (~2.3 eV).[3,8,11] However, this narrowing induces defects states that tend to decrease the per-photon photocatalytic efficiency of the material by lowering the photocharge mean free path and increasing their recombination rates.[10,12−18]

Many studies have theoretically investigated possible pathways to circumvent these undesirable effects induced by N-doping of TiO_2 films. The most promising approach is based on acceptor–donor codoping that would suppress the charge disparities via local electronic passivation, while maintaining visible light photosensitization.[19−23] Dopant pairs such as (C +W), (V+N), (Nb+N), and (W+N) have all been proposed as possible candidates that would maintain proper band alignment required for active radical production in aqueous environment under solar illumination.[20,21,24,25] Among these pairs, tungsten

Received: November 14, 2017
Revised: January 24, 2018

DOI: 10.1021/acs.jpcc.7b11266
J. Phys. Chem. C XXXX, XXX, XXX–XXX

(W) and nitrogen (N) codoping has been outlined as a candidate of choice.[19−21,23]

Some experimental evidence of the WN-codoping approach has been recently put forth. On one hand, Cui et al.[26] and Thind et al.[27,28] independently showed that codoping has led to a favorable E_g reduction, with increased degradation kinetics as compared to the case for TiO_2:N samples. On the other hand, Kubacka et al. demonstrated similar results where they have clearly observed an improvement of optoelectronic properties of TiO_2:WN and an easier formation of −OH radicals at the photoanode surface.[29] However, in all cases, the exact optoelectronic properties and mechanisms have yet to be elucidated. Folli et al.[30] and Bloh et al.[31] reported that W and N incorporation (via wet chemistry synthesis routes) altered the band gap structure of the TiO_2:WN films. Unfortunately, most of their dopants were in interstitial locations, resulting in the formation of undesired deep gap states. In other words, practical demonstration and understanding of the beneficial substitutional type acceptor−donor passivated codoping of TiO_2:WN films is still lacking. Therefore, the main purpose and motivation of this study is to practically investigate and optimize codoping strategies to overcome the limitations associated with monodoping. In particular, insights into the per-photon efficiency of TiO_2 based photoanodes through the determination of their photocharge lifetimes and associated mean-free paths is of paramount interest. In this context, this study reports on a systematic investigation of photocharge lifetimes and their variation as a function of various doping schemes of sputtered TiO_2 films.

We used visible light flash photolysis time-resolved microwave conductivity measurements (FP-TRMC) to study the photocharge decay upon illumination of different TiO_2 photoanodes, namely undoped (TiO_{2-x}), monodoped (TiO_2:N and TiO_2:W), and codoped (TiO_2:WN) films as a function of dopant incorporation and varying doping levels. The photoanodes were prepared using a one-step reactive magnetron sputtering process. These were subjected to different characterization techniques including scanning electron microscopy (SEM), X-ray diffraction (XRD), and X-ray photoelectron spectroscopy (XPS) to qualify their structure, morphology, and chemical composition as a function of their doping states. In parallel, FP-TRMC was used to ascertain the effects of various doping configurations of the sputtered TiO_2 films on their optoelectronic behavior, namely, their characteristic photocharge lifetimes. We were thus able to demonstrate the much longer lifetimes exhibited by the optimally codoped TiO_2:WN, confirming thereby the occurrence of the acceptor−donor passivation. Finally, the application of these differently doped photoanodes to the electrophotocatalytic (EPC) degradation of a water pollutant (i.e., atrazine) confirmed that the optimally codoped TiO_2:WN photoanodes are the most effective as compared to other doped TiO_2 films. In fact, we were able to establish a direct correlation of the fundamental optoelectronic properties observed via TRMC with results obtained while using the TiO_2:WN films as photoanodes in the electro-photocatalytic degradation of a pesticide, atrazine under solar illumination.

EXPERIMENTAL SECTION

The TiO_2:WN films were deposited from the cosputtering of both a 3 in. diameter TiO_2 target (99.995% purity) and a 3 in. diameter W target (99.95% purity) using RF (13.56 MHz) magnetron sputter guns operating at a constant power density of 8.8 W/cm^2 for the TiO_2 target and a varying RF power density for the W target. Prior to deposition, the chamber was cryo-pumped to a base pressure of 2×10^{-8} Torr. High-purity Ar (99.999%) and N_2 (99.995%) gases were then introduced into the chamber. The gas flow rates were monitored to maintain a constant pressure of 1.45 mTorr in the chamber during the sputter-deposition process. To control the N incorporation in the TiO_2:WN films, the relative nitrogen mass flow rate ratio R_{N2} (i.e., $[N_2]/([N_2] + [Ar])$) was varied between 0 and 15%. The W incorporation was controlled by varying the W target power density (W_{power}) from 0.06 to 0.25 W/cm^2. The operating parameters to obtain desired N and W doping concentrations were set on the basis of the optimization work done previously on TiO_2:N and TiO_2:WN films.[7,8] The TiO_2:WN films were concomitantly deposited onto silicon, quartz, and Ti substrates. These were mounted on a holder located off-axis at a distance of 20 cm from the sputtering targets and heated during deposition by a quartz lamp heater to an on-substrate temperature of ∼470 °C. Prior to film deposition, the target was systematically sputter-cleaned with Ar ions for ∼15 min with the shutters closed. The thickness of the TiO_2:WN films was in situ monitored by means of a calibrated quartz-crystal microbalance and ex situ measured through cross-sectional scanning electron microscopy (SEM) by means of a Jeol JSM-6300F microscope. The thicknesses of all films was of about 300 nm. No post acceleration voltage was intentionally applied to the substrates during the sputter-deposition process (they were nonetheless subjected to a built-in plasma sheath bias of ∼−14 V during their growth).

The sputtering based doping process is highly reproducible (as this is one of the inherent advantages of such physical deposition technique); it allows a very tight control of the doping level through the fine adjustment of the various deposition parameters (power, pressure, bias, substrate temperature, gas flow ratio, etc.). Indeed, many samples for each doping conditions were deposited (in different deposition batches), and the initially targeted doping concentrations were always achieved almost perfectly within the precision of the XPS measurements (which is estimated to 0.1 at. %). The crystalline structure of the films on quartz substrates was characterized by means of a PANalytical X-Pert Pro X-ray diffractometer (XRD) system using Cu Kα radiation of 1.5418 Å. The atomic composition and chemical bonding states of the films were systematically investigated by means of X-ray photoelectron spectroscopy (XPS). High-resolution XPS core level spectra of all the samples were collected by using the ESCALAB 220i-XL spectrophotometer (Thermo VG Scientific Ltd.), equipped with a monochromatized Al Kα (1486.6 eV) twin-anode source after a systematic in situ surface cleaning by means of 5 keV Ar^+ ion sputtering gun with an average ∼0.15 mA current. The obtained spectra were fitted using the CasaXPS ver. 2.3.15 software with Shirley background approximation. Surface charge effects were controlled for by verifying the location of the presputter cleaned C 1s peak (C−C bond). All atomic species were fitted by using fixed values for intrinsic properties such as peak shape (i.e., GL(30)), and the doublet area/separation relationships taken from the NIST Standard Reference Database 20, Version 4.1 (https://srdata.nist.gov/xps/). The atomic concentrations were evaluated by using their relative sensitivity factors (RSF) defined in the NIST databases. Given the overlapped nature of the tungsten spectra, both the W 4f and W 4d (not shown) binding energy windows were used to ensure appropriate quantification. FP-

DOI: 10.1021/acs.jpcc.7b11266
J. Phys. Chem. C XXXX, XXX, XXX−XXX

TRMC measurements were performed using a microwave generator (μwave) operating at either 7 or 20 GHz as a probe for the photoconductive decay in the sample cavity. The pulsed light excitation was produced using an yttrium aluminum garnet (YAG) optical parametric oscillator to provide light pulses at 10 Hz with a wavelength of 420 nm and an intensity of ~1 mW/cm^2. The pulses were 3−5 ns wide with a ~5 ns detector response time. The photogenerated carriers modulate the μwave transmission coefficient ,which, in turn, is transformed into a change in voltage using a PIN diode.

RESULTS AND DISCUSSION

All of the sputter-deposited TiO_2 films were systematically examined via SEM. These were all found to exhibit a low surface roughness with no apparent porosity. Figure 1 shows a typical cross-sectional SEM micrograph of a ~250 nm thick TiO_2:WN thin film, where a dense morphology along with a smooth surface can be clearly seen. No differences in morphology were observed between the TiO_2 samples of various doping schemes (i.e., TiO_{2-x}, TiO_2:W, TiO_2:N, and TiO_2:WN). From cross-sectional SEM images, we were able to determine the actual film thickness for the various films (all films are in the ~200−400 nm range).

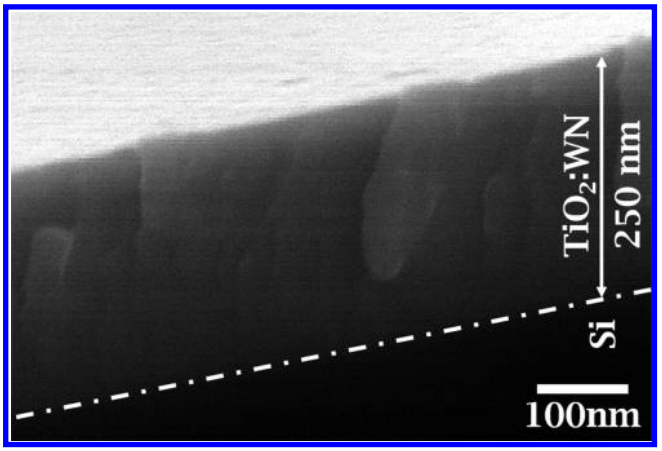

Figure 1. Typical cross-sectional SEM micrograph of the sputter-deposited TiO_2:WN films. The image shown here is of the TiO_2:WN #2 sample, 250 nm thick with the front facing face exposed by cleaving of the Si substrate.

The crystallinity of our codoped TiO_2:WN thin films was investigated through systematic XRD measurements as a function of the doping scheme. Figure 2 presents elected XRD spectra to illustrate the main differences between the undoped, N-doped, W-doped, and WN-codoped TiO_2 films. Typically, at deposition temperatures of ~475 °C, the anatase phase is formed.[7] However, in the case of TiO_{2-x} films, we know that they crystallize in the rutile (R) polymorph with its characteristic (110), (101), (200), (111), (210), (211), and (220) diffraction peaks present (identified from left to right; JCPDS card #88−1175). In fact, this is an expected result of sputter depositing TiO_2 near the anatase−rutile transition point (~500−600 °C) if no oxygen is introduced during the sputtering (preferential sputtering of O atoms causes oxygen vacancy (V_O) formation[7,32]). The presence of oxygen vacancies enhances light absorption of TiO_{2-x} at ~420 nm due to V_O defect bands just below the CBM, a requirement for visible light excitation for the TRMC experiments. In the case of

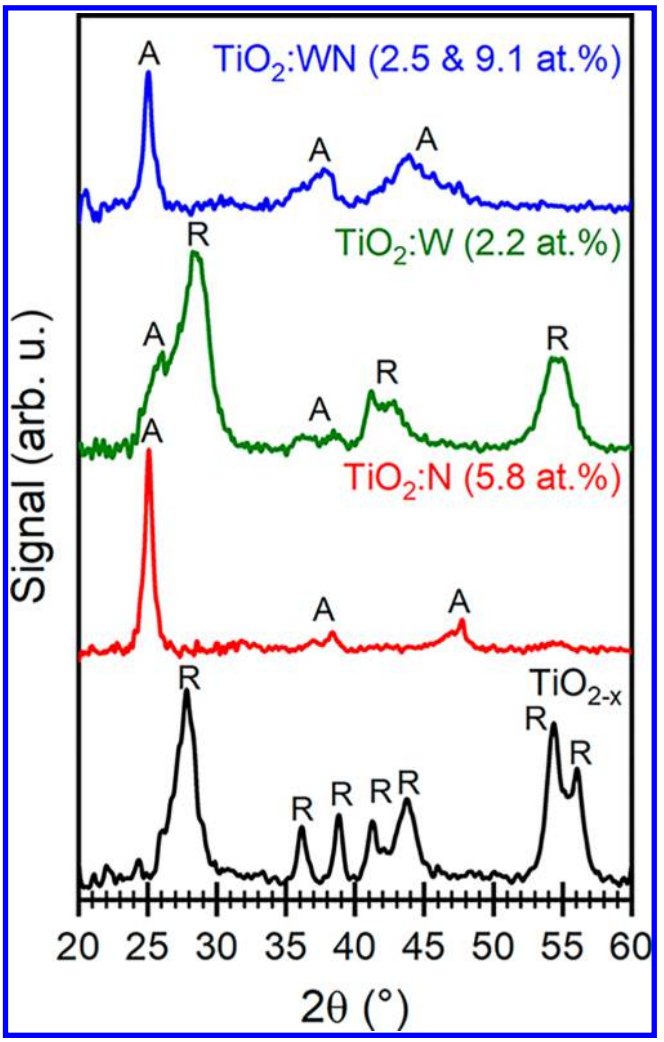

Figure 2. Typical XRD spectra of the sputter-deposited TiO_2, TiO_2:N, TiO_2:W, and TiO_2:WN thin films. The anatase (A) and rutile (R) phases are identified.

TiO_2:N, we note the sole presence of the anatase polymorph with its characteristic (101), (004), and (200) peaks (identified from left to right; JCPDS card #21−1272). The N atoms are expected to fill out a sufficient amount of V_O to favor the formation of the anatase phase. Interestingly, the coexistence of both A and R phases is observed upon W doping. W atoms can only substitute for Ti ones (due to size constraints)[33] and therefore cannot fill oxygen vacancies. Tungsten is, however, expected to increase the V_O formation energy,[22,23] resulting in both phases being formed. Finally, when W and N dopants are introduced in the TiO_2 structure, a well-defined anatase phase is formed with an estimated crystallite size of about ~25 nm (determined using Williamson-Hall analysis and Scherrer formula approximation). This indicates that both dopants work synergistically at the lattice level not only to compensate for oxygen vacancies but also to reduce the strain, most likely because of local charge compensation.

To characterize the chemical bonding states of the sputtered films, XPS analyses of the N 1s, Ti 2p, O 1s, W 4f (this is also the Ti 3p window), and W 4p core level spectra were performed. After appropriate deconvolution of the XPS spectra for all studied samples (Table 1), the various doping-induced changes in the chemical states present in a typical TiO_2:WN

DOI: 10.1021/acs.jpcc.7b11266
J. Phys. Chem. C XXXX, XXX, XXX−XXX

Table 1. X-ray Photoelectron Spectroscopy Derived Dopant Atomic Concentrations (at. %), X-ray Diffraction Determined Dominant Crystalline Structures, and a First-Order Approximation Factor $([Ti^{3+}] + [Ti^{2+}])/[Ti_{total}]$ for the V_O Density[a]

name	nitrogen (at. %)	tungsten (at. %)	crystallinity	$([Ti^{3+}] + [Ti^{2+}])/[Ti_{total}]$
TiO_{2-x}	0	0	rutile	0.30
TiO_2:N #1	*5.8 ± 0.1*	0	anatase	0.48
TiO_2:W #1	0	*0.7 ± 0.1*	anatase & rutile	0.21
TiO_2:W #2	0	*2.2 ± 0.1*	anatase & rutile	0.39
TiO_2:W #3	0	*3.1 ± 0.1*	amorphous	0.35
TiO_2:WN #1	*6.4 ± 0.1*	*0.8 ± 0.1*	amorphous	0.45
TiO_2:WN #2	*7.7 ± 0.1*	*1.6 ± 0.1*	amorphous	0.40
TiO_2:WN #3	*9.1 ± 0.1*	*2.5 ± 0.1*	anatase	0.28
TiO_2:WN #4	*7.7 ± 0.1*	*2.6 ± 0.1*	anatase	0.39

[a]The error on the XPS contents represents the smallest detectable atomic concentration under the experimental conditions used.

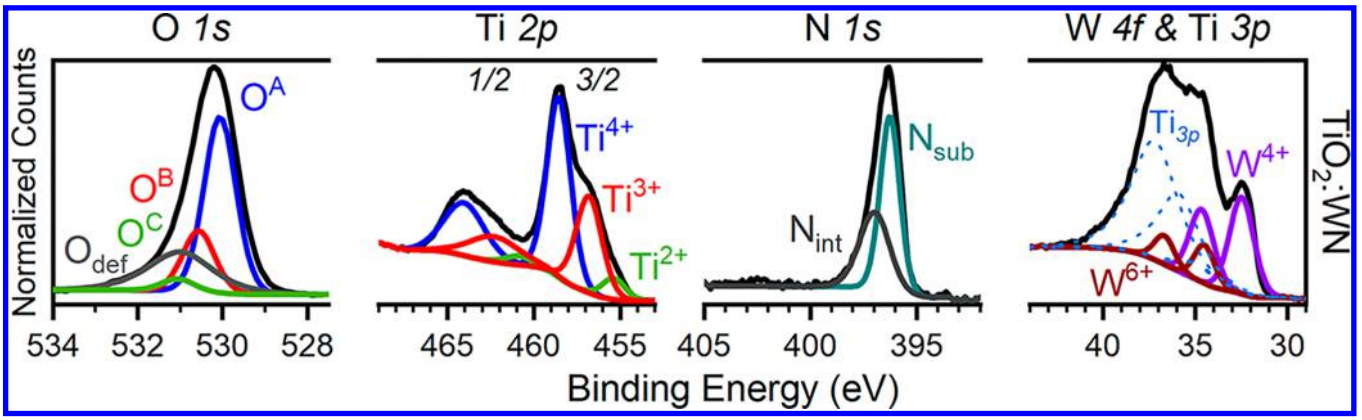

Figure 3. High-resolution XPS spectra of the O 1s, Ti 2p, N 1s, and W 4f core levels (from left-to-right) of the TiO_2:WN #2 thin film. The Ti 3p deconvoluted states are dashed to prioritize visibility of the W 4f states. For display purposes, normalized counts are used for the vertical axis.

codoped film are shown in Figure 3 (TiO_2:WN #2 sample used for display purposes). For visual simplicity, all of the doping schemes can be seen in the TiO_2:WN codoped sample with no hampering overlap. Additionally, the Ti 3p core-level energy signatures in the W 4f and Ti 3p shared window are dashed to visually lighten the figure. For the TiO_{2-x} films, the Ti $2p_{3/2}$ peak can be decomposed into two main components corresponding to two oxidation states of Ti, namely, Ti^{4+} and Ti^{3+} at 458.6 and 456.9 eV, respectively. Their corresponding Ti $2p_{1/2}$ energy levels can be found at 5.7 and 5.5 eV higher binding energy (BE) with a $2p_{1/2}$:$2p_{3/2}$ branching ratio of 1:2. These can also be observed in the Ti 3p spectra with the main Ti^{4+} 3p peak at 37.2 eV and the T^{3+} and Ti^{2+} at 1.30 and 2.27 eV lower BE, respectively.[7,33−36] The presence of Ti^{3+} is due to the formation of the $2Ti^{3+}−V_O''$ defect association pair, as a consequence of preferential sputtering of the TiO_2 target.[7,32] These states can be mirror derived from the O 1s spectra with the main O^A peak at 529.9 eV assigned to lattice oxygen in the TiO_2 matrix and the O^B|O^C peaks assigned to substoichiometric lattice oxygen species (in Ti^{3+} and Ti^{2+} lattice environments, respectively) each at subsequently ∼0.5 eV higher binding energy.[34,35] Additionally, we note the presence of a fourth component, denoted as O_{def} at 530.7 eV, which is typically associated with defective surface oxygen and surface hydroxide species.[34,35,37] Upon nitrogen incorporation in the films, the N 1s peak is seen to exist in two characteristic components: N_{sub} and N_{int} at 396.2 and 397.2 eV, respectively. The N_{sub} peak is known to arise from substitutional −Ti−N− type bonds, and the N_{int} peak is most likely interstitial −O−N type bonds within the titania crystal structure.[3,6,7,10,13,14] The introduction of N into the titania is accompanied by the appearance of Ti^{2+} oxidation states in the Ti 2p spectra (Ti^{2+} $2p_{3/2}$ at 455.3 eV and the $2p_{1/2}$ component at 460.9 eV BE).[3,38] These reduced valence states are typically associated with electronic defects originating from heavily substoichiometric lattice structures.[3,4,7,15,39] Concomitant sputtering of a W target in tandem with the TiO_2 target was used for W doping. This resulted in the presence of two main features in the W 4f BE window. These are associated with the W^{6+} and W^{4+} states (in the oxide form) with their main $4f_{7/2}$ components at 34.5 and 32.3 eV, respectively. Their corresponding $4f_{5/2}$ doublets are found at 2.2 eV higher BE with a 3:4 branching ratio.[33,40−43] The TiO_2:WN films exhibit W and N binding energy signatures that combine the XPS features of each monodoped sample accordingly. Both the W and N dopants can be associated with mainly substitutional type incorporation replacing Ti and O atoms, respectively. Finally, using the $([Ti^{3+}] + [Ti^{2+}])/[Ti_{total}]$ ratio as an indicator of the V_O density, the XPS analysis reinforces the XRD observations, indicating that codoped films have lower defect densities as compared to their N-doped counterparts. A summary of the XPS quantitative dopant content along with the corresponding TiO_2 polymorph determined by XRD for all the TRMC tested films is presented in Table 1. This is accompanied by the relative area ratio $([Ti^{3+}] + [Ti^{2+}])/[Ti_{total}]$ for the studied samples. We note that the sample with 9.1 at. % nitrogen and 2.5 at. % tungsten shows the lowest approximated V_O density.

To better understand the effect of WN-codoping on the photoactivity of TiO_2 thin films, a detailed investigation of the charge carrier dynamics was necessary. To this end, FP-TRMC measurements were carried out to probe the time-resolved charge in conductivity $\sigma(t)$ induced by pulsed laser excitation of

DOI: 10.1021/acs.jpcc.7b11266
J. Phys. Chem. C XXXX, XXX, XXX−XXX

undoped, monodoped, and codoped TiO_2 films. During laser excitation, the change in microwave power transmission ($\Delta P(t)$) from the sample cavity as a function of time is recorded. It is proportional to the change in photoconductance ($\Delta\sigma(t)$) of the sample by a sensitivity factor A, which is determined by the known dimensions and characteristics of the sample cavity and hardware used, according to the following relation:[18,44−47] $\Delta P(t)/P(t) = A\cdot\Delta\sigma(t)$. Thus, with $\Delta\sigma(t) \sim \mu\cdot\Delta N$ (where μ is the charge mobility, and ΔN the charge population change), the time evolution of $\Delta P(t)/P(t)$ gives information about the recombination or trapping of charge carriers (further theoretical and experimental explanations can be found elsewhere[18,44−47]). Figure 4 shows typical TRMC

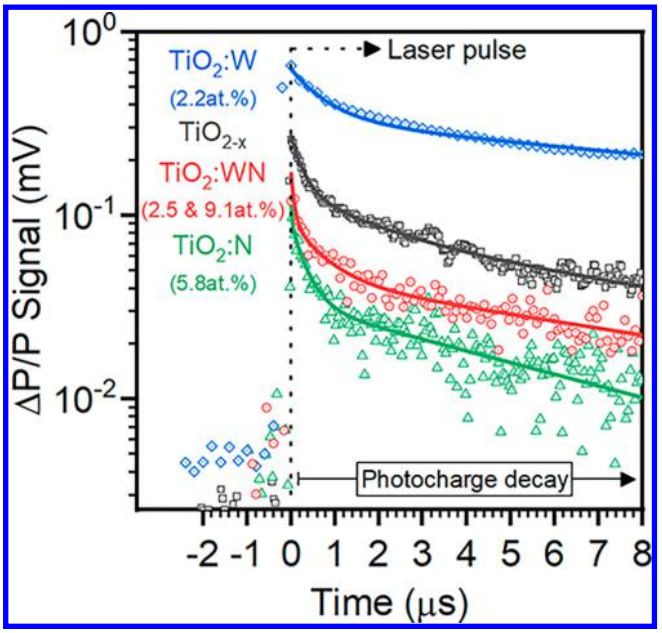

Figure 4. Representative FP-TRMC signals of the TiO_{2-x}, TiO_2:N, TiO_2:W, and TiO_2:WN thin films (doping concentrations of the samples presented can be found in the figure legend). These were excited with a 5 ns wide, 420 nm laser pulse. The prepulse baseline was $\sim 10^{-2}$ mV.

decay signals for the TiO_2, TiO_2:N, TiO_2:W, and TiO_2:WN films following their illumination by a 5 ns pulse duration of the laser emitting at 420 nm. One can note a clear difference in the signal amplitude for the different doping schemes. It is known that the $\Delta P(t)/P(t)$ of charge carriers in undoped and doped TiO_2 films is not directly proportional to the excitation light intensity (I_{ex}).[18,48] This change in intensity $\Delta P(t)/(I_{ex}\cdot P(t))$ is typically affected by three main factors: (i) trap filling effects at low excitation energy, (ii) recombination effects at high excitation energy, and (iii) dopant induced donor and/or acceptor populations,[18,44−48] all of which can be at work here. Here, focus is put on the extraction of lifetime data from the decay curves of Figure 4, as they depend purely on the time variation of the signal and not the overall signal intensity. To derive the photocharge lifetimes from the TRMC data, the $A\cdot\Delta\sigma(t)$ traces were fitted using a triple exponential function, representative of the three decay processes that affect the charge carriers in the material. Thus, $A\cdot\Delta\sigma(t)$ can be written as $A\cdot\Delta\sigma(t) = \sum A_n\cdot\exp(-t/\tau_n)$, where A_n and τ_n are the respective proportionality and the time constants of each of the three decay processes. In other words, all the lifetime curves can be separated into three decay regimes that were associated with three characteristic time constants, namely, τ_{trap}, τ_{rec}, and τ_{surf} (with their respective time scales on the order of 0.05, 1, and 10 μs).[4] Thus, τ_{trap}, τ_{rec}, and τ_{surf} characterize charge trapping ($e^-| h^+ \rightarrow e^-_{tr}|h^+_{tr}$), charge recombination ($e^- + h^+|e^-_{tr} + h^+|e^- + h^+_{tr} \rightarrow h\upsilon$), and surface reactions ($e^- + O_2 \rightarrow O_2^-$), respectively.[4] Figure 5 presents the extracted characteristic

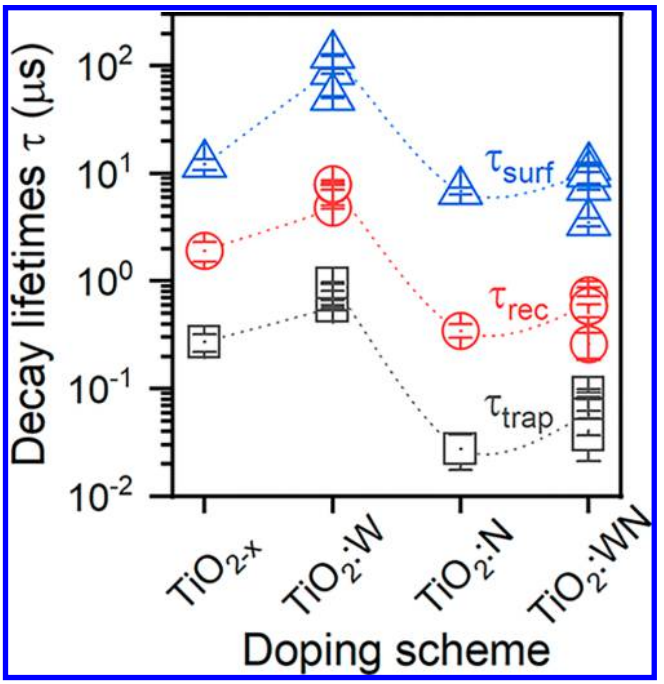

Figure 5. Photocharge lifetimes for all three characteristic decay lifetimes (τ_{trap}, τ_{rec}, and τ_{surf}) as a function of doping scheme.

time constants of the different TiO_2, TiO_2:N, TiO_2:W, and TiO_2:WN photoanodes. We note that there is a clear dependence of the photocharge lifetimes with the doping scheme, with the W-doped samples showing the highest overall lifetimes (this will be discussed further). Interestingly, in the case of WN-codoped thin films, we note an almost order of magnitude variation among samples with various dopant loadings. These characteristic lifetimes are presented in Table 2.We can note that total dopant incorporation efficiencies are insufficient in highlighting a relationship between codoping and photocharge lifetimes.

Table 2. Extracted Characteristic Photocharge Lifetimes (from FP-TRMC Fittings) for the WN Codoped Samples

name	τ_{trap} (μs)	τ_{rec} (μs)	τ_{surf} (μs)
TiO_2:WN #1	*0.058 ± 0.021*	*0.59 ± 0.13*	*9.9 ± 1.9*
TiO_2:WN #2	*0.037 ± 0.016*	*0.26 ± 0.07*	*3.5 ± 0.3*
TiO_2:WN #3	*0.077 ± 0.015*	*0.75 ± 0.13*	*11.5 ± 1.2*
TiO_2:WN #4	*0.092 ± 0.007*	*0.59 ± 0.40*	*7.4 ± 0.4*

In an effort to correlate the obtained time constant values with the film composition and bonding states of the dopants, we have systematically analyzed the XPS spectra for the different TiO_2 doping schemes. Table 3 summarizes the XPS derived concentration of each dopant along with its incorporation state (i.e., substitutional/interstitial for nitrogen, and W^{6+}/W^{4+} for tungsten). Passivated codoping models mainly focus on W^{6+} and N_{sub} species.[19−21,23] W^{4+} is assumed to have little to no local electronic effect upon substituting for a

DOI: 10.1021/acs.jpcc.7b11266
J. Phys. Chem. C XXXX, XXX, XXX−XXX

Table 3. XPS Derived Quantifications for Each Dopant Subspecies[a]

name	N_{sub} (at. %)	N_{int} (at. %)	W^{6+} (at. %)	W^{4+} (at. %)
TiO_{2-x}	0	0	0	0
TiO_2:N #1	*4.2 ± 0.1*	*1.6 ± 0.1*	0	0
TiO_2:W #1	0	0	*0.3 ± 0.1*	*0.4 ± 0.1*
TiO_2:W #2	0	0	*0.7 ± 0.1*	*1.6 ± 0.1*
TiO_2:W #3	0	0	*1.1 ± 0.1*	*2.0 ± 0.1*
TiO_2:WN #1	*4.1 ± 0.1*	*2.2 ± 0.1*	*0.2 ± 0.1*	*0.5 ± 0.1*
TiO_2:WN #2	*4.6 ± 0.1*	*3.1 ± 0.1*	*0.4 ± 0.1*	*1.2 ± 0.1*
TiO_2:WN #3	*5.6 ± 0.1*	*3.5 ± 0.1*	*1.1 ± 0.1*	*1.4 ± 0.1*
TiO_2:WN #4	*5.8 ± 0.1*	*1.8 ± 0.1*	*1.0 ± 0.1*	*1.6 ± 0.1*

[a] N_{sub} and N_{int} denote the substitutional and interstitial type nitrogen, and W^{6+} and W^{4+} denote the oxidative species of the W dopant atoms. The statistical error represents the smallest detectable atomic concentration given the experimental conditions.

Ti^{4+} atom,[33] and N_{int} is typically associated with the formation of −O−N type ions where nitrogen assumes a positive valence.[12−14] From these ideas, we can propose that two defects created by N_{sub} incorporation can be locally compensated for by the introduction of a W^{6+} atom. In other words, we can define an empirical XPS derived acceptor−donor passivation parameter: $2[W^{6+}] - [N_{sub.}]$. This parameter is expected to predict the reduction in defect states brought on via local passivation of charge disparities.[19,21] This, in turn, should manifest itself as an increase of photocharge lifetimes through the reduction of V_O defect centers that would otherwise form in an uncompensated environment. Consequently, the TRMC variation of photocharge lifetimes as a function of $2[W^{6+}] - [N_{sub.}]$ is presented in Figure 6.

We clearly note that the introduction of W^{6+} states increases the photocharge lifetimes considerably. Interestingly, the passivation effect brought in via introduced W^{6+} applies to both W monodoped and WN codoped samples. In the case of

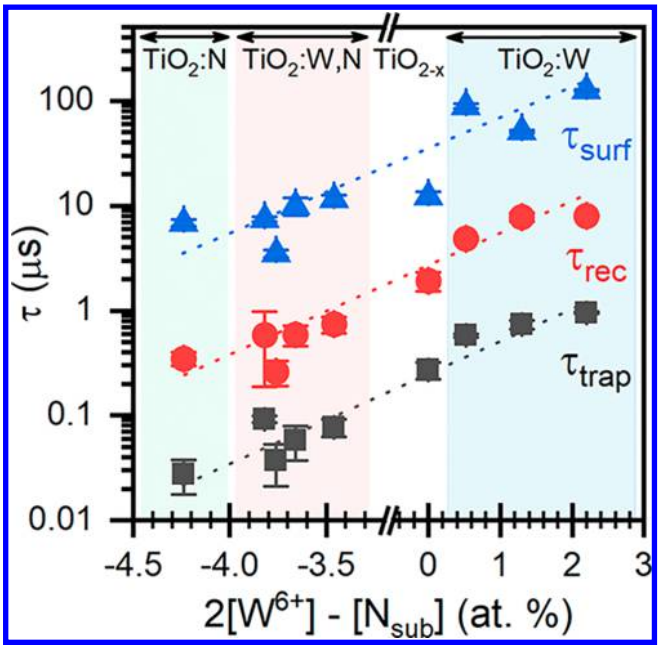

Figure 6. Variation of photocharge time constants as a function of approximated W^{6+} passivation of N_{sub} species (in the case of TiO_2:WN) and V_O (for TiO_2:W).

TiO_2:N, we see that the lifetimes are greatly hindered by the local charge defects brought up by the N_{sub} charge disparity forcing the formation of V_O. In the case of TiO_2:WN codoped films, the W^{6+} species are partially balancing the electronic disparity brought on by N_{sub}, allowing the lifetimes to converge closer to the undoped TiO_{2-x}. Finally, in the case of TiO_2:W samples, the W^{6+} seem to be mitigating the effects of naturally occurring V_O (i.e., we can directly observe the predicted increase in V_O formation energy as a consequence of W^{6+} incorporation[22,23]). These results clearly indicate that codoping with a suitable acceptor−donor pair, such as W and N, in turn increases the photocharge lifetimes significantly via suppression of the $2Ti^{3+}-V_O''$ defect association states. This enables the material to maintain a high photosensitivity (matching that of optimally doped TiO_2:N with $E_g \sim 2.3$ eV), while increasing its associated photocharge lifetimes to values comparable to those of TiO_{2-x} (~0.27, 1.9, and 12.2 μs for τ_{trap}, τ_{rec}, and τ_{surf}, respectively).

On the basis of these observations, we would predict that TiO_2:WN should perform better than any W or N monodoped titania when used as photoanodes in a visible light electrophotocatalytic processes. To assess the validity of such a prediction, the same TiO_2 thin films studied here were deposited onto Ti grids (as large as 6 in. in diameter) and used as photoanodes in a 1 L home built EPC reactor, details of which are presented elsewhere.[49] The performance of our photoanodes was directly evaluated toward the degradation of an agricultural pollutant, namely atrazine. Atrazine is a potent endocrine disruptor widely used in North America as a pesticide/herbicide. Critically, studies have reported the persistence of atrazine in surface, ground, and drinking water.[50,51] This problem is compounded by the fact that photolysis of atrazine is only possible with high-energy UV radiation (dechlorination mechanism).[52] In other words, there is an urgent need for a low-cost, environmentally friendly approach for the degradation of atrazine by using readily available sunlight. Atrazine was selected as a relevant electrophotocatalytic testbed to prove the effectiveness of the codoped TiO_2:WN photoanodes under sunlight. Further details on the subject can be found elsewhere.[52] For the purpose of the present study, synthetic solutions containing atrazine concentrations of 60 μg/L (60 ppb, as these are typical concentrations of heavily polluted areas) were prepared and treated in our EPC reactor under AM1.5G solar simulator while continuously circulating them with treatment times reaching up to 6 h. The exact EPC degradation mechanisms are elaborated upon elsewhere.[52] Figure 7 shows typical time-dependent degradation curves of atrazine by the different photoanodes studied here (i.e., TiO_{2-x}, TiO_2:N, TiO_2:W, and TiO_2:WN). One can note that all the photoanodes successfully degraded atrazine after 3 h of treatment time, allowing the residual pollutant concentrations to reach 1−2 ppb (the environmentally acceptable limit). However, one can note that the kinetics of atrazine degradation heavily depends on the photoanode nature. Indeed, although it takes ~3 h for the EPC treatment of atrazine to reach the ~1.5 ppb threshold using a TiO_{2-x} based photoanode, this time is reduced to ~45 min with a TiO_2:WN based photoanode. The pseudo-first-order degradation kinetic constants for each studied photoanode were extracted and are presented in Table 4. It is clearly seen that compared to the case for TiO_{2-x}, TiO_2:N doping doubles the rate of atrazine degradation, confirming that the photosensitization (effective reduction of the bandgap size) permits

DOI: 10.1021/acs.jpcc.7b11266
J. Phys. Chem. C XXXX, XXX, XXX−XXX

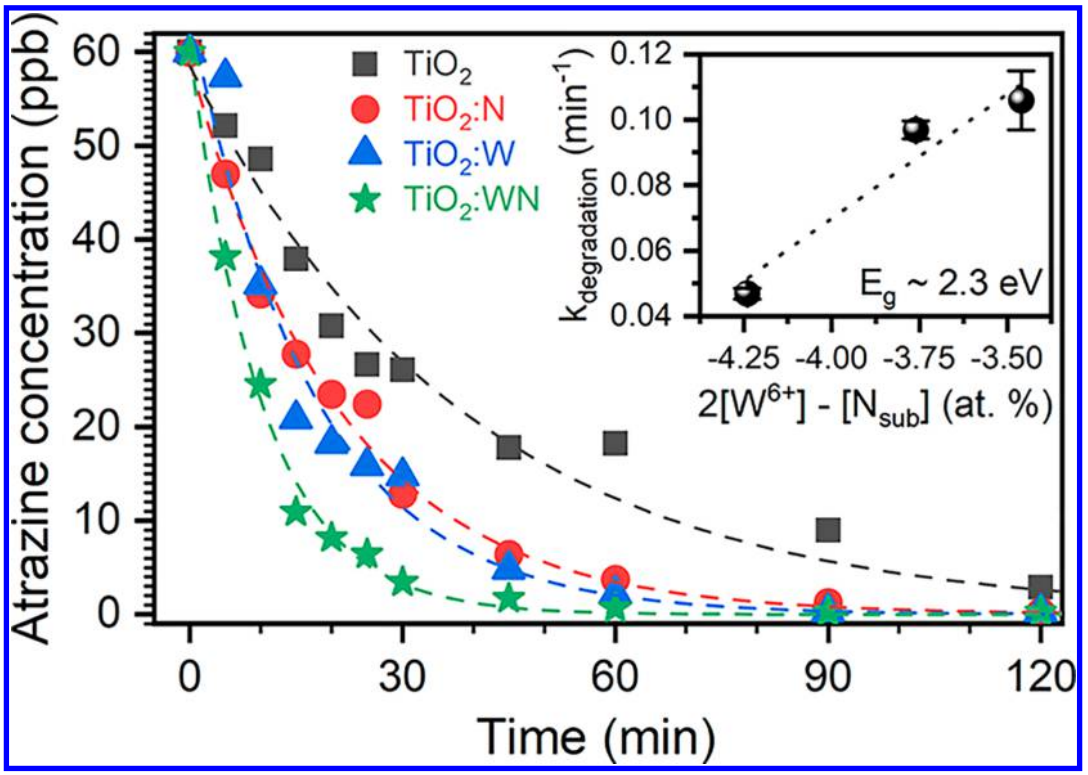

Figure 7. Electrophotocatalytic performance of the best TiO_{2-x}, TiO_2:N, TiO_2:W, and TiO_2:WN photoanodes under AM1.5G light with a 60 ppb initial concentration of atrazine. The inset shows the extracted degradation constants (pseudo-first-order) as a function of W^{6+} passivation for photoanodes with $E_g \sim 2.3$ eV (i.e., TiO_2:N #1 and TiO_2:WN #2 & #3).

Table 4. Extracted Pseudo-First-Order Degradation Constants for the Photoanodes Evaluated for the EPC Degradation of Atrazine under AM1.5G Illumination with Their Corresponding E_g Values

name	degradation constants (min^{-1})	E_g (eV)
TiO_{2-x}	*0.026 ± 0.0017*	*3.2 ± 0.1*
TiO_2:W #2	*0.057 ± 0.0053*	*3.0 ± 0.1*
TiO_2:N #1	*0.047 ± 0.0017*	*2.3 ± 0.1*
TiO_2:WN #2	*0.097 ± 0.0027*	*2.3 ± 0.1*
TiO_2:WN #3	*0.106 ± 0.0090*	*2.3 ± 0.1*

the use of a greater portion of the solar spectrum for the EPC process. The exact quantification of the bandgap associated with each doping scheme was done and previously reported elsewhere.[8] The E_g values for TiO_{2-x}, TiO_2:N, TiO_2:W, and TiO_2:WN films are summarized in Table 4. Interestingly, even if the E_g of TiO_2:W films is larger than that of TiO_2:N (3.0 eV for the 2.8 at. % W-doped photoanode vs 2.3 eV for the 5.8 at. % N-doped photoanode), their EPC degradation performance was found to be very similar to that of TiO_2:N (Figure 7). This is believed to be a direct consequence of the rather longer lifetimes of photocharges in the TiO_2:W films, which compensate for their lack of visible light photon sensitivity. In other words, whereas TiO_2:N films profit from their increased photosensitivity to the visible spectrum, the TiO_2:W samples offer longer lifetimes and therefore increased reaction probability of produced photocharges. When the two phenomena are combined in the codoping scheme, we can observe that these two contributions act synergistically, allowing reaction constants to increase of about 1 order of magnitude, going from 0.026 min^{-1} for the TiO_{2-x} to 0.106 min^{-1} for the optimally codoped TiO_2:WN photoanodes. To highlight the added value of the passivation, the degradation constants of photoanodes with identical E_g values (around 2.3 eV) were plotted against the passivation parameter ($2[W^{6+}] - [N_{sub.}]$) and reported in the inset of Figure 7. Even if we have only 3 points, we can note that there is a marked increase of the degradation efficiency of atrazine with the increase of the passivation parameter associated with longer photocharge lifetimes. This reinforces that for photoanodes with identical photoharvesting capabilities (i.e., similar bandgaps), we obtain an increase in the EPC performance by directly increasing the photocharge lifetimes via passivated acceptor−donor type doping using W and N. Specifically, through a W dopant induced reduction in the $2Ti^{3+}-V_O''$ defect pair density.

CONCLUSION

In summary, we have demonstrated the effectiveness of using a reliable RF magnetron sputtering process for the in situ controlled doping and codoping of TiO_2 thin films, allowing the synthesis of TiO_{2-x}, TiO_2:N, TiO_2:W, and TiO_2:WN films. A partial indicator of acceptor−donor passivation is presented in the form of a relaxation of the crystalline strain when both W and N are incorporated into the structure, allowing the titania to recover a well-defined anatase phase. These results are corroborated by XPS analyses, which revealed the presence of both W and N in mostly substitutional states for the mono- and codoped TiO_2 films. However, detailed analysis of the visible light FP-TRMC signals revealed that three regimes are responsible for the photocharge decay: charge trapping ($e^-|h^+ \rightarrow e^-_{tr}|h^+_{tr}$), charge recombination ($e^- + h^+|e^-_{tr} + h^+|e^- + h^+_{tr} \rightarrow h\upsilon$), and surface reactions ($e^- + O_2 \rightarrow O_2^-$). Typical lifetimes for TiO_{2-x} films for these three regimes were determined to be around 0.05, 1, and 10 μs, respectively.

DOI: 10.1021/acs.jpcc.7b11266
J. Phys. Chem. C XXXX, XXX, XXX−XXX

Doping with W unilaterally increases the photocharge lifetimes, whereas N doping showed the lowest lifetimes. Interestingly, the synergetic codoping with both W and N was shown to lead to an order of magnitude increase in the photocharge lifetimes, bringing them to about 0.077, 0.75, and 11.5 μs (from 0.03, 0.35, and 6.8 μs, respectively, for the monodoped TiO_2:N thin films). It is to be noted that W monodoping provided even longer lifetimes (as long as, 0.95, 7.99, and 125.8 μs, respectively). However, the wider bandgap of the TiO_2:W films (~3.0 eV) limits their capacity to harvest visible light and hence limits their overall EPC performance. This suggests that a balance should be met between narrower bandgap and longer photocharge lifetimes to optimize the EPC degradation performance, as is well demonstrated here, for the case of codoped TiO_2:WN photoanodes toward atrazine degradation. Finally, by correlating the atrazine degradation efficiency to the approximated passivation parameter, our results highlight that the presence of W^{6+} states in the films is important to achieve an effective passivation in synergy with substitutional nitrogen. These studies have practically led to the optimization of the EPC degradation of a real pollutant (atrazine).

AUTHOR INFORMATION

Corresponding Author

*M. A. El Khakani. E-mail: elkhakani@emt.inrs.ca.

ORCID

N. Delegan: 0000-0002-1240-6409

Notes

The authors declare no competing financial interest.

ACKNOWLEDGMENTS

The authors acknowledge the financial support from NSERC (the Natural Science and Engineering Research Council of Canada) and the FRQNT (Le Fonds de Recherche du Québec-Nature et Technologies) through its strategic Network "Plasma-Québec".

REFERENCES

(1) O'Regan, B.; Grätzel, M. A Low-Cost, High-Efficiency Solar Cell Based on Dye-Sensitized Colloidal TiO2 Films. *Nature* **1991**, *353* (6346), 737−740.

(2) Khan, S. U. M.; Al-Shahry, M.; Ingler, W. B. Efficient Photochemical Water Splitting by a Chemically Modified N-TiO2. *Science* **2002**, *297* (5590), 2243−2245.

(3) Emeline, A. V.; Kuznetsov, V. N.; Rybchuk, V. K.; Serpone, N. Visible-Light-Active Titania Photocatalysts: The Case of N-Doped TiO 2 s—Properties and Some Fundamental Issues. *Int. J. Photoenergy* **2008**, *2008*, 1−19.

(4) Fujishima, A.; Zhang, X.; Tryk, D. TiO2 Photocatalysis and Related Surface Phenomena. *Surf. Sci. Rep.* **2008**, *63* (12), 515−582.

(5) Hashimoto, K.; Irie, H.; Fujishima, A. TiO 2 Photocatalysis: A Historical Overview and Future Prospects. *Jpn. J. Appl. Phys.* **2005**, *44* (12), 8269−8285.

(6) Asahi, R.; Morikawa, T.; Ohwaki, T.; Aoki, K.; Taga, Y. Visible-Light Photocatalysis in Nitrogen-Doped Titanium Oxides. *Science* **2001**, *293* (5528), 269−271.

(7) Delegan, N.; Daghrir, R.; Drogui, P.; El Khakani, M. A. Bandgap Tailoring of in-Situ Nitrogen-Doped TiO2 Sputtered Films Intended for Electrophotocatalytic Applications under Solar Light. *J. Appl. Phys.* **2014**, *116* (15), 153510.

(8) Pandiyan, R.; Delegan, N.; Dirany, A.; Drogui, P.; El Khakani, M. A. Probing the Electronic Surface Properties and Bandgap Narrowing of in Situ N, W, and (W,N) Doped Magnetron-Sputtered TiO 2 Films Intended for Electro-Photocatalytic Applications. *J. Phys. Chem. C* **2016**, *120* (1), 631−638.

(9) Scanlon, D. O.; Dunnill, C. W.; Buckeridge, J.; Shevlin, S. a; Logsdail, A. J.; Woodley, S. M.; Catlow, C. R. a; Powell, M. J.; Palgrave, R. G.; Parkin, I. P.; et al. Band Alignment of Rutile and Anatase TiO2. *Nat. Mater.* **2013**, *12* (9), 798−801.

(10) Di Valentin, C.; Pacchioni, G.; Selloni, A. Origin of the Different Photoactivity of N-Doped Anatase and Rutile TiO2. *Phys. Rev. B: Condens. Matter Mater. Phys.* **2004**, *70* (8), 85116.

(11) Daghrir, R.; Drogui, P.; Delegan, N.; El Khakani, M. A. Electrochemical Degradation of Chlortetracycline Using N-Doped Ti/TiO2 Photoanode under Sunlight Irradiations. *Water Res.* **2013**, *47* (17), 6801−6810.

(12) Di Valentin, C.; Pacchioni, G.; Selloni, A.; Livraghi, S.; Giamello, E. Characterization of Paramagnetic Species in N-Doped TiO 2 Powders by EPR Spectroscopy and DFT Calculations. *J. Phys. Chem. B* **2005**, *109* (23), 11414−11419.

(13) Lynch, J.; Giannini, C.; Cooper, J. K.; Loiudice, A.; Sharp, I. D.; Buonsanti, R. Substitutional or Interstitial Site-Selective Nitrogen Doping in TiO 2 Nanostructures. *J. Phys. Chem. C* **2015**, *119* (13), 7443−7452.

(14) Peng, F.; Cai, L.; Yu, H.; Wang, H.; Yang, J. Synthesis and Characterization of Substitutional and Interstitial Nitrogen-Doped Titanium Dioxides with Visible Light Photocatalytic Activity. *J. Solid State Chem.* **2008**, *181* (1), 130−136.

(15) Torres, G. R.; Lindgren, T.; Lu, J.; Granqvist, C.-G.; Lindquist, S.-E. Photoelectrochemical Study of Nitrogen-Doped Titanium Dioxide for Water Oxidation. *J. Phys. Chem. B* **2004**, *108* (19), 5995−6003.

(16) D'Arienzo, M.; Siedl, N.; Sternig, A.; Scotti, R.; Morazzoni, F.; Bernardi, J.; Diwald, O. Solar Light and Dopant-Induced Recombination Effects: Photoactive Nitrogen in TiO 2 as a Case Study. *J. Phys. Chem. C* **2010**, *114* (42), 18067−18072.

(17) Liu, B.; Wen, L.; Zhao, X. The Photoluminescence Spectroscopic Study of Anatase TiO 2 Prepared by Magnetron Sputtering. *Mater. Chem. Phys.* **2007**, *106* (2−3), 350−353.

(18) Katoh, R.; Furube, A.; Yamanaka, K.; Morikawa, T. Charge Separation and Trapping in N-Doped TiO 2 Photocatalysts: A Time-Resolved Microwave Conductivity Study. *J. Phys. Chem. Lett.* **2010**, *1* (22), 3261−3265.

(19) Yin, W.-J.; Tang, H.; Wei, S.-H.; Al-Jassim, M. M.; Turner, J.; Yan, Y. Band Structure Engineering of Semiconductors for Enhanced Photoelectrochemical Water Splitting: The Case of TiO2. *Phys. Rev. B: Condens. Matter Mater. Phys.* **2010**, *82* (4), 45106.

(20) Çelik, V.; Mete, E. Range-Separated Hybrid Exchange-Correlation Functional Analyses of Anatase TiO2 Doped with W, N, S, W/N, or W/S. *Phys. Rev. B: Condens. Matter Mater. Phys.* **2012**, *86* (20), 205112.

(21) Li, M.; Zhang, J.; Zhang, Y. First-Principles Calculation of Compensated (2N, W) Codoping Impacts on Band Gap Engineering in Anatase TiO2. *Chem. Phys. Lett.* **2012**, *527*, 63−66.

(22) Long, R.; English, N. J. Synergistic Effects on Band Gap-Narrowing in Titania by Codoping from First-Principles Calculations. *Chem. Mater.* **2010**, *22* (5), 1616−1623.

(23) Long, R.; English, N. J. First-Principles Calculation of Nitrogen-Tungsten Codoping Effects on the Band Structure of Anatase-Titania. *Appl. Phys. Lett.* **2009**, *94* (13), 132102.

(24) Wang, D.; Zou, Y.; Wen, S.; Fan, D. A Passivated Codoping Approach to Tailor the Band Edges of TiO2 for Efficient Photocatalytic Degradation of Organic Pollutants. *Appl. Phys. Lett.* **2009**, *95* (1), 012106.

(25) Gai, Y.; Li, J.; Li, S.-S.; Xia, J.-B.; Wei, S.-H. Design of Narrow-Gap TiO2: A Passivated Codoping Approach for Enhanced Photoelectrochemical Activity. *Phys. Rev. Lett.* **2009**, *102* (3), 36402.

(26) Cui, X.; Rong, S.; Cao, Y.; Yin, Y.; Li, S.; Li, M. One-Step Hydrothermal Synthesis of Nitrogen and Tungsten Codoped TiO2 Nanorods with High Visible Light Photocatalytic Activity. *Appl. Phys. A: Mater. Sci. Process.* **2013**, *113* (1), 47−51.

DOI: 10.1021/acs.jpcc.7b11266
J. Phys. Chem. C XXXX, XXX, XXX−XXX

(27) Thind, S. S.; Wu, G.; Tian, M.; Chen, A. Nanomaterials for Promising Environmental Applications. *Nanotechnology* **2012**, *23* (47), 475706.
(28) Thind, S. S.; Wu, G.; Chen, A. Synthesis of Mesoporous Nitrogen−tungsten Co-Doped TiO2 Photocatalysts with High Visible Light Activity. *Appl. Catal., B* **2012**, *111−112*, 38−45.
(29) Kubacka, A.; Bachiller-Baeza, B.; Colón, G.; Fernández-García, M. Doping Level Effect on Sunlight-Driven W,N-Co-Doped TiO2-Anatase Photo-Catalysts for Aromatic Hydrocarbon Partial Oxidation. *Appl. Catal., B* **2010**, *93* (3−4), 274−281.
(30) Folli, A.; Bloh, J. Z.; Beukes, E.-P.; Howe, R. F.; Macphee, D. E. Photogenerated Charge Carriers and Paramagnetic Species in (W,N)-Codoped TiO 2 Photocatalysts under Visible-Light Irradiation: An EPR Study. *J. Phys. Chem. C* **2013**, *117* (42), 22149−22155.
(31) Bloh, J. Z.; Folli, A.; Macphee, D. E. Adjusting Nitrogen Doping Level in Titanium Dioxide by Codoping with Tungsten: Properties and Band Structure of the Resulting Materials. *J. Phys. Chem. C* **2014**, *118* (36), 21281−21292.
(32) Brassard, D.; El Khakani, M. a.; Ouellet, L. Substrate Biasing Effect on the Electrical Properties of Magnetron-Sputtered High-K Titanium Silicate Thin Films. *J. Appl. Phys.* **2007**, *102* (3), 034106.
(33) Sathasivam, S.; Bhachu, D. S.; Lu, Y.; Chadwick, N.; Althabaiti, S. a.; Alyoubi, A. O.; Basahel, S. N.; Carmalt, C. J.; Parkin, I. P. Tungsten Doped TiO2 with Enhanced Photocatalytic and Optoelectrical Properties via Aerosol Assisted Chemical Vapor Deposition. *Sci. Rep.* **2015**, *5*, 10952.
(34) Biesinger, M. C.; Payne, B. P.; Grosvenor, A. P.; Lau, L. W. M.; Gerson, A. R.; Smart, R. S. C. Resolving Surface Chemical States in XPS Analysis of First Row Transition Metals, Oxides and Hydroxides: Sc, Ti, V, Cu and Zn. *Appl. Surf. Sci.* **2010**, *257* (7), 887−898.
(35) Jackman, M. J.; Thomas, A. G.; Muryn, C. Photoelectron Spectroscopy Study of Stoichiometric and Reduced Anatase TiO 2 (101) Surfaces: The Effect of Subsurface Defects on Water Adsorption at Near-Ambient Pressures. *J. Phys. Chem. C* **2015**, *119* (24), 13682−13690.
(36) Thind, S. S.; Wu, G.; Tian, M.; Chen, A. Significant Enhancement in the Photocatalytic Activity of N, W Co-Doped TiO 2 Nanomaterials for Promising Environmental Applications. *Nanotechnology* **2012**, *23* (47), 475706.
(37) Kitano, M.; Funatsu, K.; Matsuoka, M.; Ueshima, M.; Anpo, M. Preparation of Nitrogen-Substituted TiO2 Thin Film Photocatalysts by the Radio Frequency Magnetron Sputtering Deposition Method and Their Photocatalytic Reactivity under Visible Light Irradiation. *J. Phys. Chem. B* **2006**, *110* (50), 25266−25272.
(38) Wong, M.-S.; Pang Chou, H.; Yang, T.-S. Reactively Sputtered N-Doped Titanium Oxide Films as Visible-Light Photocatalyst. *Thin Solid Films* **2006**, *494* (1−2), 244−249.
(39) Rumaiz, A. K.; Woicik, J. C.; Cockayne, E.; Lin, H. Y.; Jaffari, G. H.; Shah, S. I. Oxygen Vacancies in N Doped Anatase TiO[sub 2]: Experiment and First-Principles Calculations. *Appl. Phys. Lett.* **2009**, *95* (26), 262111.
(40) Mishra, T.; Mahato, M.; Aman, N.; Patel, J. N.; Sahu, R. K. A Mesoporous WN Co-Doped Titania Nanomaterial with Enhanced Photocatalytic Aqueous Nitrate Removal Activity under Visible Light. *Catal. Sci. Technol.* **2011**, *1* (4), 609.
(41) Li, J.; Xu, J.; Dai, W. L.; Li, H.; Fan, K. One-Pot Synthesis of Twist-like Helix Tungsten-Nitrogen-Codoped Titania Photocatalysts with Highly Improved Visible Light Activity in the Abatement of Phenol. *Appl. Catal., B* **2008**, *82* (3−4), 233−243.
(42) Ng, K. T.; Hercules, D. M. Studies of Nickel-Tungsten-Alumina Catalysts by X-Ray Photoelectron Spectroscopy. *J. Phys. Chem.* **1976**, *80* (19), 2094−2102.
(43) Sun, M.; Xu, N.; Cao, Y. W.; Yao, J. N.; Wang, E. G. Nanocrystalline Tungsten Oxide Thin Film: Preparation, Microstructure, and Photochromic Behavior. *J. Mater. Res.* **2000**, *15* (4), 927−933.
(44) Ahrenkiel, R. K.; Johnston, S. W. Interaction of Microwaves with Photoelectrons in Semiconductors. *J. Vac. Sci. Technol. B Microelectron. Nanom. Struct.* **2008**, *26* (4), 1508.
(45) Savenije, T. J.; Huijser, A.; Vermeulen, M. J. W.; Katoh, R. Charge Carrier Dynamics in TiO2 Nanoparticles at Various Temperatures. *Chem. Phys. Lett.* **2008**, *461* (1−3), 93−96.
(46) Martin, S. T.; Herrmann, H.; Choi, W.; Hoffmann, M. R. Time-Resolved Microwave Conductivity. Part 1.—TiO 2 Photoreactivity and Size Quantization. *J. Chem. Soc., Faraday Trans.* **1994**, *90* (21), 3315−3322.
(47) Martin, S. T.; Herrmann, H.; Hoffmann, M. R. Time-Resolved Microwave Conductivity. Part 2.—Quantum-Sized TiO 2 and the Effect of Adsorbates and Light Intensity on Charge-Carrier Dynamics. *J. Chem. Soc., Faraday Trans.* **1994**, *90* (21), 3323−3330.
(48) Nakajima, S.; Katoh, R. Time-Resolved Microwave Conductivity Study of Charge Carrier Dynamics in Commercially Available TiO_2 Photocatalysts. *J. Mater. Chem. A* **2015**, *3* (30), 15466−15472.
(49) Daghrir, R.; Drogui, P.; Ka, I.; El Khakani, M. A. Photoelectrocatalytic Degradation of Chlortetracycline Using Ti/TiO2 Nanostructured Electrodes Deposited by Means of a Pulsed Laser Deposition Process. *J. Hazard. Mater.* **2012**, *199−200*, 15−24.
(50) Giroux, I.; Roy, N.; Lamontagne, C. Présence de Pesticides Dans l'Eau Souterraine En Milieu Agricole: Étude Pilote Du Bassin Versant de La Rivière Châteauguay. *Can. Water Resour. J.* **2010**, *35* (4), 527−542.
(51) Trentacoste, S. V.; Friedmann, a S.; Youker, R. T.; Breckenridge, C. B.; Zirkin, B. R. Atrazine Effects on Testosterone Levels and Androgen-Dependent Reproductive Organs in Peripubertal Male Rats. *J. Androl.* **2001**, *22* (1), 142−148.
(52) Komtchou, S.; Dirany, A.; Drogui, P.; Delegan, N.; El Khakani, M. A.; Robert, D.; Lafrance, P. Degradation of Atrazine in Aqueous Solution with Electrophotocatalytic Process Using TiO2−x Photoanode. *Chemosphere* **2016**, *157*, 79−88.

DOI: 10.1021/acs.jpcc.7b11266
J. Phys. Chem. C XXXX, XXX, XXX−XXX

Article 5

In-situ co-doping of TiO_2:WN films deposited by means of a magnetron reactive co-sputtering process for the development of photoanodes intended for visible-light electro-photocatalytic degradation of emerging pollutants; N. Delegan, R. Pandiyan, S. Komtchou, A. Dirany, P. Drogui, and M. A. El Khakani; Journal of Applied Physics 123, 205101 (2018)

In-situ co-doping of sputter-deposited TiO_2:WN films for the development of photoanodes intended for visible-light electro-photocatalytic degradation of emerging pollutants

N. Delegan, R. Pandiyan, S. Komtchou, A. Dirany, P. Drogui, and M. A. El Khakani

Citation: Journal of Applied Physics **123**, 205101 (2018); doi: 10.1063/1.5025830
View online: https://doi.org/10.1063/1.5025830
View Table of Contents: http://aip.scitation.org/toc/jap/123/20
Published by the American Institute of Physics

In-situ co-doping of sputter-deposited TiO_2:WN films for the development of photoanodes intended for visible-light electro-photocatalytic degradation of emerging pollutants

N. Delegan,[1] R. Pandiyan,[1] S. Komtchou,[2] A. Dirany,[2] P. Drogui,[2] and M. A. El Khakani[1,a)]
[1]*Institut National de la Recherche Scientifique, Centre-Énergie, Matériaux et Télécommunications, 1650 Blvd. Lionel-Boulet, Varennes, Qubec J3X-1S2, Canada*
[2]*Institut National de la Recherche Scientifique, Centre-Eau, Terre et Environnement, 490 Rue de la Couronne, Qubec G1K-9A9, Canada*

(Received 13 February 2018; accepted 1 May 2018; published online 22 May 2018)

We report on the magnetron sputtering deposition of *in-situ* codoped TiO_2:WN films intended for electro-photocatalytic (EPC) applications under solar irradiation. By varying the RF-magnetron sputtering deposition parameters, we were able to tune the *in-situ* incorporation of both N and W dopants in the TiO_2 films over a wide concentration range (i.e., 0–9 at. % for N and 0–3 at. % for W). X-ray photoelectron spectroscopy analysis revealed that both dopants are mostly of a substitutional nature. The analysis of the UV-Vis transmission spectra of the films confirmed that the optical bandgap of both TiO_2:N and TiO_2:WN films can be significantly narrowed (from 3.2 eV for undoped-TiO_2 down to ~2.3 eV for the doped ones) by tuning their dopant concentrations. We were thus able to pinpoint an optimal window for both dopants (N and W) where the TiO_2:WN films exhibit the narrowest bandgap. Moreover, the optimal codoping conditions greatly reduce the recombination defect state density compared to the monodoped TiO_2:N films. These electronically passivated TiO_2:WN films are shown to be highly effective for the EPC degradation of atrazine (pesticide pollutant) under sunlight irradiation (93% atrazine degraded after only 30 min of EPC treatment). Indeed, the optimally codoped TiO_2:WN photoanodes were found to be more efficient than both the undoped-TiO_2 and equally photosensitized TiO_2:N photoanodes (by ~70% and ~25%, respectively) under AM1.5 irradiation. *Published by AIP Publishing.*
https://doi.org/10.1063/1.5025830

INTRODUCTION

Since the pioneering work of Fujishima and Honda in 1972 on titanium dioxide (TiO_2) water splitting,[1] the research on the photocatalytic properties of TiO_2 and its varied forms has continued to attract great attention. In fact, TiO_2 offers a unique combination of unpaired features among which are its wide bandgap and high chemical stability[1–5] in addition to its availability and affordability. All these facts have made TiO_2 the candidate of choice for applications in solar energy conversion[1,2,5] and photo-degradation of contaminants.[6,7]

Fundamentally, TiO_2 is an n-type semiconductor with a wide intrinsic bandgap (E_g) of 3.0 eV and 3.2 eV for rutile and anatase polymorphs, respectively. This inherently restricts the photoactivity of titania based devices to the ultra-violet (UV) range (which represents only ~4% of the irradiance of the sunlight) and limits to a certain extent its implementation in large scale industrial photo-processes.[8] It is thus understandable that substantial research effort is aimed at extending the photosensitivity of TiO_2 to the visible light range (which represents ~40% of solar irradiance) through the narrowing of its bandgap via varied approaches including self-doping,[9] dye-sensitization,[2,4] cationic doping,[4,7] and anionic doping.[3,4,6,7] For the latter approach, substitutional nitrogen (N) doping has been shown to be very effective, as it leads to the formation of discrete N_{2p} acceptor states within the E_g above the valence band maximum (VBM), reducing thereby the bandgap energy from 3.2 eV (anatase) to ~2.3 eV (N-doped anatase).[4,6,7] In this context, we have demonstrated in a previous study[7] that the *in-situ* N-doping induced E_g narrowing of sputtered TiO_2 films was directly correlated with the significant increase in their electro-photocatalytic (EPC) capacity to degrade the chlortetracycline (CTC) contaminant under sunlight exposure. In fact, N doping is a more complex process which induces different energy states within the semiconductor's forbidden gap.[10–17] Some of these energy levels act as acceptor states within the E_g and therefore effectively reduce the energy required for photoexcitation, while others act as charge traps and/or recombination centers, thereby hindering the photocharge transport. Notably, the introduction of N into the TiO_2 lattice has been shown to lead to two types of these energy states associated with the dopant being into substitutional or interstitial sites. The substitutional doping is associated with the formation of N_{2p} acceptor levels just above the O_{2p} levels, whereas the interstitial one is related to isolated N-O type deep gap states within the E_g that may act as photocharge recombination centers.[10–15] In addition, the defects induced by the presence of both dopants are usually compensated for by the oxide structure via the formation of oxygen vacancies (V_O), which in turn act as potent recombination

a)Author to whom correspondence should be addressed: elkhakani@emt.inrs.ca

centers located beneath the conduction band minimum (CBM).[14,16] In sum, both experimental and theoretical studies[10–17] indicate that mono-doping (with N, for example) while being very effective in narrowing the bandgap concomitantly creates recombination centers that tend to reduce the extracted photogenerated current.[4,7] This limits the full exploitation of the photocatalytic efficiency gain from the absorption edge redshift.[5] To counteract this limitation, density of states (DOS) models[18–24] have shown that it is possible to minimise the undesired side-effects arising from N-doping by achieving an electronically passivated acceptor-donor co-doping approach. The latter would suppress the charge defects acting as recombination centers while maintaining an enhanced visible light absorption.[5,18–21,23,24] By theoretically investigating different dopant couples,[21,23] tungsten (W) and nitrogen (N) were identified as the most interesting pair that would narrow the E_g while minimizing the recombination of photogenerated excitons through electronic passivation of uncompensated charges.[18–20,22] Recent chemical synthesis approaches have attempted simultaneous W and N codoping (WN-codoping) of TiO_2, leading to substantial bandgap narrowing.[25–30] However, these studies showed mainly interstitial type of N-doping and the presence of other contaminants such as amino groups and carbonaceous species (inherent to precursors used in chemical methods). So far, the observed increase in EPC activity was mainly associated with the effective bandgap reduction and surface area increase[25,26,28] with almost no focus and/or optimisation of the electronic passivation induced by the co-doping approach. This calls for a more systematic experimental study of the structural, electronic, and chemical effects resulting from W and N codoping of TiO_2, over the largest dopant range accessible. The objective is to achieve substitutional doping and identify the optimal doping concentrations, leading to both the narrowest bandgap and a minimum of photocharge trapping and/or recombination (i.e., longer lifetimes of the photogenerated charges). Practically, an effective co-doping of the TiO_2:WN photoanodes will translate into higher EPC photocurrent, which in turn will degrade more efficiently a given contaminant in water.

In this paper, we report on the *in-situ* co-doping of TiO_2 films by both W and N atoms by using a reactive magnetron-sputtering process. By concomitantly adjusting the N_2-to-Ar gas flow ratio and the W-to-TiO_2 target power ratio in the RF-sputtering plasma source, we were able to control the W and N incorporation rates into the films, over the (0–3) at.% and (0–9) at.% concentration ranges, respectively. The effects of both mono-doping (N and W taken separately) and WN-codoping approaches on the structural, optical, and chemical properties of the sputtered TiO_2 films have been systematically investigated. By achieving detailed experimental analyses of the energy band structure of the doped TiO_2 films, we have recently demonstrated that optimal W and N doping contents correspond not only to the narrowest E_g value of ~2.2 eV but also to favorable Fermi level (E_F), CBM, and VBM band positions.[31] In the present paper, the codoped TiO_2:WN films are shown to not only possess favorable optoelectronic properties but also most interestingly exhibit densities of oxygen vacancies and photocharge recombination centers lower than in their mono-doped counterparts, confirming thereby the achievement of an electronically passivated acceptor-donor co-doping approach. To assess the practical advantages of such a co-doping approach, the optimised TiO_2:WN films were integrated into photoanodes for the EPC degradation of atrazine (a pesticide and residual contaminant in water) under simulated AM1.5 solar light and found to deliver superior EPC performance of their mono-doped photoanode counterparts.

EXPERIMENTAL

All the films were deposited from the sputtering of a TiO_2 target by using an RF (13.56 MHz) magnetron gun operating at a constant power density of 8.8 W/cm^2. The *in-situ* N-doping of the films was achieved through the introduction of N_2 in conjunction with the Ar sputtering gas, whereas W-doping was obtained through the co-sputtering of both TiO_2 and W targets (3 in. diameter and 99.99% purity). For the WN-codoping, both N_2 gas and W target co-sputtering were combined with the main TiO_2 target sputtering. Prior to deposition, the chamber was cryopumped to a base pressure of 2×10^{-8} Torr. Thereafter, high purity Ar (99.999%) and N_2 (99.995%) gases were introduced into the deposition chamber. High purity O_2 (99.995%) was also used for the deposition of the reference TiO_2. The gas flow rates were monitored to maintain a constant pressure of 1.4 mTorr inside the chamber during the sputter-deposition process. In order to control the N incorporation in the TiO_2:WN and TiO_2:N films, the relative nitrogen mass flow rate ratio R_{N2} (i.e., $[N_2]/([N_2]+[Ar])$ was varied between 0% and 15%. The W incorporation was controlled by varying the W target power density (W_{power}) from 50 mW/cm^2 to 250 mW/cm^2. The TiO_2:WN films were simultaneously deposited onto different substrates, including (i) undoped and double side-polished Si(100), (ii) quartz, and (iii) deployed (10 cm × 11 cm) Ti-grids. The substrates were mounted on a holder located off-axis at a distance of 20 cm from the target and heated during deposition by a quartz lamp heater to an actual on-substrate temperature of ~470 °C. Prior to film deposition, the target was systematically sputter-cleaned with Ar ions for ~15 min with the shutters closed. The thickness of the TiO_2:WN films was *in-situ* monitored by means of a calibrated quartz-crystal microbalance and *ex-situ* measured through cross-section scanning electron microscopy (SEM) observations by means of a Jeol JSM-6300F SEM system. No post-acceleration voltage was intentionally applied to the substrates during the sputter-deposition process (they were nonetheless subjected to a built-in plasma sheath bias of ~−14 V during their growth). The atomic composition and chemical bonding states of the films were systematically investigated by means of X-ray photoelectron spectroscopy (XPS). The XPS spectra were collected by using the ESCALAB 220i-XL spectrophotometer, equipped with an Al$K\alpha$ (1486.6 eV) twin-anode source, after a systematic *in-situ* surface cleaning by means of 5 keV Ar^+ ion sputtering gun. The crystalline structure of the films on quartz substrates was characterized by means of a PANalytical X-Pert Pro X-ray diffractometer (XRD) system using Cu$K\alpha$ radiation of 1.5418 Å. The ultra-violet and

visible (UV-Vis) transmittance and reflectance spectra of the TiO_2:WN films were systematically measured by using an Agilent/Varian Cary 5000 system. Thus, their E_g values were derived from UV-Vis Tauc plot extrapolation. The EPC properties of the TiO_2:WN films deposited onto deployed titanium-grid substrates (used as photoanodes) were evaluated in an EPC reactor of which details are described elsewhere.[32]

RESULTS AND DISCUSSION

The structural and morphological features arising from the concomitant incorporation of N and W atoms into TiO_2 were studied via cross-sectional SEM observations. We have previously shown that the introduction of N_2 in the deposition chamber leads to an energetic competition between the dissociation of N_2 molecules and the production of ions that contribute to the sputtering process itself.[7] Here, we focus on the concomitant interplay between W and N sources and their effects on the deposited films. Figure 1(a) presents the deposition rate as a function of W_{power} (bottom x-axis; with R_{N2} kept constant at 6%) and R_{N2} (top x-axis; with W_{power} kept constant at 132 mW/cm^2). We note that N_2 introduction creates a competitive balance between the energy consumption for N_2 molecule dissociation and sputtering ion production with an optimal deposition point at around 7% R_{N2}. It is expected that this optimal point should shift to higher R_{N2} as more power is put in the system. Additionally, we note that increasing the power imposed on the W target while maintaining R_{N2} constant linearly increased the deposition rate. This power dependence of the deposition rate is typical for metallic targets in a sputtering process.[33] The morphology of the sputter-deposited TiO_2:WN films showed no significant differences as a function of deposition parameters. From that perspective, all the sputter-deposited films were found to be dense and smooth and exhibit a uniform apparent morphology regardless of W_{power} or R_{N2}. A typical cross sectional SEM image of a TiO_2:WN film can be seen in Fig. 1(b), and the deposition parameters for this film were the crossover point from Fig. 1(a): $W_{power} = 132$ mW/cm^2 and $R_{N2} = 6\%$. The thicknesses of the films investigated here are in the 200–400 nm range, depending on the deposition conditions. The exact film thickness will be used for each corresponding film for the determination of its optical absorption coefficient.

The effectiveness of our sputtering process to incorporate N and W dopants in the TiO_2:WN films was investigated by means of XPS analysis of the N *1s*, Ti *2p*, O *1s*, W *4f*, and W *4p* core level spectra. The variation of deposition parameters W_{power} and R_{N2} on the incorporation of each dopant is presented in Fig. 2. Figure 2(a) shows the incorporation of W (left y-axis) and N (right y-axis) atoms with varying R_{N2}, while W_{power} is maintained constant at 132 mW/cm^2. From

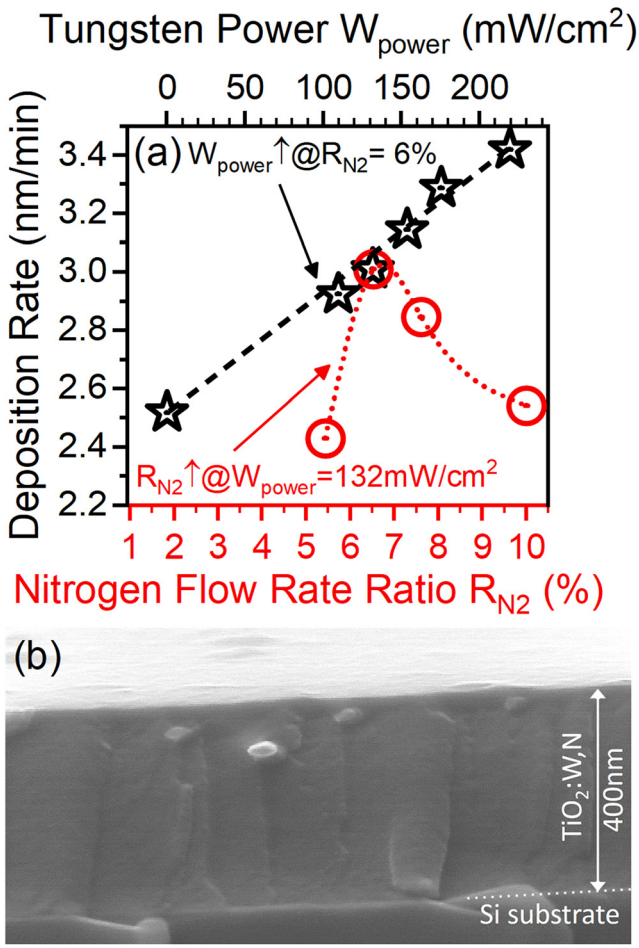

FIG. 1. (a) Variation of the deposition rate at constant R_{N2} (black dashed-dotted line) with varying W_{power} and the variation with constant W_{power} with varying R_{N2} (red dashed line). (b) SEM micrograph of a $W_{power} = 132$ mW/cm^2 and $R_{N2} = 6\%$ deposited TiO_2:WN film.

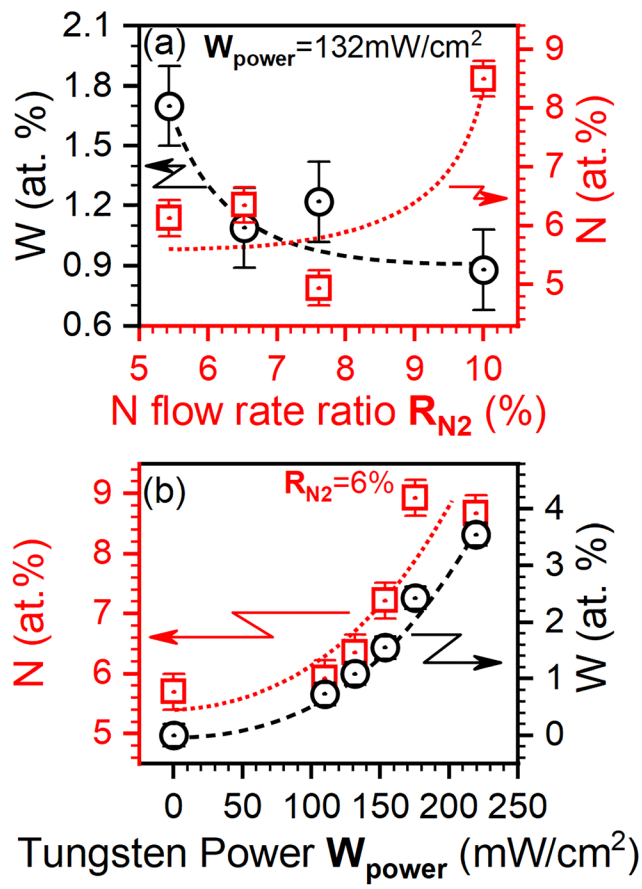

FIG. 2. (a) W and N incorporation rate (left and right hand y-axes, respectively) at constant W_{power} with varying R_{N2} and (b) N and W incorporation (left and right hand y-axes, respectively) at constant R_{N2} with varying W_{power}.

Fig. 2(a), one can see that the increase in R_{N2} translates into a progressive increase in N incorporation. However, it is also seen that the increase in N incorporation occurs to the detriment of W incorporation. The increase in the N content with R_{N2} is a direct consequence of an increased amount of N atoms in the plasma mix during the deposition process. This results in more N atoms available for incorporation, which enter in a sort of competition with W atoms (at a fixed power on the W target), lowering thereby their incorporation when R_{N2} is increased. In contrast, when the R_{N2} is fixed (at 6% here) and W_{power} is increased, the incorporation of both N and W steadily increases with W_{power}, as shown in Fig. 2(b). This behavior can be explained by two facts: (i) the incorporation of W into the TiO_2 lattice is expected to increase the solubility limit of the N dopant.[5,23] The solubility increase is caused mainly by the introduction of W atoms into the TiO_2 lattice which lowers the formation energy of substitutional N and increases the total free valence of the matrix.[21,23,24] Second, (ii) the increase in W_{power}, while keeping a constant R_{N2}, leads to more sputtered W atoms and concomitantly provides additional energy for the dissociation of N_2 molecules into N atoms. Figures 2(a) and 2(b) highlight the ability of our process to precisely control the incorporation levels of each dopant in the sputtered TiO_2 films through the appropriate tuning of both W_{power} and R_{N2}. Finally, the fundamental characteristics of the XPS binding energy (BE) spectra were found to be very similar within the investigated concentration ranges (i.e., 0 to ~3 at. % and 0 to ~9 at. % for W and N contents, respectively). Indicating that for these doping levels, the chemical bonding of these films may vary in content (depending on the doping levels), but their nature remains the same.

Figure 3 shows the high-resolution BE spectra of the O *1s*, Ti *2p*, N *1s*, and W *4f* (from left to right, respectively) core levels for different films, namely, TiO_2, TiO_2:N, TiO_2:W, and TiO_2:WN films (from bottom to top, respectively). These core level spectra were deconvoluted into their different components corresponding to various local electronic environments (oxidation/bonding states). For the TiO_2 films, the Ti $2p_{3/2}$ peak can be decomposed into two main components corresponding to two oxidation states of Ti, namely, Ti^{IV} and Ti^{III} at 458.6 eV and 456.9 eV, respectively, with their corresponding Ti $2p_{1/2}$ energy levels found at 5.7 eV and 5.5 eV higher BE, having 1:2 branching ratios.[7,26,34–36] For subsequent W *4f* fitting purposes (as the Ti *3p* energy window overlaps the W *4f* peak energies), Ti *3p* peaks were deconvoluted to reveal Ti^{IV} and Ti^{III} oxidation state peaks at 37.1 eV and 35.7 eV, respectively,[37,38] in full agreement with the Ti *2p* derived quantifications. The presence of Ti^{III} can be attributed to sub-stoichiometric species formed mainly as a result of preferential sputtering during thin film deposition.[7,39] Given that Ar^+ ion etch-cleaning is used to eliminate surface carbonaceous contaminants prior to acquisition, the Ti^{III} quantification is assumed to be slightly

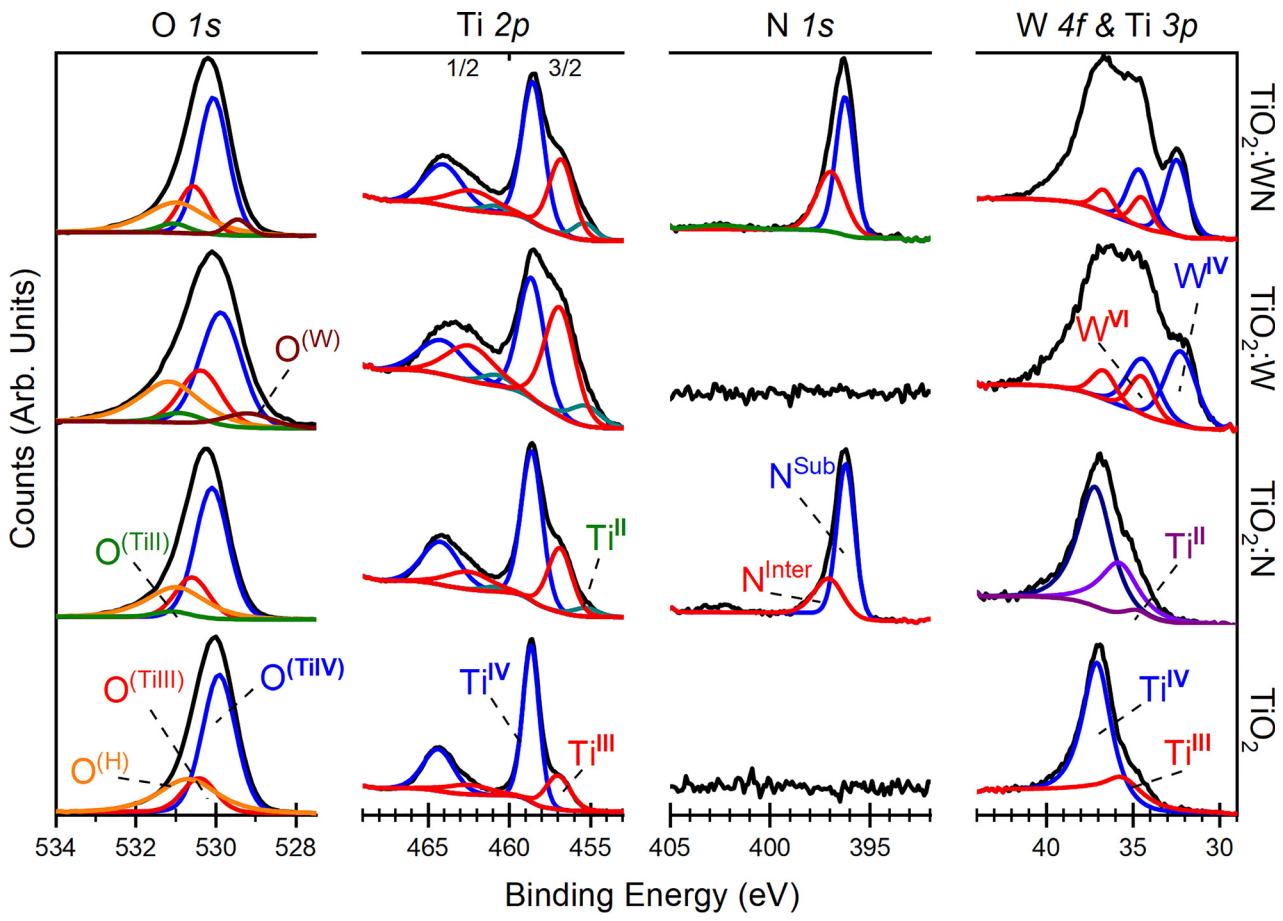

FIG. 3. High-resolution XPS spectra of the O 1s, Ti 2p, N 1s, and W 4f core levels (from left-to-right) of the TiO_2, TiO_2:N, TiO_2:W, and TiO_2:WN films (from bottom-to-top) as a function of each doping scheme. Ti 3p signatures obscured in the case of W containing films as to prioritise visibility of W 4f levels.

overestimated. However, this contribution is expected to remain unchanged for all surveyed samples as surface etch-cleaning parameters were kept constant.[7,35,39] This feature is important as its presence is indicative of V_O in the lattice, a defect associated with high levels of photocharge recombination.[4,8,40] The Ti *2p* states can be inferred in the corresponding O *1s* core levels. The main $O^{(TiIV)}$ peak at 529.9 eV is associated with lattice oxygen in the TiO_2 matrix; we note that sub-stoichiometric lattice oxygen can also be distinguished and identified as $O^{(TiIII)}$ at ∼0.5 eV higher binding energy.[34,35] Additionally, we note the presence of a third peak, denoted as $O^{(H)}$ at 530.7 eV and about double the FWHM of the other O *1s* peaks. Commonly, this peak is attributed to O *1s* defective oxygen and surface hydroxide species.[34,35,41] This contribution is expected to remain of similar relative intensity in relation to the main O *1s* peaks for all films.[34,35] The XPS derived composition of undoped films, calculated from relative peak intensities, is found to be $\sim TiO_{1.87}$.

As nitrogen gas is introduced into the deposition chamber (TiO_2:N films), the appearance of the N *1s* peak in the film's XPS spectra can be observed with two characteristic components: N^{sub} and N^{inter} at 396.2 eV and 397.2 eV binding energies, respectively. The N^{sub} peak is known to arise from substitutional -Ti-N- type bonds, and the N^{inter} peak is associated with interstitial -O-N type bonds within the titania crystal structure.[4,6,7,11–13] The relative intensity of the peaks confirms that most of the doping is of the substitutional type, associated with the visible light photosensitisation of TiO_2:N via the introduction of N *2p* levels just above the O *2p* composed VBM.[4,6,7,11–13] However, the introduction of N into the thin films is accompanied with the appearance of Ti^{II} oxidation state species in the Ti *2p* BE spectra (Ti^{II} $2p_{3/2}$ at 455.3 eV and the $2p_{1/2}$ component at 5.6 eV higher BE) and Ti *3p* (Ti^{II} *3p* at 34.8 eV).[4,42] This reduced state can also be inferred on the O *1s* spectra with the appearance of $O^{(TiII)}$ (∼1 eV higher BE than the $O^{(TiIV)}$ peak).[34,37] These reduced valence states are known to arise from the electronic distortions induced by nitrogen doping, reducing Ti^{IV} species into Ti^{III}, and on a much lesser extent into Ti^{II}. These bonding states are indicative of the lattice compensating for localised deep charge defects (known to arise from interstitial type N doping), mainly via the formation of V_O.[4,7,8,14,40] If the substitutional type of doping is considered, the obtained stoichiometry of the N-doped films is $\sim TiO_{1.69}$:$N_{0.12}$ (total N ∼6.3 at. %, with N_{sub} ∼4.2 at. %); this relatively low O content indicates a high density of V_O present within the thin films, justifying the significant increase in highly reduced Ti species.

The addition of tungsten (W) in the co-sputtering process, via sputtering of a metallic W target concomitantly with the TiO_2 target sputtering, leads to the appearance of two main features in the W *4f* BE window of the TiO_2:W thin-films (Fig. 3). These W *4f* peaks are due to the W^{VI} and W^{IV} states in the oxide form with the main $4f_{7/2}$ components appearing at 34.5 eV and 32.3 eV, respectively, with the corresponding $4f_{5/2}$ doublets found at 2.2 eV higher BE with a 3:4 peak intensity ratio.[36,43–46] The appearance of the $O^{(W)}$ peak at 529.2 eV in the O *1s* spectra can be inferred, as some of oxygen species are associated with W.[45] The XPS derived composition of these films is $\sim TiO_{1.84}$:$W_{0.06}$ (total W ∼2.3 at. %). From these analyses, we note that W doped films present lower density of V_O than N doped films. This aligns with theoretical models, predicting that W-doping should reduce the formation of V_O (increase in formation energy) as compared to N-doping.[20]

Due to size constraints, W and N are mostly expected to substitute for Ti and O atoms, respectively (nonetheless, interstitial N is also possible as above discussed), and -W-N- type bonds are energetically superimposed to -Ti-N- type bonds.[47,48] Therefore, little effect is expected in the N *1s* and corresponding cation signatures. Thus, it can be confirmed that both the W and N species are incorporated into mostly substitutional locations within the TiO_2 matrix as they present identical chemical energy states as TiO_2:N[4,6,7] and TiO_2:W.[36,43–45] This being said, the XPS derived composition of this codoped film is $\sim TiO_{1.83}$:$W_{0.04}N_{0.09}$ (N ∼ 4.9 at. % and W ∼ 1.2 at. %). This film composition indicates that there is a lack of O in the films, at a similar atomic proportion as in the undoped samples (which were interestingly deposited with additional oxygen during sputtering). This indicates that there are less oxygen vacancies in the codoped films as compared to the N-monodoped ones. This is in accordance with theoretical models that predict that when both dopants (W and N) are introduced simultaneously, there is a significant reduction of electronic defect formation (such as V_O).[5,18–21,23,24] Table I summarises the XPS derived dopant levels of the TiO_2:WN films along with their corresponding thickness, as determined from SEM cross-section observations.

Our previous work has shown that the N substitutional doping significantly affects the optical properties of the N-doped TiO_2 films, namely, narrowing their bandgap.[7] Hence, the effect of W and N dual doping on the optical properties of the TiO_2:WN films was systematically investigated as a function of the doping scheme (i.e., N, W, and WN).

TABLE I. Film thickness (as derived from SEM observations) and total dopant contents (from XPS) for the samples used in the UV-Vis. characterizations.

N (at. %)	W (at. %)	Thickness (nm)
0.0	0.0	200
2.4	0.0	260
5.7	0.0	250
0.0	0.6	400
0.0	2.3	380
0.0	3.1	430
2.5	2.4	300
5.9	0.7	310
6.4	1.1	300
7.2	1.6	300
8.9	2.4	410
4.9	1.2	370
8.5	0.9	270
7.7	0.2	270
7.9	0.3	280
8.7	3.6	340
6.4	3.6	270

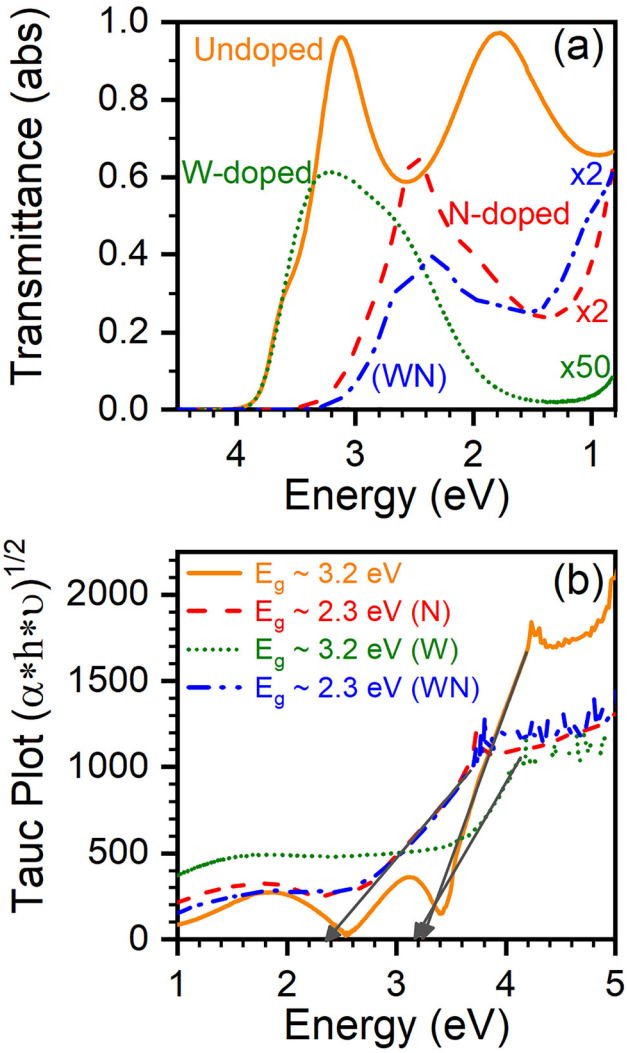

FIG. 4. (a) Selected UV-Vis transmittance spectra of the sputter-deposited TiO_2, TiO_2:N, TiO_2:W, and TiO_2:WN films. (b) Tauc plots of those films with their corresponding extrapolated E_g values.

Figure 4(a) shows UV-Vis transmittance spectra of the $TiO_{1.87}$, $TiO_{1.84}$:$W_{0.06}$, $TiO_{1.69}$:$N_{0.12}$, and $TiO_{1.83}$:$W_{0.04}N_{0.09}$ films deposited onto quartz substrates. We note a significant red shift of the absorption band edge of the spectra from about 320 nm for undoped TiO_2 films to ~420 nm for the $TiO_{1.69}$:$N_{0.12}$ films and to ~440 nm for $TiO_{1.83}$:$W_{0.04}N_{0.09}$ films. In agreement with our previous work, our results showed that any doping content beyond this doping point did not necessarily translate into further red shifting of the absorption edge.[7] It is to be noted that the W-doped films ($TiO_{1.84}$:$W_{0.06}$) showed the same absorption edge as undoped TiO_2 films (no red-shift). This confirms that it is indeed nitrogen that produces energy states responsible for the observed photosensitization of the TiO_2:WN films in the visible. In order to derive a quantitative value of the E_g for these thin films, the corresponding UV-Vis spectra (transmittance and reflectance used to extract the absorption coefficient) were analyzed according to the Tauc formalism,[44] where the E_g value can be deduced from the *x*-intercept of the tangential extrapolation of the Tauc plots, as shown in Fig. 4(b). We note that indeed both the $TiO_{1.69}$:$N_{0.12}$ and $TiO_{1.83}$:$W_{0.04}N_{0.09}$ samples show significant optical E_g reduction to around ~2.3 eV, while the $TiO_{1.87}$ and $TiO_{1.84}$:$W_{0.06}$ films exhibit an E_g of ~3.2 eV, consistent with indirect gap values quoted for titania in the literature.[4,8] These results confirm that W doping has no significant impact on the absorption edge of the films, while the N doping induced visible photosensitisation is still effective in the co-doping scheme. In order to get a broader picture, the E_g values were derived for numerous TiO_2:WN codoped films with a broader range of doping levels and reported in a sort of a 2D map of which X and Y axes are N and W doping levels, as shown in Fig. 5. We note that in the Y-axis (W concentration) there is a very little to no effect on the E_g variation (varying W by about 3 at. % induces only a small ~0.2 eV change in the E_g value), mostly through the creation of shallow states below

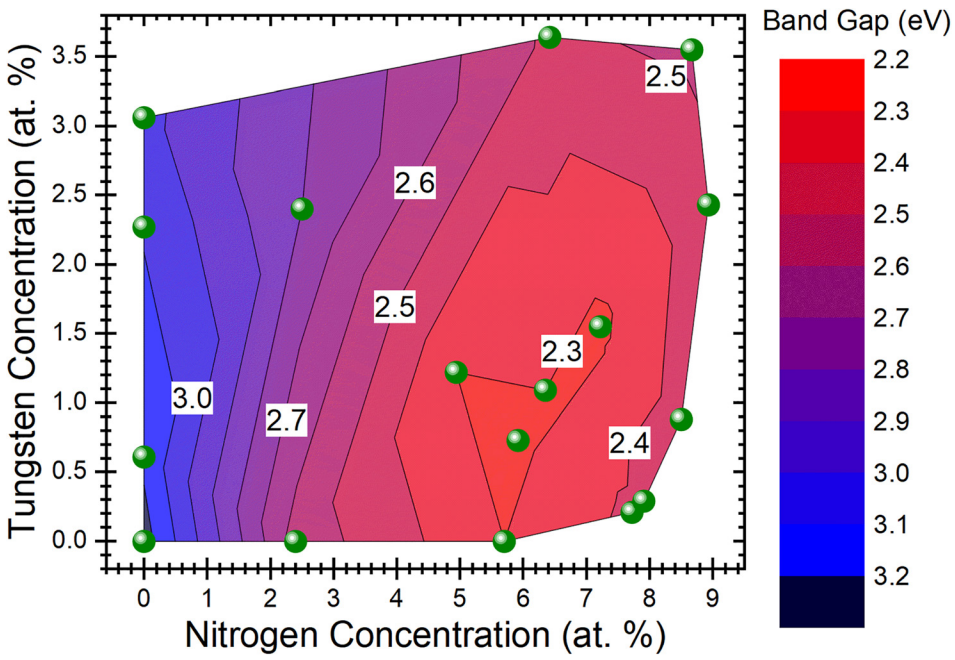

FIG. 5. 2D-map displaying the variation of E_g as a function of both nitrogen and tungsten doping concentrations. The color scale (on the right-hand side) depicts the bandgap values.

the CB.[19,49] In contrast, the main determining factor for bandgap narrowing of the TiO_2:WN films (and thereby their photosensitisation to visible light) is their N doping level. Additionally, we noticed that beyond an N-doping level ~6 at. % of N, no additional gain in visible light absorption can be obtained. This points up the existence of an optimal nitrogen doping concentration range (5–6 at. %) where the E_g stays at its lowest value of ~2.3 eV (a bandgap value that ensures effective visible light photosensitization of TiO_2 films). This observation, along with the theoretical prediction[20] that states that the acceptor-donor passivation is most efficient with the N:W ratio close to 2:1, is what guided the selection of our representative TiO_2:WN samples to be used for further analysis. Thus, the following film compositions were investigated: $TiO_{1.87}$, $TiO_{1.84}$:$W_{0.06}$, $TiO_{1.69}$:$N_{0.12}$, and $TiO_{1.83}$:$W_{0.04}N_{0.09}$. In order to better understand the relationship between EPC performance and dopant induced band-gap narrowing, one has to have access to other physical parameters, such as the Fermi energy, work function, and valence band maximum (VBM)/conduction band minimum (CBM) energy levels (a study that is beyond the scope of the present paper). In fact, the measurement and quantification of the above-mentioned optoelectronic characteristics of the doped TiO_2 films in order to reconstruct the band energy diagrams are a thorough study that has been reported elsewhere.[31] We briefly highlight here some of the relevant insights gained from this study:[31] first, (i) W-doping keeps most of the E_g features unchanged outside of the introduction of new states below the CBM, (ii) N-doping shrinks the E_g mostly via the introduction of new midgap N *2p* states above the mostly O *2p* populated VBM while reducing the work function, and (iii) WN-codoping shrinks the E_g mostly via hybridizing N *2p* states with VBM O *2p* states while leaving most other features unchanged.[31] In summary, while both N-doped and WN-codoped samples show a significant reduction in their E_g, the acceptor-donor codoped samples are expected to outperform monodoped ones due to less midgap states, defect states, and better placements of the VBM energy levels.[31]

It is worth reiterating that the crystallinity of the films plays a key role in their EPC properties as it determines features such as the bandgap and average crystallite size (mean free path of charges).[4,8] Therefore, we have used XRD to investigate the crystalline structure of our films as a function of their doping scheme, and the obtained spectra are displayed in Fig. 6. The $TiO_{1.87}$ films are seen to crystallize in the anatase (A) phase with the characteristic (101), (103), (004), (112), (200), (105), and (211) peaks (JCPDS No.: 84-1286) with the main A(101) peak at 25.4° with 0.4° of full width at half maximum (FWHM). The Williamson-Hall size-strain analysis[50] revealed lattice parameters typical of anatase under low tensile strain (~0.66%), as shown in Table II. This is most likely due to the oxygen vacancies present in the structure, causing some of the Ti atoms to reduce from Ti^{IV} to Ti^{III} (as shown above by XPS), increasing their atomic radii. When nitrogen is incorporated into the structure, the crystalline quality of the TiO_2:N films is significantly reduced as seen in Fig. 6 [signal to noise ratio and FWHM ~ 0.7° for A(101)]. The tensile strain of the TiO_2:N films increased to ~2.75%, explaining the observed relative

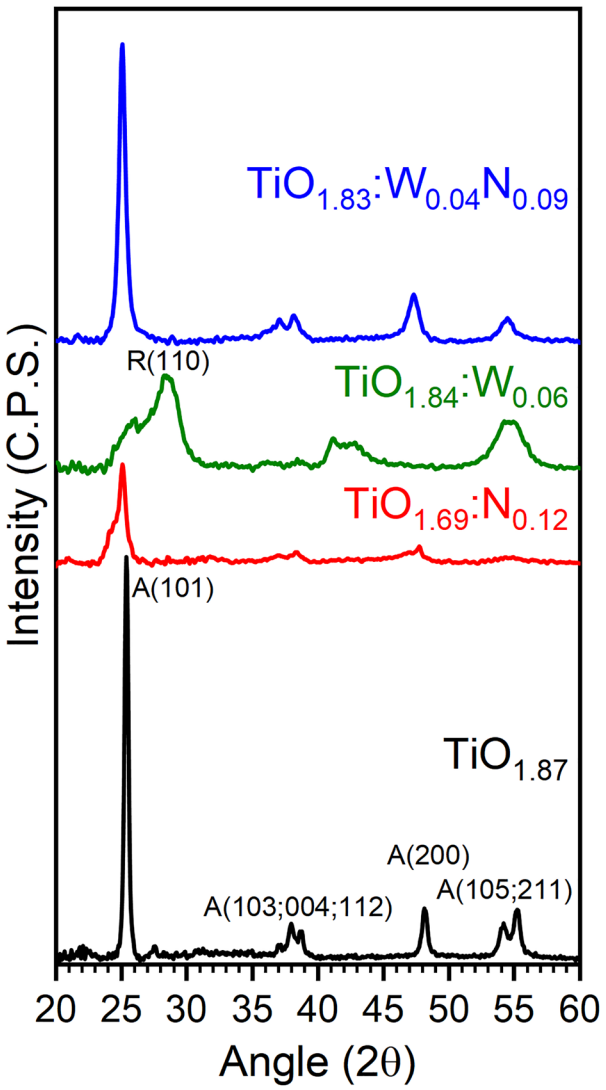

FIG. 6. Typical XRD spectra of the sputter-deposited TiO_2, TiO_2:N, TiO_2:W, and TiO_2:WN films.

deterioration of their crystalline quality. This strain exists due to a couple of reasons: (i) N-doping reduces the formation energy of V_O facilitating sub-stoichiometric oxide formation[4,23,24,51,52] and (ii) interstitial N-doping will impose a certain stretching of the lattice.[53] In the case of W doping, the crystallinity of the TiO_2:W films is also seen to be greatly affected. Given that W^{VI} and Ti^{IV} are of similar ionic radii (around 0.600 Å and 0.605 Å), substitutional W^{VI} doping should not affect the TiO_2 lattice structure significantly. However, as shown by XPS analysis in Fig. 3, we note the presence of W^{IV} species in the TiO_2 structure, and this reduced state is of higher atomic radii (0.660 Å) and is associated with the distortion of the crystal lattice to higher 2θ values.[36] Additionally, W^{IV} species (WO_2 type crystal) naturally crystallize in a rutile structure.[54] In fact, this and the W doping generated strain (as high as ~4.06%) in the lattice induce the TiO_2:W films to transition into the rutile polymorph.[7,36] In Fig. 6, the rutile phase peaks are seen to be predominant and very broad (with a FWHM as large as ~2.1° for the R(110) peak). The less intense anatase peak A(101) is also found to be very broad with a FWHM of ~1.9°.

TABLE II. Williamson-Hall calculated lattice parameters based on the XRD spectra of Fig. 4 for the various doping schemes alongside theoretical TiO_2 lattice values.

Sample	TiO_2	$TiO_{1.89}$	$TiO_{1.84}$:$W_{0.06}$	$TiO_{1.69}$:$N_{0.12}$	$TiO_{1.83}$:$W_{0.04}N_{0.09}$
a (nm)	0.378	0.378	N/A	0.381	0.384
b (nm)	0.378	0.378	N/A	0.381	0.384
c (nm)	0.950	0.944	N/A	0.966	0.934
c/a	0.251	0.250	N/A	0.254	0.243
Vol. (nm^3)	0.136	0.135	N/A	0.140	0.138
Crys. Size (nm)	N/A	27.68	6.40	7.00	32.93
Internal strain (η)	0.00%	0.66%	4.10%	2.75%	1.90%

Interestingly, in the case of WN-codoping, the anatase phase is recovered with a high crystalline quality (the FWHM of the anatase (101) peak is ~0.5°) and a moderate tensile strain (estimated to ~1.9%). The crystallite size (of ~30 nm) of these codoped films was found to be very comparable to that of undoped $TiO_{1.87}$ films. Moreover, one can note that the strain in the WN-codoped films is lower as compared to their monodoped counterparts (i.e., W-doped and N-doped; see Table II). This recovery of the anatase phase seems to be a direct result of local dopant charge passivation, leading to a reduction of structural defects that arise from uncompensated lattice charges. Indeed, substitutional W and N dopants have been reported to result in a charge-passivated lattice with lower V_O formation.[21–24]

Finally, in order to assess the electro-photocatalytic properties of our doped TiO_2 films, while taking advantage of their visible light photosensitisation and the acceptor-donor passivated codopants, the codoped $TiO_{1.83}$:$W_{0.04}N_{0.09}$ films along with $TiO_{1.87}$, $TiO_{1.69}$:$N_{0.12}$, and $TiO_{1.84}$:$W_{0.06}$ films were deposited onto both sides of deployed Ti-grid substrates (10 cm × 11 cm) and used as photoanodes. Those photoanodes were integrated into a home built electro-photocatalytic (EPC) reactor (of which details can be found elsewhere[32]). The EPC performance of our photoanodes was assessed towards the degradation of a real emerging contaminant that is atrazine. Atrazine is a pollutant that is widely used as a pesticide in agriculture. For the purpose of the present study, synthetic solutions containing atrazine concentrations of 60 μg/l (60 ppb, as these are the typical concentrations of heavily polluted areas) were prepared and treated in our EPC reactor under an AM 1.5 G solar simulator while continuously circulating the solution during the treatment time which was of up to 2 h. The reaction kinetics for the four different types of photoanodes are shown in Fig. 7(a). We note that while $TiO_{1.87}$ is found to degrade atrazine, the degradation reaction is relatively slow (after 1 h of treatment, ~20 ppb of atrazine I is still present in the solution). In the case of $TiO_{1.69}$:$N_{0.12}$ photoanodes, the degradation efficiency is seen to improve due to the photosensitisation effect of nitrogen doping, allowing the use of a higher portion of visible light photons for the generation of excitons to be used in the photocatalytic process.[7,32] Surprisingly, $TiO_{1.84}$:$W_{0.06}$ photoanodes were found to perform similarly (within the statistical error margin) to the photosensitized $TiO_{1.69}$:$N_{0.12}$, even if their bandgap is much larger than that of N-doped TiO_2. This effect is mainly attributed to the W induced increase in the photocharge lifetimes of the TiO_2:W films, as compared to the N-doped photoanodes.[19,49,55] In fact, a more systematic study of the effect of the doping scheme on the photocharge lifetimes has been carried out and reported

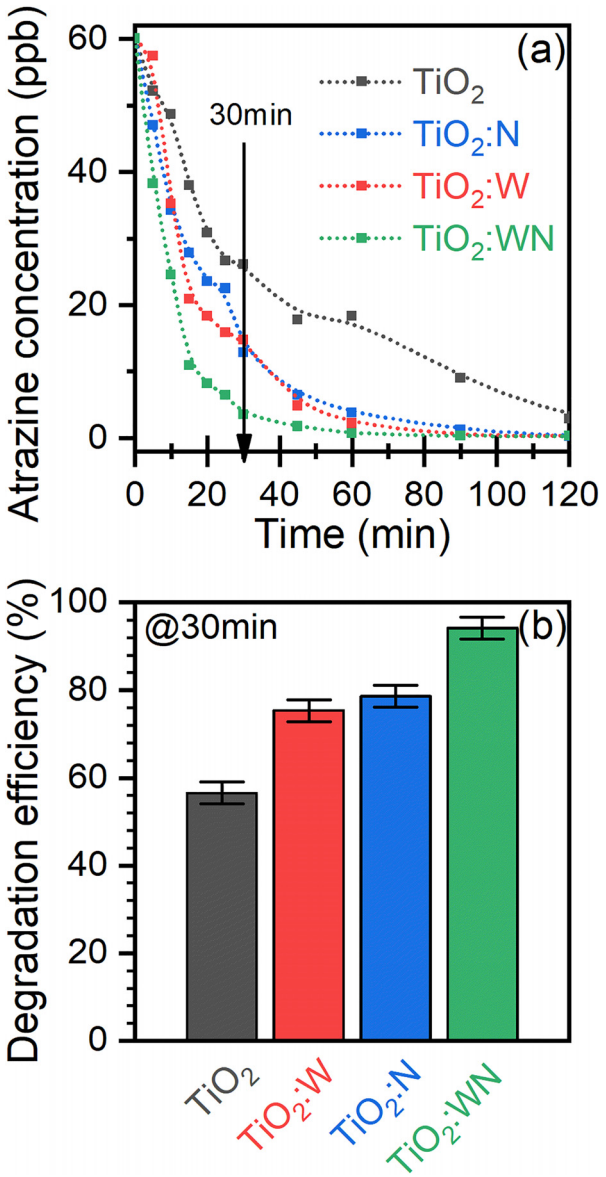

FIG. 7. (a) Residual atrazine concentration as a function of EPC degradation time and (b) electro-photocatalytic degradation efficiency of atrazine, under AM1.5 solar irradiation, for the four different photoanodes (i.e., TiO_2, TiO_2:N, TiO_2:W, and TiO_2:WN thin-films).

elsewhere.[55] Important to underline here is that the W dopant was found to increase the formation energy of V_O defects and to locally passivate charge disparities when co-introduced with N.[55] These effects have led to WN-codoped samples exhibiting a very good visible-light sensitivity while having photocharge lifetimes up to three times longer than those measured in their N-doped TiO_2 counterparts (photocharge trapping decay constant of 90 ± 7 ns for TiO_2:WN *versus* 30 ± 10 μs for TiO_2:N).[55] This corroborates well with the fact that the codoped TiO_2:WN photoanodes are the most effective ones for atrazine degradation, as can be clearly seen in Fig. 7(b). Indeed, after just 30 min of treatment, the TiO_2:WN photoanodes degraded 94% of the atrazine present in the solution (this represents 24% and 71% more than the N-doped and the undoped TiO_2 photoanodes, respectively). Those results clearly confirm the benefit of the TiO_2 photoanode WN-codoping for the EPC degradation of pollutants. In fact, nitrogen doping allows for photosensitivity of the photoanodes in the visible domain, thereby permitting the additional use of visible light photons for photocatalysis. However, part of this advantage is counteracted by N doping induced deep states in the E_g which act as recombination centers trapping the photogenerated charges. This drawback, in turn, can be minimised via the electronically passivated WN-codoping approach, allowing for the recovery of a significant increase in EPC performance,[21,23,24] as exhibited here by our TiO_2:WN photoanodes.

CONCLUSION

In summary, we were able to develop and apply a reliable RF magnetron sputtering process for the fabrication on *in-situ* doped and codoped TiO_2 films with different W and N doping concentrations, in the 0–3 at. % and 0–9 at. % ranges, respectively. All the deposited films have shown a dense, smooth, and uniform apparent morphology, regardless of their doping conditions. By adjusting the relevant operating parameters, namely, W_{power} and R_{N2}, we were able to fine-tune the incorporation of W and N dopants into the TiO_2 films. The XPS analyses have revealed that both the W and N species are mostly incorporated into substitutional doping locations in the TiO_2 matrix. The N-doping was shown to increase significantly the density of V_O defects ($TiO_{1.69}$:$N_{0.12}$ composition as compared to the undoped $TiO_{1.87}$). In contrast, the (WN) codoping was found to minimise the formation of V_O (i.e., $TiO_{1.83}$:$W_{0.04}N_{0.09}$). From the optoelectronic viewpoint, both N-doping and WN-codoping were found to induce a significant red shift of the absorption edge, leading to a bandgap narrowing by ~0.9 eV. Thus, the bandgap of both TiO_2:N and TiO_2:WN films was found to be in the visible range with a value as low as 2.3 eV. N-doping was pinpointed as the most determining factor for bandgap narrowing. An N-doping concentration of ~5.5 at. % was identified as the optimal content for the narrowest bandgap. Higher N-doping contents do not translate into additional narrowing of the bandgap. On the other hand, XRD results have shown a significant decrease in the crystalline quality of the films and an increase in their lattice strain in the case of mono-doping. This was particularly observed in the case of W-doped films, where the relatively strong tensile strain has led to a transition from the anatase to the rutile phase. This drawback of mono-doping was significantly reduced when the codoping scheme was adopted, as the lattice strain was found to diminish significantly along with the recovery of high crystallinity (of the anatase phase) of the codoped films. Finally, our EPC experiments have shown that TiO_2:WN codoped photoanodes are the most effective for atrazine degradation (93% of atrazine was degraded within the first 30 min of treatment time under AM1.5 G solar radiation). Indeed, the codoped TiO_2:WN photoanodes have performed 71% better than the undoped-TiO_2 and 24% better than the N-doped TiO_2:N ones, during the first 30 min of treatment. This emphasizes the benefit of using WN-codoped TiO_2 for EPC applications through the enhanced harvesting of visible light (as evidenced by improved EPC performance) in comparison to N-doped photoanodes. The developed TiO_2:WN photoanodes definitely open up new prospects for the degradation of emerging contaminants in water while using the direct sunlight radiation.

ACKNOWLEDGMENTS

The authors would like to acknowledge the financial support from NSERC (the Natural Science and Engineering Research Council of Canada) and the FRQNT (Le Fonds de Recherche du Québec-Nature et Technologies) through its strategic Network "Plasma-Québec."

[1]A. Fujishima and K. Honda, Nature **238**, 37 (1972).
[2]B. O'Regan and M. Grätzel, Nature **353**, 737 (1991).
[3]S. U. M. Khan, M. Al-Shahry, and W. B. Ingler, Science **297**, 2243 (2002).
[4]A. V. Emeline, V. N. Kuznetsov, V. K. Rybchuk, and N. Serpone, Int. J. Photoenergy **2008**, 1.
[5]I. S. Cho, C. H. Lee, Y. Feng, M. Logar, P. M. Rao, L. Cai, D. R. Kim, R. Sinclair, and X. Zheng, Nat. Commun. **4**, 1723 (2013).
[6]R. Asahi, Science **293**, 269 (2001).
[7]N. Delegan, R. Daghrir, P. Drogui, and M. A. El Khakani, J. Appl. Phys. **116**, 153510 (2014).
[8]A. Fujishima, X. Zhang, and D. Tryk, Surf. Sci. Rep. **63**, 515 (2008).
[9]D. O. Scanlon, C. W. Dunnill, J. Buckeridge, S. A. Shevlin, A. J. Logsdail, S. M. Woodley, C. R. A. Catlow, M. J. Powell, R. G. Palgrave, I. P. Parkin, G. W. Watson, T. W. Keal, P. Sherwood, A. Walsh, and A. A. Sokol, Nat. Mater. **12**, 798 (2013).
[10]C. Di Valentin, G. Pacchioni, A. Selloni, S. Livraghi, and E. Giamello, J. Phys. Chem. B **109**, 11414 (2005).
[11]C. Di Valentin, G. Pacchioni, and A. Selloni, Phys. Rev. B **70**, 85116 (2004).
[12]J. Lynch, C. Giannini, J. K. Cooper, A. Loiudice, I. D. Sharp, and R. Buonsanti, J. Phys. Chem. C **119**, 7443 (2015).
[13]F. Peng, L. Cai, H. Yu, H. Wang, and J. Yang, J. Solid State Chem. **181**, 130 (2008).
[14]G. R. Torres, T. Lindgren, J. Lu, C.-G. Granqvist, and S.-E. Lindquist, J. Phys. Chem. B **108**, 5995 (2004).
[15]M. D'Arienzo, N. Siedl, A. Sternig, R. Scotti, F. Morazzoni, J. Bernardi, and O. Diwald, J. Phys. Chem. C **114**, 18067 (2010).
[16]B. Liu, L. Wen, and X. Zhao, Mater. Chem. Phys. **106**, 350 (2007).
[17]R. Katoh, A. Furube, K. Yamanaka, and T. Morikawa, J. Phys. Chem. Lett. **1**, 3261 (2010).
[18]W.-J. Yin, H. Tang, S.-H. Wei, M. M. Al-Jassim, J. Turner, and Y. Yan, Phys. Rev. B **82**, 45106 (2010).
[19]V. Çelik and E. Mete, Phys. Rev. B **86**, 205112 (2012).
[20]M. Li, J. Zhang, and Y. Zhang, Chem. Phys. Lett. **527**, 63 (2012).
[21]R. Long and N. J. English, Chem. Mater. **22**, 1616 (2010).
[22]R. Long and N. J. English, Appl. Phys. Lett. **94**, 132102 (2009).
[23]D. Wang, Y. Zou, S. Wen, and D. Fan, Appl. Phys. Lett. **95**, 12106 (2009).

[24]Y. Gai, J. Li, S.-S. Li, J.-B. Xia, and S.-H. Wei, Phys. Rev. Lett. **102**, 36402 (2009).
[25]X. Cui, S. Rong, Y. Cao, Y. Yin, S. Li, and M. Li, Appl. Phys. A **113**, 47 (2013).
[26]S. S. Thind, G. Wu, M. Tian, and A. Chen, Nanotechnology **23**, 475706 (2012).
[27]S. S. Thind, G. Wu, and A. Chen, Appl. Catal. B: Environ. **111–112**, 38 (2012).
[28]A. Kubacka, B. Bachiller-Baeza, G. Colón, and M. Fernández-García, Appl. Catal. B: Environ. **93**, 274 (2010).
[29]A. Folli, J. Z. Bloh, E.-P. Beukes, R. F. Howe, and D. E. Macphee, J. Phys. Chem. C **117**, 22149 (2013).
[30]J. Z. Bloh, A. Folli, and D. E. Macphee, J. Phys. Chem. C **118**, 21281 (2014).
[31]R. Pandiyan, N. Delegan, A. Dirany, P. Drogui, and M. A. El Khakani, J. Phys. Chem. C **120**, 631 (2016).
[32]R. Daghrir, P. Drogui, I. Ka, and M. A. El Khakani, J. Hazard. Mater. **199–200**, 15 (2012).
[33]L. I. Maissel, R. Glang, and P. P. Budenstein, J. Electrochem. Soc. **118**, 114C (1971).
[34]M. C. Biesinger, B. P. Payne, A. P. Grosvenor, L. W. M. Lau, A. R. Gerson, and R. S. C. Smart, Appl. Surf. Sci. **257**, 887 (2010).
[35]M. J. Jackman, A. G. Thomas, and C. Muryn, J. Phys. Chem. C **119**, 13682 (2015).
[36]S. Sathasivam, D. S. Bhachu, Y. Lu, N. Chadwick, S. a. Althabaiti, A. O. Alyoubi, S. N. Basahel, C. J. Carmalt, and I. P. Parkin, Sci. Rep. **5**, 10952 (2015).
[37]F. Werfel and O. Brümmer, Phys. Scr. **28**, 92 (1983).
[38]J. Riga, C. Tenret-Noël, J. J. Pireaux, R. Caudano, J. J. Verbist, and Y. Gobillon, Phys. Scr. **16**, 351 (1977).
[39]D. Brassard, M. a. El Khakani, and L. Ouellet, J. Appl. Phys. **102**, 34106 (2007).
[40]A. K. Rumaiz, J. C. Woicik, E. Cockayne, H. Y. Lin, G. H. Jaffari, and S. I. Shah, Appl. Phys. Lett. **95**, 262111 (2009).
[41]M. Kitano, K. Funatsu, M. Matsuoka, M. Ueshima, and M. Anpo, J. Phys. Chem. B **110**, 25266 (2006).
[42]M.-S. Wong, H. Pang Chou, and T.-S. Yang, Thin Solid Films **494**, 244 (2006).
[43]T. Mishra, M. Mahato, N. Aman, J. N. Patel, and R. K. Sahu, Catal. Sci. Technol. **1**, 609 (2011).
[44]J. Li, J. Xu, W. L. Dai, H. Li, and K. Fan, Appl. Catal. B: Environ. **82**, 233 (2008).
[45]K. T. Ng and D. M. Hercules, J. Phys. Chem. **80**, 2094 (1976).
[46]M. Sun, N. Xu, Y. W. Cao, J. N. Yao, and E. G. Wang, J. Mater. Res. **15**, 927 (2000).
[47]Y.-C. Nah, I. Paramasivam, R. Hahn, N. K. Shrestha, and P. Schmuki, Nanotechnology **21**, 105704 (2010).
[48]Y. Zhao, W. Hu, Y. Xia, E. Smith, Y. Zhu, C. Dunnill, and D. Gregory, J. Mater. Chem. **17**(41), 4436 (2007).
[49]X. Li, F. Li, C. Yang, and W. Ge, J. Photochem. Photobiol. A: Chem. **141**, 209 (2001).
[50]G. Williamson and W. Hall, Acta Metall. **1**, 22 (1953).
[51]A. Kumar and T. Mohanty, J. Phys. Chem. C **118**, 7130 (2014).
[52]L. Wan, J. F. Li, J. Y. Feng, W. Sun, and Z. Q. Mao, Mater. Sci. Eng. B **139**, 216 (2007).
[53]Y. Shen, T. Xiong, T. Li, and K. Yang, Appl. Catal. B: Environ. **83**, 177 (2008).
[54]F. J. Wong and S. Ramanathan, J. Mater. Res. **28**, 2555 (2013).
[55]N. Delegan, R. Pandiyan, S. Johnston, A. Dirany, S. Komtchou, P. Drogui, and M. A. El Khakani, J. Phys. Chem. C **122**, 5411 (2018).

Article 6

Sputter deposited WN-codoped TiO_2 thin-films for visible light applications – a dielectric and structural study of defect-pair passivation; N. Delegan, R. Pandiyan, T. Teranishi, S. Komtchou, A. Dirany, P. Drogui, and M. A. El Khakani; Submission Pending

Sputter deposited WN-codoped TiO_2 thin-films for visible light applications – a dielectric and structural study of defect-pair passivation.

N. Delegan,[1] R. Pandiyan,[1] T. Teranishi,[2] S. Komtchou,[3] A. Dirany,[3] P. Drogui,[3] and M. A. El Khakani[*,1]

[1]Institut National de la Recherche Scientifique, Centre-Énergie, Matériaux et Télécommunications, 1650 Blvd. Lionel-Boulet, Varennes, QC, J3X-1S2, Canada

[2]Okayama University, 3-1-1 Tsushima-naka, Kita-ku, Okayama 700-8530, Japan

[3]Institut National de la Recherche Scientifique, Centre-Eau, Terre et Environnement, 490 Rue de la Couronne, Quebec, QC, G1K-9A9, Canada

[*]Corresponding author: *elkhakani@emt.inrs.ca* Tel.: *1-514-228-6922*

Author Information

N. Delegan[1], *delegan@emt.inrs.ca*

R. Pandiyan[1], *rajesh.pandiyan@emt.inrs.ca*

T. Teranishi[2], *terani-t@cc.okayama-u.ac.jp*

S. Komtchou[3], *simon.komtchou@ete.inrs.ca*

A. Dirany[3], *ahmad.dirany@ete.inrs.ca*

P. Drogui[3], *patrick.drogui@ete.inrs.ca*

M. A. El Khakani[*,1], *elkhakani@emt.inrs.ca*

Abstract

Nitrogen doping is widely used to form mid-gap defect states in the TiO_2 band-gap (E_g); photosensitizing the material well into the visible light spectrum. However, incorporation of nitrogen into TiO_2 promotes the formation of oxygen vacancies (V_O), reducing the per-photon efficiency of the TiO_2:N. To mitigate this problem, herein we propose an approach based on acceptor-donor passivation. This is achieved through the *in-situ* codoping of TiO_2 by both W and N dopants, using an RF-magnetron sputtering deposition process. Thus, codoped TiO_2:WN films with a wide incorporation range for both W and N dopants (0-10 at.%) were prepared and their properties investigated. Compositional and structural analyses (by means of XPS and XRD techniques, respectively) revealed that both dopants are mostly of substitutional nature in the TiO_2 lattice. Additionally, nitrogen doping was confirmed to narrow the E_g of the material from 3.2 eV down to ~2.3eV regardless of doping scheme. These results, in conjuncture with high frequency dielectric spectroscopy revealed that codoping greatly reduced V_O concentrations, as tracked by their GHz dielectric contribution. Finally, these optoelectronic improvements were shown to directly translated into improved visible-light driven net-photocurrents of the TiO_2:WN photoanodes as compared to the TiO_2:N and TiO_2 ones (~0.18 versus ~0.09 and ~0.05 $mA \cdot cm^{-2}$, respectively).

Keywords

RF-magnetron sputtering; *in-situ* WN-codoping; TiO_2 doping; bandgap narrowing; electronic passivation; doped TiO_2 dielectric spectroscopy.

Introduction

Titanium dioxide (TiO_2) is an n-type semiconductor that continues to attract much attention in the field of environmental pollutant remediation albeit its wide intrinsic bandgap (E_g), limiting its photo-reactivity to the UV portion of sunlight (only ~4% of the total solar flux) [1–5]. In recent years, much attention has been placed on narrowing the bandgap (E_g) of TiO_2 (3.2 eV for anatase, 3.0 eV for rutile). Thus, achieve visible light driven photoactivity, which is wanted for industrial scalability of the material. To this end, anionic type doping of titania has shown much promise [2–4, 6–10]. Most notably, substitutional nitrogen doping has been reported to reduce the E_g of TiO_2 to values as low as ~2.2eV [7, 8], effectively photosensitising the material well into the visible part of the light spectrum. However, nitrogen doping was also shown to induce the formation of oxygen vacancy (V_O) defects, which in-turn reduce the per-photon photocatalytic efficiency of the material [10–17].

To mitigate this limitation, herein we present a novel *in-situ* tungsten and nitrogen WN-codoping approach for the fabrication of acceptor-donor passivated TiO_2:WN photoanodes. These thin-films exhibit both visible light photosensitivity and reduced densities of V_O defects as compared to anion monodoped TiO_2:N. Theoretical models guided the choice of the W and N codopants. These *ab initio* results highlighted potential codopant pairs that would maintain proper band alignment, while reducing defects induced by local charge disparities [18–24]. So far, while some experimental studies succeeded in demonstrating red-shifted TiO_2:WN, few have displayed dopant states coherent with substitutional type WN-codoping [25–32]. Additionally, most of these TiO_2:WN films were achieved via chemical synthesis routes. This is synonymous with the presence of contaminants (such as carbonaceous species, precursor residues, etc.) in the films, making analysis of the WN-codoping's optoelectronic benefits difficult.

In this paper we report on the use of an optimized, one-step reactive magnetron sputtering process for the preparation of acceptor-donor passivated TiO_2:WN films. This work builds on our previous studies of sputter-deposited doped TiO_2 films [8, 33] [REF TiO2:W]. In these studies, we showed that management of V_O defects is key for the achievement of efficient and visible-light sensitive WN-codoped films. Thus, herein, focus is put on the investigation of the beneficial effects that arise from WN-codoping as compared to monodoped samples, with a particular attention given to the thin-films' V_O content. This is achieved via comparative study of the sputtered-TiO_2 films' stoichiometry, crystalline structure, and high frequency dielectric spectroscopy. Were thus able to pinpoint the benefits of an optimized *in-situ* acceptor-donor codoping on the enhanced photoactivity of the TiO_2:WN photoanodes. Indeed, the sunlight generated photocourrent by the TiO_2:WN photoanodes was shown to be three times higher that that produced by the undoped TiO_2 counterparts.

Materials and Methods

The TiO_2:WN films were sputter-deposited from a 7.62 cm in diameter TiO_2 target (99.99% purity) using an RF (13.56 MHz) magnetron sputtering process with a constant power density of 5.5 $W \cdot cm^{-2}$ applied to the target. The sputtering chamber was cryo-pumped to a base pressure of 2×10^{-8} Torr prior to deposition. Thereafter, high purity Ar (99.999 %) was introduced in the chamber with the gas flow rates monitored as to maintain a constant pressure of 1.44 mTorr during the sputter-deposition process. Nitrogen and tungsten incorporations were accomplished by injecting N_2 (99.995 %) gas into the chamber and by concomitant sputtering of a 7.62 cm in diameter WO_3 target (99.95% purity), respectively. The WO_3 target was used instead of a typically employed metallic-W sputtering-target as to increase the amount of oxygen atoms in the RF sputtering plasma, and minimise thereby the oxygen vacancies in the TiO_2:WN films. The N incorporation

in the TiO_2:WN films was controlled by adjusting the relative nitrogen mass flow rate ratio R_{N2} (*i.e.* 100% × $[N_2]/([N_2]+[Ar])$) between 0 and 20 %, while the W incorporation was controlled by varying the power density (W_{power}) applied to the WO_3 target (in the 0.11 to 0.66 $W \cdot cm^{-2}$ range). These sputtering deposition parameters were chosen based on our previous studies on TiO_2:N, TiO_2:W, and TiO_2:WN films [7, 8, 33] [REF TiO2:W]. The TiO_2:WN films were concomitantly deposited onto silicon, quartz, Ti, and ITO substrates. These were mounted on a holder located off-axis at a distance of 20 cm from the sputtering target. Additionally, they were heated during deposition by a quartz lamp heater to an on-substrate temperature of ~470 °C.

Prior to film deposition, the substrates and targets were systematically sputter-cleaned with Ar ions for ~15 min with the shutters closed. No post-acceleration bias was applied to the substrates during the sputtering process. However, the substrates were subjected to a built-in plasma sheath bias of ~-15 V. The thickness of the TiO_2:WN films was *in-situ* monitored by means of a calibrated quartz-crystal microbalance and *ex-situ* measured through cross-sectional high-resolution SEM images by means of a Jeol JSM-6300F microscope. The crystalline structure of the films was characterized by means of a PANalytical X-Pert Pro X-ray diffractometer (XRD) system using Cu$K\alpha$ radiation of 1.5418 Å. Their atomic composition and chemical bonding states were systematically investigated by means of X-ray photoelectron spectroscopy (XPS). The XPS spectra were collected by using the ESCALAB 220i-XL spectrophotometer (Thermo VG Scientific Ltd., UK), equipped with an Al$K\alpha$ (1486.6 eV) twin-anode source. These spectra were collected after a systematic *in-situ* surface cleaning by means of a 5 keV Ar^+ ion sputtering gun. The ultra-violet and visible (UV-Vis) transmittance and reflectance spectra of the TiO_2:WN films were measured by using an Agilent/Varian Cary 5000 system. Thus, their E_g values were deduced from the *x*-intercept of their tangential UV-Vis Tauc plot extrapolation. Photocurrent and EPC degradation

measurements were performed under AM 1.5G simulated solar light (solar simulator model SS50AAA from Photo emission Tech., INC, Camarillo, USA, equipped with a 150 W Xenon lamp). The photocurrent measurements were performed by integrating the samples as photoanodes in a homebuilt quartz (for visible light illumination) PEC cell (250 ml working volume). The cell was equipped with a three-electrode Voltalab 80 system (Radiometer analytical) with a rotating working electrode (CVT 101, Radiometer analytical) and a potentiostat/galvanostat (Tacussel 20V/1A PGP 201). The reference electrode was a saturated Ag/AgCl/KCl electrode, while a platinum wire assembly (Taccusel Pt XM 140) was used as the cathode. For these tests, the TiO_2 thin-films (both doped and undoped) were sputter deposited onto 2.54 cm x 2.54 cm ITO/Quartz substrates. The ITO served as transparent back contact, whereas the rest of the sample periphery was sealed-off with chemically inert epoxy.

In order to perform high-frequency dielectric measurements, planar top electrodes with a 20 μm gap and 200 nm thickness were sputter-deposited onto the TiO_2 thin films by DC sputtering of an Gold (Au) target through a laser etched stainless-steel mask using a Sanuy Denshi DC-701 quick coater. The sputtering current and time was maintained at 10 mA and 1 h, respectively as to obtain the desired thickness. The thin film's dielectric signal was measured via microscope-aligned micro-probe using an E4991A Agilent Tech. network analyser. Accurate spatial models of the sample, electrode, and substrate environment were developed and calculated via electromagnetic field simulations using the Sonnet 13 software suite. The complex permittivity of the sputter deposited thin films in the low MHz to GHz range was determined by fitting measured susceptance onto that calculated data as to extract the TiO_2:W thin film ε' and $\tan(\delta)$ (i.e. $\tan(\delta) = \varepsilon''/\varepsilon'$ and measured $\varepsilon = \varepsilon' + i\varepsilon''$). The dielectric dispersion caused by the interfacial contributions and dipole polarisations was fitted using the empirical relation: $\frac{\varepsilon(\omega)-\varepsilon_\infty}{\varepsilon_0-\varepsilon_\infty} = \sum_{i=1}^{contributions} g_i \left(\frac{1}{1+i\omega\tau_i}\right)$ where

ε_∞ is the permittivity contribution from ionic and electronic resonances, ε_0 the low-frequency permittivity, with g_i and τ_i being the proportionality coefficient and characteristic relaxation time of contributions *i* respectively. A more detailed description of the experimental procedure can be found elsewhere.[34] [REF TiO2:W]

Results and Discussion

Figure 1 (a) shows a typical cross-sectional SEM micrograph of a ~450 nm thick TiO_2:WN thin film on an Si substrate. All of the sputter deposited films were dense and had low surface roughness. No significant differences in morphology were observed between samples of various doping schemes, *i.e.* undoped, W-doped, N-doped, and WN-codoped thin films. Film thicknesses for all samples deposited samples were maintained in the 400-500 nm range. Thin film deposition rates were of 2.0 ±0.5 $nm \cdot min^{-1}$. The sputter deposition rates varied slightly as a result of the varying plasma deposition environments required for the preparation of undoped, W-doped, and N-doped, and WN-codoped TiO_2; *i.e.* Ar plasma with reactive O_2 gas, or with concomitant sputtering of the WO_3 target, and/or with reactive N_2 gas.

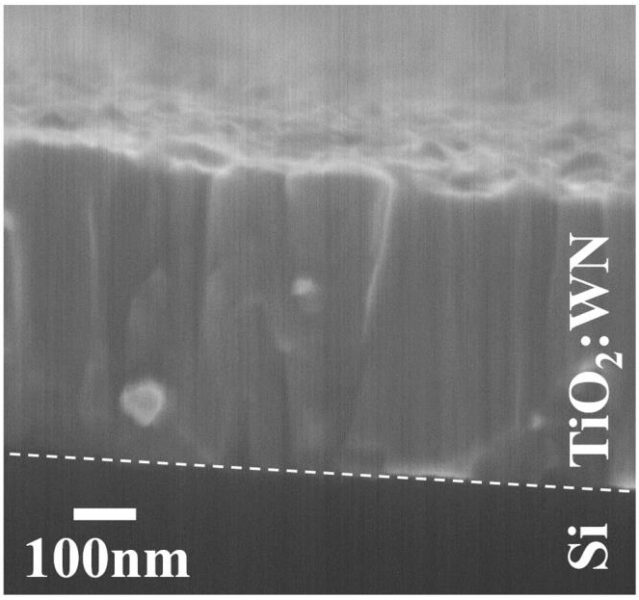

Figure 1 – Typical cross-sectional SEM micrograph of the sputter-deposited TiO_2:WN films. The image shown here is for a film with a W and N doping content of 3.1 at.% and 4.3 at.% respectively having a thickness of ~450 nm.

The dopant incorporation efficiency of the RF-sputtering approach was tracked as a function of deposition parameters W_{power} and R_{N2} via quantitative XPS. These results are presented in Figure 2 (a) and (b) for tungsten ([$W_{tot.}$] at.%) and substitutional nitrogen ([$N_{sub.}$] at.%), respectively. We note from Figure 2 (a) that [$W_{tot.}$] incorporation follows a quasi-linear relationship with applied WO_3 target power (W_{power}). This holds true even when reactive N_2 gas is mixed into the deposition gas (as is the case for WN-codoped thin film deposition). Indicating that [$W_{tot.}$] incorporation is directly dependent on the amount of atomic tungsten present in the deposition plasma. Figure 2 (b) presents the incorporation efficiency of nitrogen as a function of R_{N2} at various fixed levels of W_{power}. We note that incorporation increases steadily with R_{N2}, regardless of applied W_{power}. This trend is seen to plateau past R_{N2} ~15% due to two main factors. Firstly, the sputter-deposited films

reach their solubility limits of [$N_{sub.}$] in the titania lattice. Secondly, the N_2 gas concentration reaches a thermodynamically unfavorable proportion in the Ar sputtering gas (in agreement with our earlier studies of sputter deposited TiO_2:N thin films) [7]. Comparing the [$N_{sub.}$] vs R_{N2} at varying W_{power}, we see that nitrogen incorporation drops slightly with increased power on the WO_3 target. It is likely that increasing W_{power} produces an increase in atomic O (from the WO_3 target) within the deposition plasma. This lowers the overall nitrogen incorporation in the films through competition and transient formation of vacuum pump evacuated gaseous nitrogen-oxygen species (*e.g.* NO_2, NO, etc.).

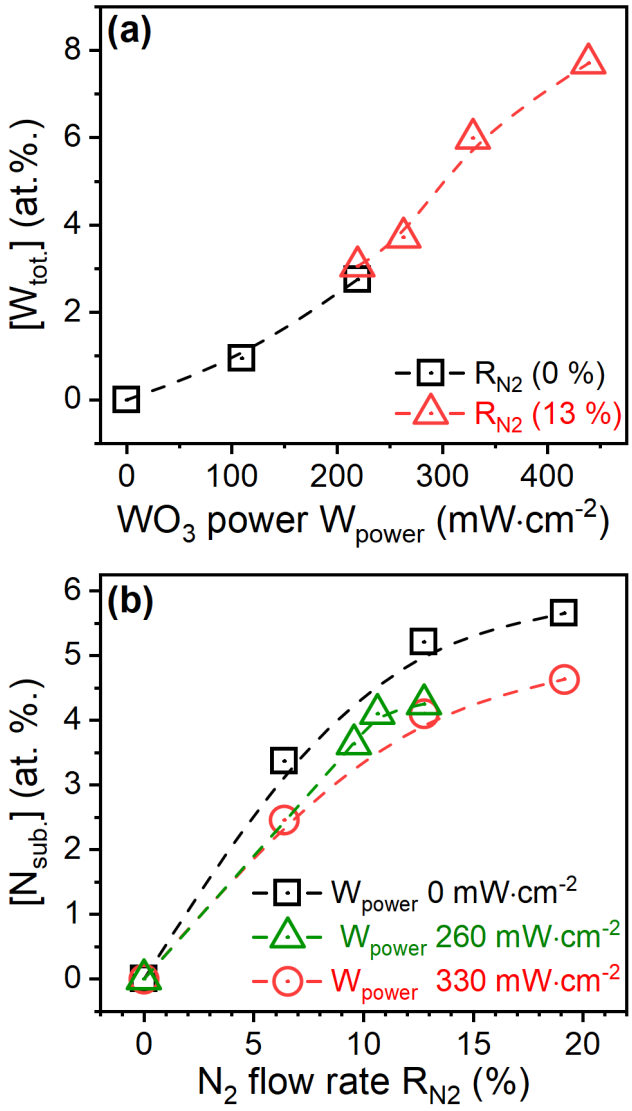

Figure 2 – Dopant incorporation efficiencies as a function of (a) variable WO_3 power (W_{power}) at fixed nitrogen mass flow rates (R_{N2}), and (b) variable R_{N2} at three different fixed W_{power}.

The chemical composition of the deposited thin films was investigated using high-resolution XPS of the O *1s*, Ti *2p*, N *1s*, W *4d*, and W *4f* core level spectra. The deconvoluted spectra are presented in Figure 3 (a), (b), (c), (d), and (e) for the TiO_2, TiO_{2-x}, TiO_2:W, TiO_2:N, and TiO_2:WN type samples, respectively. The energy windows are displayed in order of decreasing binding energy (BE) from left to right.

The undoped TiO_2 XPS spectra in Figure 3 (a) shows that the Ti $2p_{3/2}$ peak can be decomposed into two components, representative of the Ti^{IV} and Ti^{III} oxidation states at 458.6 eV and 456.9 eV, respectively. With their corresponding Ti $2p_{1/2}$ energy levels at ~5.6 eV higher BE [7, 26, 35–37]. The presence of reduced states such as Ti^{III} is symptomatic of sub-stoichiometric features, *i.e.* oxygen-vacancy (V_O) association pairs: $2[Ti^{III}]$-$[V_O^{\cdot\cdot}]$. All of these Ti $2p_{3/2}$ states can be mirror derived from the Ti *3p* signatures, and their corresponding bonding pairs are reflected in the O *1s* spectra. The overlapping Ti *3p* signatures within the W *4f* BE window are greyed out as to visually lighten the figure. Analysis of the XPS O *1s* energy signatures reveals the main TiO_2 lattice oxygen O^A peak at 529.9 eV. It is accompanied with the sub-stoichiometrically bonded O^B at ~0.5eV higher binding energy [35, 36]. The third signature O_{def} is observed at slightly higher BE, associated with defective oxygen species and surface hydroxides [35, 36, 38]. Sputter-deposition with a 100% Ar-gas environment lead to the formation of TiO_{2-x} type films as shown in Figure 3 (b). Such sub-stoichiometric structures, commonly referred to as Magneli phases, show similar properties to those ofTiO_2 films, but with significantly stronger signatures of V_O defects [3, 4, 7, 14, 39]. In their Ti *2p* spectra we note that the defective Ti^{III} peak is significantly increased, and a newly visible Ti^{II} peak that be observed (Ti^{II} $2p_{3/2}$ at 455.3 eV and the $2p_{1/2}$ component at 460.9 eV BE)[3, 40]. Mirrored in the O *1s* energy window, we note a newly visible O^C peak assigned to sub-stoichiometric lattice oxygen species (in the Ti^{II} lattice environment) at ~530.9 eV [35, 36].

Concomitant WO_3-sputtering alongside the main TiO_2 target resulted in the presence of two main W *4f* features in their XPS BE window. These are representative of the W^{VI} ($W_{Ti}^{\cdot\cdot}$) and W^{IV} (W_{Ti}^{x}) states in the tungsten oxide form with the main $4f_{7/2}$ components at 34.5 eV and 32.3 eV, respectively. The $4f_{7/2}$ components are accompanied by their corresponding $4f_{5/2}$ doublets at ~2.2 eV higher BE [30, 37, 41–43]. The $[W^{IV}]$:$[W^{VI}]$ ratio was about 3:2 for most W-doped samples. It

is to be noted that the W *4d* energy window, while insufficiently resolved to discern oxidative states of W, was scanned to assure accurate deconvolution of the Ti *3p* and W *4f* spectra (superimposed in the W *4f* BE window). We can note in the W *4d* window the presence of two doublets. First of these is the W *4d* signature with its corresponding $4d_{5/2}$ and $4d_{3/2}$ peaks at 246.4 eV and 258.8 eV, respectively [30, 37, 41–43]. Secondly, we can note an Ar *2p* doublet at 241.1 eV and 243.2 eV. This signature is constant throughout the investigated samples and arises due to the Ar^+ sputter-cleaning procedure. The Ti *2p* and O *1s* spectra of the W-doped films did not diverge much from the reference TiO_2.

Nitrogen doping (experimentally achieved via increased R_{N2}) resulted in the presence of two N components in the N *1s* BE window at 396.2 eV and 397.2 eV. The former is associated with $N_O^{\bullet}$ (substitutional -Ti-N- type nitrogen) and denoted $N_{sub.}$ and the latter with N_i (interstitial -O-N- type bonds) with the $N_{int.}$ denotation [3, 6, 7, 10, 12, 13, 32]. Additionally, nitrogen doped samples can be seen to form in highly sub-stoichiometric structures. This is evidenced by the increased Ti^{III} and Ti^{II} oxidation state signatures (within the Ti *2p* window) as compared to stoichiometric TiO_2 [3, 4, 7, 14, 32, 39, 40]. However, these V_O signatures are significantly lower than those of TiO_{2-x} type films. In fact, this is a direct result of the $N_O^{\bullet}$ species incorporation, on one hand filling many oxygen vacancies and on the other, creating local charge misbalance via the introduction of extra h^+ promoting the formation of some V_O. This will be further discussed later in the text, in light of the high frequency dielectric spectroscopy studies.

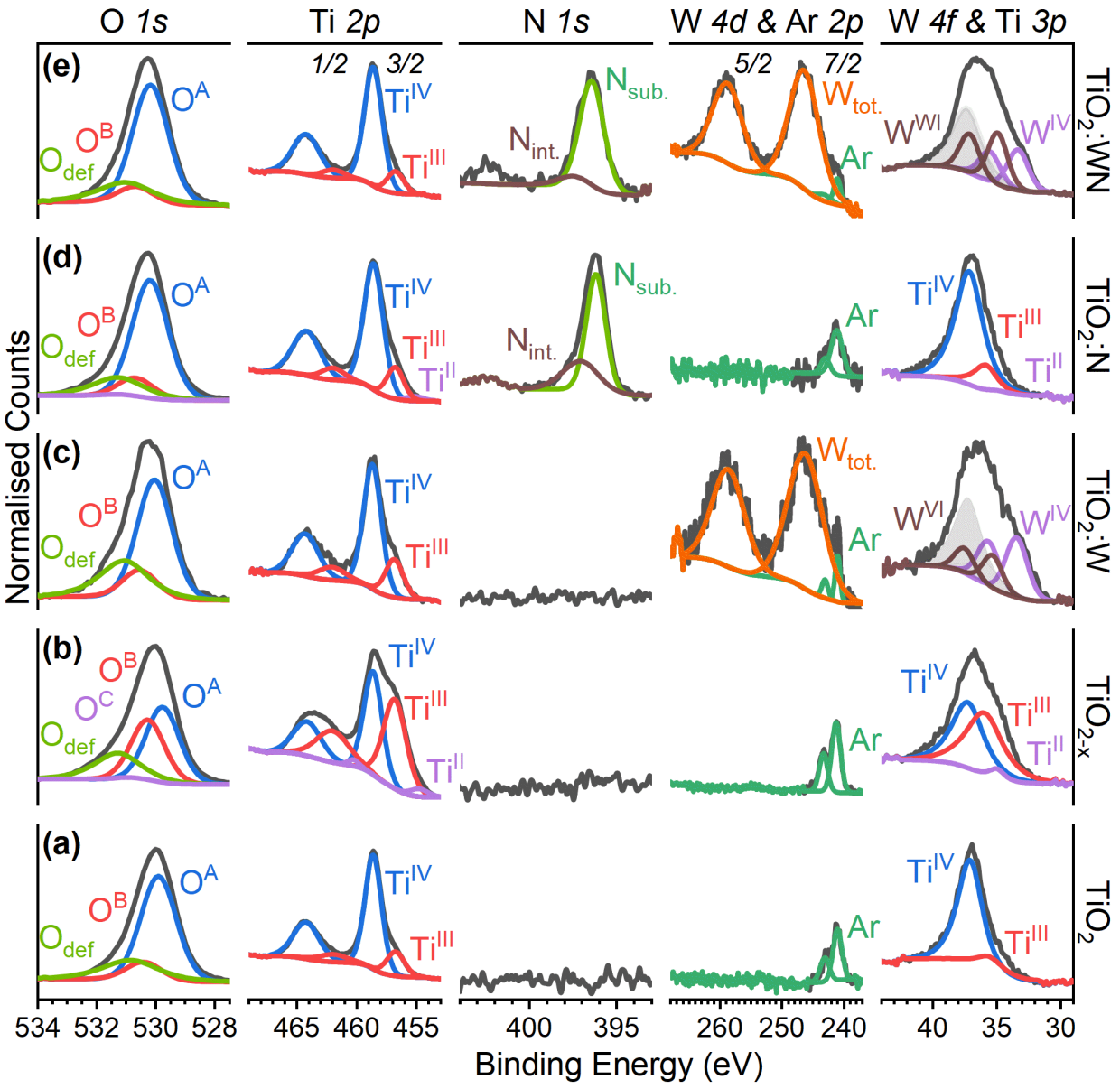

Figure 3 – Representative XPS signals deconvoluted by chemical species. From left to right we see the BE energy windows of the O *1s*, Ti *2p*, N *1s*,W *4d* (also Ar *2p*), and W *4f* (also Ti *3p*) orbitals. From bottom to top we note the (a) TiO_2, (b) TiO_{2-x}, (c) TiO_2:W, (d) TiO_2:N, and (e) TiO_2:WN type samples. The Ti *3p* signatures within the W *4f* BE window are greyed-out for the W containing samples as to visually lighten the figure.

When both W and N are co-introduced simultaneously, XPS features of both substitutional tungsten in the oxide form and substitutional nitrogen were detected. Most of the XPS characteristics were in alignment with those seen for the monodoped samples. However, a few key differences could be noted. Firstly, using the $[Ti^{IV}]/([Ti^{III}]+[Ti^{II}])$ ratio as an indicator of the V_O density, it can be unequivocally stated that WN-codoping leads to reduced V_O densities. This is reinforced by the disappearance of the Ti^{II} signature in the Ti *2p* window for the TiO_2:WN samples as compared to equally doped TiO_2:N samples. Secondly, an inversion in the W population from mostly $[W^{IV}]$ (in the case of TiO_2:W) to mostly $[W^{VI}]$ (for TiO_2:WN thin films) can be observed. Indeed, this is coherent with models showing that on a lattice level $[W^{VI}]$ is charge compensating the nitrogen codopant, *i.e.* formation of the $[W_{Ti}'']$-2$[N_O^{\bullet}]$ charge-compensation pair [20]. These chemical observations were reinforced by XRD observed structural features of the TiO_2:WN thin-films [18].

Figures 4 (a), (b), and (c) show the XRD spectra for the W-doped, N-doped, and WN-codoped TiO_2 from left to right (the figures are arranged in increasing dopant loading from bottom to top). Figure 4 (a) shows that the rutile polymorph is dominant at low tungsten incorporation levels. As previously noted from the XPS observations, these samples have a high $[W^{IV}]$:$[W^{VI}]$ ratio. W^{IV} species (WO_2-type crystal) naturally form in a rutile-like structure, favoring the W-doped system to crystalize as such [44]. Higher doping levels result in both the anatase and rutile phases being observed. This is likely a result of tungsten solubility limits within the titania lattice being reached, causing a segregation of the mostly $[W^{IV}]$-induced rutile and $[W^{VI}]$-containing anatase phases [37]. Similarly, one can note that the N-doped films also exhibit a dopant induced phase change phenomenon. Figure 4 (b) shows that low N-doping leads to a deterioration of the anatase phase quality due to the formation of V_O lattice defects. Whereas heavier doping results in the formation

of an oxynitride phase [7, 8]. This particular structure is known to form with N-doping of heavily sub-stoichiometric Magneli phases (*i.e.* crystalized pseudo-stable phases of TiO_{2-x}).

Simultaneous doping with both the acceptor $N_O^{\bullet}$ and donor W_{Ti}'' species translated to a marked improvement in the crystalline properties of the films. Figure 4 (c) shows that regardless of individual dopant concentrations, as long as their relative dopant ratios are maintained anywhere between ~1:1-2 for [W]:[N], a well defined anatase phase is obtained with no signs of secondary structures. Additionally, the extracted XRD anatase peak FWHM showed a marked improvement in the codoping regime as compared to monodoped samples. With the A(101) peak FWHM of ~0.42° for TiO_2 widening from ~0.47 to ~0.65° for increasingly doped TiO_2:N and then recovering/improving to anywhere from ~0.30 to ~0.44° for the TiO_2:WN. All of these improvements are a direct consequence of the acceptor-donor passivation interplay. As remarked upon in the XPS section, W_{Ti}'' and $N_O^{\bullet}$ dopants charge compensate on a lattice level, resulting in higher solubility of each while raising the V_O formation energy [18–22]. This effect is aided by the better size compatibility of W_{Ti}'' (0.600 Å atomic radii) as compared to W_{Ti}^{x} (0.660 Å atomic radii) with the lattice Ti_{Ti}^{x} (0.605 Å). Further compounded by the lower ratio of $[W^{IV}]$:$[W^{VI}]$ in the TiO_2:WN thin films as compared to TiO_2:W [37]. The aforementioned factors lead to a noted reduction is the dopant induced anatase lattice tensile strain as determined via Willianson-Hall analysis. The strain was determined to be: 0.32±0.09 % for TiO_2, 2.32±0.21 % for TiO_2:N, and 0.24±0.16 % for optimally doped TiO_2:WN [45]. Such structural improvements allowed the formation of a well defined (albeit slightly deformed; with a small compression of the *c* and expansion of the *a* lattice parameters) anatase phase [18, 21, 22].

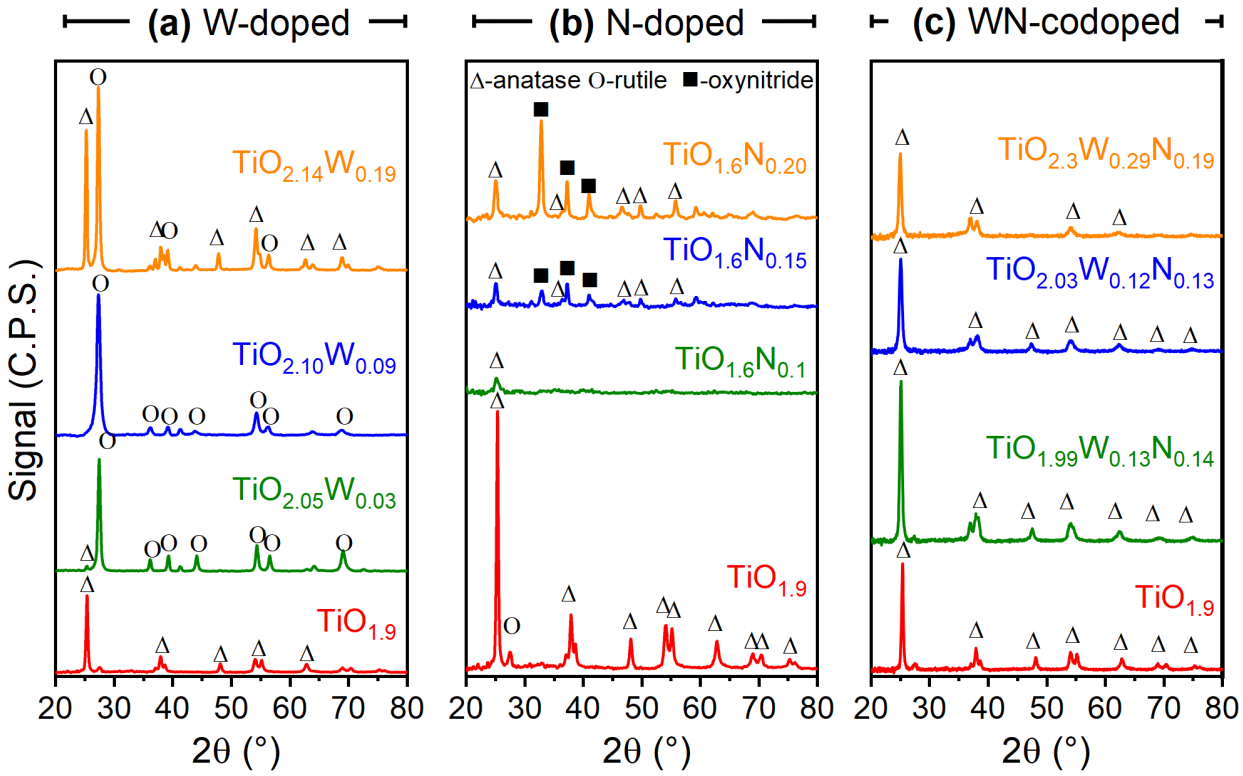

Figure 4 – XRD spectra of the (from left to right) W-doped, N-doped and WN-codoped films. The reference undoped TiO_2 spectra is included in each sample set.

The acceptor-donor passivating scheme's improvements on the material's visible-light photosensitivity were investigated via UV-Vis transmittance and reflectance spectra. Figure 5 (a) presents typical transmittance spectra for the undoped, N-doped, W-doped, and WN-codoped samples. We note that all doped samples showed a red-shifted absorption edge and had increased overall absorbance. While W-doped samples show a small red shift (E_g reduced to 3.0 eV from 3.2 eV), this is mainly form the formation of shallow states below the CBM. This small change is considered insufficient for visible-light photoactivity. We note the highest visible light photosensitivity for the N-doped and WN-codoped films. Our previous works have confirmed that this red-shift is not expected to further improve upon increased dopant loading [7, 8]. Tauc plot extrapolated E_g values for all doping schemes are presented as a function of nitrogen incorporation

in Figure 5 (b). We note that regardless of doping scheme or dopant loading, nitrogen is the dominant factor concerning the thin film's visible-light photosensitivity, *e.g.* all samples with $N_{sub.}$ ~5 at.% have an E_g of ~2.3-2.4 eV.

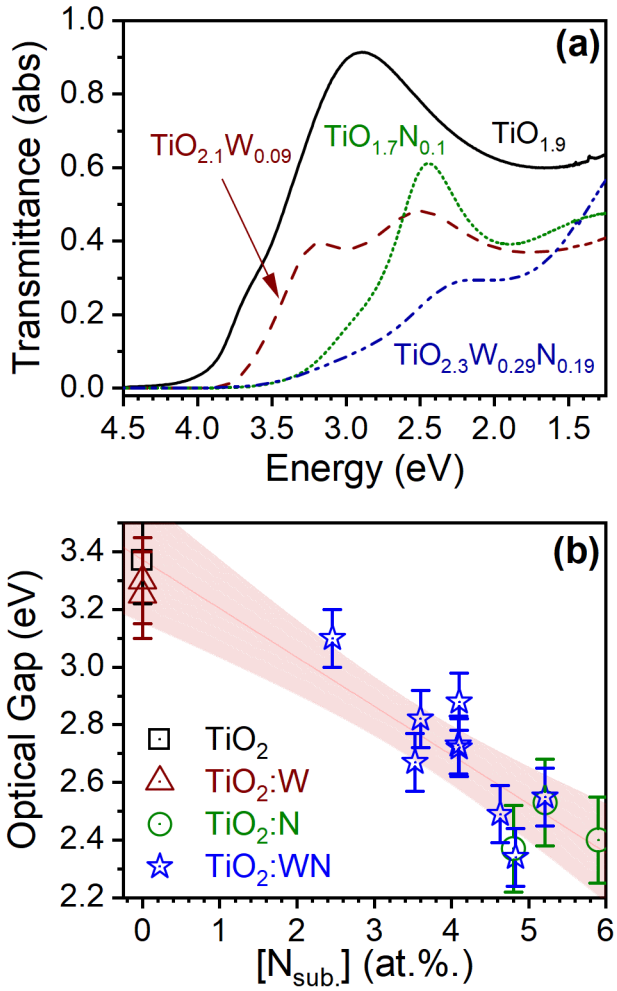

Figure 5 – (a) Typical transmittance spectra of the TiO_2 based films as a function of doping scheme. (b) Variation of effective optical band gap (E_g) as a function of [$N_{sub.}$] content.

In order to study the intrinsic benefits of WN-codoping for the reduction of defect formation, high frequency dielectric spectroscopy (HF-DS) measurements of the sputter deposited films were performed. HF-DS allows the differentiation of various dielectric contributions based on their active frequency range. The total dielectric constant of the material being the combined

contribution of interfacial effects, intrinsic dipoles, ionic contributions, and electronic oscillations, *i.e.* $\varepsilon_{total} \approx \varepsilon_{interface} + \varepsilon_{dipole} + \varepsilon_{ionic} + \varepsilon_{electronic}$. Critically, we previously demonstrated that HF-DS allows us to discern the sub-MHz range $\varepsilon_{interface}$ contributions and the MHz-GHz $\varepsilon_{VO\text{-}dipole}$ contributions associated with V_O defects (*i.e.* $2[Ti^{III}]$-$[V''_O]$) [34, 46, 47] [REF TiO2:W]. Whereas permittivity in the THz and infrared, *i.e.* $\sim\varepsilon'_\infty$ is associated with $\sim \varepsilon_{ionic} + \varepsilon_{electronic}$ and is known to remain relatively constant [REF TiO2:W]. Figures 6 (a) and (b) show typical ε' and ε'' HF-DS spectra for the undoped ($TiO_{1.90}$), oxygen deficient ($TiO_{1.7}$), N-doped ($TiO_{1.5}N_{0.3}$), and WN-codoped ($TiO_{2.4}W_{0.3}N_{0.3}$) type samples.

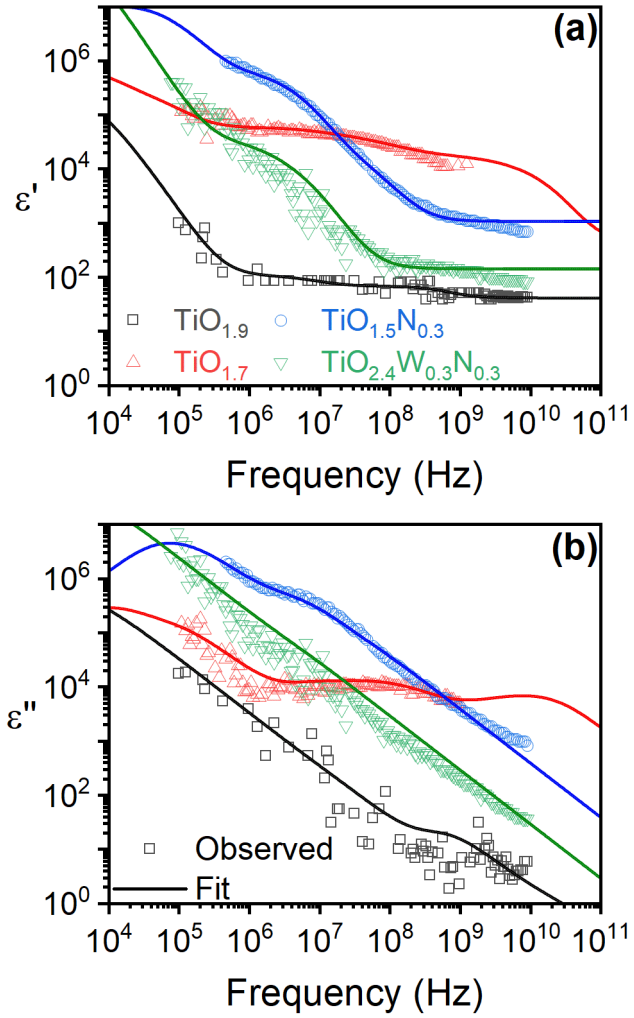

Figure 6 – Typical observed/fitted (symbols/line) (a) ε′ and (b) ε″ HF-DS spectra for the undoped ($TiO_{1.90}$), oxygen deficient ($TiO_{1.7}$), N-doped ($TiO_{1.5}N_{0.3}$), and WN-codoped ($TiO_{2.4}W_{0.3}N_{0.3}$).

All of the samples showed a strong interfacial contribution tapering off in the MHz range [REF TiO2:W]. More importantly, we can note that the sub-stoichiometric samples ($TiO_{1.7}$) show a broad $\varepsilon_{VO\text{-}dipole}$ contribution in the MHz-GHz regime associated with oxygen vacancies, *i.e.* 2[Ti^{III}]-[V''_O] [REF TiO2:W]. Interestingly, this feature is seen to be somewhat reduced for the $TiO_{1.5}N_{0.34}$ sample. Further insight can be obtained from Figure 7 (a) which presents the ε′ HF-DS spectra in

the MHz-GHz regime for a variety of TiO_2:N samples. Figure 7 (b) shows the ε' values at 1 GHz as a function of nitrogen doping. In accordance with Figure 6, the V_O dielectric signature is seen here to be strongly dependent on the nitrogen content of the films and their oxygen deficiency. When transitioning from a stoichiometric regime to a nitrogen doped one (bottom guiding line in Figure 7 (b)), we note an increase in the V_O signature of about one order of magnitude. By replacing some of the lattice oxygen, $N_O^{\bullet}$ type doping creates local charge disparities, lowering the formation energy of V_O. This effect is seen to saturate upon reaching the $N_O^{\bullet}$ solubility limits in the material. However, if compared to sub-stoichiometric titania films (top guiding line in Figure 8 (a)), nitrogen doping leads to a reduction in the V_O signature due to preferential filling of the vacancies, *i.e.* $N_O^{\bullet}$ type doping. This is true up to an optimal $N_O^{\bullet}$ doping point, past which the increase in local charge disparities outweighs the benefits provided by nitrogen vacancy filling.

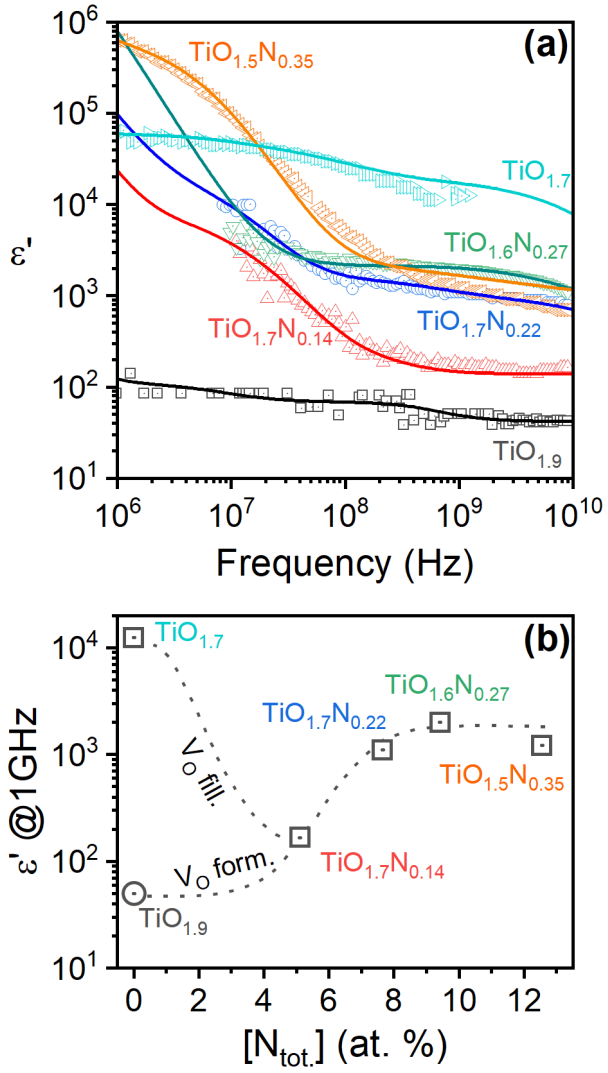

Figure 7 – (a) ε′ HF-DS spectra for the undoped ($TiO_{1.90}$), oxygen deficient ($TiO_{1.7}$), and carrying levels of N-doped titania thin films. (b) Extracted ε′ values at 1 GHz as a function of nitrogen content. Dotted line added as a visual guide.

Critically, Figure 6 shows that optimally WN-codoped samples show a significantly reduced V_O $\varepsilon_{VO\text{-}dipole}$ signature in the MHz-GHz regime. This is in direct alignment with our previous results, showing that the newly formed $[W_{Ti}'']$-$2[N_O^{\bullet}]$ charge-compensation pairs reduce the V_O formation. In order to confirm this hypothesis, we studied the TiO_2:WN $\varepsilon_{VO\text{-}dipole}$ response at 1 GHz when one dopant was fixed, and one varied. Figure 8 presents these ε′ values at 1 GHz as a function of

nitrogen content [$N_{tot.}$] at fixed tungsten content [$W_{tot.}$] ~ 3.8 at.% (bottom-left; in black) and of [$W_{tot.}$] at fixed [$N_{tot.}$] ~ 7.5 at.% (top-right; in red). Indeed, we can note that at fixed [W_{Ti}''], any increase in nitrogen leads to an increase in the V_O signature due to added h^+ ([$N_O^\bullet$]). In reverse, at fixed [$N_O^\bullet$], additional [W_{Ti}''] passivated an increasing portion of h^+ (brought on by $N_O^\bullet$), decreasing the formation of V_O. It is likely that this effect saturates once all of the codopants have change-compensated, *i.e.* when all of the eligible tungsten and nitrogen formed defect-association pairs [W_{Ti}'']-2[$N_O^\bullet$]. However, we do not have sufficient data to observe this experimentally.

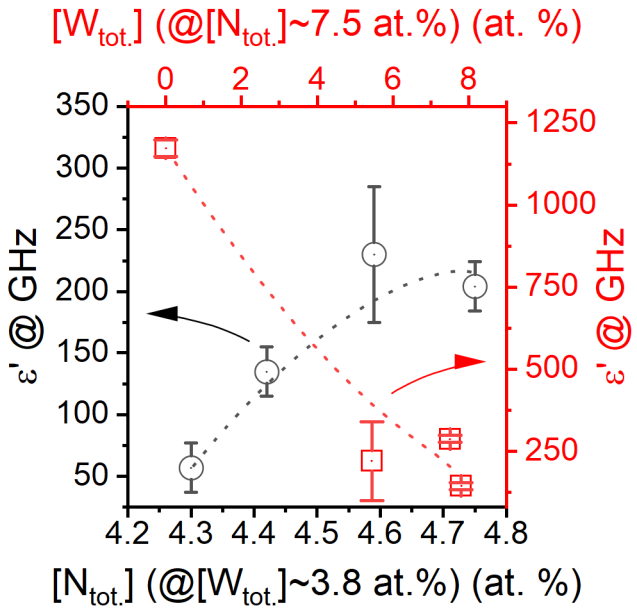

Figure 8 – Extracted ε′ values at GHz as a function of nitrogen content [$N_{tot.}$] at fixed tungsten content [$W_{tot.}$] ~ 3.8 at.% (bottom-left in black) and of [$W_{tot.}$] at fixed [$N_{tot.}$] ~ 7.5 at.% (top-right in red). (COMMENT: REPLACE NTOT AND WTOT WITH SUB?)

Finally, solar-light (AM 1.5G) driven photocurrent tests were performed as to investigate the electro-photo-catalytically relevant contribution of the optoelectronic improvements brought on by WN-codoping. Optimized TiO_2:N and TiO_2:WN with an E_g~2.3eV were investigated alongside reference TiO_2. These were integrated as photoanodes in a homebuilt quartz EPC cell. The

obtained AM 1.5G driven net-photocurrents as a function of applied extraction potential are presented in Figure 9. As expected, in the low potential range, TiO_2 samples showed best performance, with net photocurrents of about ~0.05 $mA \cdot cm^{-2}$ driven by the UV-light in the solar spectrum. However, upon application of sufficient extraction potential (*e.g.* >1.5V), the doped samples greatly outperform the reference thin films. With the N-doped and WN-codoped thin films reaching net photocurrents of ~0.09 $mA \cdot cm^{-2}$ and ~0.18 $mA \cdot cm^{-2}$, respectively (values taken at ~2.25V). This increase in performance is a direct consequence of the dopant induced visible light photosensitivity, allowing both the TiO_2:N and TiO_2:WN to utilise a significantly higher portion of photons to drive charge separation. The added benefit of acceptor-donor passivated codoping can be directly observed through the increase in photocurrent for the WN-codoped samples as compared to identically photosensitised N-doped samples. We can note from Figure 9 that the combination of visible-light photosensitivity and acceptor-donor passivated codoping translates to about two times higher extracted photocurrent. In a separate study, we noted that the co-introduction of the W dopant decreased the formation V_O defects [33]. This resulted in optimized WN-codoped thin films having photocharge lifetime constants up to three times longer than those measured in their N-doped counterparts. Specifically, the photocharge trapping decay constants were of 90 ± 7 ns for TiO_2:WN *versus* 30 ± 10 µs for TiO_2:N [33]. This improvement translated to increased efficiency of exciton transport within the codoped material as compared to the monodoped one. Herein explaining the marked improvement in observed photocurrent production.

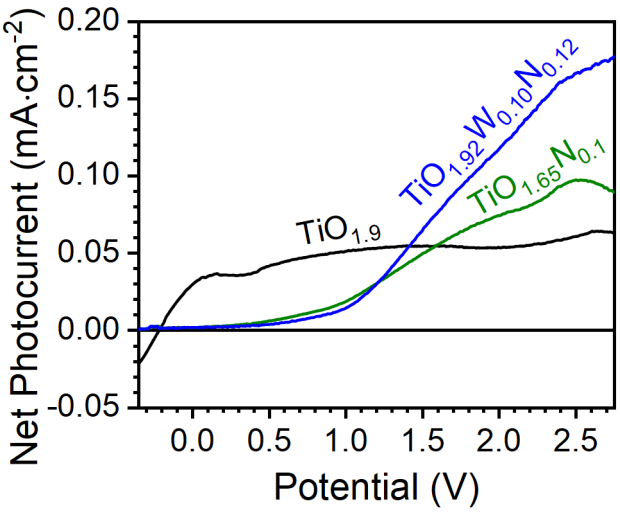

Figure 9 –Net-photocurrents under 1.5AM light as a function of extraction potential (V) for undoped, N-doped, and WN-codoped TiO_2 thin films integrated as photoanodes.

Conclusions

In summary, we have successfully synthesised *in-situ* doped and codoped TiO_2, TiO_2:N, TiO_2:W, and TiO_2:WN thin films via a reliable RF-magnetron sputtering process. Careful analysis of the XPS signatures revealed the presence of both W and N dopants in mostly substitutional states (W_{Ti}'' and $N_O^{\bullet}$) for the mono- and codoped thin films. More importantly, TiO_2:WN thin films had a significant reduction in V_O densities. These results were corroborated by XRD analysis which revealed that WN-codoping not only increased the solubility limits for each dopant, but also drastically improved crystallinity, ensuring formation of a well-defined anatase phase for a wide range of dopant concentrations. UV-Vis spectra demonstrated that both TiO_2:N and TiO_2:WN type films had a red-shifted absorption edge well into the visible-light spectrum. Further analysis showed that substitutional nitrogen doping was the lead contributor to visible light photosensitivity of the monodoped and codoped thin films with all samples having a substitutional nitrogen content of ~5 at.% showing an E_g ~2.3 eV. The reduction of V_O defects was reiterated and confirmed via

HF-DS studies. These demonstrated that WN-codoping was successful in passivating the formation of the GHz active 2[Ti^{III}]-[V''_O] defect pairs via the formation of [W_{Ti}'']-2[$N_O^{\bullet}$] charge-compensation pairs. Finally, the practical benefits of the visible light photosensitivity were directly demonstrated via visible-light driven net-photocurrent tests, where TiO_2:WN samples outperformed identically photosensitised TiO_2:N samples. In these tests, TiO_2:WN (~0.18 $mA \cdot cm^{-2}$) photoanodes showed a two fold increase in photocurrent as compared to TiO_2:N (~0.09 $mA \cdot cm^{-2}$), and three/four-fold increase as compared to undoped TiO_2 (~0.05 $mA \cdot cm^{-2}$).

Acknowledgements

The authors would like to acknowledge the financial support from NSERC (the Natural Science and Engineering Research Council of Canada) and the FRQNT (Le Fonds de Recherche du Québec-Nature et Technologies) through its strategic Network "Plasma-Québec". The authors declare that they have no conflict of interest.

References

1. O'Regan B, Grätzel M (1991) A low-cost, high-efficiency solar cell based on dye-sensitized colloidal TiO2 films. Nature 353:737–740 . doi: 10.1038/353737a0

2. Khan SUM, Al-Shahry M, Ingler WB (2002) Efficient photochemical water splitting by a chemically modified n-TiO2. Science (80-) 297:2243–5 . doi: 10.1126/science.1075035

3. Emeline A V., Kuznetsov VN, Rybchuk VK, Serpone N (2008) Visible-Light-Active Titania Photocatalysts: The Case of N-Doped TiO 2 s—Properties and Some Fundamental Issues. Int J Photoenergy 2008:1–19 . doi: 10.1155/2008/258394

4. FUJISHIMA A, ZHANG X, TRYK D (2008) TiO2 photocatalysis and related surface

phenomena. Surf Sci Rep 63:515–582 . doi: 10.1016/j.surfrep.2008.10.001

5. Hashimoto K, Irie H, Fujishima A (2005) TiO 2 Photocatalysis: A Historical Overview and Future Prospects. Jpn J Appl Phys 44:8269–8285 . doi: 10.1143/JJAP.44.8269

6. Asahi R (2001) Visible-Light Photocatalysis in Nitrogen-Doped Titanium Oxides. Science (80-) 293:269–271 . doi: 10.1126/science.1061051

7. Delegan N, Daghrir R, Drogui P, El Khakani MA (2014) Bandgap tailoring of in-situ nitrogen-doped TiO 2 sputtered films intended for electrophotocatalytic applications under solar light. J Appl Phys 116:153510 . doi: 10.1063/1.4898589

8. Pandiyan R, Delegan N, Dirany A, et al (2016) Probing the Electronic Surface Properties and Bandgap Narrowing of in situ N, W, and (W,N) Doped Magnetron-Sputtered TiO 2 Films Intended for Electro-Photocatalytic Applications. J Phys Chem C 120:631–638 . doi: 10.1021/acs.jpcc.5b08057

9. Scanlon DO, Dunnill CW, Buckeridge J, et al (2013) Band alignment of rutile and anatase TiO2. Nat Mater 12:798–801 . doi: 10.1038/nmat3697

10. Di Valentin C, Pacchioni G, Selloni A (2004) Origin of the different photoactivity of N-doped anatase and rutile TiO2. Phys Rev B 70:085116 . doi: 10.1103/PhysRevB.70.085116

11. Di Valentin C, Pacchioni G, Selloni A, et al (2005) Characterization of Paramagnetic Species in N-Doped TiO 2 Powders by EPR Spectroscopy and DFT Calculations. J Phys Chem B 109:11414–11419 . doi: 10.1021/jp051756t

12. Lynch J, Giannini C, Cooper JK, et al (2015) Substitutional or Interstitial Site-Selective

Nitrogen Doping in TiO 2 Nanostructures. J Phys Chem C 119:7443–7452 . doi: 10.1021/jp512775s

13. Peng F, Cai L, Yu H, et al (2008) Synthesis and characterization of substitutional and interstitial nitrogen-doped titanium dioxides with visible light photocatalytic activity. J Solid State Chem 181:130–136 . doi: 10.1016/j.jssc.2007.11.012

14. Torres GR, Lindgren T, Lu J, et al (2004) Photoelectrochemical Study of Nitrogen-Doped Titanium Dioxide for Water Oxidation. J Phys Chem B 108:5995–6003 . doi: 10.1021/jp037477s

15. D'Arienzo M, Siedl N, Sternig A, et al (2010) Solar Light and Dopant-Induced Recombination Effects: Photoactive Nitrogen in TiO 2 as a Case Study. J Phys Chem C 114:18067–18072 . doi: 10.1021/jp105426t

16. Liu B, Wen L, Zhao X (2007) The photoluminescence spectroscopic study of anatase TiO 2 prepared by magnetron sputtering. Mater Chem Phys 106:350–353 . doi: 10.1016/j.matchemphys.2007.06.012

17. Katoh R, Furube A, Yamanaka K, Morikawa T (2010) Charge Separation and Trapping in N-Doped TiO 2 Photocatalysts: A Time-Resolved Microwave Conductivity Study. J Phys Chem Lett 1:3261–3265 . doi: 10.1021/jz1011548

18. Yin W-J, Tang H, Wei S-H, et al (2010) Band structure engineering of semiconductors for enhanced photoelectrochemical water splitting: The case of TiO2. Phys Rev B 82:045106 . doi: 10.1103/PhysRevB.82.045106

19. Çelik V, Mete E (2012) Range-separated hybrid exchange-correlation functional analyses

of anatase TiO2 doped with W, N, S, W/N, or W/S. Phys Rev B 86:205112 . doi: 10.1103/PhysRevB.86.205112

20. Li M, Zhang J, Zhang Y (2012) First-principles calculation of compensated (2N, W) codoping impacts on band gap engineering in anatase TiO2. Chem Phys Lett 527:63–66 . doi: 10.1016/j.cplett.2012.01.009

21. Long R, English NJ (2010) Synergistic Effects on Band Gap-Narrowing in Titania by Codoping from First-Principles Calculations. Chem Mater 22:1616–1623 . doi: 10.1021/cm903688z

22. Long R, English NJ (2009) First-principles calculation of nitrogen-tungsten codoping effects on the band structure of anatase-titania. Appl Phys Lett 94:132102 . doi: 10.1063/1.3114608

23. Wang D, Zou Y, Wen S, Fan D (2009) A passivated codoping approach to tailor the band edges of TiO2 for efficient photocatalytic degradation of organic pollutants. Appl Phys Lett 95:012106 . doi: 10.1063/1.3174917

24. Gai Y, Li J, Li S-S, et al (2009) Design of Narrow-Gap TiO2: A Passivated Codoping Approach for Enhanced Photoelectrochemical Activity. Phys Rev Lett 102:036402 . doi: 10.1103/PhysRevLett.102.036402

25. Cui X, Rong S, Cao Y, et al (2013) One-step hydrothermal synthesis of nitrogen and tungsten codoped TiO2 nanorods with high visible light photocatalytic activity. Appl Phys A 113:47–51 . doi: 10.1007/s00339-013-7896-8

26. Thind SS, Wu G, Tian M, Chen A (2012) Significant enhancement in the photocatalytic

activity of N, W co-doped TiO 2 nanomaterials for promising environmental applications. Nanotechnology 23:475706 . doi: 10.1088/0957-4484/23/47/475706

27. Thind SS, Wu G, Chen A (2012) Synthesis of mesoporous nitrogen–tungsten co-doped TiO2 photocatalysts with high visible light activity. Appl Catal B Environ 111–112:38–45 . doi: 10.1016/j.apcatb.2011.09.016

28. Folli A, Bloh JZ, Beukes E-P, et al (2013) Photogenerated Charge Carriers and Paramagnetic Species in (W,N)-Codoped TiO 2 Photocatalysts under Visible-Light Irradiation: An EPR Study. J Phys Chem C 117:22149–22155 . doi: 10.1021/jp408181r

29. Bloh JZ, Folli A, Macphee DE (2014) Adjusting Nitrogen Doping Level in Titanium Dioxide by Codoping with Tungsten: Properties and Band Structure of the Resulting Materials. J Phys Chem C 118:21281–21292 . doi: 10.1021/jp507264g

30. Mishra T, Mahato M, Aman N, et al (2011) A mesoporous WN co-doped titania nanomaterial with enhanced photocatalytic aqueous nitrate removal activity under visible light. Catal Sci Technol 1:609 . doi: 10.1039/c1cy00042j

31. Sajjad AKL, Shamaila S, Zhang J (2012) Study of new states in visible light active W, N co-doped TiO2 photo catalyst. Mater Res Bull 47:3083–3089 . doi: 10.1016/j.materresbull.2012.08.032

32. Asahi R, Morikawa T, Irie H, Ohwaki T (2014) Nitrogen-Doped Titanium Dioxide as Visible-Light-Sensitive Photocatalyst: Designs, Developments, and Prospects. Chem Rev 114:9824–9852 . doi: 10.1021/cr5000738

33. Delegan N, Pandiyan R, Johnston S, et al (2018) Lifetime Enhancement of Visible Light

Induced Photocharges in Tungsten and Nitrogen in situ Codoped TiO 2 :WN Thin Films. J Phys Chem C 122:5411–5419 . doi: 10.1021/acs.jpcc.7b11266

34. Teranishi T, Akiyama N, Ayano K, et al (2012) Quasi-millimeter-wave absorption behavior in Y/Yb-stabilized zirconia ceramics. Appl Phys Lett 100:242903 . doi: 10.1063/1.4729147

35. Biesinger MC, Payne BP, Grosvenor AP, et al (2011) Resolving surface chemical states in XPS analysis of first row transition metals, oxides and hydroxides: Cr, Mn, Fe, Co and Ni. Appl Surf Sci 257:2717–2730 . doi: 10.1016/j.apsusc.2010.10.051

36. Jackman MJ, Thomas AG, Muryn C (2015) Photoelectron Spectroscopy Study of Stoichiometric and Reduced Anatase TiO 2 (101) Surfaces: The Effect of Subsurface Defects on Water Adsorption at Near-Ambient Pressures. J Phys Chem C 119:13682–13690 . doi: 10.1021/acs.jpcc.5b02732

37. Sathasivam S, Bhachu DS, Lu Y, et al (2015) Tungsten Doped TiO2 with Enhanced Photocatalytic and Optoelectrical Properties via Aerosol Assisted Chemical Vapor Deposition. Sci Rep 5:10952 . doi: 10.1038/srep10952

38. Kitano M, Funatsu K, Matsuoka M, et al (2006) Preparation of nitrogen-substituted TiO2 thin film photocatalysts by the radio frequency magnetron sputtering deposition method and their photocatalytic reactivity under visible light irradiation. J Phys Chem B 110:25266–72 . doi: 10.1021/jp064893e

39. Rumaiz AK, Woicik JC, Cockayne E, et al (2009) Oxygen vacancies in N doped anatase TiO2: Experiment and first-principles calculations. Appl Phys Lett 95:262111 . doi: 10.1063/1.3272272

40. Wong M-S, Pang Chou H, Yang T-S (2006) Reactively sputtered N-doped titanium oxide films as visible-light photocatalyst. Thin Solid Films 494:244–249 . doi: 10.1016/j.tsf.2005.08.132

41. Li J, Xu J, Dai WL, et al (2008) One-pot synthesis of twist-like helix tungsten-nitrogen-codoped titania photocatalysts with highly improved visible light activity in the abatement of phenol. Appl Catal B Environ 82:233–243 . doi: 10.1016/j.apcatb.2008.01.022

42. Ng KT, Hercules DM (1976) Studies of nickel-tungsten-alumina catalysts by x-ray photoelectron spectroscopy. J Phys Chem 80:2094–2102 . doi: 10.1021/j100560a009

43. Sun M, Xu N, Cao YW, et al (2000) Nanocrystalline Tungsten Oxide Thin Film: Preparation, Microstructure, and Photochromic Behavior. J Mater Res 15:927–933 . doi: 10.1557/JMR.2000.0132

44. Wong FJ, Ramanathan S (2013) Heteroepitaxy of distorted rutile-structure WO2 and NbO2 thin films. J Mater Res 28:2555–2563 . doi: 10.1557/jmr.2013.247

45. Williamson G., Hall W. (1953) X-ray line broadening from filed aluminium and wolfram. Acta Metall 1:22–31 . doi: 10.1016/0001-6160(53)90006-6

46. Teranishi T, Kanemoto R, Hayashi H, Kishimoto A (2017) Effect of the (Ba + Sr)/Ti ratio on the microwave-tunable properties of Ba 0.6 Sr 0.4 TiO 3 ceramics. J Am Ceram Soc 100:1037–1043 . doi: 10.1111/jace.14700

47. Teranishi T, Hayashi H, Kishimoto A, Tsurumi T (2012) Broadband spectroscopy of the complex conductivity of polycrystalline yttria-stabilized zirconia. Mater Sci Eng B 177:69–73 . doi: 10.1016/j.mseb.2011.09.039